16
Topics in Organometallic Chemistry

Topics in Organometallic Chemistry

Recently Published and Forthcoming Volumes

Surface and Interfacial Organometallic Chemistry and Catalysis
Volume Editors: C. Copéret, B. Chaudret
Vol. 16, 2005

Chiral Diazaligands for Asymmetric Synthesis
Volume Editors: M. Lemaire, P. Mangeney
Vol. 15, 2005

Palladium in Organic Synthesis
Volume Editor: J. Tsuji
Vol. 14, 2005

Metal Carbenes in Organic Synthesis
Volume Editor: K. H. Dötz
Vol. 13, 2004

Theoretical Aspects of Transition Metal Catalysis
Volume Editor: G. Frenking
Vol. 12, 2005

Ruthenium Catalysts and Fine Chemistry
Volume Editors: C. Bruneau, P. H. Dixneuf
Vol. 11, 2004

New Aspects of Zirconium Containing Organic Compounds
Volume Editor: I. Marek
Vol. 10, 2004

Precursor Chemistry of Advanced Materials
CVD, ALD and Nanoparticles
Volume Editor: R. Fischer
Vol. 9, 2005

Metallocenes in Stereoselective Synthesis
Volume Editor: T. Takahashi
Vol. 8, 2004

Transition Metal Arene π-Complexes in Organic Synthesis and Catalysis
Volume Editor: E. P. Kündig
Vol. 7, 2004

Organometallics in Process Chemistry
Volume Editor: R. D. Larsen
Vol. 6, 2004

Organolithiums in Enantioselective Synthesis
Volume Editor: D. M. Hodgson
Vol. 5, 2003

Organometallic Bonding and Reactivity: Fundamental Studies
Volume Editor: J. M. Brown, P. Hofmann
Vol. 4, 1999

Activation of Unreactive Bonds and Organic Synthesis
Volume Editor: S. Murai
Vol. 3, 1999

Lanthanides: Chemistry and Use in Organic Synthesis
Volume Editor: S. Kobayashi
Vol. 2, 1999

Alkene Metathesis in Organic Synthesis
Volume Editor: A. Fürstner
Vol. 1, 1998

Surface and Interfacial Organometallic Chemistry and Catalysis

Volume Editors: Christophe Copéret · Bruno Chaudret

With contributions by

J.-M. Basset · F. Bonino · S. Bordiga · R. L. Brutchey · J.-P. Candy
B. Chaudret · C. Copéret · A. Damin · H.-J. Freund · K. L. Fujdala
B. C. Gates · E. Groppo · C. Lamberti · C. Prestipino · T. Risse
A. Roucoux · T. D. Tilley · A. Zecchina

Springer

The series *Topics in Organometallic Chemistry* presents critical reviews of the present and future trends in polymer and biopolymer science including chemistry, physical chemistry, physics and material science. It is adressed to all scientists at universities and in industry who wish to keep abreast of advances in the topics covered.
As a rule, contributions are specially commissioned. The editors and publishers will, however, always be pleased to receive suggestions and supplementary information. Papers are accepted for *Topics in Organometallic Chemistry* in English.
In references *Topics in Organometallic Chemistry* is abbreviated *Top Organomet Chem* and is cited as a journal.

Springer WWW home page: http://www.springeronline.com
Visit the TOMC content at http://www.springerlink.com/

Library of Congress Control Number: 2005928333

ISSN 1436-6002
ISBN-10 3-540-26496-5 Springer Berlin Heidelberg New York
ISBN-13 978-3-540-26496-5 Springer Berlin Heidelberg New York
DOI 10.1007/b105251

Springer is a part of Springer Science+Business Media

springeronline.com

Printed in Germany

Cover design: *Design & Production* GmbH, Heidelberg
Typesetting and Production: LE-TEX Jelonek, Schmidt & Vöckler GbR, Leipzig

Printed on acid-free paper 02/3141 YL – 5 4 3 2 1 0

Volume Editors

Christophe Copéret

Laboratoire de Chimie Organometallique de Surface
43 Bd du 11 Novembre 1918
69616 Villeurbanne, France
coperet@cpe.fr

Bruno Chaudret

Laboratoire de Chimie de Coordination du CNRS
route de Narbonne
31077 Toulouse Cédex 04, France
chaudret@lcc-toulouse.fr

Editorial Board

Topics in Organometallic Chemistry
Also Available Electronically

For all customers who have a standing order to The Handbook of Environmental Chemistry, we offer the electronic version via SpringerLink free of charge. Please contact your librarian who can receive a password or free access to the full articles by registering at:

springerlink.com

If you do not have a subscription, you can still view the tables of contents of the volumes and the abstract of each article by going to the SpringerLink Homepage, clicking on "Browse by Online Libraries", then "Chemical Sciences", and finally choose The Handbook of Environmental Chemistry.

You will find information about the

- Editorial Board
- Aims and Scope
- Instructions for Authors
- Sample Contribution

at springeronline.com using the search function.

Preface

Molecular chemistry has laid down the rules for understanding and preparing well-defined organometallic and metallo-organic complexes that have been central to the development of homogeneous catalysts. The goal of this book is to show that molecular chemistry is also a tool for studying much larger systems, such as those involved in heterogeneous catalysis. Heterogeneous catalysts are typically made of oxide materials, metallic particles, or organometallic components. While the main part of the catalyst is constituted by the bulk of the material, the catalytic events take place at the interface between the reactant phase and the surface of the material, and more specifically at the active sites. Thus, these systems correspond to large ensembles of atoms (metal particles or oxides), which are composed of organometallic and metallo-organic building blocks, and active sites, which can be described as organometallic and metallo-organic centres. It is therefore obvious that molecular organometallic (and inorganic) chemistry must play an essential role in the field of heterogeneous catalysis whether discussing the method of preparation of catalysts, the understanding of catalytic phenomena on surfaces, or the rational development of better catalysts. In this book, we have therefore addressed these various questions through selected examples. The first two chapters focus on the molecular understanding of known industrial heterogeneous catalysts. The third contribution discusses the synthesis and the properties of tailored oxide materials. The next paper addresses the use of surface science as a tool for understanding the active sites of heterogeneous catalysts. The fifth chapter tackles the preparation of well-defined active sites through surface organometallic chemistry and their relation to the understanding of industrial processes. The sixth contribution discusses the use of metal clusters as a model of metallic particles. Finally, the remaining two chapters focus on the use of well-defined organometallic complexes for the synthesis of nanoparticles and their use in catalysis.

Villeurbanne, Toulouse,
September 2005

Bruno Chaudret
and Christophe Copéret

Contents

Top Organomet Chem (2005) 16: 1–35
DOI 10.1007/b138072

Published online: 14 September 2005

Anatomy of Catalytic Centers in Phillips Ethylene Polymerization Catalyst

A. Zecchina (✉) · E. Groppo · A. Damin · C. Prestipino

Department of Inorganic, Physical and Materials Chemistry and NIS Centre of Excellence, University of Torino, Via P. Giuria 7, 10125 Torino, Italy
adriano.zecchina@unito.it

Abstract A relevant fraction of the polyethylene produced in the world (about 30%) is obtained with the Phillips process. Many efforts in the last 30 years have been devoted to establish the valence state and the structure of the catalytically active species formed by reduction with ethylene. However, no certain conclusions have been obtained so far, even using a CO-prereduced simplified system. In this review it will be shown that the CO-reduced system, although highly homogeneous from the point of view of the valence state (definitely II) and nuclearity, is heterogeneous as far the local structure of the sites is concerned. Only Cr(II) ions with the lowest coordination (which unfortunately are only a minor fraction of the total) are responsible for the catalytic activity, while the overwhelming majority of surface sites play the role of spectator under normal reaction conditions. In the second part of the review the proposed initiation/polymerization mechanisms are fully reported. A peculiarity of the Cr/SiO_2 system, which makes it unique among the polymerization catalysts (Ziegler–Natta, metallocenes, etc.), lies in the fact that it does not requires any activator (such as aluminium alkyls etc.) because ethylene itself is able to create the catalytic center from the surface chromate precursor. It will be shown that a unifying picture has not yet been achieved, even in this case. The aim of

this review is to illustrate, on one side, how much progress has been made recently in the understanding of the site's structure and, on the other side, the strategies and the techniques which can be adopted to study the catalyst under working conditions. It will be shown that the methods adopted for the Cr/SiO_2 system have paradigmatic character and can be extended to other catalytic systems.

Keywords Chromium · Ethylene polymerization · Phillips catalyst

Abbreviations

CT	Charge transfer
DFT	Density functional theory
DRS	Diffuse reflectance spectroscopy
EPR	Electron paramagnetic resonance
EXAFS	Extended X-ray absorption fine structure spectroscopy
FT	Fourier transform
FTIR	Fourier transformed infrared spectroscopy
IR	Infrared spectroscopy
MAO	Methylalumoxane
NMR	Nuclear magnetic resonance
PE	Polyethylene
RT	Room temperature
SIMS	Secondary ions mass spectroscopy
TOF	Turnover frequency
UV-Vis	Ultraviolet-visible spectroscopy
XANES	X-ray absorption near edge structure spectroscopy
XPS	X-ray photoelectron spectroscopy
α_{OCrO}	angle O – Cr – O
α_{SiOSi}	angle Si – O – Si
ν_{AB}	A-B stretching mode
$\tilde{\nu}_{AB}$	A-B stretching frequency
$\Delta\tilde{\nu}$(CO)	variation of the C – O stretching frequency with respect to that in the gas phase

1 Introduction

The discovery of olefin polymerization catalysts in the early 1950s by Ziegler and Natta represents a milestone in industrial catalysis. Tremendous evolution has taken place since then: today, fourth generation Ziegler–Natta catalysts and metallocene-based "single-site" catalysts display activity and stereo-selectivity close to those of enzymatic processes optimized by nature over millions of years. The production of polyolefins is nowadays a multibillion industrial activity and, among all the synthetic polymers, polyethylene has the highest production volume [1]. Three classes of olefin polymerization catalysts can be distinguished: (i) Phillips-type catalysts, which are composed of a chromium oxide supported on an amorphous material such as

silica [2–7]; (ii) Ziegler–Natta catalysts, which consist of a transition metal compound and an activator (aluminum alkyl, methylalumoxane MAO, etc.) whose function is to introduce an alkyl group into the coordination sphere of the metal [1, 8–12]; (iii) single-site homogeneous catalysts or supported-homogeneous catalysts, like metallocene catalysts [13–15], which also need an activator.

The Cr/SiO_2 Phillips catalysts, patented in 1958 by Hogan and Banks [2], are nowadays responsible for the commercial production of more than one third of all the polyethylene sold world-wide [7, 16].

The Phillips catalyst has attracted a great deal of academic and industrial research over the last 50 years. Despite continuous efforts, however, the structure of active sites on the Phillips-type polymerization systems remains controversial and the same questions have been asked since their discovery. In the 1950s, Hogan and Banks [2] claimed that the Phillips catalyst "is one of the most studied and yet controversial systems". In 1985 McDaniel, in a review entitled "Chromium catalysts for ethylene polymerization" [4], stated: "we seem to be debating the same questions posed over 30 years ago, being no nearer to a common view". Nowadays, it is interesting to underline that, despite the efforts of two decades of continuous research, no unifying picture has yet been achieved.

Briefly, the still-open questions concern the structure of the active sites and the exact initiation/polymerization mechanism [17]. The difficulties encountered in the determination of the structure of the active sites of the real catalyst are associated with several factors. Among them is the problem associated with the initial reduction step, consisting in the reaction between ethylene and the anchored chromate or dichromate precursors, a process which leads to the formation of the real active sites. In fact, in this reaction ethylene oxidation products (including H_2O) are formed which, as they remain partially adsorbed on the catalyst, make the characterization of the surface sites of the reduced Cr/SiO_2 system a highly complex problem. Fortunately the reduction of the oxidized precursors can also be performed with a simpler reductant like CO, with formation of a single oxidation product (CO_2), which is not adsorbed on the sample [4]. This CO-reduced catalyst, containing prevalently anchored Cr(II), has consequently been considered as a "model catalyst" and an ideal playground where the application of sophisticated in situ characterization methods could finally give the opportunity to solve the mystery of the structure of active sites and of the initiation mechanism.

The aim of this contribution is to illustrate, on one side, how much progress has been made in the understanding of the site's structure and, on the other side, to illustrate the open question and to propose new strategies which should be adopted to study the catalyst under working conditions.

2
Spectroscopic Characterization of the Catalyst

2.1
Surface of the Silica Support

The Cr/SiO_2 system is one of the simplest examples of a catalyst where the sites are formed by anchoring a well-known chromium compound to the hydroxyl groups of the silica surface. This specific support/molecular precursor interaction confers to the chromium sites unique catalytic properties, differentiating the Cr/SiO_2 system from other Cr-based catalysts. It is thus evident that a brief description of the surface structure of SiO_2, together with a discussion of the surface models and of the modifications induced by thermal treatments, are of vital importance to understand the anchoring process and the chromium localization.

To this end we recall that the rigid tetrahedron SiO_4 is the building block of all siliceous materials: from quartz, through microporous zeolites, to amorphous silica. The reason why such a relatively rigid unit is able to aggregate in many different ways lies in the peculiar bond between two SiO_4 moieties. In contrast with the rigidity of the O – Si – O angle, it costs virtually no energy to change the Si – O – Si angle in the 130–180° range. Because of such flexibility, amorphous silica is easily formed and shows a great stability. It consists of a network of such building blocks with a random distribution of the Si – O – Si angle centered around 140°.

Peripheral SiO_4 groups located on the external surfaces of the silica particles carry OH groups, which terminate the unsaturated valences. Different types of surface hydroxyls have been identified, differing either by the number of hydroxyl groups per Si atom, or by their spatial proximity. Roughly, OH groups can be divided as following: (i) isolated free (single silanols), ≡ SiOH; (ii) geminal free (geminal silanols or silanediols), $= Si(OH)_2$; (iii) vicinal, or bridged, or OH groups bound through the hydrogen bond (H-bonded single silanols, H-bonded geminals, and their H-bonded combinations). On the SiO_2 surface there also exist surface siloxane groups or ≡ Si – O – Si ≡ bridges exposing oxygen atoms on the surface.

A model of a fully hydroxylated unreconstructed SiO_2 surface, obtained using a slab of amorphous silica [18] and saturating the dangling bonds with OH groups, is shown in Fig. 1a. From this model it is evident that the average OH number per 100 $Å^2$ is around five and that a fraction of them are located at distances $\leq$ 2–3 Å and then can interact via hydrogen bonding [19–21]. Correspondingly, the IR spectrum of amorphous silica treated at low temperature is characterized by a broad band in the OH stretching region (at about 3600–3100 cm^{-1}).

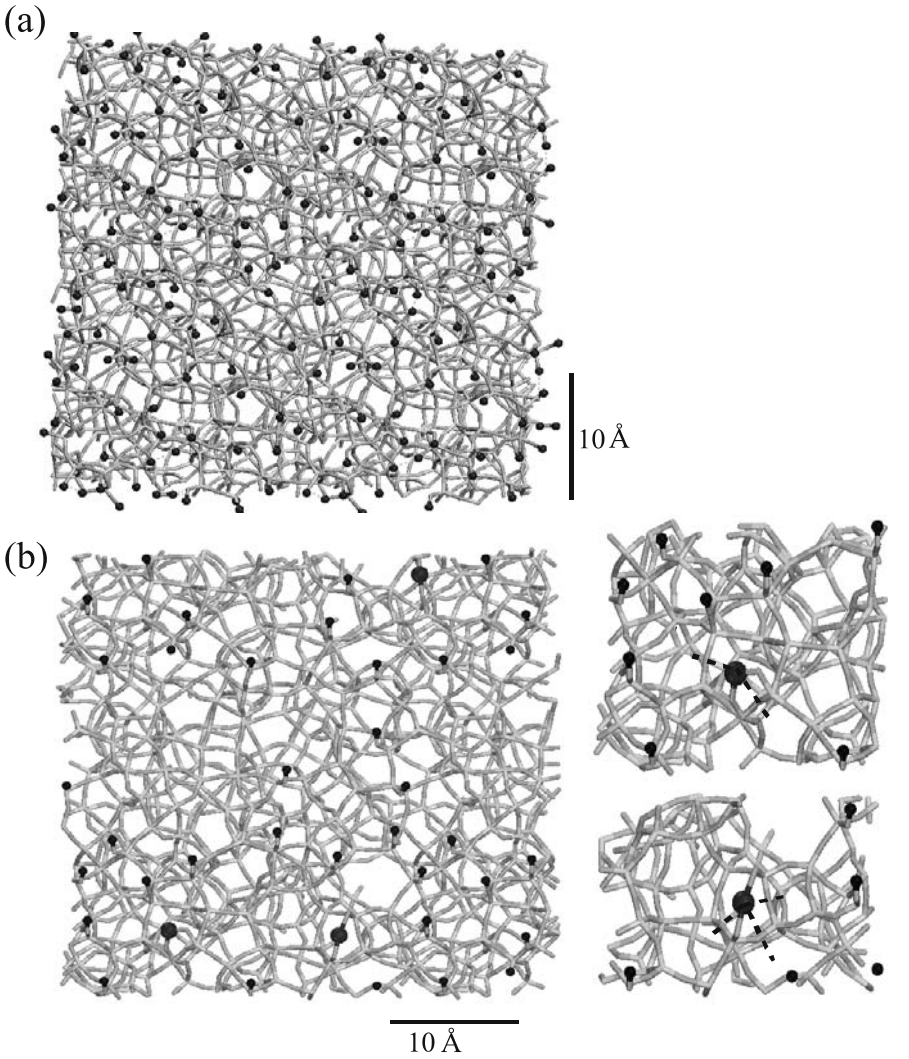

Fig. 1 **a** Model of an unreconstructed SiO_2 surface fully hydroxylated. The model was obtained by cutting a slab of amorphous silica and saturating the dangling bonds with OH groups [18]. **b** Representation of the Cr/SiO_2 surface obtained by grafting Cr(II) ions on a partially hydroxylated SiO_2 surface. In the zoomed *inserts* are clearly visible the different environment of two of the chromium ions. The interaction of the Cr sites with weak ligands (siloxane bridges or OH groups) are evidenced by dashed lines. *Light* and *dark gray* sticks connect together silicon and oxygen atoms, respectively. *Little black* balls represent hydrogen atoms and the big *black* balls represent Cr(II) ions

By increasing the temperature of treatment, the species interacting via hydrogen bonding react via elimination of a water molecule and form a new (possibly strained) siloxane bond, according with the reaction path reported

in Scheme 1. Correspondingly, the samples dehydrated at high temperature show only a very sharp IR band at about 3748 cm^{-1}, attributed to the OH stretch of isolated surface silanols [22–27]. On the basis of the extensive literature published so far [17, 19, 21] it can be stated with confidence that silica samples outgassed at about 873 K in vacuo are characterized by a silanol concentration very near to one OH per 100 $Å^2$. This means that nearly all the silanols are isolated and that their average distance is about 7–10 Å.

The siloxane bridges formed upon dehydroxylation can be classified into several groups, depending upon the structure of the immediate surroundings. A schematic but more detailed version of the dehydration process reported in Scheme 1 and of the formed structures is given in Scheme 2 [17]. These structures are characterized by the presence of two-, three-, four-, etc. membered silicon open rings. The strain present in these structures decreases going from left to right, parallel to the increase of the Si – O – Si bond angle: $\alpha'_{SiOSi} < \alpha''_{SiOSi} < \alpha'''_{SiOSi} < \alpha''''_{SiOSi}$. In the model of a fully hydroxylated unreconstructed silica surface reported in Fig. 1a, we can quite easily find silanols belonging to two-, three-, four-, etc. membered silicon open rings. Of course,

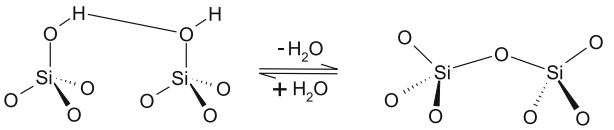

Scheme 1 Reaction between two adjacent silanol groups interacting via H-bonding (*dashed line*) on the silica surface leads to formation of strained siloxane bonds and molecular water

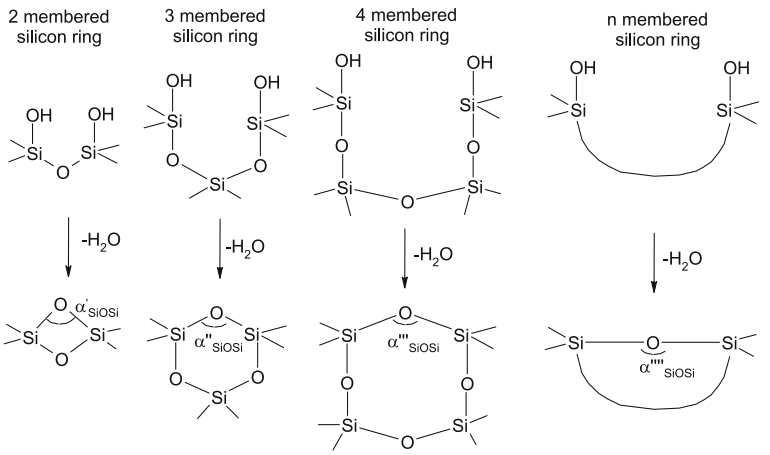

Scheme 2 Different siloxane bridge structures formed upon dehydroxylation of silica surface. The increasing dimension of silicon rings and, consequently, of the Si – O – Si angle reflects a decreasing of the strain of these structures

Scheme 2 is still oversimplified, because it does not take into consideration that the two silicon atoms directly involved in the hydroxyl condensation are also linked to other rings in a three-dimensional mode and that part of the surface strain could be localized on these rings. The appearance in the IR spectra of new vibrations in the 880–940 cm^{-1} region, attributed to the modes of strained siloxane bridges in two membered rings [26, 28–32], well evidences this fact.

For all the above mentioned reasons the full classification of the siloxane bridges formed upon dehydroxylation of amorphous silica surface is an extremely complex task. In the context of the Phillips catalyst, it is important to underline here that dehydroxylation of the silica surface is necessarily associated with the appearance of surface strain. This may have deep consequences on the structure of chromium centers grafted on the silica surface in the Cr/SiO_2 system and therefore on the activity of the catalyst, as we will describe in the following sections. In fact, as the anchoring process involves suitably spaced OH groups, it is evident that the surface structure of silica has great influence on the bonding and location of the anchored species.

2.2 Anchoring Process and Structure of Anchored Cr(VI)

The Phillips Cr/silica catalyst is prepared by impregnating a chromium compound (commonly chromic acid) onto a support material, most commonly a wide-pore silica, and then calcining in oxygen at 923 K. In the industrial process, the formation of the propagation centers takes place by reductive interaction of Cr(VI) with the monomer (ethylene) at about 423 K [4]. This feature makes the Phillips catalyst unique among all the olefin polymerization catalysts, but also the most controversial one [17].

As summarized previously, the surface of the silica used for anchoring the Cr(VI) is fully covered by hydroxyl groups ($\equiv Si-OH$). The surface silanols are only weakly acidic and hence can react with the stronger H_2CrO_4 acid with water elimination, thus acting as anchoring sites. The anchoring process is an acid–base type reaction and occurs at temperatures between 423 and 573 K. In this esterification reaction surface hydroxyl groups are consumed, and chromium becomes attached to the surface by oxygen linkages ($Si-O-Cr$), in the hexavalent state (see Scheme 3).

The molecular structure of the anchored Cr(VI) has been a strong point of discussion in the literature, and several molecular structures (monochromate, dichromate, polychromates) have been proposed (see Scheme 3). The nature of the silica support, the chromium loading, and the activation method can all influence the chemical state of the supported chromium.

Weckhuysen et al. [6, 33] have recently published several UV-Vis DRS works devoted to investigate the surface chemistry of supported chromium catalysts as a function of the support composition. The same authors [34] have also tried

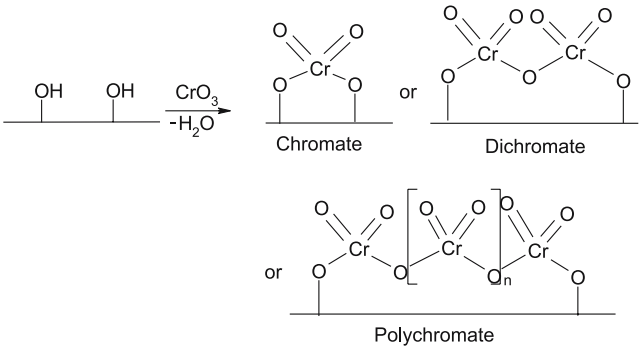

Scheme 3 Anchoring reaction of chromate on a silica support. Adjacent surface hydroxyl groups are consumed and chromium attaches to the surface by oxygen linkages, either in mono-, di- or polychromate forms

to establish the monochromates/dichromates ratio on the basis of the different intensities of the charge transfer (CT) bands present in the spectra of calcined samples ("monochromates": bands at 44 100, 30 600 and 20 300 cm^{-1}; "dichromates": bands at 45 500, 36 600 and 25 000 cm^{-1}). They have inferred that the nuclearity of Cr is extremely sensitive to the support type and more particularly to the specific preparation method. By analyzing the $O \rightarrow Cr(VI)$ CT transitions in UV-Vis DRS spectra of the calcined catalysts, the main chromium species were shown to be a mixture of hexavalent dichromate (band in the 30 000 cm^{-1} region) and monochromate (band in the 28 000 cm^{-1} region) on laboratory sol-gel silica supports (700 m^2/g); while monochromate dominates on industrial pyrogenic silica supports (Cab-O-Sil, 300 m^2/g) characterized by low chromium loadings. They have also found that the dichromate-to-monochromate ratio increases with chromium loading.

Raman spectroscopy has also been widely used to characterize the SiO_2-supported Cr(VI) oxide species, as a function of chromium loading and calcination temperature, in air and in vacuo [6, 33, 35, 36]. Hardcastle et al. [36] have shown that variation of calcination temperature dramatically changes the Raman spectrum of $Cr(VI)/SiO_2$, which is related to the dehydroxylation of SiO_2 at high temperatures. Only a single strong Raman band characteristic of the dehydrated surface chromium oxide species on the silica support was observed at 986 cm^{-1}. In a recent work [37], Dines and Inglis have reported the Raman spectra of the $Cr(VI)/SiO_2$ system obtained in controlled atmosphere by using an excitation λ of 476.5 nm. The spectrum shows a single band at 990 cm^{-1} and a weak shoulder centered at 1004 cm^{-1}. The 990 cm^{-1} band was attributed to the symmetric CrO stretching vibration associated with terminal $Cr = O$ bonds of the surface chromium species, and the shoulder at 1004 cm^{-1} to the antisymmetric CrO stretch.

Raman experiments are confirmed by XPS and secondary ion mass spectrometry (SIMS) measurements performed by Thüne et al. [38] on a surface

science model sample, obtained by impregnating flat Si(100) conducting single crystal substrate covered by amorphous silica with aqueous CrO_3 solution [38–43]. The key observation is that a model catalyst with a 2 Cr/100 Å^2 loading shows only $Cr_1Si_1O_x$ fragments, while on a second sample, where a part of the chromium was forced to form clusters, Cr_2O_x fragments are easily detectable. Combining the XPS and SIMS techniques, the authors concluded that this is a strong evidence that chromate can only anchor to the silica surface as a monomer [38].

From all these data it can be concluded that the dominant oxidized species on Cr/SiO_2 samples, characterized by a chromium content in the 0–1% (by weight), is the monochromate. As the concentration of the most active samples is in the 0.5–1% range, hereafter we will only consider the monochromate for further considerations concerning the structure of anchored species. On the basis of Scheme 2, the anchoring of chromic acid on suitably spaced OH doublets can originate different species, characterized by an increasing α_{OCrO} bond angle and consequently by a decreasing strain, as illustrated in Scheme 4.

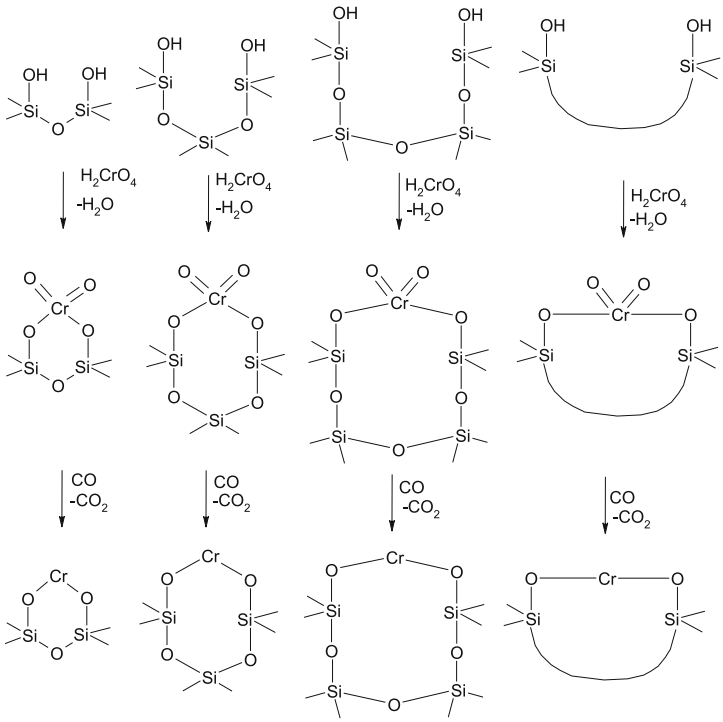

Scheme 4 Cr(VI) anchoring reaction on silicon membered rings of increasing dimensions (and decreasing strain) and the successive CO-reduction. Surface anchoring sites are those reported in Scheme 2

2.3 Reduction Process and Structure of Reduced Chromium

When a calcined Cr(VI)/SiO_2 catalyst is fed with ethylene at 373–423 K, an induction time is observed prior to the onset of the polymerization. This is attributed to a reduction phase, during which chromium is reduced and ethylene is oxidized [4]. Baker and Carrick obtained a conversion of 85–96% to Cr(II) for a catalyst exposed to ethylene at 400 K; formaldehyde was the main by-product [44]. Water and other oxidation products have been also observed in the gas phase. These reduction products are very reactive and consequently can partially cover the surface. The same can occur for reduced chromium sites. Consequently, the state of silica surface and of chromium after this reduction step is not well known. Besides the reduction with ethylene of Cr(VI) precursors (adopted in the industrial process), four alternative approaches have been used to produce supported chromium in a reduced state:

(i) Thermal reduction of Cr(VI)/SiO_2 with CO or H_2 [45–54]
(ii) Photochemical reduction of Cr(VI)/SiO_2 with CO or H_2 [55–60]
(iii) Exchange of silica hydroxyls with organometallic reagents containing reduced chromium [46, 61]
(iv) Ion exchange with aqueous solutions of Cr(III) [62–64]

2.3.1 Oxidation State of Reduced Chromium

Thermal reduction at 623 K by means of CO is a common method of producing reduced and catalytically active chromium centers. In this case the induction period in the successive ethylene polymerization is replaced by a very short delay consistent with initial adsorption of ethylene on reduce chromium centers and formation of active precursors. In the CO-reduced catalyst, CO_2 in the gas phase is the only product and chromium is found to have an average oxidation number just above 2 [4, 7, 44, 65, 66], comprised of mainly Cr(II) and very small amount of Cr(III) species (presumably as α-Cr_2O_3 [66]). Fubini et al. [47] reported that reduction in CO at 623 K of a diluted Cr(VI)/SiO_2 sample (1 wt. % Cr) yields 98% of the silica-supported chromium in the +2 oxidation state, as determined from oxygen uptake measurements. The remaining 2 wt. % of the metal was proposed to be clustered in α-chromia-like particles. As the oxidation product (CO_2) is not adsorbed on the surface and CO is fully desorbed from Cr(II) at 623 K (reduction temperature), the resulting catalyst acquires a model character; in fact, the siliceous part of the surface is the same of pure silica treated at the same temperature and the anchored chromium is all in the divalent state.

The CO-reduced catalyst polymerizes ethylene much like its ethylene-reduced hexavalent parent and produces almost identical polymer [4]. Since the polymer properties are extremely sensitive to the catalyst pretreatment,

this is a strong endorsement for the conclusion that Cr(II) is probably also the precursor of the active species on the commercial catalyst after reduction by ethylene. Further evidence comes from XPS experiments, which showed analogous spectra for the CO or ethylene reduced catalysts [67].

Anchored Cr(II) are very reactive and adsorb oxygen with a brilliant flash of chemioluminescence, converting the chromium back to its original orange hexavalent state [2–4, 68]. The intensity of this yellow-orange light flash decreases with increasing reduction temperature of the catalyst and decreasing initial calcination temperature. This chemioluminescence has an orange emission line at 625.8 nm and is due to oxygen atoms (O^*) which are formed at coordinatively unsaturated Cr(II) sites [7]. The ease with which this reversal reaction occurs suggests that there is a little rearrangement during reduction at 623 K. Fubini et al. [47], by means of calorimetric measurements, pointed out the occurrence of two distinct reoxidation processes, one very fast (i.e., little or non-activated), the other very slow and definitely activated, the transition between them being quite abrupt. At room temperature the former is by far more important. This process can be simply thought of as the breaking of an oxygen molecule onto a chromium ion giving rise to a surface chromate. No activation energy is required, in particular if account is taken that π-bonded oxygen molecule (peroxidic-like structure) probably acts as the intermediate for the reaction [69].

2.3.2
Structure of Cr(II) Sites

As in the case of the Cr(VI) species, the structure of Cr(II) on the silica surface has also been in much dispute in the past and has been widely investigated by several spectroscopic (such as UV-Vis DRS [7, 34, 45, 47, 70], IR [30, 47–50, 53, 54, 71–77], EXAFS-XANES [33, 66], EPR [33], XPS [67, 78–80] etc.) and chemical techniques.

The UV-Vis DRS spectrum of the CO-reduced Cr/SiO_2 sample (0.5 wt. % Cr loading on pyrogenic silica) shows a strong absorption in the CT region (there are at least two overlapped components at about 28 000 and 30 000 cm^{-1}) and two bands in the d – d region, (at transition energies of about 12 000 and 7500 cm^{-1}) (Fig. 2, curve 1). Transitions in the 7000–10 000 and 10 000–13 000 cm^{-1} regions have been previously attributed to coordinatively unsaturated Cr(II) species [33, 45, 47, 48, 65, 70]. The spectrum is characteristic of diluted samples and is independent from the type of siliceous support. In principle, the location and intensity of d – d bands should allow the determination of the coordination state and of the symmetry of a transition metal ion. Unfortunately, due to the lack of data on homogeneous Cr(II) compounds, the only safe conclusion which can be derived from the presence of a doublet in the 7500–12 000 cm^{-1} region is that the Cr(II) centers are in highly distorted structure and that the ions are preferentially sensing

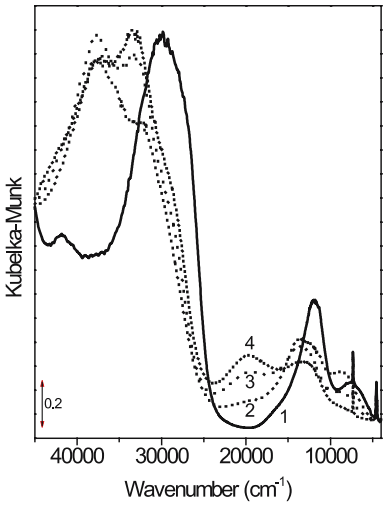

Fig. 2 UV-Vis DRS spectra of reduced $Cr(II)/SiO_2$ sample (0.5 wt % by Cr loading) upon increasing dosages of CO at RT. *Curve 1* $Cr(II)/SiO_2$ reduced in CO at 623 K. *Curves 2–4* increasing dosages of CO from 0.1 mbar to 50 mbar (unpublished spectra)

the crystal field caused by two strong SiO^- ligands. This broad conclusion is in agreement with the Cr(II) structures which can be derived by CO reduction from the anchored structures discussed before, as reported in Scheme 4. Of course, the structures represented in Scheme 4 do not consider surface relaxation which increases the crystal field stabilization. It can be hypothesized that surface locations are certainly present where, beside the strong $Si-O^-$, other weaker ligands (like the oxygens of adjacent SiOSi bridges) contribute to the ligand field stabilization.

Recently, Espelid and Børve performed detailed ab initio calculations on the number, energy region, and electric-dipole oscillator strength of the observable electronic transitions of coordinatively unsaturated mononuclear Cr(II) sites, changing from pseudo-tetrahedral to pseudo-octahedral geometries as a function of the α_{OCrO} bond angle [81]. This study helps in the assignment of the UV-Vis spectra discussed above. The mononuclear Cr(II) species were represented by three cluster models : a pseudo-tetrahedral site, *T*, with an angle of 116°; a pseudo-octahedral site, *O*, with an angle of 180°; and a site with an intermediate α_{OCrO} bond angle (135°), *I*. When the theoretical results and the experimental observations are compared, it can be concluded that there is a reasonable correspondence between the calculated frequencies of *T* sites and the experimental frequencies.

The assignment given so far is further demonstrated by the study of the spectroscopic modifications induced by the interaction with CO (Fig. 2, curves 2–4). Upon increasing the CO pressure at RT we observe the consumption of the two d – d bands described before (12 000 and 7500 cm^{-1})

and the intermediate growth of two bands shifted at higher values (14 000 and 8600 cm^{-1}). Analogously, in the CT region, the consumption of the CT band at 28 000–30 000 cm^{-1} occurs, accompanied by the growth of a new intense band at 37 700 cm^{-1}. The clear appearance of two isosbestic points at 10 000 and 13 100 cm^{-1} indicates a 1 : 1 transformation Cr(II) + CO → Cr(II)···CO. Further increase of the CO pressure leads to the disappearance of the 14 000–8600 cm^{-1} doublet and to the formation of a new absorption centered at 20 000 cm^{-1}. The isosbestic point at 16 000 cm^{-1} ensures that we are dealing with the addition of a second CO molecule, following a Cr(II)···CO + CO → Cr(II)···$(CO)_2$ process which is accompanied by the appearance of a CT component at about 33 400 cm^{-1}.

These two-step features, which will be further proved by the FTIR spectra of adsorbed CO, can be summarized as follows. The adsorption of CO, being accompanied by the increase of the coordination number due to the formation of mono- and dicarbonyl species, causes a shift of the d – d transitions toward the values more typical of the octahedral coordination. Furthermore, in the presence of CO (electron donor molecule) more energy is required to transfer electrons from O to Cr; as a consequence, the O → Cr(II) CT transition shifts at higher frequencies (from 28 000–30 000 to 33 700 cm^{-1}). At increasing CO pressure the CO → Cr(II) CT transition also becomes visible (band at 33 400 cm^{-1}). Analogous features have been reported in the past for NO adsorption on the reduced Cr/SiO_2 system [48, 82].

From the UV-Vis data the following structural picture is emerging. Several types of Cr(II) sites are present on the amorphous silica surface. All the grafted Cr(II) species have a coordination sphere constituted by two strong SiO^- ligands. When the strong SiO^- ligands belong to the smallest cycles they form with Cr(II) an angle α_{OCrO} near to tetrahedral value (left side of Scheme 4). In this case we speak of pseudo-tetrahedral structure (*T*). The O – Cr bond is expected to be quite covalent. The angle α_{OCrO} gradually grows when cycle dimension increases and for large cycles it is approaching 180° (right side of Scheme 4). In this case we can speak of pseudo-octahedral complexes. Due to surface relaxation, a variable number of weak siloxane ligands is certainly present in the coordination sphere of the Cr(II) ions. On the standard reduced sample Cr(II) sites in distorted tetrahedral environment are the most abundant and protruding species, characterized by a high adsorption activity. Nevertheless, a small fraction of more saturated Cr(II) sites, unable to coordinate CO molecules, is contemporarily present, as demonstrated by the permanence of a residue of the unperturbed d – d bands at the maximum CO coverage and of the broad absorption in the 20 000–15 000 cm^{-1} range observed for the sample before CO dosage.

At this point, we can schematically represent the structure of Cr(II) sites as $(SiO)_2Cr^{II}L_n$, where L represents a weak ligand (oxygen of a SiOSi bridge) and *n* is a not fully known figure which increases upon activation at high temperature. The adsorption of CO at room temperature on grafted Cr(II) sites

is accompanied by a modification of their coordination number, following reactions reported in Eq. 1:

$$(SiO)_2Cr^{II}L_n \xrightarrow{CO} (SiO)_2Cr^{II}L_n(CO) \xrightarrow{CO} (SiO)_2Cr^{II}L_n(CO)_2 \quad (1)$$

Actually, the scheme has only a qualitative character, because it does not take into consideration that the α_{OCrO} angle can vary in a wide interval, as discussed above. Furthermore, we have to consider that the adsorption of molecules is always associated with a surface relaxation phenomenon. The relaxation may occur starting from an increment of the Cr–L distance to a complete displacement of the ligand L, as we will discuss.

IR spectroscopy of adsorbed carbon monoxide has been used extensively to characterize the diluted, reduced Cr/silica system [48–54, 60, 76, 77]. CO is an excellent probe molecule for Cr(II) sites because its interaction is normally rather strong. The interaction of CO with a transition metal ion can be separated into electrostatic, covalent σ-dative, and π-back donation contributions. The first two cause a blue shift of the $\tilde{\nu}_{CO}$ (with respect to that of the molecule in the gas phase, 2143 cm^{-1}), while the last causes a red shift [83–89]. From a measurement of the $\tilde{\nu}_{CO}$ of a given Cr(II) carbonyl complex, information is thus obtained on the nature of the Cr(II)$\cdots$CO bond.

Figure 3a shows the spectra of CO adsorbed at room temperature on a typical Cr(II)/SiO_2 sample. At low equilibrium pressure (bold black curve), the spectrum shows two bands at 2180 and 2191 cm^{-1}. Upon increasing the CO pressure, the 2191 cm^{-1} component grows up to saturation without frequency change. Conversely, the 2180 cm^{-1} component evolves into an intense band at 2184 cm^{-1} and a shoulder at 2179 cm^{-1}. The bands at 2191, 2184, and 2179 cm^{-1}, which are the only present at room temperature for pressures lower than 40 Torr, are commonly termed "the room temperature triplet" and are considered the finger print of the Cr(II)/SiO_2 system (grey curve in Fig. 3). A new weak band at around 2100 cm^{-1} appears at room temperature only at higher CO pressure. As this peak gains intensity at lower temperature, it will be discussed later. The relative intensity of the three components change as a function of the OH content (i.e., with the activation temperature and/or the activation time) [17].

The interpretation of these spectra given in the literature can be summarized as follows (see Scheme 5, gray part). The 2191 cm^{-1} peak is the stretching mode of CO σ-bonded on a Cr(II) site possessing a high polarizing ability, named as B sites in [48, 53, 54, 77, 90, 91]. The 2180 cm^{-1} peak is the stretching mode of CO adsorbed on Cr(II) sites possessing some d–π bonding ability. These sites are named as A sites in [48, 53, 54, 77, 90, 91]. Upon increasing the CO pressure at room temperature, the 2191 cm^{-1} band gradually increases and reaches a saturation plateau, suggesting that at room temperature $Cr^{II}{}_B$ sites can only coordinate one CO ligand and that $Cr^{II}{}_B$ is an isolated site, as an increase of the surface coverage is not able to perturb the

$\tilde{\nu}_{CO}$ of the $Cr^{II}{}_B\cdots CO$ complex [74, 92, 93]. Conversely, the 2180 cm^{-1} peak is gradually replaced by the 2184–2178 cm^{-1} doublet. This behavior has been interpreted in terms of the easy addition of a second CO molecule with formation of a dicarbonylic species. Thus, the doublet at 2184–2178 cm^{-1} may be assigned to the symmetric and antisymmetric modes of a dicarbonyl formed

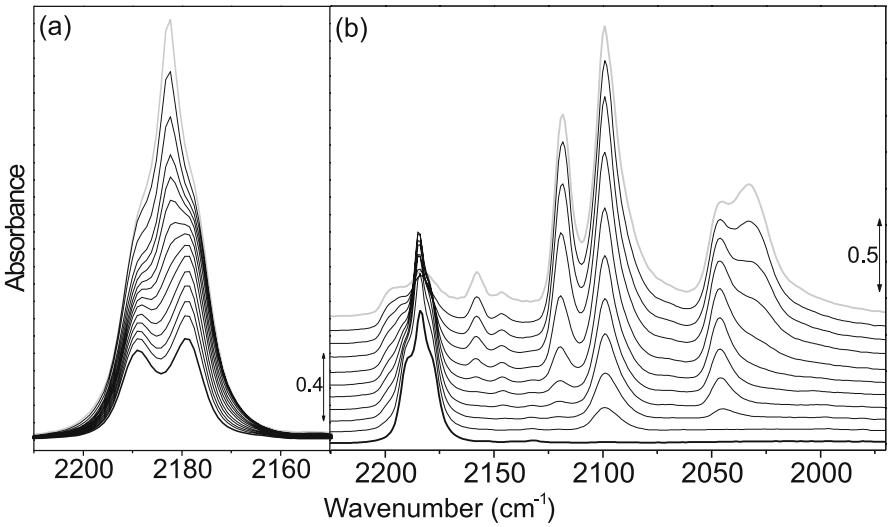

Fig. 3 IR spectra of CO adsorbed on a $Cr(II)/SiO_2$ (1.0 wt % Cr loading) activated at 923 K and reduced in CO at 623 K. *Curves from top to bottom* show effect of gradual lowering of the CO pressure. **a** Adsorption at RT; **b** adsorption at 77 K (unpublished spectra)

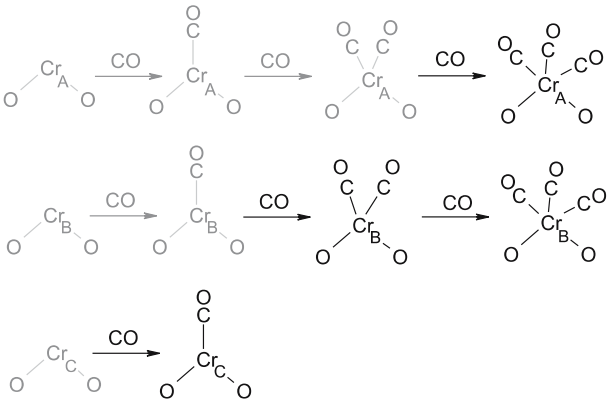

Scheme 5 Schematic picture of CO addition to isolated Cr(II) species, according to the multiple CO addition model [48, 53, 54, 77, 99]. Carbonyl species observable at RT are shown in *gray*; carbonyl species observable at 77 K are shown in *black*

at $Cr^{II}{}_A$ sites [54, 77]. This elementary interpretation is not straightforward because the more intense band of the doublet is located at higher frequency, in contrast with all known cases of dicarbonyls [88, 89, 94–97]. The explanation can lie in the prevailing σ character of the bond between chromium and CO, which may allow a negative sign for the coupling constant of the two carbonyls. This interpretation has some implications. First, it is evident that $Cr^{II}{}_A$ sites are more coordinatively unsaturated than $Cr^{II}{}_B$ sites, as they are able to coordinate a second CO molecule at room temperature. A second deduction is that $Cr^{II}{}_A$ sites have higher tendency to give d-π interactions. The absence of bands at $\tilde{\nu} < 2000\ cm^{-1}$ demonstrates that no bridging CO structures are formed upon CO dosage at room temperature [94, 98].

The examination of the $\tilde{\nu}_{CO}$ bands in the 2200–2179 cm^{-1} region at room temperature reveals that Cr(II) sites are distributed in two basic structural configurations, namely Cr_A and Cr_B. These results confirm the view illustrated before concerning the structural complexity of the Cr(II) system. Cr_A sites seem to correspond to the first family of chromates represented in Scheme 4, while Cr_B sites correspond to a family characterized by a larger α_{OCrO} bond angle. It is important to underline here that, when we speak about Cr_A and Cr_B sites, we are referring to two families of structures instead of simply to two different well-defined sites.

If a unifying picture has been achieved in the interpretation of the CO room temperature triplet, different views are still present concerning the low temperature spectra of CO on $Cr(II)/SiO_2$. The remarkable sequence of spectra illustrated in Fig. 3b corresponds to increasing coverages of CO adsorbed at 77 K on $Cr(II)/SiO_2$. These characteristic and complex spectra are independent of the silica used to support the chromium phase (pirogenic silica, aerogel, xerogel). For this reason they can be considered as a highly reproducible finger print of the system. The IR bands can be clearly divided into two groups, depending on the CO equilibrium pressure. At very low equilibrium pressure ($P_{CO} < 50$ Torr) only the "room temperature triplet" is present. Upon increasing the pressure, a second series of intense bands in the 2140–2050 cm^{-1} region (i.e., at $\tilde{\nu}$ lower than $\tilde{\nu}_{CO}$ gas) grows up at the expenses of the bands formed in the first phase. This behavior, together with the multiplicity of peaks, suggests that the bands in the 2140–2050 cm^{-1} interval belong to polycarbonylic species formed by addition of further CO molecules to the species responsible for the triplet at 2191–2179 cm^{-1}. It should be noted that a new component is also present at about 2200 cm^{-1}. This band is assigned to monocarbonylic species formed on a third family of sites (Cr_C). As in the case of the room temperature triplet, the relative intensity of the components in the 2140–2050 cm^{-1} interval changes dramatically with different thermal treatments [17].

The IR spectra obtained at 77 K have been already thoroughly discussed in the past and their assignment has caused an interesting controversy in the specialized literature. In particular, the most crucial question associated

with the whole set of low frequency bands is why the addition of further CO ligands causes such a dramatic shift towards lower frequencies and an equally dramatic increase of the integrated intensity. In attempts to answer this problem, Rebenstorf et al. [49–52, 76] and Zecchina et al. [45, 47, 48, 75] proposed two radically different interpretations of the carbonyl bands at 77 K. The first interpretation is based on the formation of bridged CO species on Cr(II) – Cr(II) pairs; the second is based on multiple CO addition on isolated Cr(II) sites. It is useful to remember that isolated centers derive from CO reduction of surface monochromates, while paired Cr(II) – Cr(II) centers mainly derive from reduction of dichromate precursors. Considering that monochromates are the most abundant species on our samples, the second interpretation is highly preferred [17].

This interpretation [48, 53, 54, 77, 99] is based on the hypothesis that at low temperature/high pressure we have further insertion of CO into the coordination sphere of isolated Cr(II) ions, assumed as the dominant species, following Scheme 5 (black part). According to this hypothesis, the added CO molecules have the character of linear species and no bridged carbonyls are involved. The $Cr^{II}{}_A$ and $Cr^{II}{}_B$ families are able to coordinate further CO ligands at low temperature/high pressure, suggesting that the involved $Cr^{II}{}_A$ and $Cr^{II}{}_B$ species are both highly coordinatively unsaturated (although at different degrees). The Cr_C species, on the contrary, adsorb only one CO because they possess the highest coordination.

This interpretation, however, faces a new problem: If the low frequency bands are not due to bridging species, what is the explanation of the distinct downward shift of the $\tilde{\nu}_{CO}$ bands upon CO addition and also of their strong intensity? Authors of quoted works [48, 53, 54, 77, 99] have probably solved this contradiction. The surface process depicted is not a simple ligand insertion into a pre-existing coordinative vacancy, but more likely a ligand displacement reaction of the type reported in Eq. 2:

$$(SiO)_2Cr^{II}L_{n,n-1}(CO)_{1,2} \xrightarrow{CO} (SiO)_2Cr^{II}L_{n-1,n-2}(CO)_3 + 1,2L, \qquad (2)$$

where the insertion of the additional CO is associated with the simultaneous expulsion of a weakly bonded surface ligand L (presumably, the bridging oxygen of the siloxane groups). In other words, the adsorption of CO is accompanied by local relaxation, a fact that is not unknown in surface science. On this basis it is evident that, although the Cr(II)···CO bond is strong (a fact which explains both the low frequency and the high intensity of the IR bands), the CO removal is easy. In fact, the total enthalpy of the process can be small because the positive enthalpic contribution of the formation of strong CO bonds is partially cancelled by the negative contribution of the displacement of the L ligands (ensuring crystal field stabilization to the naked Cr(II) sites).

Espelid and Børve [100] have recently explored the structure, stability, and vibrational properties of carbonyls formed at low-valent chromium bound to silica by means of simple cluster models and density functional theory (DFT) [101]. These models, although reasonable, do not take into consideration the structural situations discussed before but they are a useful basis for discussion. They found that the pseudo-tetrahedral mononuclear Cr(II) site is characterized by the highest coordination energy toward CO.

On the basis of all the literature reviewed above, we are now able to summarize the main results concerning the structure of Cr(II) sites [17]:

(i) The structure of anchored Cr(II) ions is extremely heterogeneous. This Cr(II) structural variability is favored by the amorphous nature of the silica support and can be influenced by the thermal treatments. In fact, on the surface of the amorphous silica support, numerous locations of the anchored Cr(II) ions are conceivable, which differ in the number, type, and position of surface ligands. Figure 1b, where three Cr(II) ions have been grafted in different positions on two vicinal oxygens, tries to represent this complex situation. From this picture it is evident that some Cr(II) ions are protruding out of the surface more than others, depending on the geometry and the strain of their environment. Different possible coordinative situations of Cr(II) centers are reported in the zoomed inserts of the picture. All the Cr(II) ions are grafted to the silica surface through two strong SiO^- ligands, but they differ in the type, number, and position of additional weaker ligands, such as siloxane bridges or (more rarely) residual OH groups. When the SiO^- ligands belong to small silicon membered rings, they form with Cr(II) ion an angle near to the tetrahedral value (top inset in Fig. 1b). The resulting O – Cr bond is quite covalent and the Cr(II) are protruding on the silica surface. Upon increasing the ring dimensions we pass from a pseudo-tetrahedral structure to the less protruding pseudo-octahedral one (bottom inset in Fig. 1b), characterized by a less strain and a higher ionicity of the resulting O – Cr bond.

(ii) Focusing attention on the coordination sphere of the Cr(II) sites, it is concluded that they differ from each other in the number of the effective coordination vacancies, ν. The greater is ν, the more unsaturated is the Cr(II) site and more molecules can be adsorbed on it. However, it must be noted that ν does not necessarily coincide with the maximum number of adsorbed molecules, because the weak ligands L can be more or less easily displaced from their position when stronger ligands (e.g., NO) interact with the chromium center. Of course, the displacement of a weak ligand may require a high partial pressure of the ligand. This could explain the necessity to lower the temperature to 77 K to insert a third CO ligand into the Cr(II) coordination sphere, but also their easy removal [77, 99]. The displacement of one or more weak ligands may not only happen with CO and NO, but also with the ethylene monomers during the initial stages of the polymerization reaction. This means that, if the Cr(II) sites

characterized by $n = 0$ and 1 are certainly the most active species in the polymerization, the sites with $n > 1$ could also become active, provided that the energy required to displace the weak ligands L is not so great and the ethylene pressure sufficiently high.

3 Catalytic Activity and Polymerization Mechanism

The ability of the Phillips catalyst in polymerizing ethylene without the intervention of any activator, makes it unique among all the olefin polymerization catalysts. It is generally accepted that for catalytic reactions involving olefin insertion and oligomerization (e.g., Ziegler–Natta and metallocene catalysts) the metal active site must possess one alkyl or hydride ligand and an available coordination site. Very frequently the active catalyst is prepared in situ from a transition metal compound not having the active ligand and an activator (aluminium alkyl, methylalumoxane MAO, etc.) whose function is to introduce an alkyl group in the coordination sphere of the metal. By analogy with the Ziegler–Natta type catalysts, the first step of the reaction should be the insertion of a monomer molecule into a vacant position of the Cr site carrying an alkyl group (structure II in Scheme 6), via a d-π interaction. The second step is a migratory insertion reaction that extends the growing alkyl chain by one monomer unit, thereby regenerating the vacant coordination site at the metal center (structure III in Scheme 6). This means that, if a Ziegler–Natta-like polymerization mechanism is also assumed for the Phillips catalyst, ethylene has to play three important roles simultaneously and/or successively:

(i) Reduction agent, reducing the chromate species in an oxidation state of +6 into coordinatively unsaturated active chromium precursor in a lower oxidation state (this process is absent on CO/reduced catalyst)
(ii) Alkylation agent, alkylating the potential active chromium species resulting in the formation of active sites (species I in Scheme 6, where R is unknown)
(iii) Propagation agent, acting as monomer for chain propagation of the active sites

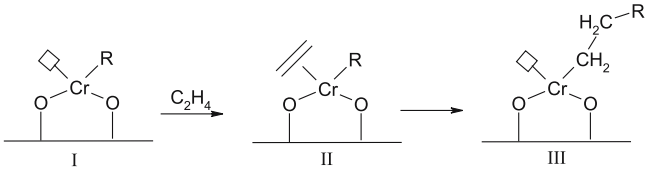

Scheme 6 Scheme of the initiation mechanism in ethylene polymerization according to a Ziegler–Natta-like behavior

As said in the introduction, the CO-reduced system is active in ethylene polymerization and the resulting polymer is generally considered almost the same as that obtained with the industrial catalyst [4]. Because of its simplicity, hereafter we will discuss only the polymerization on this model catalyst.

3.1 Active Sites and Turnover Number

Several attempts have been made to determine the number of active sites on the reduced Cr/SiO_2 catalyst [17]. McDaniel et al. [4], by analyzing the resulting polymer by ^{13}C NMR, found that about 10% of the chromium sites were active. Ghiotti et al. [53] measured the number of alkyl chains produced on a reduced Cr/SiO_2 sample by means of IR spectroscopy and found that the number of active sites reaches about 10% of the total chromium content. Kantcheva et al. [102] estimated the number of active sites in a reduced catalyst by integrating the absorbance of the $\tilde{\nu}_{as}(CH_2)$ band and knowing the number of ethylene molecules added to the IR cell. The concentration of active sites estimated at the start of ethylene polymerization (1.2×10^{19} sites/g = 2.0×10^{-5} mol/g) corresponds approximately to the number reported by Hogan (2.5×10^{-5} mol active Cr sites/g) in the case of an industrial Cr/SiO_2 catalyst [3]. In conclusion, the vast majority of results points toward a fraction of site not far from 10%.

These values are in contrast both with the results of poisoning experiments and with the results of Bade et al. [103] obtained by gel permeation chromatography (GPC) analysis of the polymer formed. In the case of the poisoning experiments, the percentage of chromium involved in the polymerization has been determined to be much higher (about 34% in the case of hydrogen sulfide poison [63, 104] and 20–50% in the case of CO poison [105]). However, the technique is only good when the selectivity of the poison for the active site is appropriate and this is not the case for the Phillips catalyst; in this case the technique can only give an upper limit of the active-site concentration [105, 106]. Conversely, Bade et al. [103] determined that only 0.1% of the chromium is active. However, the low number of active sites could be a consequence of the adopted conditions, room temperature and low ethylene pressure, as suggested by the absence of fragmentation of the silica support at the end of the experiment.

Concerning the polymerization activity of the CO-reduced catalyst, Myers et al. [63] reported a turnover frequency (TOF) of 0.58 C_2H_4 molecules/s for a polymerization conducted at 323 K in an ethylene pressure of 100 Torr on a $Cr(II)/SiO_2$ catalyst (oxidized at 1173 K and reduced in CO at 673 K). Rebenstorf [107] obtained, at a temperature of 353 K and an ethylene pressure of 500 Torr, a TOF of about 0.44 C_2H_4 molecules/s. Szymura et al. [108] reported a polymer yield of 25.5 g(PE)/g(catalyst) for a 300 m^2/g silica loaded with 5 wt. % Cr, during polymerization at 300 K and atmospheric pressure over

a CO prereduced catalyst. This value corresponds to a TOF of about 0.26 C_2H_4 molecules/s at atmospheric pressure. By assuming that the concentration of active sites is 10% for all samples and hypothesizing a direct relationship between TOF and ethylene pressure, the converted TOF values (for 20 Torr ethylene pressure at about 300 K) ranges in the 0.5 – 1.2 C_2H_4 molecules/s interval [17].

3.2 First Spectroscopic Attempts to Determine the Polymerization Mechanism

The high TOF and the low concentration of the active sites have limited the application of traditional spectroscopic techniques to observe the species involved during the initiation mechanism. In 1988 Ghiotti et al. [53] carried out ethylene polymerization on a CO-reduced Cr/SiO_2 system at room temperature and at low pressure. The idea was that short contact times and low pressures should yield short length chains, thus allowing the study of the initial steps of polymerization reaction. Only two bands at 2920 and 2851 cm^{-1}, growing with time in a parallel way at nearly constant rates, were observed and readily assigned to the antisymmetric and symmetric stretching vibrations of CH_2 groups of living polymeric chains growing on the silica external surface. No evidence of terminal groups could be obtained.

In 1994 Zecchina et al. [77] tried to overcome the problem of very fast reaction speeds by collecting fast time-resolved spectra of ethylene polymerization. Fast FTIR spectra can be obtained by reducing the spectral resolution (proportional to the movable mirror translation) and by collecting the interferograms without performing the FT. The latter are performed at the end of the experiment [77, 109–113]. The sequence of spectra collected every 0.75 s is reported in Fig. 4; the last spectrum was collected after only 15 s from the ethylene injection into the cell. Following the considerations outlined before about the number of ethylene molecules inserted per second at each chromium center at room temperature and pressure of about 0.02 atm (not far from 1 molecule/s), the detection of the presence of methyl groups in the initiation stage was conceivable. From the sequence, it is evident that, even if the time used to perform the measure was extremely short, the spectra did not show evidence of alkyl precursors formation. From this experiment, the metallacycle hypothesis (vide infra) received strong (but not fully conclusive) support.

It is worth noticing that in the first spectra of the series shown in Fig. 4 the two methylenic bands at 2920–2851 cm^{-1} appear slightly asymmetric, with a broad tail at higher frequencies. This feature becomes less evident at increasing polymerization times, since the intensity of the CH_2 bands increases. At least two different explanations can be advanced. (i) Methylene groups next to a low valent chromium would be influenced by the presence of the chromium itself and thus exhibit a distinct difference in the stretching frequency with respect to that of a methylene group in the middle of the

polymer chain. (ii) CH_2 belonging to the small and strained metallacycles present in the firsts stages of the polymerization are characterized by stretching frequencies higher than that of CH_2 belonging to linear infinite polymeric chains. As the polymerization proceeds, the strain of the cyclic structures decreases and the CH_2 groups become indistinguishable from those of long linear chains. On the basis of the data reported in Fig. 4, it is not possible to make a choice between the two alternatives, which are not mutually exclusive.

The presence of methylenic bands shifted at higher frequency in the very early stages of the polymerization reaction has also been reported by Nishimura and Thomas [114]. A few years later, Spoto et al. [30, 77] reported an ethylene polymerization study on a Cr/silicalite, the aluminum-free ZSM-5 molecular sieve. This system is characterized by localized nests of hydroxyls [26, 27, 115], which can act as grafting centers for chromium ions, thus showing a definite propensity for the formation of mononuclear chromium species. In these samples two types of chromium are present: those located in the internal nests and those located on the external surface. Besides the doublet at 2920–2850 cm^{-1}, two additional broad bands at 2931 and 2860 cm^{-1} are observed. Even in this favorable case no evidence of CH_3 groups was obtained [30, 77]. The first doublet is assigned to the CH_2 stretching mode of the chains formed on the external surface of the zeolite. The bands at 2931 and

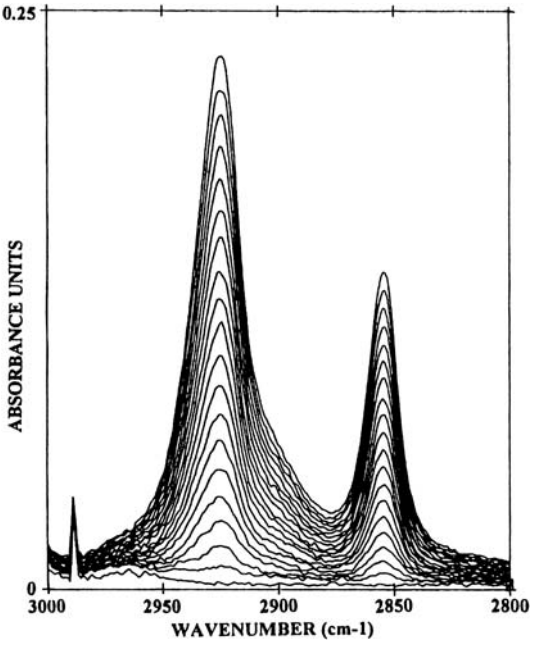

Fig. 4 Fast time-resolved spectra of ethylene polymerization reaction on CO-reduced Cr/SiO_2 sample. Initial ethylene pressure was 10 Torr. Last spectrum after 15 s. Reprinted from [77]. Copyright (1994) by Elsevier

2860 cm^{-1} were assigned by Spoto et al. [30, 77] to CH_2 modes of polymeric chains growing on chromium sites located inside the zeolite framework. Due to the spatial hindrance caused by the framework walls, polymeric chains initiated at internal chromium centers cannot grow freely and only very short chains can be obtained. The CH_2 stretching frequencies are shifted with respect to those of the infinite chains formed on the external surface.

3.3 Polymerization Mechanisms Proposed in the Literature

3.3.1 Ethylene Coordination, Initiation and Propagation Steps

From the results discussed so far, it is evident that only CH_2 groups have been observed in the very early stages of the ethylene polymerization reaction. Of course, this could be due to formation of metallacycles, but can be also a consequence of the high TOF which makes the observation of the first species troublesome. To better focalize the problem it is useful to present a concise review of the models proposed in the literature for ethylene coordination, initiation, and propagation reactions.

Two types of mechanisms are generally accepted for the propagation of transition-metal-catalyzed olefin polymerization systems: the Cossee [116] and the Green–Rooney [117] mechanisms. The Cossee mechanism requires a vacant coordination site on the metal center in the position adjacent to the growing alkyl chain. A monomer molecule π-coordinates to the metal and then inserts into the alkyl chain, which grows of one monomer unit (see Scheme 6). The Green–Rooney mechanism requires two vacant coordination sites at the metal center. The growing polymer chain first eliminates an α-hydrogen to produce a metal-carbene species. An ethylene molecule then coordinates at the remaining vacant site, followed by addition across the metal-carbene double bond in a metathesis-type reaction to form a metallacycle species. Reductive elimination causes the ring opening, thus producing an alkyl chain that has been extended by one monomer unit, together with the restoration of the original vacant coordination sites at the metal center.

Although the standard Cossee-type mechanism is especially suited for the Ziegler–Natta polymerization processes (where an alkyl group is preliminarily inserted into the coordination sphere of the transition metal center through the intervention of an activator), the standard Cossee [116] type of propagation mechanism is also assumed to be valid for the Cr/SiO_2 system. In the absence of any activator providing the alkyl group, the main problem is to explain the initiation of the first chain, i.e. the nature of R in species I of Scheme 6. This crucial point has stimulated a great debate and several hypothesis have been advanced. In Scheme 7 the majority of proposed mechanisms are reported.

All mechanisms proposed in Scheme 7 start from the common hypotheses that the coordinatively unsaturated Cr(II) site initially adsorbs one, two, or three ethylene molecules via a coordinative d-π bond (left column in Scheme 7). Supporting considerations about the possibility of coordinating up to three ethylene molecules come from Zecchina et al. [118], who recently showed that Cr(II) is able to adsorb and trimerize acetylene, giving benzene. Concerning the oxidation state of the active chromium sites, it is important to notice that, although the Cr(II) form of the catalyst can be considered as "active", in all the proposed reactions the metal formally becomes Cr(IV) as it is converted into the "active" site. These hypotheses are supported by studies of the interaction of molecular transition metal complexes with ethylene [119, 120]. Groppo et al. [66] have recently reported that the XANES feature at 5996 eV typical of Cr(II) species is progressively eroded upon in situ ethylene polymerization.

From Scheme 7, the extraordinary complexity of the species that can be formed, at least in principle, during the initiation step can be appreciated. It is important to underline that the number of possible initiation mechanisms can be greater than the seven indicated in Scheme 7, because several mechanisms can be found not only coming from top to bottom in a vertical way, but also following a zig-zag path. Furthermore, most of the species reported here could be in equilibrium during the early stages of the polymerization reaction, increasing the complexity of the scenario.

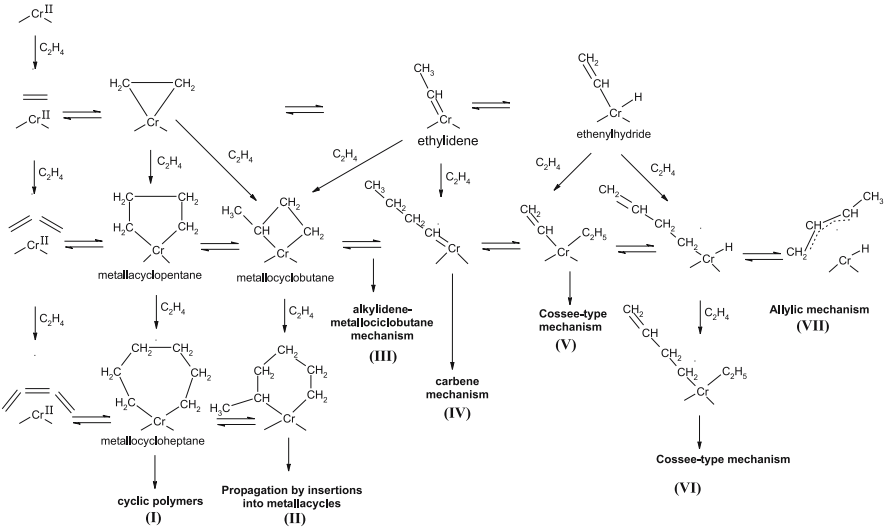

Scheme 7 Initiation mechanisms proposed in literature for the CO-reduced Cr/SiO_2 catalyst. *Vertical direction* shows evolution of the initial species upon addition of one ethylene molecule. *Horizontal direction* shows all the possible isomeric structures characterized by an average C_2H_4/Cr ratio equal to 1, 2, and 3

So far we have considered only mechanisms involving a single Cr(II) ion, because the centers have been found to be isolated, at least for low Cr loadings. However, the intervention of multiplets of Cr(II) centers cannot be excluded. In fact, it can be hypothesized that an eventual cyclic intermediate formed initially (mechanism I and II) can also evolve into Cr(II)-$(CH_2)_n$-Cr(II) species, where the chain is anchored to two different chromium centers. In these conditions chromium species carry only a linear chain and the system differs from all the "double bridged" structures illustrated up to now.

The role of coordinated ethylene is evidenced by the recent ab initio calculation performed by Espelid and Børve [121–123], who have shown that ethylene may coordinate in two different ways to the reduced Cr(II) species, either as a molecular complex or covalently bound to chromium. At longer Cr – C distances (2.36–2.38 Å) an ethylene-chromium π-complex forms, in which the four d electrons of chromium remain high-spin coupled and the coordination interaction is characterized by donation from ethylene to chromium. Cr(II) species in a pseudo-tetrahedral geometry may adsorb up to two equivalents of ethylene. In the case of a pseudo-octahedral Cr(II) site a third ethylene molecule can also be present. The monoethylene complex on the pseudo-tetrahedral Cr(II) site was also found to undergo a transformation to covalently bound complex, characterized by shorter Cr – C distances (about 2.02 Å), in which the donation bond is supplemented by back donation from Cr_{3d} into the π^* orbital of the olefin. This implies that chromium formally gets oxidized to Cr(IV), adopting a triplet spin state.

3.3.2
Standard Cossee Model for Initiation and Propagation

To solve the problem of the initiation of the first polymer chain, Hogan [3] suggested that polymer chains were initiated by monomer insertion into a Cr – H bond. The resulting metal-alkyl species then propagates via a Cossee mechanism [116] (mechanisms V and VI in Scheme 7). A prerequisite for this scheme is that there must be a Cr – H bond present prior to the onset of polymerization. Some authors have suggested that surface silanol groups provide a source of additional hydrogen atoms [124, 125]. Hydride transfer may occur between a silanol group and a supported Cr(II) ion to yield an O^{2-} species and a Cr(III) – H bond, into which the first ethylene can insert [124]. Alternatively, it has been proposed that ethylene adsorption directly onto a surface silanol group is followed by its coordination to an adjacent chromium ion, along with the migration of a proton from the silanol group onto the metal center [125].

However, the inverse correlation between activity and hydroxyl concentration [4] and the fact that excellent catalysts can be obtained with systems completely dehydroxylated by chemical means [126] (e.g., by fluorination) makes this mechanism unlikely. The only viable direction is to hypothesize that the starting structure for polymerization may evolve directly from a re-

action between ethylene and the divalent chromium species, as reported in Scheme 7.

3.3.3
Carbene Model for Initiation and Propagation

Starting from the coordination of only one ethylene molecule, a carbene mechanism has been proposed [117], via formation of an ethylidene-chromium(IV) species through a metal-catalyzed transfer of hydrogen between the carbon atoms in ethylene (mechanism IV in Scheme 7). Kantcheva and co-workers [102] suggested a carbene mechanism on the basis of IR spectroscopy results. They assigned a band at 3016 cm^{-1} in the initial polymerization stage to $\tilde{\nu}_{CH}$ of $Cr = CH - R$ groups. This mechanism does not need an extra hydrogen for initiation. Previously, Ghiotti et al. [53] proposed an alternative carbene mechanism, where the carbene was formed during a reversible hydrogen abstraction from the α-CH_2 groups to a surface oxygen atom. Contrary to the former carbene mechanism [102], the latter [53] avoids hydrogen scrambling, concurring with the conclusion of McDaniel and Kantor [127] that no hydrogen shift occurs during the propagation reaction.

Another possibility is that carbene species are generated via the dissociative adsorption of ethylene onto two adjacent chromium sites [71]. A second ethylene molecule then forms an alkyl chain bridge between the two chromium sites; this can subsequently propagate via either the Cossee or the Green–Rooney mechanism.

Recently, Amor Nait Ajjou et al. [128–130] prepared a working catalyst through thermal transformation of dialkylchromium(IV) structure, accompanied by release of the corresponding alkane, as reported in Eq. 3:

$$(\equiv SiO)_2Cr(CH_2CMe_3)_2 \xrightarrow{70\,^{\circ}C} (\equiv SiO)_2Cr = CHCMe_3 + CMe_4 \qquad (3)$$

The stoichiometry of this conversion is in accordance with a carbene starting structure. An alternating alkylidene/metallacyclobutane mechanism [102, 131–133], which has precedent in the ethylene polymerization catalyzed by a Ta(III) neopentilydene complex [134], has been proposed where the chromium alkylidenes undergo [2+2] cycloaddition to give chromacyclobutane intermediates (mechanism III in Scheme 7).

3.3.4
Metallacycles Model for Initiation and Propagation

Experimental results supporting the metallacycles model for initiation and propagation have also been proposed [77, 99, 135, 136]. As already discussed, Ghiotti et al. [53] and Zecchina et al. [77] did not obtain IR spectral evidence indicating the presence of vinyl or methyl groups in the firsts stages

of polymerization. They believed that terminal groups were not present in the polymer chains, i.e., the chains formed cyclic structures with both ends attached to the active site. They proposed two structures, a metallacycle involving only one Cr ion, or a polyethylene chain bridged over two nearby chromium ions. The second cyclic structure, first proposed by Rebenstorf and Larsson [46], was also supported some years later by Zielinski et al. [71].

Support for the metallacyclic structure has recently been obtained from reactions between organometallic chromium complexes and ethylene where five-membered metallacycles are formed [135]. Further insertions may then take place to one of the two chromium–carbon single bonds, thus forming larger metallacycles. The metallacyclic species may propagate as such until termination occurs by hydrogen transfer from one of the β-methylene groups to the opposite α-carbon, thus forming linear polymer chains with one methyl and one vinyl end group as expected.

Several studies report the formation of 1-hexene in the early stages of ethylene polymerization [129, 136, 137]. Jolly and co-workers [135] recently reported that homogeneous chromium-based catalysts may show high selectivity with respect to trimerization of ethylene to 1-hexene. They proposed a mechanism involving chromacyclic intermediates, some of which have been isolated and structurally characterized. The key to this mechanism is suggested to lie in the relative stability towards intramolecular β-H-transfer of the metallacyclopentane ring compared to the metallacycloheptane ring.

Ruddick and Badyal [136] studied the desorbing species on a prereduced Phillips catalyst using mass spectrometry and concluded that only 1-hexene was formed. The formation of 1-hexene has been proposed to proceed via metallacyclic intermediates; this involves coordination of two ethylene molecules to form a chromacyclopentane species. Recently Giannini et al. [120] investigated the chemistry of the calix[4]arene tungsten(IV) system and discovered a variety of olefin rearrangements which are very close to those often supposed to occur on metal oxides. In particular, the rearrangements of ethylene lead to the formation not only of alkylidenes and alkylidynes but also of metallacycles structures such as metallacyclopropane and metallacyclopentane. The peculiarities of the oxygen set of donor atoms of a calix[4]arene structure makes the comparison with a metalla-oxo surface particularly appropriate [120, 138].

The calculations of Espelid and Børve [121, 123] on the pseudo-tetrahedral Cr(II) cluster have shown that only a very low barrier separates the double ethylene π-complex from forming a chromacyclopentane structure. In the same way, the triethylene π-complex which forms on the pseudo-octahedral Cr(II) sites may undergo ring-fusion reactions, either to form a chromacyclopentane structure with a coordinating ethylene molecule or, alternatively, to form a chromacycloheptane species. Rearrangement of the monoethylene complex to either ethylidenechromium or ethenylhydridochromium, on the other hand, is much less favorable for thermodynamical reasons, as de-

scribed previously. Hence, it appears likely that, according to the quantum mechanical calculations, chromacyclopentane or chromacycloheptane are the dominating initial species at the mononuclear Cr(II) site.

3.3.5
Conclusions and Future Improvements

From these contributions it is evident that there is still no agreement on the initiation mechanism and that new experimental studies are needed. Unfortunately the high polymerizing rate and the small fraction of low-coordinated chromium sites represent the major obstacles in studies of the initiation step. This means that in order to be able to identify the first species in the polymerization reaction using a spectroscopic technique the time needed to perform the measure must be shorter than the short life-time of the very active species formed during the initiation. Progress in this direction can be achieved either by improving the time response of the instrument or by finding means of slowing down the reaction speed, or both. Furthermore, the spectroscopies adopted must be sensitive because they should be potentially able to identify species formed on a very low fraction of sites (for instance in the 0–10% interval).

Among all the spectroscopic techniques reviewed here, IR spectroscopy is the most versatile and the most used in the attempt to identify the precursors of ethylene polymerization, being able to directly discern between the vibrational manifestations of different species even under operando conditions. IR spectroscopy is, in principle, able to distinguish between all the structures illustrated in Scheme 7. In this respect we briefly focus attention on the fact that, among all the proposed mechanisms, the only one not involving species characterized by methyl groups is the metallacycle mechanism. In this case, all the initiation species are characterized only by methylenic groups belonging to rings of increasing dimension. As the stretching modes of methyl groups are almost two times more intense than CH_2 stretching modes, we expect that methyl groups, if present, should be visible in the first stages of polymerization, when the chain length is modest, i.e., the ratio CH_2/CH_3 is relatively small.

Very recently, Bordiga et al. [99] designed and performed new experiments allowing the collection of FTIR spectra at low temperature and in the presence of CO, which is known to reduce the polymerization speed. Under these conditions, the reduced rate allowed the observation of shorter olygomeric chains [99]. In Fig. 5 it is evident that, at the lowest reaction times, the $\tilde{\nu}(CH_2)$ peaks were located at 2931 and 2860 cm^{-1}, i.e., at values distinctly different from those observed in the normal experiments (2920 and 2851 cm^{-1}), see Fig. 4. Only after prolonged contact time these new components were overshadowed by the usual bands of the long polymeric chains. In conclusion, these results demonstrate that the study of the reaction in the presence of the

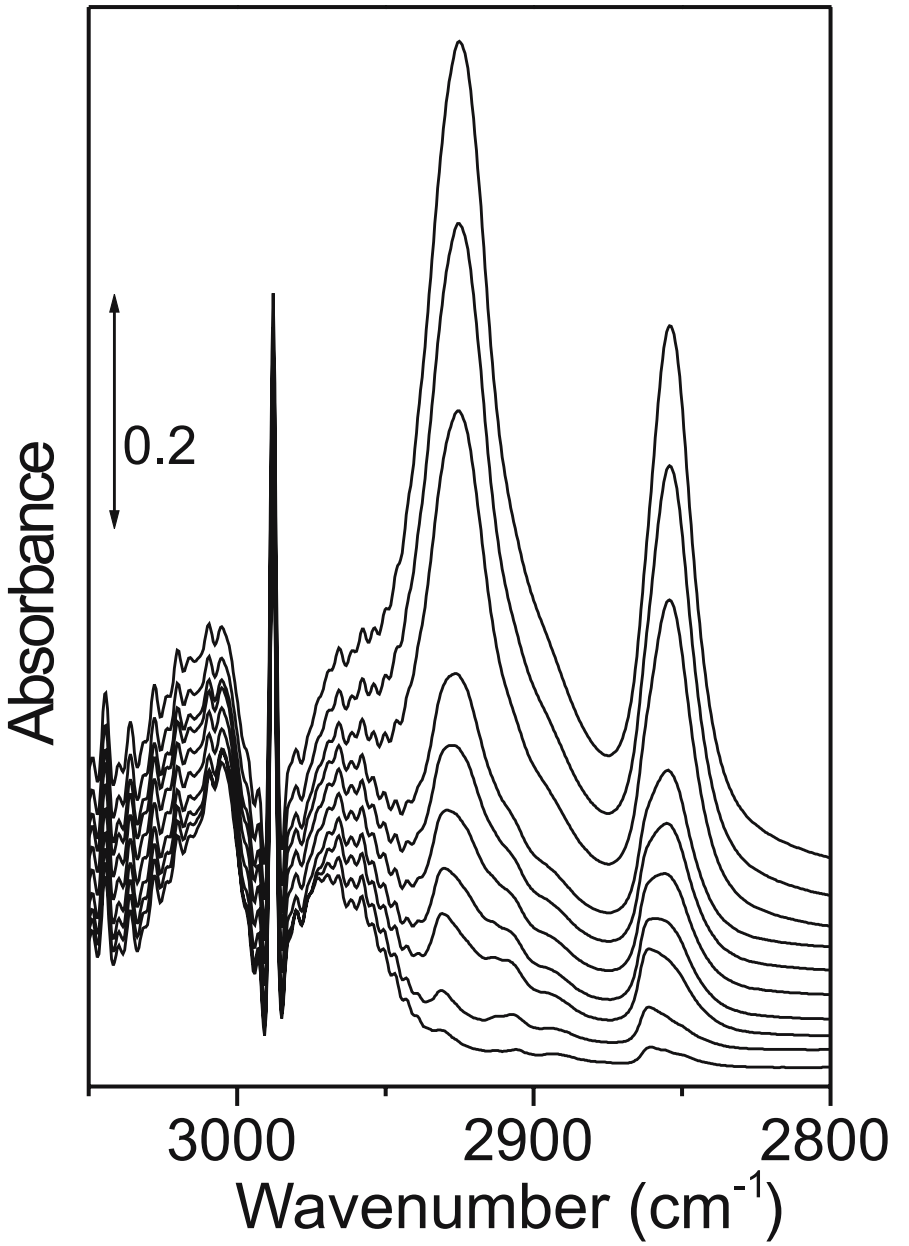

Fig. 5 Temperature-resolved ethylene polymerization on CO-reduced Cr/SiO_2 catalyst in the 100–300 K range in presence of pre-adsorbed CO (increasing temperature from *bottom* to *top*). Reprinted from [99]. Copyright (2003) by Elsevier

CO poison can probably allow observation of the $\tilde{\nu}(CH_2)$ modes of the first products of the polymerization.

4 Open Questions and Perspectives

We have illustrated in detail the efforts made in the last few decades to discover the structure of the active sites of the Phillips catalyst and to solve the mystery of the initiation step, which is unique among the polymerization catalysts because it proceeds without activators. From the survey of the literature it can be safely concluded that much progress has been achieved in the understanding of the surface structure and catalytic activity of the Cr/SiO_2 system. In particular, concerning the surface structure, the following points now appear to be firmly established:

(i) On $Cr(VI)/SiO_2$ diluted samples (0.5–1.0 wt. % Cr loading) the predominant anchored species are monochromates.
(ii) On CO-reduced diluted sample chromium is isolated and prevalently in divalent state. The average Cr(II)-Cr(II) distance, in the case of a 1 wt. % $Cr(II)/SiO_2$ system, is about 10 Å.
(iii) Due to the amorphous character of the support, different families of Cr(II) structures are present on the surface, which can be identified via accurate spectroscopic methods and classified into three distinct families ($Cr^{II}{}_A$, $Cr^{II}{}_B$ and $Cr^{II}{}_C$).
(iv) The majority of Cr(II) sites are highly coordinatively unsaturated and can adsorb up to three CO, three NO and three acetylene molecules.
(v) The initiation step proceeds by ethylene coordination on Cr(II) with formation of d-π complexes.
(vi) Ab initio modeling is starting to play a fundamental role in the elucidation of surface structures and of adsorption, initiation and polymerization mechanisms.

Despite all these achievements, several questions remain still unanswered, in particular:

(i) The precise structure of the three different families of Cr(II) sites ($Cr^{II}{}_A$, $Cr^{II}{}_B$ and $Cr^{II}{}_C$) on the CO-reduced catalysts is still under investigation
(ii) The precise structure, the relative abundance, and the TOF of the most active sites is still unknown, probably because they are present in low concentration
(iii) Determination of the species formed in the initiation steps is still at the infancy

From the comparison of the achievements and open problems new perspectives are emerging. In particular, the results collected in these pages demonstrate that the synergic use of different and complementary spectroscopic

techniques can provide more and more detailed information about the structure of chromium on the amorphous silica surface. Pursuing this goal, new, more sensitive characterization methods and more finalized strategies for the study of the really active sites must be adopted, not only from an experimental but also from a theoretical point of view. The more extended use of in situ spectroscopic investigations under conditions as close as possible to the real catalytic conditions is the first logical step. Among the new strategies, the intelligent modification of silica support (for instance via introduction of foreign atoms like Ti, Zr, etc.) or the utilization of crystalline silica support can represent an innovative path. These new studies are encouraged by the fact that most of the open problems mentioned above are not characteristic of the Cr/SiO_2 system. In fact, similar questions are commonly encountered for the vast majority of catalysts, since direct experimental observation of working centers and intermediates is invariable absent in the literature.

Note Added in Proof

After the submission of this contribution, new relevant results in the field of the characterization of the Phillips catalyst have been published. In particular, in [139], the first Raman spectra of molecular adducts (CO and N_2) formed on Cr(II) sites are reported, thus obtaining indirect information about the Cr(II) anchored species, complementary to those reported in Sect. 2.3.2. These results have been achieved by using an ad hoc selected laser line (able to excite a ligand to Cr charge transfer transition that does not relax in a radiative channel), and adopting as a support a silica aerogel behaving as an optically uniform medium in the region of work. These two combined strategies, never simultaneously applied before, allowed to obtain great quality Raman spectra of surface species, demonstrating that Raman spectroscopy can have great sensitivity towards surface species present in small concentration. The improvement can be quantified by comparing published spectra of the oxidized $Cr(VI)/SiO_2$ system (see discussion in Sect. 2.2), with the more intense and much richer one obtained under the experimental conditions adopted in [139]. New spectroscopic features, assigned to terminal $O = Cr = O$ species, are clearly observed. The absence of any other narrow bands in the 800–900 cm^{-1} region, also when the silica fluorescence background has been eliminated, definitely exclude a significant presence of polymeric chromium species, at least at low chromium loadings, as already suggested (but not safely demonstrated) in the past and in contrast with the case of Cr(VI) anchored on other oxide supports [6, 33, 35–37]. The same experimental strategies have been improved in [140], where the Cr(II)-framework modes at 568 and 1009 cm^{-1} have been observed for the first time.

As far as the initiation mechanism is concerned, the first complete characterization of the C_2H_4 π-complexes formed on Cr(II) sites has been re-

ported [141]. These results are particularly important in the view of the understanding of the polymerization mechanism, since the C_2H_4 coordination and the formation of π-bonded complexes are the first steps of the reaction, as discussed in Sect. 3.3.1. Finally, the relation existing between the structure of the Cr(II) active sites, the catalytic activity and the properties of the resulting polymers has been highlighted in [142].

Acknowledgements Acknowledgements are due to F. Cesano for the unpublished DRS UV-Vis spectra reported in Fig. 2 and to G. Ricchiardi, J.G. Vitillo, S. Bordiga, C. Lamberti and G. Spoto for fruitful discussions.

References

1. Böhm LL (2003) Angew Chem Int Edit 42:5010
2. Hogan JP, Banks RL (1958) US Pat 2, 825:721
3. Hogan JP (1970) J Polym Sci 8:2637
4. McDaniel MP (1985) Adv Catal 33:47
5. Clark A (1970) Catal Rev 3:145
6. Weckhuysen BM, Wacks IE, Shonheydt RA (1996) Chem Rev 96:3327
7. Weckhuysen BM, Schoonheydt RA (1999) Catal Today 51:215
8. Ziegler K (1954) Belgian Patent 533, 362
9. Ziegler K, Holzkamp E, Martin H, Breil H (1955) Angew Chem 67:541
10. Natta G (1955) J Polym Sci 16:143
11. Natta G (1956) Angew Chem Int Edit 68:393
12. Wilke G (2003) Angew Chem Int Edit 42:5000
13. Brintzinger HH, Fischer D, Mulhaupt R, Rieger B, Waymouth RM (1995) Angew Chem Int Edit 34:1143
14. Theopold KH (1998) Eur J Inorg Chem 15
15. Duchateau R (2002) Chem Rev 102:3525
16. Theopold KH (1997) Chemech 27:26
17. Groppo E, Lamberti C, Bordiga S, Spoto G, Zecchina A (2005) Chem Rev 105:115
18. Materials Studio Getting Started, Accelrys Inc., San Diego (2002)
19. Borello E, Zecchina A, Morterra C (1967) J Phys Chem 71:2938
20. Zhuravlev LT (1987) Langmuir 3:316
21. Zhuravlev LT (2000) Colloid Surf A 173:1
22. Ugliengo P, Garrone E (1984) J Mol Catal 54:439
23. Mortier WJ, Sauer J, Lercher JA, Noller H (1984) J Phys Chem 88:905
24. Stave MS, Nicholas JB (1993) J Phys Chem 97:9630
25. Sauer J, Ugliengo P, Garrone E, Saunders VR (1994) Chem Rev 94:2095
26. Bordiga S, Ugliengo P, Damin A, Lamberti C, Spoto G, Zecchina A, Spano G, Buzzoni R, Dalloro L, Rivetti F (2001) Top Catal 15:43
27. Bordiga S, Roggero I, Ugliengo P, Zecchina A, Bolis V, Artioli G, Buzzoni R, Marra G, Rivetti F, Spano G, Lamberti C (2000) J Chem Soc Dalton Trans 3921
28. Morrow BA, Devi A (1972) Trans Faraday Soc 68:403
29. Boccuzzi F, Coluccia S, Ghiotti G, Morterra C, Zecchina A (1978) J Phys Chem 82:1298
30. Spoto G, Bordiga S, Garrone E, Ghiotti G, Zecchina A, Petrini G, Leofanti G (1992) J Mol Catal 74:175

31. Zecchina A, Bordiga S, Spoto G, Marchese L, Petrini G, Leofanti G, Padovan M (1992) J Phys Chem 96:4985
32. Ferrari AM, Garrone E, Spoto G, Ugliengo P, Zecchina A (1995) Surf Sci 323:151
33. Weckhuysen BM, Schoonheydt RA, Jehng JM, Wachs IE, Cho SJ, Ryoo R, Kijlstra S, Poels E (1995) J Chem Soc Faraday Trans 91:3245
34. Weckhuysen BM, Verberckmoes AA, DeBaets AR, Schoonheydt RA (1997) J Catal 166:160
35. Vuurman MA, Wachs IE, Stufkens DJ, Oskam A (1993) J Mol Catal 80:209
36. Hardcastle FD, Wachs IE (1988) J Mol Catal 46:173
37. Dines TJ, Inglis S (2003) Phys Chem Chem Phys 5:1320
38. Thune PC, Linke R, van Gennip WJH, de Jong AM, Niemantsverdriet JW (2001) J Phys Chem B 105:3073
39. Thune PC, Verhagen CPJ, vandenBoer MJG, Niemantsverdriet JW (1997) J Phys Chem B 101:8559
40. Thune PC, Loos J, Lemstra PJ, Niemantsverdriet JW (1999) J Catal 183:1
41. Thune PC, Loos J, de Jong AM, Lemstra PJ, Niemantsverdriet JW (2000) Top Catal 13:67
42. Thune PC, Loos J, Wouters D, Lemstra PJ, Niemantsverdriet JW (2001) Macromol Symp 173:37
43. van Kimmenade EME, Kuiper AET, Tamminga Y, Thune PC, Niemantsverdriet JW (2004) J Catal 223:134
44. Baker LM, Carrick WL (1968) J Org Chem 33:616
45. Zecchina A, Garrone E, Ghiotti G, Morterra C, Borello E (1975) J Phys Chem 79:966
46. Rebenstorf B, Larsson R (1981) J Mol Catal 11:247
47. Fubini B, Ghiotti G, Stradella L, Garrone E, Morterra C (1980) J Catal 66:200
48. Ghiotti G, Garrone E, Della Gatta G, Fubini B, Giamello E (1983) J Catal 80:249
49. Rebenstorf B (1977) Acta Chem Scand A 31:877
50. Rebenstorf B (1991) J Mol Catal 66:59
51. Rebenstorf B (1989) Acta Chem Scand A 43:413
52. Rebenstorf B (1989) J Mol Catal 56:170
53. Ghiotti G, Garrone E, Zecchina A (1988) J Mol Catal 46:61
54. Ghiotti G, Garrone E, Zecchina A (1991) J Mol Catal 65:73
55. Pershin AN, Shelimov BN, Kazansky VB (1979) Kinet Katal 20:1298
56. Pershin AN, Shelimov BN, Kazansky VB (1981) Kinet Katal 22:1526
57. Kazansky VB (1983) Kinet Katal 24:1338
58. Anpo M, Tanahashi I, Kubokawa Y (1982) J Phys Chem 86:1
59. Shelimov BN, Elev IV, Kazansky VB (1986) J Catal 98:70
60. Kohler SD, Ekerdt JG (1994) J Phys Chem 98:4336
61. Zecchina A, Spoto G, Bordiga S (1989) Faraday Discuss Chem Soc 87:149
62. Przhevalskaya LK, Shvets VA, Kazansky VB (1975) J Catal 39:363
63. Myers DL, Lunsford JH (1986) J Catal 99:140
64. Lunsford JH, Fu SL, Myers DL (1988) J Catal 111:231
65. Krauss H-L, Stach H (1975) Z Anorg Allg Chem 414:97
66. Groppo E, Prestipino C, Cesano F, Bonino F, Bordiga S, Lamberti C, Thune PC, Niemantsverdriet JW, Zecchina A (2005) J Catal 230:98
67. Merryfield R, McDaniel MP, Parks G (1982) J Catal 77:348
68. Morys P, Gorges U, Krauss HL (1984) Z Naturforsh, B: Anorg Chem, Org Chem 39B:458
69. Morys P, Gerritze R, Krauss HL (1977) Z Naturforsch B 31:774

70. Weckhuysen BM, Deridder LM, Schoonheydt RA (1993) J Phys Chem 97:4756
71. Zielinski P, Lana IGD (1992) J Catal 137:368
72. Zielinski PA, Szymura JA, Lana IGD (1992) Catal Lett 13:331
73. Kim CS, Woo SI (1992) J Mol Catal 73:249
74. Zecchina A, Scarano D, Bordiga S, Spoto G, Lamberti C (2001) Adv Catal 46:265
75. Garrone E, Ghiotti G, Morterra C, Zecchina A (1987) Z Naturforsh B 42:728
76. Rebenstorf B, Larsson R (1981) Z Anorg Allg Chem 478:119
77. Zecchina A, Spoto G, Ghiotti G, Garrone E (1994) J Mol Catal 86:423
78. Cimino A, Cordischi D, Derossi S, Ferraris G, Gazzoli D, Indovina V, Minelli G, Occhiuzzi M, Valigi M (1991) J Catal 127:744
79. Cimino A, De Angelis BA, Luchetti A, Minelli G (1976) J Catal 45:316
80. Gazzoli D, Occhiuzzi M, Cimino A, Minelli G, Valigi M (1992) Surf Interface Anal 18:315
81. Espelid O, Borve KJ (2001) Catal Lett 75:49
82. Zecchina A, Garrone E, Morterra C, Coluccia S (1975) J Phys Chem 79:978
83. Yermakov YI, Zacharov VA (1975) Adv Catal 24:173
84. Lupinetti AJ, Frenking G, Strauss SH (1998) Angew Chem Int Edit 37:2113
85. Strauss SH (2000) J Chem Soc Dalton 1
86. Xu Q (2002) Coord Chem Rev 231:83
87. Willner H, Aubke F (1997) Angew Chem Int Edit 36:2403
88. Zecchina A, Bordiga S, Turnes Palomino G, Scarano D, Lamberti C, Salvalaggio M (1999) J Phys Chem B 103:3833
89. Bolis V, Barbaglia A, Bordiga S, Lamberti C, Zecchina A (2004) J Phys Chem B 108:9970
90. Gaspar AB, Martins RL, Schmal M, Dieguez LC (2001) J Mol Catal A 169:105
91. Gaspar AB, Brito JLF, Dieguez LC (2003) J Mol Catal A 203:251
92. Scarano D, Spoto G, Bordiga S, Zecchina A (1992) Surf Sci 176:281
93. Scarano D, Spoto G, Bordiga S, Carnelli L, Ricchiardi G, Zecchina A (1994) Langmuir 10:3094
94. Braterman PS (1975) Metal carbonyl spectra. Academic, London
95. Lamberti C, Bordiga S, Salvalaggio M, Spoto G, Zecchina A, Geobaldo F, Vlaic G, Bellatreccia M (1997) J Phys Chem 101:344
96. Lamberti C, Turnes Palomino G, Bordiga S, Berlier G, D'Acapito F, Zecchina A (2000) Angew Chem Int Ed 39:2138
97. Bordiga S, Turnes Palomino G, Arduino D, Lamberti C, Zecchina A, Otero Areán C (1999) J Mol Catal A 146:97
98. Kettle SFA, Paul I (1972) In: Stone FGA, West R (eds) Advances in organometallic chemstry. Academic, New York, p 199
99. Bordiga S, Bertarione S, Damin A, Prestipino C, Spoto G, Lamberti C, Zecchina A (2003) J Mol Catal A 204:527
100. Espelid O, Borve KJ (2002) J Catal 205:177
101. Geerlings P, De Proft F, Langenaeker W (2003) Chem Rev 103:1793
102. Kantcheva M, Bushev V, Klissurski D (1994) J Catal 145:96
103. Bade OM, Blom R, Ystenes M (1998) J Mol Catal A 135:163
104. Myers DL, Lunsford JH (1985) J Catal 92:260
105. McDaniel MP, Martin SJ (1991) J Phys Chem 95:3289
106. Grayson ME, McDaniel MP (1991) J Mol Catal 65:139
107. Rebenstorf B, Chem ZAA (1984) 513:103
108. Szymura JA, DallaLana IG, Fiedorow R, Zielinski PA (1996) Macromolecules 29:3103

109. Smith GD, Palmer RA (2002) Fast time-resolved mid-infrared spectroscopy using an interferometer. In: Chalmers JM, Griffiths PR (eds) Handbook of vibrational spectroscopy, vol 1. Wiley, Chichester, p 625
110. Otero Arean C, Escalona Platero E, Spoto G, Zecchina A (1989) J Mol Catal 56:211
111. Escalona Platero E, Otero Arean C, Scarano D, Spoto G, Zecchina A (1991) Mater Chem Phys 29:347
112. Geobaldo F, Spoto G, Bordiga S, Lamberti C, Zecchina A (1997) J Chem Soc Faraday Trans 93:1243
113. Spoto G, Bordiga S, Ricchiardi G, Scarano D, Zecchina A, Borello E (1994) J Chem Soc Faraday Trans 90:2827
114. Nishimura M, Thomas JM (1993) Catal Lett 21:149
115. Artioli G, Lamberti C, Marra GL (2000) Acta Cryst B 56:2
116. Cossee P (1964) J Catal 3:80
117. Ivin KJ, Rooney JJ, Stewart CD, Green MLH, Mahtab JR (1978) J Chem Soc Chem Commun 604
118. Zecchina A, Bertarione S, Damin A, Scarano D, Lamberti C, Prestipino C, Spoto G, Bordiga S (2003) Phys Chem Chem Phys 5:4414
119. Freundlich JS, Schrock RR, Cummins CC, Davis WM (1994) J Am Chem Soc 116:6476
120. Giannini L, Solari E, Floriani C, Chiesi-Villa A, Rizzoli C (1998) J Am Chem Soc 120:823
121. Espelid O, Borve KJ (2000) J Catal 195:125
122. Espelid O, Borve KJ (2002) J Catal 206:331
123. Espelid O, Borve KJ (2002) J Catal 205:366
124. Groeneveld C, Wittgen PPMM, Swinnen HPM, Wernsen A, Schuit GCA (1983) J Catal 83:346
125. Jozwiak WK, Lana IGD, Fiedorow R (1990) J Catal 121:183
126. McDaniel MP, Welch MB (1983) J Catal 82:98
127. McDaniel MP, Kantor DM (1983) J Polym Sci A–Polym Chem 21:1217
128. Amor Nait Ajjou J, Rice GL, Scott SL (1998) J Am Chem Soc 120:13436
129. Amor Nait Ajjou J, Scott SL (1997) Organometallics 16:86
130. Amor Nait Ajjou J, Scott SL, Paquet V (1998) J Am Chem Soc 120:415
131. Krauss HL, Hagen K, Hums E (1985) J Mol Catal 28:233
132. Amor Nait Ajjou J, Scott SL (2000) J Am Chem Soc 122:8968
133. Scott SL, Amor Nait Ajjou J (2001) Chem Eng Sci 56:4155
134. Turner HW, Schrock RR, Fellman JD, Holmes SJ (1983) J Am Chem Soc 105:4942
135. Emrich R, Heinemann O, Jolly PW, Kruger C, Verhovnik GPJ (1997) Organometallics 16:1511
136. Ruddick VJ, Badyal JPS (1998) J Phys Chem B 102:2991
137. Krauss HL, Hums E (1979) Z Naturforsh B: Anorg Chem, Org Chem 34B:1628
138. Huang CZ, Ahn J, Kwon S, Kim J, Lee J, Han YH, Kim H (2004) Appl Catal A 258:173
139. Groppo E, Damin A, Bonino F, Zecchina A, Bordiga S, Lamberti C (2005) Chem Mater 17:2019
140. Damin A, Bonino F, Bordiga S, Groppo E, Lamberti C, Zecchina A (2005) Chem Phys Chem 6 in press
141. Groppo E, Lamberti C, Bordiga S, Spoto G, Zecchina A (2005) J Phys Chem B 109:15024
142. Groppo E, Lamberti C, Spoto G, Bordiga S, Magnacca G, Zecchina A (2005) J Catal in press

Top Organomet Chem (2005) 16: 37–68
DOI 10.1007/b138073

Published online: 14 September 2005

Single Site Catalyst for Partial Oxidation Reaction: TS-1 Case Study

S. Bordiga (✉) · A. Damin · F. Bonino · C. Lamberti

Department of Inorganic, Physical and Materials Chemistry
and NIS Centre of Excellence, Università di Torino, Via P. Giuria 7, 10125 Torino, Italy
silvia.bordiga@unito.it

Abstract We briefly underline the relevance of TS-1 catalyst for industrial applications in mild oxidation reactions using hydrogen peroxide as oxidant and review the experimental works employed over last two decades for understanding the structure of the Ti centers in the bare TS-1 material. After an animated and controversial debate that has lasted in the literature until 1994, several works (reviewed here in depth) have definitively assessed that Ti atoms occupy framework positions substituting a Si atom and forming tetrahedral

[TiO_4] units. The literature concerning the interaction of TS-1 with ligand molecules is briefly discussed. There is unanimous consensus that ligand adsorption causes the distortion from the T_d-like symmetry of the [TiO_4] units. As the TS-1 catalyst works in aqueous solution, particular attention has been devoted to the interaction with water; the same holds for ammonia as it is a reactant in the ammoximation of cyclohexanone to give cyclohexanone oxime. Finally, the interaction of TS-1 with H_2O/H_2O_2 solutions is reviewed in detail. Particular attention is paid to very recent results that have significantly improved knowledge of the catalyst in conditions as close as possible to working conditions. UV-Vis, Raman (under resonance conditions) and X-ray absorption (both in the XANES and EXAFS regions) spectroscopies have been determinant in highlighting the structure of the species formed by adsorption of H_2O_2 on Ti centers inside the TS-1 framework. The following observations demonstrate a synergic role between Ti(IV) centers and hydrogen peroxide: (i) the O – O species, responsible for the yellow color of the TS-1/H_2O/H_2O_2 system, is a side-on peroxo complex, probably generated by the reversible rupture of one Ti – O – Si bridge, with the formation of Ti(O_2H) and H – O – Si groups; (ii) the stability of this peroxo complex is low in the absence of an excess of H_2O; (iii) a strong enhancement of the acidity of the TS-1/H_2O_2/H_2O system with respect to that of TS-1/H_2O have been observed.

Keywords EXAFS · H_2O_2 · Hydroperoxo complexes · IR · Raman · Partial oxidations · Peroxo complexes · Titanosilicate · TS-1 · UV-Vis · XANES

Abbreviations

DRS	Diffuse reflectance spectroscopy
EPR	Electron paramagnetic resonance
EXAFS	Extended X-ray absorption spectroscopy
FT	Fourier transform
FTIR	Fourier transformed infrared spectroscopy
IR	Infrared
TS-1	Titanium silicalite-1
UV-Vis	Ultraviolet-visible spectroscopy
XANES	X-ray absorption near edge structure spectroscopy

1 Introduction

By single-site catalysts we mean catalysts where the breaking and formation of chemical bonds occurs at isolated active centers whose chemical activity is dominated by the electronic properties of a single atomic species or of a small cluster of atoms that can act in an independent way with respect to others.

Homogeneous catalysts are very often known as examples of single-site catalysts characterized by complete structural definition and (presumably) complete knowledge of the chemical processes occurring at their catalytic centers. It is a matter of fact that the homogeneous catalysts are molecular complexes constituted by an active core containing a single active atom (of-

ten metallic) or a cluster of atoms and that these active species or cluster of species operate as individual entities (in solution of an inert solvent). In all these complexes, the catalytic activity is essentially dominated by the mono- or polymetallic cores. This does not mean that the ligands surrounding the active core are not playing a role in the catalytic events. In fact they have many vital functions. Among these are:

- Modulation of the electron density on the frontier atomic orbitals centered on the active atom(s) with LUMO and HOMO character
- Control or preservation of the geometry of the site (in terms of structure, number, and location of the metal atoms and of coordinative vacancies) during the catalytic cycles
- Cooperative activity in the diffusion of the reactants from and to the active center

True examples of single-site catalysts are enzymes, where active sites are made mainly by metallic centers (mono- or polynuclear species) whose coordination sphere is completely defined by ligands [1–4]. The strength of enzymes is the combined effect of metal center activity with the specific behavior of metal coordination sphere ligands. These species play a key role, being optimized to create an environment suitable for: (i) metal centers approaching and coordinating by reactants; (ii) product removal from the catalytic centers at the end of the reaction in order to avoid further reactions.

Among heterogeneous catalysts, very few are generally agreed examples of single-site catalysts. Generally speaking heterogeneous catalysts are characterized by a large variety of sites among which only a small fraction, sometimes only a small percentage, are catalytically active [5, 6].

The difficulty is that characterization techniques are usually not selective towards active sites, so very often the main spectroscopic features are not evidence for active sites manifestations. However, it is possible to find some exceptions mainly among functionalized materials, such as zeolites. One of the few well established examples is TS-1 [7], a zeolite discovered in 1983 behaving as a catalyst for partial oxidation reactions in H_2O_2/H_2O solutions [8–20].

In this zeolitic material a very low percentage of Ti(IV), dispersed in a pure siliceous microporous matrix (with the MFI framework, the same as that of the ZSM-5 zeolite), is able to oxidize in mild conditions many substrate with extremely high activity and selectivity (see Sect. 2). However, after more than three decades, a complete picture of reaction mechanisms is still missing. Major problems related to characterization are due to the extremely high dilution of Ti(IV) in the zeolitic matrix and the presence of high amounts of water in the reaction media. The first point requires characterization techniques very sensitive and selective towards Ti(IV). For instance, XRD measurements have been able to recognize the presence of Ti(IV) in the framework only indirectly, via the measured unit cell volume increase [21, 22], but attempts to

directly localize Ti(IV) have not given unambiguous interpretations [22–26]. This is the main reason why spectroscopic techniques have been so widely employed to characterize TS-1. Combined use of them have been able to clarify that Ti(IV) occupies framework positions in the MFI lattice (Sect. 3) and expands its coordination sphere upon contact with extra ligands (Sect. 4). Many studies have been performed following the reactivity of Ti(IV) towards extra ligands from the gas phase (see Sect. 4), but a deep characterization of Ti(IV) in presence of H_2O_2 aqueous solution was missing and only very recently it has been achieved (see Sect. 5).

2
Oxidation Reactions Catalyzed by TS-1

The selective catalytic oxidation of organic compounds with an environmental attractive oxidant, aqueous H_2O_2, is a challenging goal of fine chemistry. Over the past two decades, heterogeneous Ti(IV)-based catalysts have received much attention for their application in this field. Highly active and selective catalysts can be produced by dispersing Ti atomically in a silica matrix [27, 28], or by grafting isolated Ti species to the surface of silica [29–31], mesoporous molecular sieves [32, 33], layered aluminosilicates [34], polyoxometallates [35, 36], or by isomorphously substituting Ti for silicon in molecular sieve frameworks [7, 17, 37–39]. Titanium silicalite-1 (TS-1) belongs to this last category as it is obtained by inserting Ti in the MFI lattice.

TS-1 is a material that perfectly fits the definition of "single-site catalyst" discussed in the previous Section. It is an active and selective catalyst in a number of low-temperature oxidation reactions with aqueous H_2O_2 as the oxidant. Such reactions include phenol hydroxylation [9, 17], olefin epoxidation [9, 10, 14, 17, 40], alkane oxidation [11, 17, 20], oxidation of ammonia to hydroxylamine [14, 17, 18], cyclohexanone ammoximation [8, 17, 18, 41], conversion of secondary amines to dialkylhydroxylamines [8, 17], and conversion of secondary alcohols to ketones [9, 17], (see Fig. 1). Few oxidation reactions with ozone and oxygen as oxidants have been investigated.

TS-1-catalyzed processes are advantageous from the environmental point of view as the oxidant is aqueous hydrogen peroxide, which turns into water, and the reactions are operated in liquid phase under mild conditions, showing very high selectivity and yields, thus reducing problems and the costs of by-product treatments. Confinement of the metal species in the well-defined MFI pore system endows TS-1 with shape selectivity properties analogous to enzymes. For these features the application of the terms "mineral enzyme" or "zeozyme" to TS-1 is appropriate [42].

Among the reactions mentioned before, the early industrial applications of TS-1 catalyst were the hydroxylation of phenol (10 000 ton/year) and the

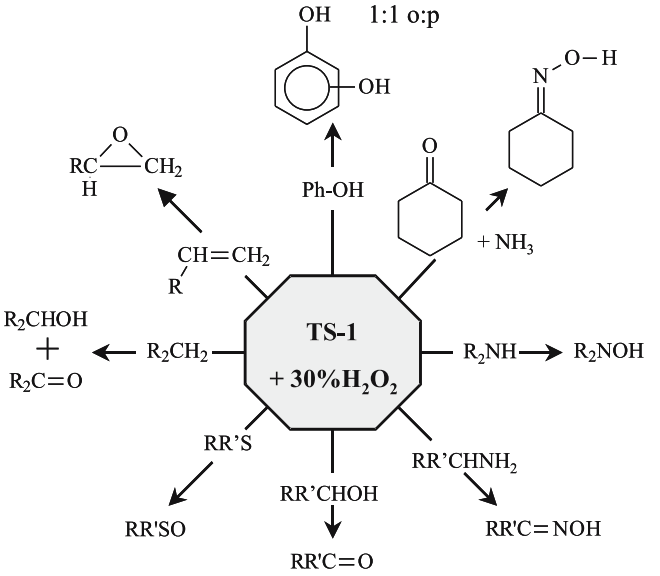

Fig. 1 Schematic representation of the most relevant oxidation reactions catalyzed by TS-1

ammoximation of cyclohexanone to cyclohexanonoxime (12 000 ton/year), both developed by Enichem. Recently, Sumitomo started producing cyclohexanonoxime in Japan (> 60 000 ton/year) [43], while Enichem developed up to pilot plant scale the production of propylene oxide in Italy (6 ton/day) [44].

The unique activity and selectivity of TS-1 is nowadays believed to be due to isolated sites of tetrahedral Ti atoms inserted in the vicarious position of silicon in the MFI framework (see Sect. 3). The isolated and tetracoordinated Ti centers are able to expand their coordination sphere up to six by interaction with extra ligands [45] (see Sect. 4). It has also been demonstrated that Ti centers interact with hydrogen peroxide to form peroxo species (see Sect. 5) [46–50]. The framework composition of TS-1 can be defined as: $x\mathrm{TiO_2} \cdot (1 - x)\mathrm{SiO_2}$, and the upper limit for x (the Ti mole fraction) is around 0.025 (vide infra Sect. 3.1). Attempts to produce TS-1 with significantly higher Ti content fail, as the excess Ti segregates as TiO_2. The change in catalytic properties resulting from the presence of extra-framework TiO_2 depends on the catalytic reaction. In the case of alkane and alkene oxidation, the differences are limited, whereas in phenol oxidation a remarkable dependence of selectivity on TiO_2 content is observed. TiO_2 is a very efficient catalyst for H_2O_2 decomposition, resulting in lower H_2O_2 selectivity; but TiO_2 can also catalyze other reactions and in this way reduce the yield of the desired products. Apart from TiO_2, many other impurities (e.g., Al^{3+} and Fe^{3+}) can be present and some of them can modify the products of a catalytic reaction [17].

Crystallite dimensions play a role in determining the rates of reactions and their control is of fundamental importance not only for the catalytic activity, but also for the selectivity, since, with low rates of the desired reaction, the relative importance of secondary reactions may be greater. The effects of crystallite dimensions have been demonstrated for 1-butene epoxidation and for phenol hydroxylation, and they are significant for many reactions carried out with liquid phase reactants [17].

As discussed in the exhaustive review of Notari [17], reaction temperature is of the upmost importance since Ti peroxo compounds decompose above 323 K. Solvents also have a remarkable effect in reaction rates and selectivity.

3
Investigation of the Bare TS-1: Anhydrous Catalyst

In the 1980s and in the beginning of the 1990s a lively debate took place in the literature concerning the structural nature of the Ti centers in TS-1: titanyl groups, extraframework defect sites, monomeric and dimeric Ti species, Ti species incorporated in edge-sharing type structures forming bridges across the zeolite channels etc. have all been inferred by different authors. The same holds for the local geometries, where Ti species having local coordinations such as tetrahedral, square pyramidal, or octahedral have been hypothesized.

The origin of the initial confusion was probably related to the difficulty encountered in the synthesis of well manufactured TS-1, which requires the use of extremely pure reagents and severe control in the synthesis conditions [7]. An imperfect synthesis implies an incomplete incorporation of Ti into the MFI framework, leading to a significant reduction of the catalytic performance and possibly to a misinterpretation of structural and spectroscopic data. Moreover, as already mentioned, the fact that only a very small amount of Ti (less than 3 wt % in TiO_2, corresponding to a molar ratio of $x = [Ti]/([Ti] + [Si]) = 0.025$ [21]) can be substituted into the MFI framework [51] does not facilitate the extraction and the attribution of the Ti contribution from the total experimental signal. Note that the $x = 0.025$ limit has been recently slightly improved [24, 52].

Nowadays there is a general consensus that the Ti(IV) atoms are incorporated as isolated centers into the framework and are substituting Si atoms in the tetrahedral positions forming $[TiO_4]$ units. The model of isomorphous substitution has been put forward on the basis of several independent characterization techniques, namely X-ray [21–23] or neutron [24–26] diffraction studies, IR (Raman) [52–57], UV-Vis [38, 54, 58], EXAFS, and XANES [52, 58–62] spectroscopies.

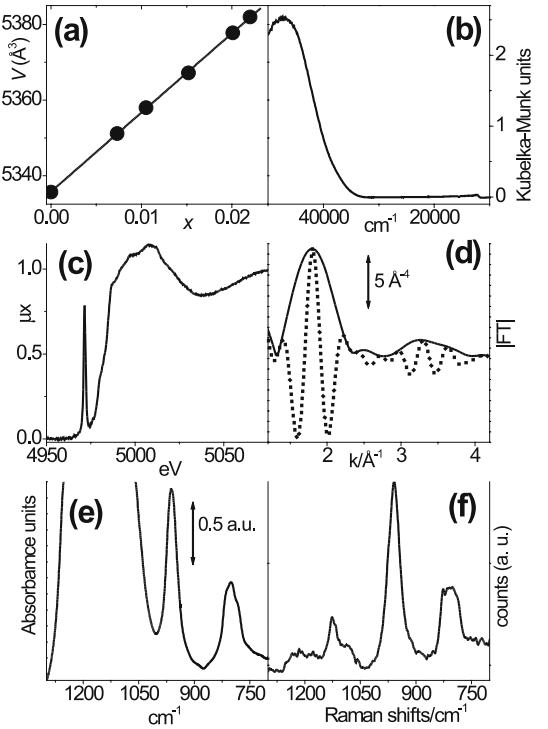

Fig. 2 Summary of the most employed characterization techniques used to investigate TS-1 catalyst under dehydrated conditions. **a** Volume cell (V) variation vs. Ti content in the material (x) as determined by XRD, data taken by Lamberti et al. [22]. **b** UV-Vis DRS spectrum, typical of solated tetrahedral Ti(IV) species [52, 54, 58]. **c** XANES spectrum, proving the T_d-like symmetry of Ti(IV) species [58, 59]. **d** Phase corrected, k^3-weighted FT (modulus and imaginary parts *full* and *dotted lines*, respectively) of the EXAFS spectrum, showing that Ti(VI) is surrounded by four oxygen neighbors at 1.79–1.81 Å [58, 59]. **e** IR spectrum in the framework stretching modes showing the appearance of the 960 cm^{-1} mode, typical of insertion of Ti inside the zeolitic framework [52, 53]. **f** Raman spectrum obtained using an exciting laser in the infrared: (λ = 1064 nm). Both 960 and 1125 cm^{-1} modes are visible [52, 55]

The most informative characterization techniques used to determine Ti species inside dehydrated TS-1 catalysts are described in Sects. 3.1–3.7. The discussion is supported by the experimental data reported in Fig. 2.

3.1 XRD

Diffraction experiments have evidenced an increase of the cell volume V which is proportional to the Ti content [21, 22, 63]. The qualitative V vs. x increase is easily obtained, however, care must be taken in using the XRD

technique as a means of determining quantitatively the fraction of framework Ti incorporation. In fact, together with the amount of incorporated Ti(x) different additional factors act in determining the cell volume V of the hosting matrix. Among the most relevant ones are: the amount of defects (silicon vacancies generating internal silanol nests, see Sect. 3.8) and the amount and the nature of molecules (mainly water and hydrocarbons) adsorbed in the channels. Only if the last two points are under control, does the direct V vs. x linear dependence hold. Millini et al. [21] recommend ammonium acetate treatment and successive calcination of the TS-1 samples measured in air to limit the dispersion of the point in the (x, V) plane. The effect of the treatment has been rationalized in terms of the relaxation of framework tensions and the cleaning of sample-related effects involving extraframework species. Lamberti et al. [22] reported that an high linearity can also be obtained by measuring activated samples under vacuum conditions (inside sealed capillaries), see Fig. 2a. The linearity of such data is in agreement with that reported by Millini et al. [21], although there is a systematic cell volume increment of about 11–14 $Å^3$ in the dehydrated samples with respect to the hydrated ones. This implies an interaction between the adsorbed water molecules and the TS-1 framework. It is not surprising, considering the effects between the polar water molecule and the internal silanol and titanol groups acting as weak Brønsted sites. This is in agreement with IR studies in which hydrogen bond interactions of medium and high strength were evidenced by observing the perturbation of the O – H stretching mode of silanols and titanols on interaction with H_2O [54, 64].

3.2 UV-Vis

The UV-vis spectra of TS-1 in vacuo gives a simple and clear proof of the presence of tetrahedral Ti(IV) in the zeolite framework [37, 38, 52, 54, 57, 58, 63, 65]: in fact a $Ti^{4+}O^{2-} \rightarrow Ti^{3+}O^{-}$ ligand to metal charge transfer (LMCT) located at $\approx 48\,000\ cm^{-1}$ (Fig. 2b) can be unambiguously assigned to the charge transfer transition from the oxygen ligand to an unoccupied orbital of a Ti(IV) ion tetrahedrally coordinated in isolated $[TiO_4]$. In fact Ti(IV) species in octahedral coordination (as in anatase or rutile) exhibit a $Ti^{4+}O^{2-} \rightarrow Ti^{3+}O^{-}$ LMCT in the 31 500–33 000 cm^{-1} [66, 67]. On the basis of the theoretical study of Ricchiardi et al. [52] the 48 000 cm^{-1} LMCT band should not be considered as a charge transfer from a single oxygen atom out of the four nearest neighbors but as a symmetric charge release, which occurs from the four nearly equivalent oxygen atoms to the Ti(IV) center in the quasi-tetrahedral $[TiO_4]$ unit, leading to the symmetric expansion of the tetrahedral unit. This point will have great relevance when resonant Raman results are discussed (Sect. 3.7).

3.3
XANES

The low Ti content (up to 3 wt % in TiO_2) makes the extraction of vibrational, energetic, and geometric features specific to TiO_4 moieties a difficult task as the experimental data are dominated by the features of the siliceous matrix. This is the reason why the structure of the local environment around Ti(IV) species inside TS-1 was only definitively assessed more than 10 years after the discovery of the material, when the atomic selectivity of X-ray absorption spectroscopies (both XANES and EXAFS) were used [58–60].

XANES spectroscopy shows that a narrow and intense pre-edge peak at 4967 eV, due to the $1s \rightarrow 3pd$ electronic transition involving Ti atoms in tetrahedral coordination, is present in well-manufactured TS-1 (Fig. 2c). Conversely this electronic transition of Ti(IV) species in TiO_2 (anatase or rutile) is characterized by a very low intensity due to the small *pd* hybridization in octahedral symmetry. Indeed the transitions $A_{1g} \rightarrow T_{2g}$ are symmetrically forbidden in the case of octahedral coordination of Ti (IV), but the transition $A_1 \rightarrow T_2$ is allowed in the case of tetrahedral coordination of Ti(IV), as in the case of $[TiO_4]$ units [52, 58–61, 63, 68].

3.4
EXAFS

Insertion of Ti atoms in a $T(OSi)_4$ site strongly perturbs the T – O distance, which increases from 1.59–1.60 Å for T = Si [69] to 1.79 – 1.81 ± 0.01 Å for T = Ti, as proved by the EXAFS experiments of Bordiga et al. [58, 59] (see Fig. 2d). Such studies were limited to the first shell, showing that Ti atoms are, within experimental errors, coordinated to four oxygen atoms located in the 1.79–1.81 Å range. Second shell studies appeared only considerably later [62, 68]. In particular, in collaboration with colleagues of the Royal Institute (London, GB), Bordiga et al. showed that the four Ti – O – Si angles are not equivalent. Two pairs of angles have been found, the narrower one of $143 \pm 5°$, and the broader of $162 \pm 5°$[68]. The four second shell Ti – Si distances lie in the $3.26–3.38 \pm 0.02$ Å interval.

3.5
IR

The IR spectra of silicon oxides, in the framework region mode, is dominated by a strong absorption around 1000 cm^{-1}, due the anti-symmetric stretching of the Si – O – Si unit (Raman inactive mode) and by a less intense absorption around 800 cm^{-1}, due the symmetric stretching of the Si – O – Si unit (Raman active mode). In the transparency window between these two modes, the IR spectra of TS-1 shows an additional absorption band located at 960 cm^{-1}

(Fig. 2e), virtually absent in perfect silicalite-1 and immediately identified as a fingerprint of TS-1 material [37, 52–55, 63, 70, 71]. A qualitative correlation between the intensity of the infrared band at 960 cm^{-1} and Ti content has been observed since the first synthesis of TS-1. Indeed, the occurrence of that band is one of the distinctive features of the material cited in the original patent [7]. However, the quantitative correlation has been reported only very recently by Ricchiardi et al. [52], owing to very serious experimental problems related to the saturation of the IR framework modes. In the same work, the nature of the 960 cm^{-1} band has been discussed in terms of theoretical calculations based on both cluster and periodical approaches.

3.6 Raman

In the early 1990s Raman spectroscopy was applied to the characterization of TS-1 catalysts [55, 56]. In such experiments, beside the 960 cm^{-1} band, already observed by IR spectroscopy (see Sect. 3.5), a new component at 1125 cm^{-1} was detected by Scarano et al. [55] (see Fig. 2f). The 1125 cm^{-1} band was recognized to be a fingerprint of the insertion of Ti atoms in the zeolitic framework [55]. This band could not be observed in the IR studies as totally overshadowed by an extremely intense band around 1000 cm^{-1} due to SiO_2 framework modes (Fig. 2e).

3.7 Resonant Raman

The remarkable effect that the resonance enhancement effect has on the intensities of the observed Raman band is clearly shown in Fig. 3. Figure 3a reports the UV-Vis DRS spectrum of dehydrated TS-1. The band at 208 nm (48 000 cm^{-1}) is LMCT, which occurs from the four nearly equivalent oxygen atoms to the Ti(IV) center in the quasi-tetrahedral $[TiO_4]$ unit, leading to the symmetric expansion of the tetrahedral unit [52] (see Sect. 3.2). The four laser lines used to collect the Raman spectra reported in Fig. 3b are also shown. It is evident that, by progressively increasing the energy of the exciting source, one will enter into the Ti-specific LMCT band and thus enhancement of the Ti-specific vibrational modes are expected. Enhancement, however, only occurs for the modes that fulfill the resonance Raman selection rules, which can be briefly summarized as follows: Resonance Raman spectroscopy is defined as a Raman experiment in which the exciting wavelength coincides with, or is near to, the wavelength of an electronic adsorption of the sample. This condition guarantees a high transfer of energy to the sample. If the electronic absorption is due to a localized center, like a transition metal atom, the excitation is also partially localized and the vibrational features of the immediate vicinity of the absorbing atom can be enhanced by several orders of

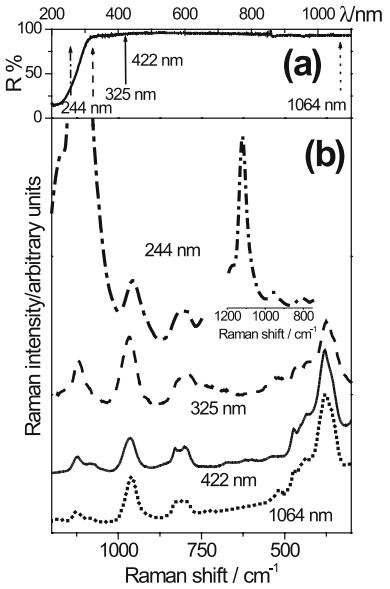

Fig. 3 **a** UV-Vis DRS spectra of dehydrated TS-1 catalyst reporting the typical 208 nm (48 000 cm^{-1}) LMCT band, see Fig. 2b; also reported are the four excitation laser lines used in this Raman study: near-IR (*dotted*), visible (*full*), near-UV (*dashed*) and far-UV (*dot-dashed*). **b** Raman spectra of dehydrated TS-1 obtained with four different lasers emitting at λ = 1064, 422, 325, and 244 nm (*dotted, full, dashed*, and *dot-dashed lines*, respectively). Raman spectra have been vertically shifted for clarity. Although the intensity of each spectrum depends upon different factors, the evolution of the $I(1125)/I(960)$ ratio by changing the laser source is remarkable. The *inset* reports the Raman spectrum collected with the 244 nm laser in its full scale, in order to appreciate the intensity of the 1125 cm^{-1} enhanced mode. Adapted from [48] with permission. Copyright (2003) by The Owner Societies 2003

magnitude, if they meet the appropriate enhancement selection rules. Two kinds of vibrations are enhanced: (i) totally symmetric vibrations with respect to the absorbing center, and (ii) vibrations along modes which cause the same molecular deformation induced by the electronic excitation [72, 73].

Figure 3b reports the Raman spectra collected on the dehydrated TS-1 using the four different lasers. Beside the typical modes of the siliceous MFI framework at 800 and 370 cm^{-1}, we observe the two Ti-specific bands at 960 and 1125 cm^{-1} mentioned in Sects. 3.5 and 3.6. It is evident that only the latter mode is enhanced by tuning the exciting laser source within the Ti-specific LMCT band. Quantitatively, from the data reported in Fig. 3b, the ratio between the intensities of the two Ti-specific modes increases progressively by moving from the near-IR to the far-UV source in particular: $I(1125)/I(960)$ = 0.25, 0.48, 0.65 and 12.50 for the 1064, 442, 325, and 244 nm lasers, respectively.

Historically, the resonant Raman effect occurring on TS-1 (enhancement of the 1125 cm^{-1} mode and invariance 960 cm^{-1} mode, see Fig. 3) was first highlighted in 1999 by Li et al. [57] and successively reproduced in the works of Ricchiardi et al. [52] in 2001 and of Bordiga et al. [48] in 2003. The correct interpretation of the experimental results was achieved only in the combined spectroscopic and ab initio works of Ricchiardi et al. [52], Bordiga et al. [64], Damin et al. [74–76] and Bonino et al. [77], showing that the 1125 cm^{-1} band corresponds to the totally symmetric stretching mode of the $[Ti(OSi)_4]$ units, while the 960 cm^{-1} mode results from the combination of three asymmetric stretching modes of the same unit. Among all Raman modes, the 1125 cm^{-1} mode is the only one enhanced when the resonance conditions are progressively switched on (by tuning the wavelength of the laser source) because it is the only vibrational mode exhibiting the same symmetry as the 48 000 cm^{-1} LMCT.

3.8
The Defective Nature of TS-1 Material: Speculative Model of Framework Sites

To better understand the role played by the microporous nature of the MFI framework hosting the active Ti sites, Zecchina's group has performed an ongoing research [24, 69, 78–86] on the Ti-free silicalite-1, synthesized according to the original patent for TS-1 [7] (i.e., simply without including TiO_2 in the reactants). It has been shown that silicalite-1 synthesized without including TiO_2 in the reactants) [7] is a defective material showing a high density of bulk Si vacancies ($^{\bullet}$) resulting in hydroxylated nests: $[Si(-O-Si\equiv)_4] \rightleftarrows [^{\bullet}(HO-Si\equiv)_4]$. The defective MFI matrix has also been observed for TS-1. It has been demonstrated by IR and microcalorimetry that the insertion of Ti heteroatoms in the MFI lattice has a mineralizing effect causing the progressive reduction of the internal defects [24, 83, 84].

In a neutron diffraction study, Lamberti et al. [24] have shown that Ti insertion in TS-1 and Si vacancies in Ti-free silicalite-1 [69] do not occur randomly and that they are preferentially hosted in the same four sites (among the twelve of the MFI framework): Si(6), Si(7), Si(11), and Si(10) sites. The correspondence of the four sites preferentially hosting the Si vacancies in defective silicalite-1 with those preferentially occupied by Ti atoms in TS-1 is striking. Moreover, it has been shown using several independent characterization techniques [58, 62, 65, 83, 84, 87] (IR, UV-Vis, EXAFS, microcalorimetry) that the insertion of the Ti heteroatoms in the MFI lattice has a mineralizing effect, causing the progressive reduction of the framework defects. Figure 4b reports the OH stretching region of the IR spectra of dehydrated TS-1 samples and the increasing Ti content in the range 0 (silicalite-1) to 2.64 atoms/unit cell. On the basis of the IR spectra, it is evident that the progressive incorporation of Ti atoms in the framework implies the parallel reduction of the OH band due to internal, defective, Si – OH groups (erosion of the

broad 3600–3200 cm^{-1} component in Fig. 4a). The combined crystallographic evidence (obtained on defective silicalite-1 and on TS-1) together with the mineralizing effect of Ti heteroatoms strongly suggest that the incorporation mechanism of the Ti atoms in the MFI framework occurs via the insertion of Ti in defective sites of silicalite-1. In this context, it is worth noting that the computational study of Ricchiardi et al. [88] indicates that the $[TiO_4]$ and the $[(OH)_4]$ units, substituting regular $[SiO_4]$ units in the MFI framework, have a rather similar size. In other words, $[TiO_4]$ and $[(OH)_4]$ units cause a similar local deformation when inserted in the MFI lattice. This can explain the tendency of the same sites to host either a defect (Si vacancy) or a Ti heteroatom. This also explains why the amount of incorporated Ti increases to the detriment of internal OH species: $[^{\bullet}(HO-Si\equiv)_4] \rightleftarrows [Ti(-O-Si\equiv)_4]$, the equilibrium being displaced to the right hand term by increasing the Ti concentration of the synthesis. The fact that three out of the four preferential T sites (T7, T10, and T11), for both Ti insertion and Si vacancy, are adjacent (see top part of Fig. 4b) to each other implies that, in principle, a fraction of Ti atoms could be located in the proximity of a Si vacancy. So, the whole picture emerging from the combined neutron diffraction and IR study (on TS-1 samples in the 0–2.64 Ti atoms/unit cell range) suggests that, beside regular $[Ti(OSi)_4]$ sites, defective $[Ti(OSi)_3OH]$ sites could also be significantly present, as pictorially represented at the bottom part of Fig. 4b (dotted and full arrows, respectively).

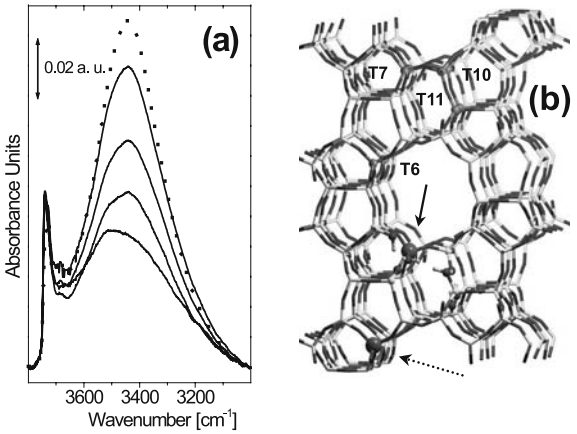

Fig. 4 **a** IR spectra, in the OH stretching region, of from top to bottom, TS-1 samples (*full line* spectra) with increasing Ti content, from 0 (silicalite-1, *dashed* spectrum) to 2.64 atoms per unit cell. All samples have been activated at 120 °C. Adapted from [24] with permission. Copyright (2001) by the ACS. **b** Schematic representation of the preferential location of Ti atoms and Si vacancies in the MFI framework (*upper part*) and their interplay (*lower part*). *Yellow* and *red* sticks represents Si and O of the regular MFI lattice; *blue* balls refer to Ti, and *red* and *white* balls to O and H of defective internal OH groups

4
TS-1 in Interaction with Ligand Molecules

Perturbation of structural, vibrational, and electronic features of the catalytic center by interaction with probe molecules is the most important experimental approach for understanding the accessibility and the reactivity of the site itself. The understanding of the system increases enormously if the experimental results are interpreted on the basis of accurate ab initio modeling. These general statements of course also hold for TS-1 [49, 52, 64, 74–77]. Unfortunately, we do not have the space to enter into a discussion of the abundant computational literature published so far on TS-1 catalyst in particular and on titanoslilcates in general. The reader can find an excellent starting point in the literature quoted in [49, 52, 64, 74–77, 88].

4.1
Interaction with Water and Ammonia

In this section we report a detailed summary of the experimental studies on the interaction of TS-1 with H_2O and NH_3. The choice of these two molecules is far from random. Interaction with water is important since the catalyst works in aqueous solution (Sect. 2). The interest in the study of NH_3 is twofold: ammonia is a reactant in the ammoximation of cyclohexanone to give cyclohexanone oxime and it is a stronger base than water, thus allowing a direct comparison between the effects induced by Lewis bases of increasing strength.

It will be shown that, upon interaction with water or ammonia, the T_d-like symmetry of the Ti(IV) centers in TS-1 is strongly distorted, as testified by UV-Vis, XANES, resonant Raman spectroscopies [45, 48, 52, 58, 64, 83, 84], and by ab initio calculations [52, 64, 74–76, 88]. As in Sect. 3 for the dehydrated catalyst, the discussion follows the different techniques used to investigate the interaction.

4.1.1
UV-Vis

UV-Vis spectroscopy has played a key role in the elucidation of the structure of Ti(IV) species in TS-1, in vacuo, in the presence of adsorbates, in presence of water, or in diluted aqueous solutions of different molecules [45, 46, 58, 64, 70, 89–91].

Interaction with water slightly modifies the UV-Vis spectrum of TS-1, causing a red shift of the $48\,000\ cm^{-1}$ edge expected as a consequence of the increase of the coordination sphere around Ti(IV) centers [45, 46, 58, 64]. Note that in TiO_2, where Ti exhibits six oxygen atoms in its first coordination

shell, the $Ti^{4+}O^{2-} \rightarrow Ti^{3+}O^{-}$ LMCT occurs around 32 000 cm^{-1}. A stronger perturbation is obtained upon dosing NH_3 (larger red shift) [46, 58, 64] but the line-shape of the UV-Vis curve still remains of the same type (one single maximum).

4.1.2 XANES and EXAFS

Interaction with H_2O (liquid drop on the sample) and with NH_3 (from the gas phase) implies a reduction of 4967 eV pre-edge peak accompanied by an increase of the white line (first resonance after the edge) intensity, witnessing the insertion of ligand molecules in the coordination shell of Ti(IV) and a modification of the local geometry from a tetrahedral to a nearly octahedral one. The perturbation of the XANES region (Fig. 5a) induced by wetting the sample is smaller than that induced by interaction with NH_3 from the gas phase [46, 64, 83, 84]. The same holds for the radial distribution around Ti (Fig. 5b). Modification of the second shell contribution in the 2.5–3.5 Å range is also noticeable. Moreover, if we compare, for the two cases, the first shell filtered Fourier back transform functions (Fig. 5c) we see that the interaction with H_2O causes only a very small decrement of the oscillation period, witnessing a small elongation of the four Ti – O bonds needed to accommodate the water molecules in the coordination sphere of Ti, while a much greater effect is caused by ammonia [46, 64].

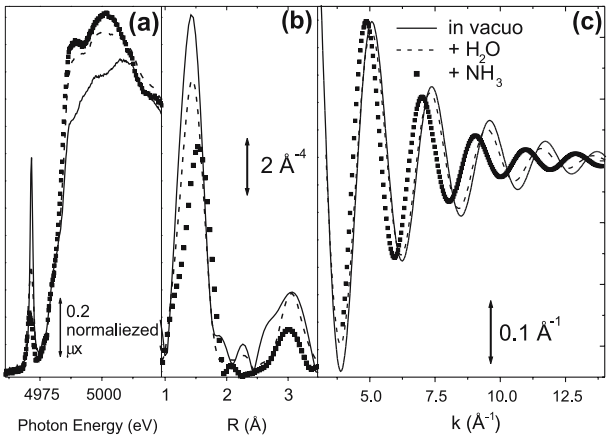

Fig. 5 XANES region, k^3-weighted Fourier transformed of the raw EXAFS functions and the corresponding first shell filtered, Fourier back transform (**a**, **b** and **c**, respectively) of TS-1 activated at 400 °C (*full lines*), after interaction with water (wet sample, *dashed lines*) and after interaction with NH_3 (P_{NH3} = 50 Torr, *dotted lines*). Adapted from [64] with permission. Copyright (2002) by the ACS

4.1.3 IR

As already discussed in Sect. 3.8, TS-1 and the parent Ti-free silicalite-1 (synthesized following the patent [7]) are rather defective materials, showing a high density of missing T atoms and so hosting internal hydroxylated cavities [24, 69, 78–86] (internal nests). The presence of internal SiOH (and possibly TiOH) groups, mutually interacting via H-bonds, makes the IR spectroscopy of H_2O and NH_3 dosed on TS-1 a rather complex matter [64, 83, 84]. In fact, in the same spectral region the following stretching modes overlap: (i) water or ammonia molecules in the liquid-like phase; (ii) water or ammonia molecules adsorbed on Ti(IV) sites or on hydroxyl groups; (iii) SiOH (TiOH) groups interacting with adsorbed molecules and/or with adjacent silanols (titanols). We will not enter into the complex spectroscopic details and the discussion of the OH stretching region (3800–2500 cm^{-1}), is referred to [64, 83, 84]. Instead, we will focus here on the evolution of the 960 cm^{-1} band which, according to the discussion reported in Sect. 3.5, is directly related to the insertion of Ti in the MFI framework.

Bordiga et al. [64] observed that the first water dosages (from the gas phase) do not affect the 960 cm^{-1} Ti-specific band, neither in position nor in intensity. This fact suggests either that interaction with silanols is favored at low P_{H_2O} or that the formation of a monomolecular Ti(IV)$\cdots OH_2$ adduct is not able to cause a significantly perturbation the 960 cm^{-1} band, which occurs only at higher pressures when more than one water molecules are adsorbed per Ti site. In this regard, quantum chemical calculations (also reported in the same work [64]) have played an important role in the interpretation of the experimental results. At higher P_{H_2O}, when manifestation of the liquid-like features are already observed, the Ti-specific band progressively shifts at higher frequency up to 971 cm^{-1}.

As was the case for water, the adsorption of ammonia also affects the intensity and the spectral position of the 960 cm^{-1} band. A clear upward shift of the maximum of the band was observed by Bordiga et al. upon NH_3 dosage [64]. However, in the case of NH_3, the molecule interacts directly with Ti even at the lowest P_{NH3}, reflecting a much higher affinity toward Ti with respect to water.

4.1.4 Raman and Resonant Raman

Figures 6a–c report the effect of H_2O adsorption on Ti(IV) sites on the Raman features of TS-1 using three different excitation sources. As far as the asymmetric modes of the $[Ti(OSi)_4]$ units are concerned, we observed a blue shift of the 960 cm^{-1} band whichever laser was used in the experiment [48, 52, 64]. More interesting are the consequences that water adsorption has on the to-

tally symmetric stretching mode of the $[Ti(OSi)_4]$ units. We observed that the enhancement of the 1125 cm^{-1} band when an UV laser is used is switched off by water adsorption [48, 52]. The collapse of the 1125 cm^{-1} band is more evident when the 244 nm source is used (Fig. 6c). The same features are observed when ammonia is dosed, see Fig. 6d (only the experiment collected with $\lambda = 1064$ nm is reported for the sake of brevity). Due to the stronger base character of ammonia with respect to water, when the same equilibrium pressures are compared, the perturbations induced by NH_3 are always more important that those induced by H_2O [64]. To allow a direct comparison between the two type of experiments reported in Fig. 6, water was dosed from the liquid phase while ammonia was dosed from the gas phase.

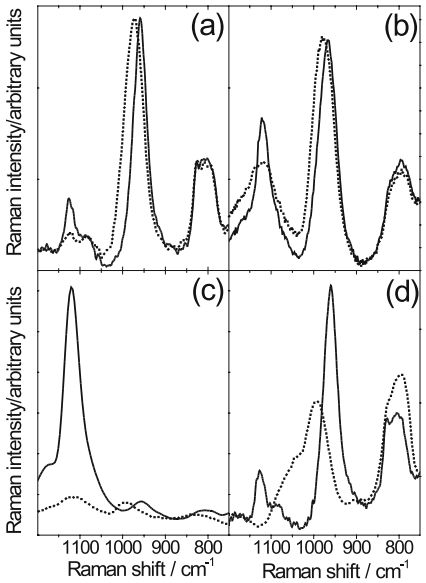

Fig. 6 Effect of ligand dosage on the Raman spectra of TS-1. Dehydrated TS-1 (*full line*), after interaction with water, from the liquid phase (*dotted line*): **a** $\lambda = 1064$ nm, **b** $\lambda = 325$ nm, **c** $\lambda = 244$ nm. **d** Dehydrated TS-1 (*full line*), after interaction with ammonia, from the gas phase (*dotted line*) $\lambda = 1064$ nm. Adapted from [48] with permission. Copyright (2003) by The Owner Societies 2003

Bordiga et al. [48, 52] explained the experimental evidence reported in Fig. 6 in terms of symmetry: once the $[Ti(H_2O)_2O_4]$ or $[Ti(NH_3)_2O_4]$ complexes are formed, the T_d-like symmetry of Ti(IV) species is destroyed in such a way that the symmetry of the vibrational modes is no longer the same as that of the LMCT, and the Raman resonance is quenched.

4.1.5 Adsorption Microcalorimetry

The main calorimetric studies on adsorption of water and ammonia on TS-1 and silicalite-1 have been reported by Bolis et al. [64, 83, 84, 86], while other contributions came from the Auroux group [92] and Janchen et al. [93]. Corma's group has investigated the interaction of water on Ti-β zeolite [39]. The most important conclusion from the available literature is that calorimetric data require a very careful analysis, as probe molecules interact both with the silanols of the internal hydroxyl nests (see Sect. 3.8) and with Ti(IV) species.

Bolis et al. [64, 83, 84, 86] performed blank experiments on the Ti-free silicalite-1 to measure directly the interaction of probe molecules with the internal silanols. The authors observed that the adsorbed amounts and the integral heats evolved are very close for the TS-1 and the silicalite-1 systems, but it was not possible to give evidence for a specific interaction between H_2O and Ti(IV) centers. Up to $P_{H_2O} < 3$ Torr, the TS-1 curves are even lower than the ones for silicalite-1; however, the difference is within the experimental error. At higher P_{H_2O}, the curves of TS-1 start increasing more rapidly than those of silicalite-1 suggesting that the interaction between H_2O and Ti(IV) is favored at higher P_{H_2O}. This fact agrees with the IR evidence that the 960 cm^{-1} band starts to be perturbed at high P_{H_2O} only (see Sect. 4.1.3). In contrast, in the case of the adsorption of NH_3, both the volumetric and calorimetric isotherms of silicalite-1 lie below those of TS-1 by a significant amount [64].

4.2 Interaction With Other Molecules

The interaction of acetonitrile has been investigated by means of IR spectroscopy by Busca's group [94, 95] on both silicalite-1 and TS-1 zeolites. In [95] the interaction with pivalonitrile is also reported. Bonino et al. [77] described the interaction of CD_3CN (deutered form in this case) and pyridine (used as probes of Lewis acid centers) with TS-1 catalyst using IR spectroscopy. Interaction of CD_3CN and pyridine with Ti(IV) centers leads to surface adducts characterized by well-defined IR spectra that can be distinguished from those ascribed to interaction with internal hydroxyl groups, which are the most abundant acid species present in TS-1. In contrast with what is observed for both H_2O and NH_3 probes (see Sect. 4.1.3), both CD_3CN and pyridine molecules result in spectroscopic features that are characteristic of TS-1 and completely absent in pure siliceous silicalite-1. The authors conclude that that Ti(IV) centers embedded in the MFI framework have a Lewis acidity strength comparable of that of Ti(IV) sites at the surface of TiO_2. In the same work the spectroscopic results are compared with computational data obtained on cluster models based on the ONIOM approach [77]. In [76] Damin et al. investigated the interaction of H_2O, NH_3, H_2CO, and CD_3CN

with Ti(IV) centers inserted in the chabazite framework (Si/Ti = 8), adopting an ab initio periodical approach.

Absorption of NH_3, NO_2, NO, and co-adsorption of NO, O_2, and NH_3 on both silicalite-1 and TS-1 has been investigated by Raj et al. [92] combining microcalorimetry with IR spectroscopy.

Yeom and Frei [96] showed that irradiation at 266 nm of TS-1 loaded with CO and CH_3OH gas at 173 K gave methyl formate as the main product. The photoreaction was monitored in situ by FT-IR spectroscopy and was attributed to reduction of CO at LMCT-excited framework Ti centers (see Sect. 3.2) under concurrent oxidation of methanol. Infrared product analysis based on experiments with isotopically labeled molecules revealed that carbon monoxide is incorporated into the ester as a carbonyl moiety. The authors proposed that CO is photoreduced by transient Ti^{3+} to HCO radical in the primary redox step. This finding opens up the possibility for synthetic chemistry of carbon monoxide in transition metal materials by photoactivation of framework metal centers.

5
TS-1 Interaction With H_2O/H_2O_2 Solutions

5.1
General Overview

Despite the numerous papers describing the catalytic activity of TS-1 (see Sect. 2), only a few works have tried to investigate the nature and the properties of the active species formed in TS-1 upon interaction with H_2O_2. This lack can be ascribed to severe experimental problems, mainly due to the presence of H_2O (which precludes the extended use of IR spectroscopy) and of the lability of complexes formed by H_2O_2 on Ti(IV) centers in TS-1. The most used technique is UV-Vis DRS spectroscopy because it is not affected by the presence of H_2O. This technique has revealed the formation, upon contact with H_2O_2 aqueous solution, of a new LMCT band from the O – O moiety to the Ti center, appearing around 26 000 cm^{-1} (385 nm) [45–48, 90, 97, 98], (vide infra the top part of Fig. 9). Other papers appeared using EPR [90, 98–102], IR [103, 104], Raman [47, 48, 103], EXAFS [46, 50, 105, 106], and ab initio [103, 106–110] approaches to investigate the complexes formed upon dosing H_2O_2 (or more complex species such as *t*-butyl hydroperoxide) on titanosilicates. This is the reason why, more than 20 years after the discovery of the material, there is still debate on the detailed structure of the O – O species formed at the catalytic center, which is thought to be the active intermediate in partial oxidation reactions. The species that can be generated at Ti sites upon H_2O_2/H_2O contact can have neutral (coordinated H_2O_2), peroxi-

dic, superoxidic, or hydroperoxidic character. The most popular view is that the active species is a Ti-hydroperoxide, which may be either monodentate (η^1) or bidentate (η^2) [10, 45, 47, 48, 50, 103, 104, 109, 110] (see Fig. 7), even if the other hypothesized structures cannot be ruled out.

Hydroperoxidic η^1 or η^2 complexes can be formed by interaction of Ti(IV) with a HO_2^- anion (the Pka of the $H_2O_2 + H_2O \leftrightarrow HO_2^- + H_3O^+$ equilibrium being 11.8 in water at 20 °C, a value comparable to the third dissociation constant of H_3PO_4) following Scheme 1a.

Deprotonation of the H_2O_2 molecule on the Ti(IV) site itself (see Scheme 1b) is another mechanism leading to Ti-hydroperoxidic species. The latter mechanism can also occur either on a perfect $[Ti-(O-Si)_4]$ site by rupture of one out of the four Ti – O – Si bridges or on a defective $[(H-O)-Ti-(O-Si)_3]$ site by elimination of a water molecule (see Schemes 2a and 2b and the discussion of Sect. 3.8).

Unfortunately, there is no Ti-hydroperoxo compound of known structure to be used as a model. Conversely, the structure of several Ti-peroxo complexes are known by diffraction studies [111–113], all of them showing the side on η^2 geometry. None of these compounds is known to be active in partial oxidation reactions [114, 115]. Similar considerations can be addressed

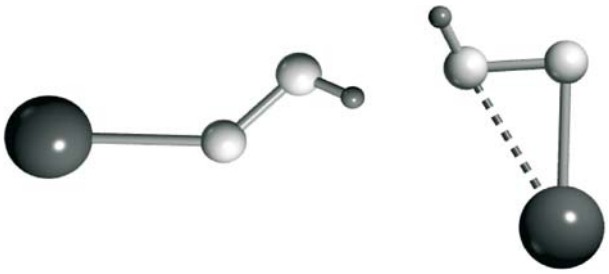

Fig. 7 Graphic representation of monodentate (η^1, *left*) and bidentate (η^2, *right*) TiOOH species). Adapted from [50] with permission. Copyright (2004) by Wiley-VCH

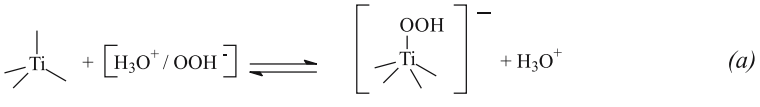

Scheme 1 Representation of equilibria between TiO_4 framework species and H_2O_2/H_2O solutions: **a** interaction with ionic species; **b** interaction with molecular species and subsequent formation of deprotonated molecule on the TiO_4. Adapted from [49] with permission. Copyright (2004) by ACS

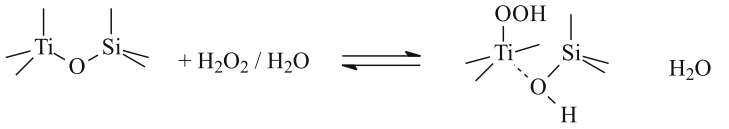

(a)

(b)

Scheme 2 Representation of equilibria between TiO_4 framework species and H_2O_2/H_2O solutions: **a** formation of hydroperoxo species upon hydrolysis of a Ti – O – Si bridge; **b** formation of hydroperoxo species toward reaction with a pre-existing defective Ti – OH species (see Sect. 3.8). Adapted from [49] with permission. Copyright (2004) by ACS

for Ti(IV)-substituted Keggin polyoxotungstate compounds [116]. Some data on alkyl-peroxo structure come from molecular compounds such as silicon–titanium complexes obtained from silsesquioxane-type species [117], or from homogeneous species obtained by chiral trialkanolamines and Ti(IV) alkoxides [118, 119]. NMR data suggest that titanium η^2-alkylperoxo complexes are the active oxidants in the catalytic cycle [119].

Concerning peroxo complexes, it is worth noticing that they can be formed in TS-1 by evolution of both η^1 or η^2 hydroperoxo complexes upon a further deprotonation in presence of water with formation of H_3O^+/H_2O. Very recently Bonino et al. [49] have shown, by titration in aqueous medium with NaOH, that the acidity of the TS-1/H_2O system is remarkably increased by addition of H_2O_2 (compare full squares with full circles in Fig. 8), a feature not observed for the Ti-free silicalite-1 system (open circles and squares in Fig. 8).

From the data reported in Fig. 8, it clearly emerges that the acidity of the silicalite-1/H_2O and of the TS-1/H_2O systems are remarkably different (compare open and full circles in Fig. 8). This difference can be explained as follows: TS-1 has two main acidic sites, Ti(IV) Lewis sites and silanols, mainly located in the internal defective nests (see Sect. 3.8), while only the latter are present in silicalite-1. Addition of H_2O_2 to silicalite-1 does not modify the titration curve (compare open circles with open squares in Fig. 8). This means that no additional acidic sites appear in the silicalite-1 system upon adding H_2O_2, i.e., that hydrogen peroxide molecules coordinated to internal silanol do not modify their acidity. Conversely, addition of H_2O_2 to TS-1 moves the whole titration curve toward lower pH values, (compare full circles with full

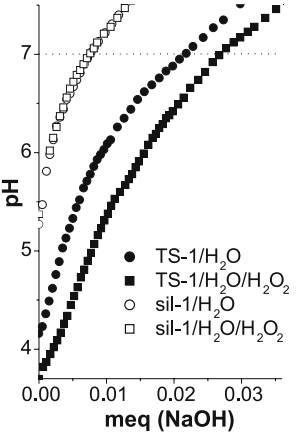

Fig. 8 pH values vs. added NaOH (meq) during the titration experiments performed on TS-1 (*full symbols*) and on silicalite-1 (*open symbols*) in presence (*squares*) and in absence (*circles*) of H_2O_2. *Horizontal dotted line* represents the pH 7.0 value. Adapted from [49] with permission. Copyright (2004) by ACS

squares in Fig. 8). This means that the acidity of the TS-1/H_2O_2/H_2O system is remarkably enhanced with respect to the acidity of the two separate systems (H_2O_2/H_2O and TS-1/H_2O). This fact is very important since it reflects the acidity of the catalyst in working conditions. Bonino et al. [49] concluded that the increased acidity of the TS-1/H_2O_2/H_2O system must be ascribed to a peculiar interaction between hydrogen peroxide and Ti(IV) centers. These data can be simply explained by assuming that TiOOH species (either formed following Schemes 1a,b or 2a,b) are the acidic species detected during the titration experiments and thus support the thesis of a deprotonation of the hydrogen peroxide molecule.

5.2 New Advances from Resonant Raman Spectroscopy

The first Raman study aimed at identifying the vibrational features of the complex obtained by dosing hydrogen peroxide on TS-1 catalyst appeared in 1999 by Tozzola et al. [103]. In that work, a near-IR laser (λ = 1064 nm) was used as exciting source. Under such conditions the authors observed the O – O stretching of peroxo complexes formed on Ti sites upon contacting TS-1 with H_2O_2/NH_3/H_2O (840 cm^{-1}) and H_2O_2/NaOH/H_2O (843 cm^{-1}) basic solutions, but the experiment failed for the TS-1/H_2O_2/H_2O system [103]. Note that the O – O stretching frequency of the H_2O_2 molecules in aqueous solution occurs at 875 cm^{-1}. The reason for the partial success was due to the fact that, in basic solutions, the peroxo species are more stable and hence they are not readily destroyed by the laser beam. The failure of the experiment

with H_2O_2/H_2O solution was explained in terms of the labile nature of the complex [103].

It thus becomes clear that the only route that can be followed to improve the quality of the Raman spectra is to operate in resonance conditions [52, 57]. Of course, as the peroxo species absorb in the visible, an exciting source in the same spectral region must be used, because in this way the vibration associated with the Ti-peroxo species can undergo a Raman enhancement phenomenon, if the selection rules are fulfilled. Bordiga et al. [47] repeated the experiment using an exciting laser with $\lambda = 442$ nm (22 625 cm^{-1}), lying on the low energy tail of the LMCT band around 385 nm (26 000 cm^{-1}) typical of the TS-1/H_2O_2/H_2O system (see top part of Fig. 9 and [45–48, 90, 97, 98]). The bottom part of Fig. 9 shows the Raman spectra, collected with the 442 nm laser, of TS-1 before and after interaction with H_2O_2/H_2O solution (dashed and full lines, respectively). Bordiga et al. [47, 48] observed that the interaction with H_2O_2 causes:

(i) Reduction in intensity and a blue shift in frequency of the 960 cm^{-1} mode, now at 976 cm^{-1}, similar to that found with water (see Sect. 4.1.4)
(ii) Quenching of the 1125 cm^{-1} mode due to a rupture of the T_d-like symmetry (see Sect. 4.1.4)
(iii) Appearance of the strong and sharp (O – O) stretching mode at 875 cm^{-1}, due to H_2O_2/H_2O solution physisorbed into the zeolite channels
(iv) Appearance of a strong and complex new feature centered at 618 cm^{-1}

Features (i–iii) are also observed when the same experiment is performed with a 1064 nm laser source [103]. Conversely the 618 cm^{-1} was not observed on the TS-1/H_2O_2/H_2O system using a 1064 nm source nor on the Ti-free silicalite-1 molecular sieve upon interaction with H_2O_2/H_2O solution with 442 nm exciting source, and was so ascribed to a Raman enhanced vibration mode of the Ti-peroxo complex [47, 48].

Assignment of the 618 cm^{-1} mode of the TS-1/H_2O_2/H_2O system came after comparison with the Raman spectrum obtained on $(NH_4^+)_3$ $(TiF_5O_2)^{3-}$ model compound. Bordiga et al. [47] observed that the Raman spectrum of $(NH_4^+)_3(TiF_5O_2)^{3-}$ exhibits a band at 898 cm^{-1} and a composite component with a maximum at 595 cm^{-1}, the latter undergoing a remarkable enhancement when the 442 nm exciting line is used. The $Ti(O)_2$ unit of the TiF_5O_2 complex has C_{2v} symmetry and the Γ_{vib} for this moiety is $2A_1 + B_1$. The three normal modes, labeled ν_1, ν_2, and ν_3, following the literature data on peroxo-metal complex in argon matrices [120–123], are assigned to: (O – O) stretching vibration with A_1 symmetry (ν_1); symmetric breathing mode of the $Ti(O)_2$ cycle with A_1 symmetry (ν_2); and asymmetric breathing mode of the $Ti(O)_2$ cycle with B_1 symmetry (ν_3). Literature data for the cyclic structures $Fe(O)_2$, $Co(O)_2$, $Ni(O)_2$, and $Ca(O)_2$ show that ν_1 mode lies in the 990–742 cm^{-1} spectral range [120–123], indicating that the band at 898 cm^{-1} is associated with the (O – O) stretching vibration. Notice that, even if this mode is totally symmetric (A_1 symmetry), its intensity is not substantially en-

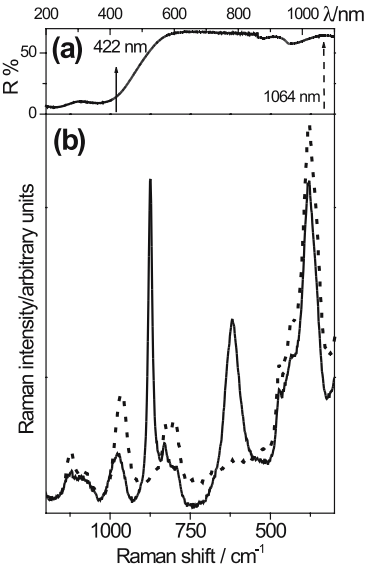

Fig. 9 **a** UV-Vis DRS spectra of TS-1 catalyst in contact with the H_2O_2/H_2O solution reporting the typical 385 nm (26 000 cm^{-1}) LMCT band of the peroxo complex. The *full arrow* represents the 422 nm laser line occurring in the LMCT of the TS-1/H_2O_2/H_2O system and used by Bordiga et al. [47, 48]. The *dashed arrow* represents the 1064 nm laser used by Tozzola et al. [103]. **b** Raman spectra, collected with the 442 nm laser, of TS-1 before and after interaction with H_2O_2/H_2O solution (*dashed and full line*, respectively). Adapted from [48] with permission. Copyright (2003) by The Owner Societies 2003

hanced in the spectrum obtained with the 442 nm source. By analogy with the data obtained on the previously cited structures, this behavior can be explained by considering that, among the two A_1 modes which meet the symmetry requirements, the ν (O – O) mode (being the Ti center not directly involved) is not affected by the resonance Raman effect [47]. Literature data on $Fe(O)_2$, $Co(O)_2$, $Ni(O)_2$, and $Ca(O)_2$ show that ν_2 and ν_3 are usually only about 30 cm^{-1} apart and are located in the range 500–600 cm^{-1} [120–123]. Due to the closeness of the two contributions and, being only the ν_2 Raman enhanced, Bordiga et al. [47, 48] associated the mode centered at 595 cm^{-1} to the symmetric breathing mode of the $Ti(O)_2$ cycle, the asymmetric mode giving a minor contribution. Supported by the similarity between the spectroscopic features, both UV-Vis and Raman, of $(NH_4^+)_3(TiF_5O_2)^{3-}$ and TS-1/H_2O_2/H_2O systems, Bordiga et al. [47, 48] concluded that the species responsible for the band at 26 000 cm^{-1} of the TS-1/H_2O_2/H_2O system is a "side-on" Ti-peroxo species (η^2 species in Fig. 7) characterized by a Raman mode at 618 cm^{-1}, which is resonance enhanced upon using by an exciting laser line falling in the LMCT transition. As reviewed in the next section, this assignment is in agreement with recent EXAFS data showing

that when H_2O_2/H_2O is added a complete modification of both first and second coordination shells around Ti is observed. This has been interpreted in terms of the appearance of a new side-on O – O ligand at 2.01 Å accompanied by the rupture of a Ti – O – Si bridge [46, 49, 50]. Such a dramatic evolution of the local environment of Ti(IV) species in TS-1 is reversible as evacuation restores the original situation. The reversible formation of the η^2 side on the peroxo complex inside TS-1 channels is obviously related to the excellent catalytic properties of TS-1 (Sect. 2).

5.3
Equilibria between Peroxo and Hydroperoxo Species in the TS-1/H_2O_2/H_2O System: In Situ UV-Vis DRS and High Resolution XANES Highlights

The well-known fact that the TS-1/H_2O_2/H_2O rapidly loses its yellow color, turning back to white (cream) within hours [46, 49] (see the evolution from curve 2 to 3 in Fig. 10a) was generally interpreted in terms of a high lability of the peroxo species responsible for the yellow color of the working catalyst. It has been shown that aging of the TS-1/H_2O_2/H_2O system for some hours does reversibly convert the yellow colored Ti-peroxo species into the uncolored one, as the addition of water on the one-day aged catalyst is able to substantially restore its yellow color (curve 4 in Fig. 10a).

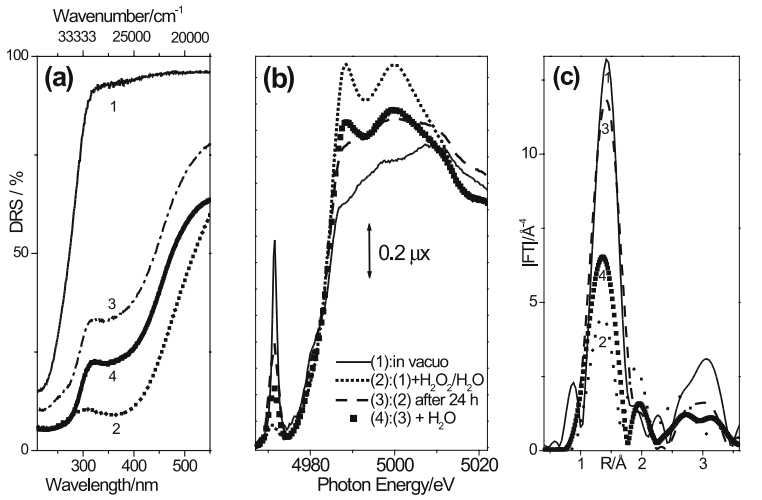

Fig. 10 **a** UV-Vis DRS spectra of TS-1 (*curve 1, full line*), immediately after contact with H_2O_2/H_2O solution (*curve 2, dotted line*), after time elapse of 24 h (*curve 3, dashed line*) and after subsequent H_2O dosage (*curve 4, scattered squares*). **b** as for **a** for the XANES spectra. **c** as for **a** for the k^3-weighted, phase uncorrected, FT of the EXAFS spectra. Spectra 2–4 of **b** and **c** have been reordered at liquid nitrogen temperature. Adapted from [49] with permission. Copyright (2004) by ACS

Formation of the side-on η^2 peroxo complex by interaction of H_2O_2/H_2O solution with the activated catalyst (curve 2 in Fig. 10b) modified drastically all XANES features: (i) the pre-edge feature falls from 0.9 to 0.16 in intensity, with a broadening for the FWHM from 1.3 to 2.4 eV, testifying the loss of the T_d symmetry; (ii) two prominent and well-defined features appear in the edge, around 4984 and 4995 eV, which are the fingerprint of the side-on η^2 Ti-peroxo complex [46, 49, 50]. After 24 h, most of the water present on the sample sublimates and the features of the side-on η^2 Ti-peroxo complex almost disappear (curve 3 in Fig. 10b). Contact of the evacuated catalyst with water turns it yellow again. Once cooled down to 77 K, it gives the scattered squares spectrum of Fig. 10b (curve 4), where all features of the side-on η^2 Ti-peroxo complex are almost restored.

This surprising results implies that water is not just a medium for transporting products on the catalytic sites but has an active role in determining the peroxo/hydroperoxo species present on the working catalyst. Scheme 3 summarizes the model hypothesized by Prestipino et al. [50] on the basis of the whole set of experiments reported by Bonino et al. [49] and by them selves [50], and here reviewed in Fig. 10.

Prestipino et al. [50] have very recently reported an experimental breakthrough in this field as they where able to dose, in situ on the activated catalyst (dotted line in Fig. 11) from the gas phase (using $KH_2PO_4 \cdot H_2O_2$ as hydrogen peroxide source), an almost anhydrous H_2O_2 vapor to the TS-1 catalyst. The XANES spectrum of TS-1 contacted with anhydrous H_2O_2 from the gas phase (full line in Fig. 11) gave results very similar to those obtained after prolonged evacuation, at 77 K, of the TS-1 sample previously contacted with H_2O_2/H_2O from the liquid phase (a spectrum similar to curve 3 in Fig. 1a). Finally, when water is added to the uncolored catalyst, previously contacted with anhydrous H_2O_2, it turns yellow and its XANES spectrum (scattered squares in Fig. 11) possesses the fingerprint features of the side-on

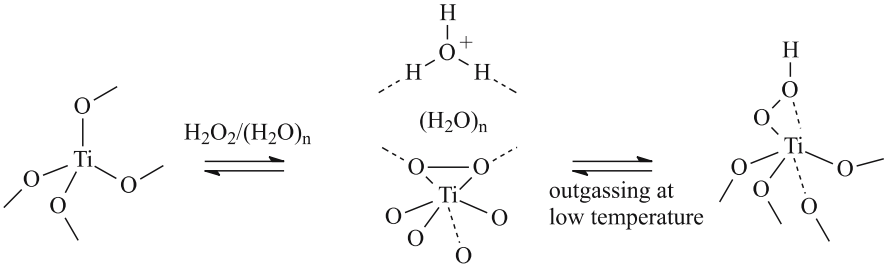

Scheme 3 Representation of equilibria between TiO_4 framework species and η^2 complexes inside TS-1 channels upon dosage of H_2O_2/H_2O (*left*) and between η^2 and η^1 complexes upon dehydration (*right*). Adapted from [50] with permission. Copyright (2004) by Wiley-VCH

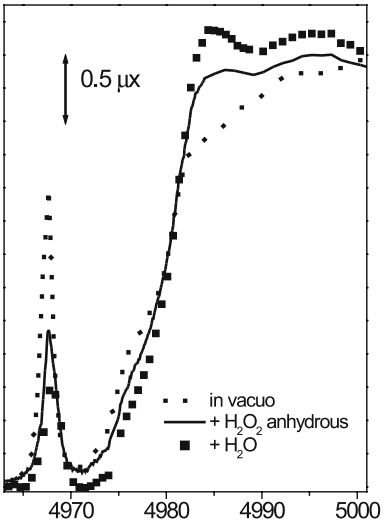

Fig. 11 High resolution XANES spectra collected at the GILDA BM8 beamline of the ESRF Grenoble (France) at liquid nitrogen temperature on the TS-1 catalyst: activated TS-1 catalyst (*dotted line*); after contact with "anhydrous" H_2O_2 from the gas phase (*full line*); after subsequent contact with water (*scattered squares*). Adapted from [50] with permission. Copyright (2004) by VCH

Ti-peroxo species. Scheme 4 completes the picture showing that the equilibrium between the uncolored end-on η^1 Ti-hydroperoxo complex and the yellow colored side-on η^2 Ti-peroxo complex is tuned by the amount of water present in the channels. The EXAFS part of the X-ray absorption spectrum confirms the picture emerging from UV-Vis DRS and XANES – that anhydrous H_2O_2 significantly modifies the first coordination around Ti, leaving the second one almost unaffected (compare dotted and dashed lines). Conversely, when H_2O is added a complete modification of both first and second shell signals is observed, which has been interpreted in terms of the rupture of a Ti – O – Si bridge [46, 49]. The new data from Prestipino et al. [50] suggest that this effect is not present in anhydrous conditions.

That observed for TS-1 is not peculiar for TS-1 only and can be observed on other titanosilicates like Ti-MSA, a mesoporous amorphous material that has Ti(VI) centers exposed on the surface of the pores [124, 125]. In this case, easier experiments could be performed by Prestipino et al. [50] as the peroxo/hydroperoxo complexes can be formed by dosing *t*-butyl hydroperoxide (which does not enter the 10-membered rings of TS-1). The XANES spectrum of Ti-MSA in vacuum is typical for almost T_d-like Ti(IV) centers (the intensity of the $A_1 \rightarrow T_2$ pre-edge peak being only 0.69, as compared with 0.91 for TS-1). Upon dosing the *t*-butyl hydroperoxide in decane solution on Ti-MSA, a spectrum similar to that obtained on TS-1 contacted with anhydrous H_2O_2 is observed on both XANES and EXAFS regions [50]. When the

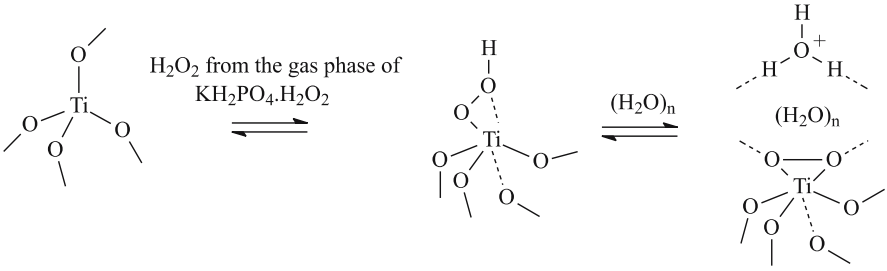

Scheme 4 Representation of equilibria between TiO_4 framework species and η^1 complexes inside TS-1 channels upon dosage of anhydrous H_2O_2 (*left*) and between η^1 and η^2 complexes upon hydration (*right*). Adapted from [50] with permission. Copyright (2004) by Wiley-VCH

t-butyl hydroperoxide diluted in H_2O is dosed, the two features in the edge of the XANES spectrum, typical of a η^2 side-on peroxo complex, start to be appreciable.

Summarizing, the in situ UV-Vis, XANES, and EXAFS studies of Bonino et al. [49] and of Prestipino et al. [50] on hydrated and anhydrous peroxo/hydroperoxo complexes on crystalline microporous and amorphous mesoporous titanosilicates have shown, for the first time, the equilibrium between η^2 side-on and η^1 end-on complexes. The amount of water is the key factor in the equilibrium displacement. In this regard please note that, owing to the hydrophobic character of TS-1, substrates such as olefins are the dominant species in the channels. This fact assures a relatively local low concentration of water, which in turn guarantees a sufficient presence of the active η^1 end-on hydroperoxo complexes under working conditions.

Note Added in Proof

After the submission of this contribution, a remarkable review authored by Ratnasamy, Srinivas and Knözinger has appeared on the investigation, by means of both experimental and theoretical methods, of the active sites and reactive intermediates in titanium silicate molecular sieves [126].

Acknowledgements This work is dedicated to Adriano Zecchina, who has been and still is a guide for us in science and an example in life.

The results reviewed here have been achieved over more than 10 years with the contribution of several colleagues coming from different academic and industrial laboratories. We are indebted for the fundamental collaboration and the stimulating discussions with R. Dovesi, P. Ugliengo, V. Bolis, E. Giamello, G. Ricchiardi and C. Prestipino (University of Torino); V. Bolis and M. Milanesio (University of Piemonte Orientale); G. Vlaic (University of Trieste); F. Boscherini (University of Bologna); G. Artioli (University of Milano); G. Petrini, G. Leofanti, M. Padovan, F. Genoni, G. Rivetti, G. Spanò, G. L. Marra, M. A. Mantegazza, M. Ricci, R. D'Aloiso (Istituto G. Donegani, Novara); G. Bellussi, A. Carati, M. G. Clerici and A. Tasso (EniTecnologie, SanDonato Milanese). Coming to the large scale

facilities used in this research, we are indebted to the staffs of: (i) The PULS group of the ADONE storage-ring, Frascati (Italy); (ii) The EXAFS3 and EXAFS13 groups of LURE in Orsay (France), (iii) the GILDA BM8 group of the ESRF storage ring in Grenoble (France); (iv) The group pf the HRPD instrument at the ISIS spallation neutron source in Didcot (UK).

References

1. Schappacher M, Weiss R, Montiel-Montoya R, Trautwein A, Tabard A (1985) J Am Chem Soc 107:3736
2. Dawson JH (1988) Science 240:433
3. Kostka KL, Fox BG, Hendrich MP, Collins TJ, Rickard CEF, Wright LJ, Munck E (1993) J Am Chem Soc 115:6746
4. Lee SK, Fox BG, Froland WA, Lipscomb JD, Munck E (1993) J Am Chem Soc 115:6450
5. McDaniel MP (1985) Adv Catal 33:47
6. Groppo E, Lamberti C, Bordiga S, Spoto G, Zecchina A (2005) Chem Rev 105:115
7. Taramasso M, Perego G, Notari B (1983) US Patent No 4410501
8. Roffia P, Tonti S, Cesana A, Mantegazza MA, Padovan M (1990) US Patent No 4918194
9. Romano U, Esposito A, Maspero F, Neri C, Clerici MG (1990) Chim Ind (Milano) 72:610
10. Clerici MG, Bellussi G, Romano U (1991) J Catal 129:159
11. Clerici MG (1991) Appl Catal 68:249
12. Bellussi G, Carati A, Clerici MG, Maddinelli G, Millini R (1992) J Catal 133:220
13. Clerici MG, Ingallina P (1993) J Catal 140:71
14. Mantegazza MA, Leofanti G, Petrini G, Padovan M, Zecchina A, Bordiga S (1994) Stud Surf Sci Catal 82:541
15. Hutter R, Mallat T, Baiker A (1995) J Catal 153:177
16. Corma A, Esteve P, Martínez A (1996) J Catal 161:11
17. Notari B (1996) Adv Catal 41:253
18. Mantegazza MA, Petrini G, Spanò G, Bagatin R, Rivetti F (1999) J Mol Catal A 146:223
19. Langhendries G, De Vos D, Baron GV, Jacobs P (1999) J Catal 187:453
20. Clerici MG (2001) Topics in Catal 15:257
21. Millini R, Massara EP, Perego G, Bellussi G (1992) J Catal 137:497
22. Lamberti C, Bordiga S, Zecchina A, Carati A, Fitch AN, Artioli G, Petrini G, Salvalaggio M, Marra GL (1999) J Catal 183:222
23. Marra GL, Artioli G, Fitch AN, Milanesio M, Lamberti C (2000) Microporous Mesoporous Mater 40:85
24. Lamberti C, Bordiga S, Zecchina A, Artioli G, Marra GL, Spanò G (2001) J Am Chem Soc 123:2204
25. Henry PF, Weller MT, Wilson CC (2001) J Phys Chem B 105:7452
26. Hijar CA, Jacubinas RM, Eckert J, Henson NJ, Hay PJ, Ott KC (2000) J Phys Chem B 104:12157
27. Dutoit DCM, Schneider M, Baiker A (1995) J Catal 153:165
28. Klein S, Thorimbert S, Maier WF (1996) J Catal 163:476
29. Jorda E, Tuel A, Teissier R, Kervennal J (1998) J Catal 175:93
30. Holmes SA, Quignard F, Choplin A, Teissier R, Kervennal J (1998) J Catal 176:173
31. Fraile JM, García JI, Mayoral JA, Vispe E (2000) J Catal 189:40
32. Maschmeyer T, Rey F, Sankar G, Thomas JM (1995) Nature 378:159

33. Krijnen S, Mojet BL, Abbenhuis HCL, Van Hooff JHC, Van Santen RA (1999) 1:361
34. Corma A, Fornes V, Pergher SB, Maesen TLM, Buglass JG (1998) Nature 396:353
35. Gao F, Yamase T, Suzuki H (2002) J Mol Catal A 180:97
36. Kholdeeva OA, Trubitsina TA, Maksimovskaya RI, Golovin AV, Neiwert WA, Kolesov BA, López X, Poblet JM (2004) Inorg Chem 43:2284
37. Vayssilov GN (1997) Catal Rev-Sci Eng 39:209
38. Blasco T, Camblor M, Corma A, J Perez-Pariente (1993) J Am Chem Soc 115:11806
39. Blasco T, Camblor MA, Corma A, Esteve P, Guil JM, Martinez A, Perdigon-Melon JA, Valencia SJ (1998) J Phys Chem B 102:75
40. Lane BS, Burgess K (2003) Chem Rev 103:2457
41. Roffia P, Leofanti G, Cesana A, Mantegazza M, Padovan M, Petrini G, Tonti S, Gervasutti P (1990) Stud Surf Sci Catal 55:43
42. Sheldon RA (1997) Stud Surf Sci Catal 110:151
43. Sumitomo (2003) April 17, press release
44. Romano U (2001) Chim Ind (Milan) 83:30
45. Zecchina A, Bordiga S, Lamberti C, Ricchiardi G, Lamberti C, Ricchiardi G, Scarano D, Petrini G, Leofanti G, Mantegazza M (1996) Catal Today 32:97
46. Zecchina A, Bordiga S, Spoto G, Damin A, Berlier G, Bonino F, Prestipino C, Lamberti C (2002) Top Catal 2:67
47. Bordiga S, Damin A, Bonino F, Ricchiardi G, Lamberti C, Zecchina A (2002) Angew Chem Int Ed 41:4734
48. Bordiga S, Damin A, Bonino F, Ricchiardi G, Zecchina A, Tagliapietra R, Lamberti C (2003) Phys Chem Chem Phys 5:4390
49. Bonino F, Damin A, Ricchiardi G, Ricci M, Spanò G, D'Aloisio R, Zecchina A, Lamberti C, Prestipino C, Bordiga S (2004) J Phys Chem B 108:3573
50. Prestipino C, Bonino F, Usseglio Nanot A, Damin A, Tasso A, Clerici MG, Bordiga S, D'Acapito F, Zecchina A, Lamberti C (2004) Chem Phys Chem 5:1799
51. Perego G, Bellussi G, Corno C, Taramasso M, Buonuomo F, Esposito A (1987) Stud Surf Sci Catal 28:129
52. Ricchiardi G, Damin A, Bordiga S, Lamberti C, Spanò G, Rivetti F, Zecchina A (2001) J Am Chem Soc 123:11409
53. Boccuti MR, Rao KM, Zecchina A, G Leofanti, Petrini G (1989) Stud Surf Sci Catal 48:133
54. Zecchina A, Spoto G, Bordiga S, Padovan M, Leofanti G (1991) Stud Surf Sci Catal 65:671
55. Scarano D, Zecchina A, Bordiga S, Geobaldo F, Spoto G, Petrini G, Leofanti G, Padovan M, Tozzola G (1993) J Chem Soc Faraday Trans 89:4123
56. Deo G, Turek AM, Wachs IE, Huybrechts DRC, Jacobs PA (1993) Zeolites 13:365
57. Li C, Xiong G, Xin Q, Liu J, Ying P, Feng Z, Li J, Yang W, Wang Y, Wang G, Liu X, Lin M, Wang X, Min E (1999) Angew Chem Int Ed 38:2220
58. Bordiga S, Coluccia S, Lamberti C, Marchese L, Zecchina A, Boscherini F, Buffa F, Genoni F, Leofanti G, Petrini G, Vlaic G (1994) J Phys Chem 98:4125
59. Bordiga S, Boscherini F, Coluccia S, Genoni F, Lamberti C, Leofanti G, Marchese L, Petrini G, Vlaic G, Zecchina A (1994) Catal Lett 26:195
60. Bordiga S, Geobaldo F, Lamberti C, Zecchina A, Boscherini F, Genoni F, Leofanti G, Petrini G, Padovan M, Geremia S, Vlaic G (1995) Nucl Instr Meth B 97:23
61. Pei S, Zajac GW, Kaduk JA, Faber J, Boyanov BI, Duck D, Fazzini D, Morrison TI, Yang DS (1993) Catal Lett 21:333
62. Le Noc L, Trong On D, Solomykina S, Echchahed B, Bél F, Cartier dit Moulin C, Bonneviot L (1996) Stud Surf Sci Catal 101:611

63. Trong On D, Kaliaguine S, Bonneviot L (1995) J Catal 157:235
64. Bordiga S, Damin A, Bonino F, Zecchina A, Spanò G, Rivetti F, Bolis V, Lamberti C (2002) J Phys Chem B 106:9892
65. Trong On D, Le Noc L, Bonneviot L (1996) Chem Commun 299
66. Borello E, Lamberti C, Bordiga S, Zecchina A, Otero Areán C (1997) Appl Phys Lett 71:2319
67. Lamberti C (1999) Microporous Mesoporous Mater 30:155
68. Gleeson D, Sankar G, Catlow CRA, Thomas JM, Spanó G, Bordiga S, Zecchina A, Lamberti C (2000) Phys Chem Chem Phys 2:4812
69. Artioli G, Lamberti C, Marra GL (2000) Acta Cryst B 56:2
70. Zecchina A, Spoto G, Bordiga S, Ferrero A, Petrini G, Leofanti G, Padovan M, Tozzola G (1991) Stud Surf Sci Catal 69:251
71. Camblor MA, Corma A, Perezpariente J (1993) Chem Commun 557
72. Nishimura Y, Hirakawa AY, Tsuboi M (1978) In: Clark RJH, Hester RE (eds) Advances in infrared and Raman spectroscopy, vol 5. Heyden, London, p 217
73. Carey PR (1982) Biochemical applications of Raman and resonance Raman spectroscopies. Academic, New York
74. Damin A, Bordiga S, Zecchina A, Lamberti C (2002) J Chem Phys 117:226
75. Damin A, Bonino F, Ricchiardi G, Bordiga S, Zecchina A, Lamberti C (2002) J Phys Chem B 106:7524
76. Damin A, Bordiga S, Zecchina A, Doll K, Lamberti C (2003) J Chem Phys 118:10183
77. Bonino F, Damin A, Bordiga S, Lamberti C, Zecchina A (2003) Langmuir 19:2155
78. Bordiga S, Roggero I, Ugliengo P, Zecchina A, Bolis V, Artioli G, Buzzoni R, Marra GL, Rivetti F, Spanò G, Lamberti C (2000) J Chem Soc Dalton Trans 3921
79. Zecchina A, Bordiga S, Spoto G, Marchese L, Petrini G, Leofanti G, Padovan M (1992) J Phys Chem 96:4985
80. Zecchina A, Bordiga S, Spoto G, Marchese L, Petrini G, Leofanti G, Padovan M (1992) J Phys Chem 96:4991
81. Zecchina A, Bordiga S, Spoto G, Marchese L, Petrini G, Leofanti G, Padovan M, Otero Areàn C (1992) J Chem Soc Faraday Trans 88:2959
82. Marra GL, Tozzola G, Leofanti G, Padovan M, Petrini G, Genoni F, Venturelli B, Zecchina A, Bordiga S, Ricchiardi G (1994) Stud Surf Sci Catal 84:559
83. Bolis V, Bordiga S, Lamberti C, Zecchina A, Carati A, Rivetti F, Spano G, Petrini G (1999) Microporous Mesoporous Mater 30:67
84. Bolis V, Bordiga S, Lamberti C, Zecchina A, Carati A, Rivetti F, Spano G, Petrini G (1999) Langmuir 15:5753
85. Bordiga S, Ugliengo P, Damin A, Lamberti C, Spoto G, Zecchina A, Spanò G, Buzzoni R, Dalloro L, Rivetti F (2001) Top Catal 15:43
86. Bolis V, Busco C, Bordiga S, Ugliengo P, Lamberti C, Zecchina A (2002) Appl Surf Sci 196:56
87. Lamberti C, Bordiga S, Arduino D, Zecchina A, Geobaldo F, Spanò G, Genoni F, Petrini G, Carati A, Villain F, Vlaic G (1998) J Phys Chem B 102:6382
88. Ricchiardi G, de Man A, Sauer J (2000) Phys Chem Chem Phys 2:2195
89. Zecchina A, Spoto G, Bordiga S, Geobaldo F, Petrini G, Leofanti G, Padovan M, Mantegazza M, Roffia P (1993) In: Guczi L, Solymosi F, Tétényi P (eds) New frontiers in catalysis. Elsevier, Amsterdam, p 719
90. Geobaldo F, Bordiga S, Zecchina A, Giamello E, Leofanti G, Petrini G (1992) Catal Lett 16:109
91. Soult AS, Poore DD, Mayo EI, Stiegman AE (2001) J Phys Chem B 105:2687
92. Raj A, Le THN, Kaliaguine S, Auroux A (1998) Appl Catal B 15:259

93. Janchen J, Vorbeck G, Stach H, Parlitz B, van Hooff JHC (1995) Stud Surf Sci Catal 94:108
94. Armaroli T, Milella F, Notari B, Willey RJ, Busca G (2001) Top Catal 15:63
95. Armaroli T, Bevilacqua M, Trombetta M, Milella F, Alejandre AG, Ramirez J, Notari B, Willey RJ, Busca G (2001) Appl Catal A 216:59
96. Yeom YH, Frei H (2001) J Phys Chem A 105:5334
97. Clerici MG, Ingallina P, Millini R (1993) In: von Ballmoos R, Higgins JB, Treacy MMJ (eds) Proc 9th Int Zeolite Conf, Montreal 1992. Butterworth-Heinemann, Boston, p 445
98. Bonoldi L, Busetto C, Congiu A, Marra G, Ranghino G, Salvataggio M, Spanò G, Giamello E (2002) Spectrochim Acta A 58:1143
99. Bal R, Chaudhari K, Srinivas D, Sivasanker S, Ratnasamy P (2000) J Mol Catal A 162:199
100. Chaudhari K, Srinivas D, Ratnasamy P (2001) J Catal 203:25
101. Srinivas D, Manikandan P, Laha SC, Kumar R, Ratnasamy P (2003) J Catal 217:160
102. Shetti VN, Manikandan P, Srinivas D, Ratnasamy P (2003) J Catal 216:461
103. Tozzola G, Mantegazza MA, Ranghino G, Petrini G, Bordiga S, Ricchiardi G, Lamberti C, Zulian R, Zecchina A (1998) J Catal 179:64
104. Lin WY, Frei H (2002) J Am Chem Soc 124:9292
105. Sankar G, Thomas JM, Catlow CRA, Barker CM, Gleeson D, Kaltsoyannis N (2001) J Phys Chem B 105:9028
106. Barker CM, Gleeson D, Kaltsoyannis N, Catlow CRA, Sankar G, Thomas JM (2002) Phys Chem Chem Phys 4:1228
107. Sinclair PE, Carlow CRA (1999) J Phys Chem B 103:1084
108. Vayssilov GN, van Santen RA (1998) J Catal 175:170
109. Sever RR, Root TW (2003) J Phys Chem B 107:4080
110. Sever RR, Root TW (2003) J Phys Chem B 107:4090
111. Ruzic-Toros Z, Kojic-Prodic B, Sljukic M (1984) Inorg Chimica Acta 86:205
112. Jeske P, Haselhorst G, Weyhermuller T, Wieghardt K, Nuber B (1994) Inorg Chem 33:2462
113. Hagadorn JR, Arnold J (1998) Organometallics 17:1355
114. Mimmoun H, Postel M, Casabianca F, Fisher J, Mitschler A (1982) Inorg Chem 21:1303
115. Yamase T, Ishikawa E, Asai Y, Kanai S (1996) J Mol Catal A 114:237
116. Gao FX, Yamase T, Suzuki H (2002) J Mol Catal A 180:97
117. Fujiwara M, Wessel H, Hyung-Suh P, Roesky HW (2002) Tetrahedron 58:239
118. Di Furia F, Licini G, Modena G, Motterle R (1996) J Org Chem 61:5175
119. Bonchio M, Licini G, Modena G, Bortolini O, Moro S, Nugent WA (1999) J Am Chem Soc 121:6258
120. Andrews L, Chertihin GV, Ricca A, Bauschlicher CW (1996) J Am Chem Soc 118:467
121. Andrews L, Chertihin GV, Thompson CA, Dillon J, Byrne S, Bauschlicher CW (1996) J Phys Chem 100:10088
122. Citra A, Chertihin GV, Andrews L, Neurock M (1997) J Phys Chem A 101:3109
123. Chertihin GV, Citra A, Andrews L, Bauschlicher CW (1997) J Phys Chem A 101:8793
124. Bellussi G, Perego C, Carati A, Peratello S, Previdi Massara E, Perego G (1994) Stud Surf Sci Catal 84:85
125. Carati A, Ferraris G, Guidotti M, Moretti G, Psaro R, Rizzo C (2003) Catal Today 77:315
126. Ratnasamy P, Srinivas D, Knözinger H (2004) Adv Catal 48:1

Top Organomet Chem (2005) 16: 69–115
DOI 10.1007/b138074

Published online: 10 September 2005

Tailored Oxide Materials via Thermolytic Molecular Precursor (TMP) Methods

Kyle L. Fujdala[1,2] · Richard L. Brutchey[1,2] · T. Don Tilley[1,2] (✉)

[1]Department of Chemistry, University of California, Berkeley, California 94720-1460, USA
tdtilley@berkeley.edu

[2]Chemical Sciences Division, Lawrence Berkeley National Laboratory, 1 Cyclotron Road, Berkeley, California 94720, USA
tdtilley@berkeley.edu

Dedicated to the memory of Karl W. Terry, who was instrumental in initiating the research described in this chapter

Abstract A review of the *thermolytic molecular precursor* (TMP) method for the generation of multi-component oxide materials is presented. Various adaptations of the TMP method that allow for the preparation of a wide range of materials are described. Further, the generation of isolated catalytic centers (via grafting techniques) and mesoporous materials (via use of organic templates) is summarized. The implications for syntheses of new catalysts, catalyst supports, nanoparticles, mesoporous oxides, and other novel materials are discussed.

Keywords Catalyst synthesis · Hybrid inorganic/organic · Mesoporous · Multicomponent oxide · Thermolytic molecular precursor (TMP) method

1 Introduction

For many years, research efforts in materials chemistry have focused on the development of new methods for materials synthesis. Traditional areas of interest have included the synthesis of catalytic, electronic, and refractory materials via aqueous methods (sol-gel and impregnation) and high-temperature reactions [1–3]. More recent strategies have focused on the synthesis of materials with tailored properties and structures, including well-defined pores, homogeneously distributed elements, isolated catalytic sites, complicated stoichiometries, inorganic/organic hybrids, and nanoparticles [4–13]. A feature

common to many of these approaches is the utilization of molecular precursors as the primary source of the elements in the desired materials, which allow greater control over the structures and properties of the final materials. Many of these processes are designed for use at relatively low temperatures, to further enhance the degree of control and allow access to metastable structures.

In recent years, new analytical methods and theoretical studies have provided important information regarding structure-function correlations for a given material, including catalytic efficiencies, electronic properties, surface characteristics, inherent stability, and particle size [12–19]. Thus, advances in materials research will result from new synthetic methods that allow control over the structures of inorganic substances. New synthetic methodologies will lead to the discovery of currently unknown materials with unique properties, and provide access to well-defined structures that can be used to test theories concerning the influence of structure on various properties (catalytic, electronic, storage, etc.). The development of new materials relies on synergistic relationships between research efforts on multiple fronts; however, in recent years advances in synthesis have occurred at a slower pace relative to those in the areas of characterization, theory, and mechanistic analysis. Therefore, the development of novel approaches for materials synthesis should remain a key area of active research.

The introduction of new synthetic techniques has led to the discoveries of many new electronic materials with improved properties [20–22]. However, similar progress has not been forthcoming in the area of heterogeneous catalysis, despite the accumulation of considerable information regarding structure-reactivity correlations for such catalysts [14–19]. The synthetic challenge in this area stems from the complex and metastable nature of the most desirable catalytic structures. Thus, in order to minimize phase separation and destruction of the most efficient catalytic centers, low-temperature methods and complicated synthetic procedures are often required [1–4]. Similar challenges are faced in many other aspects of materials research and, in general, more practical synthetic methods are required to achieve controlled, facile assembly of complex nanostructured materials [5–11].

The importance of exerting synthetic control over the structure of nanoscaled materials is evident by the dramatic differences often observed in the properties of such species. Examples of nanostructured features that influence the performance of heterogeneous catalysts include supported monolayers, highly dispersed nanoparticles, and framework mesoporosity [12, 13]. Recent progress in the development of synthetic methods for creating nanostructures has been driven largely by the search for new electronic materials. Mesoporous materials have received considerable attention with the discovery of organic templating methods (often surfactant-based) for the generation of inorganic networks [13, 23–26]. Well-defined nanoparticles and nanowires have been produced via templating methods and the formation of organic-inorganic interfaces [12, 27–30]. Hybrid inorganic-

organic materials with improved mechanical and novel electronic properties have been developed by use of organic-containing sol-gel precursors [4, 6].

In addition to nanostructural control, there is a need for simple and versatile synthetic methods that allow manipulation of structures at the atomic level, since the spatial arrangement of atoms has significant influence on the material properties. This is particularly true for catalytic materials. For example, novel reactivity is often observed for heterolinkages in mixed-element oxides (and at catalyst-support interfaces). Also, supported catalysts with isolated centers of reactivity are often cited as having superior catalytic properties, as compared to bulk metals or metal oxides [31–36]. These and other observations have led to much effort being directed toward the synthesis of well-dispersed (atomically homogeneous) mixed-element oxides. Such efforts have primarily involved modifications of the sol-gel process for the synthesis of oxide materials [1–3, 37]. Unfortunately, this approach is limited by the inherently different rates of hydrolysis for the precursors that are used, ultimately leading to significant inhomogeneity in the final materials [37–39]. Thus, it is important to develop methods that achieve controlled chemical modifications of surfaces and bulk materials via the introduction of well-defined sites and highly homogeneous atomic distributions. Most attempts to introduce isolated inorganic structures on surfaces have centered on aqueous impregnation methods, which suffer from the tendency of many metal-based species to agglomerate on the surface of a support during dehydration. A very promising strategy for the production of well-defined and highly active sites on the surface of an oxide support involves grafting of an organometallic species, followed by activation of the resulting "site" via further chemical reactions [40, 41]. This approach includes what may be described as "surface organometallic chemistry", which has been used by Basset to prepare highly active catalysts for alkane and olefin metathesis and alkane hydrogenolysis [42–47].

With the goal of obtaining atomic-level control of highly homogeneous mixed element oxide materials, we have focused on versatile strategies based on molecular precursors that are designed to have the composition and chemical properties that allow facile conversion to the desired materials. High dispersions of elements are expected to give desirable properties. For example, some materials of this type function as solid acids (e.g., $ZrO_2 - SiO_2$ and $Al_2O_3 - SiO_2$) [48–53]. In addition, many complex metal oxides have been identified as partial oxidation catalysts [54–56]. For multi-component catalysts of this kind, optimum performance should result from a maximization of surface area, homogeneity, and active site distribution.

We have employed a molecular building block approach for the generation of a range of multi-component oxides with tailored properties. This molecular precursor method employs metal complexes containing oxygen-rich ligands such as $-OSi(O^tBu)_3$, $-O_2P(O^tBu)_2$, and $-OB[OSi(O^tBu)_3]_2$. For example, complexes with the general formula $L_nM[OSi(O^tBu)_3]_m$ (where L_n = alkoxide, amide, alkyl, etc.) have proven to be excellent single-source precur-

sors to carbon-free, homogeneous mixed-element oxide materials. Thermolyses of these molecular precursors at low-temperatures (< 200 °C) provide 3-dimensional inorganic networks via the elimination of isobutene and H_2O (after condensation of the resulting hydroxyl groups). A solvent-containing gel usually results when these molecular precursors undergo thermolysis in nonpolar solvents (e.g., toluene or *n*-octane). Drying such gels via conventional means (air, high temperature, and/or reduced pressure) provides xerogels, and supercritical drying methods produce aerogels. It is often the case that both of these drying methods provide materials with very similar, and high surface areas. We have referred to this approach as the thermolytic molecular precursor (TMP) method.

Although the TMP method and the sol-gel process are both low-temperature routes to metastable materials that utilize molecular species, the TMP approach provides several advantages. For example, the use of high purity and well-defined molecular species gives accurate control over the stoichiometry of the final materials. Additionally, the preexistence of M – O – E linkages in the molecular precursor maximizes the homogeneity of the final material and leads to a large number of such heterolinkages. The TMP method also offers benefits with respect to surface properties, since the use of nonpolar solvent minimizes pore collapse upon drying, thus providing high pore volumes and surface areas. Other research groups have developed so-called "non-hydrolytic" routes to oxide materials utilizing molecular species, including the condensation of metal alkoxides with metal acetates [57] or metal halides [58].

1.1
History and Scope of this Review

As described in this review, the TMP method represents an effective approach to the synthesis of new materials, and offers several degrees of control over the structures of functional materials. This review aims to summarize the synthesis of various ligands and their use in the development of a wide-range of molecular precursors. Various applications of the TMP approach for materials synthesis (preparation of solid-state inorganic network materials, mesoporous multicomponent oxides, hybrid inorganic/organic materials, CVD applications, heterogeneous catalysts, etc.) are also addressed. Although we cannot provide a comprehensive survey of the literature in this limited account, several examples of related work by other research groups have been included.

2
Synthetic Aspects

Molecular precursors appropriate for use in the TMP method are typically oxygen-rich complexes of the form $L_nM[O_xE(OR)_y]_z$, where L = alkoxide,

amide, alkyl, E = Si, P, B, and R = ^{t}Bu or Si(O^{t}Bu)$_3$. Other functional groups are also compatible with the method (e.g., O^{i}Pr and OCMe$_2$Et); however, O^{t}Bu groups have provided the most versatility in terms of synthetic viability. The most utilized ligand precursors have been HOSi(O^{t}Bu)$_3$ (in addition to its alkali metal salts) and HOP(O)(O^{t}Bu)$_2$, with (HO)$_2$Si(O^{t}Bu)$_2$ also finding some use. More recently, synthesis of the boronous acid HOB[OSi(O^{t}Bu)$_3$]$_2$ has provided access to complexes of the form L$_n$M{OB[OSi(O^{t}Bu)$_3$]$_x$}$_y$ which are precursors to M/B/Si multicomponent oxides. Recent studies have led to molecular precursors with various combinations of oxygen-rich ligands, thus providing access to materials with three or more different heteroelements (i.e., M, Si, P, and/or B) from a single source.

2.1 Ligand Precursors

$$\mathrm{KO(O)P(O^tBu)_2 + HCl_{conc} \xrightarrow[0\,^\circ C]{H_2O} HO(O)P(O^tBu)_2 + KCl} \quad (1)$$

The synthesis of HOSi(O^{t}Bu)$_3$ was first reported by Abe and Kijima in 1969, and involves reaction of SiCl$_4$ with HO^{t}Bu, followed by hydrolysis of the resulting ClSi(O^{t}Bu)$_3$ [59] Scheme 1. Interestingly, HOSi(O^{t}Bu)$_3$ is stable at elevated temperatures (> 180 °C) in the solid state (leading to sublimation) and in solution (leading to no change). This is in stark contrast to most complexes containing M – O – Si(O^{t}Bu)$_3$ linkages, as described in later sections. The related ligand precursors (HO)$_2$Si(O^{t}Bu)$_2$ and (HO)$_2$Si[OSi(O^{t}Bu)$_3$]$_2$ can be synthesized with similar methods [60, 61].

The phosphorus-containing ligand precursor HOP(O)(O^{t}Bu)$_2$ was originally reported in 1957 by Goldwhite and Saunders [62]. The potassium salt of the desired phosphate, KOP(O)(O^{t}Bu)$_2$, is used as a stable precursor to the desired acid. This salt is prepared according to the method of Zwierzak and Kluba [63] and can be stored for extended periods at room temperature. A cold (0 °C) aqueous solution of KOP(O)(O^{t}Bu)$_2$ is treated with concentrated HCl to form HOP(O)(O^{t}Bu)$_2$ as a precipitate (Eq. 1). Rapid isolation (filtration) and subsequent crystallization affords pure product in good yields (> 80%). The

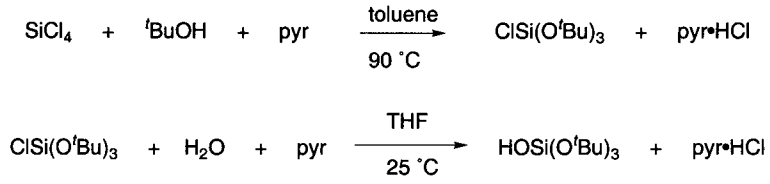

Scheme 1

product is best stored cold (– 20 °C or below), as it readily decomposes when stored at room temperature (< 24 h) to form an insoluble phosphate material.

The recently discovered ligand precursor $HOB[OSi(O^tBu)_3]_2$ was prepared by the hydrolysis of $^tBuOB[OSi(O^tBu)_3]_2$ (in C_6H_6) with one equiv of H_2O [64]. After stirring for 1 h, the solution is frozen and the solvent is removed via lyophilization under reduced pressure. Purification can be achieved via sublimation (ca. 50 °C) of the dry powder under reduced pressure to give yields in excess of 85%. Although not stable in solution for extended periods (due to condensation processes), $HOB[OSi(O^tBu)_3]_2$ is stable indefinitely in the solid state under an inert atmosphere.

2.2 $L_nM[O_xSi(O^tBu)_y]_z$ Molecular Precursors

Two principle strategies have been employed for the synthesis of siloxide-containing molecular precursors. The first involves a silanolysis, or condensation, reaction of the Si – OH groups with a metal amido, alkyl, halide, or alkoxide complex. The second method involves salt metathesis reactions of an alkali metal siloxide with a metal halide. Much of our work has been focused on formation of tris(*tert*-butoxy)siloxide derivatives of the early transition metals and main group elements. The largely unexplored regions of the periodic table include the lanthanides and later transition metals.

2.2.1 Groups 1–2

$$HOSi(O^tBu)_3 + M^0 \xrightarrow{\text{hexanes}} MOSi(O^tBu)_3 + 1/2H_2 \quad (2)$$

(M = Li, Na, K)

The simplest metal siloxide species, $MOSi(O^tBu)_3$ (M = Na, K, Li), are readily synthesized by reaction of $HOSi(O^tBu)_3$ with the desired alkali metal in pentane followed by crystallization at low temperature [65] (Eq. 2). These alkali metal siloxide salts have primarily been used as siloxide transfer reagents in the synthesis of transition metal siloxide complexes. The magnesium siloxide $Mg[OSi(O^tBu)_3]_2$ was synthesized by the reaction of dibutylmagnesium with $HOSi(O^tBu)_3$ in THF at room temperature (83% isolated yield) [66]. Although crystals sufficient for an X-ray crystallographic analysis were not obtained, solution molecular weight determination found that $Mg[OSi(O^tBu)_3]_2$ is monomeric in benzene solution. This complex hydrolyzes immediately when exposed to the atmosphere.

2.2.2 Group 4

$$M(NEt_2)_4 + 4HOSi(O^tBu)_3 \xrightarrow{\text{pentane}} M[OSi(O^tBu)_3]_4 + 4HNEt_2 \quad (3)$$

(M = Ti, Zr, Hf)

$$Ti(O^tBu)_4 + [(^tBuO)_3SiO]_2Si(OH)_2 \xrightarrow[25\,^\circ C]{\text{pentane}} 1/2\left[(^tBuO)_2Ti\{\mu\text{-}O_2Si[OSi(O^tBu)_3]_2\}\right]_2 + 2^tBuOH \quad (4)$$

The molecular precursors $M[OSi(O^tBu)_3]_4$ (where M = Ti, Zr, Hf) are readily synthesized by reaction of the appropriate metal amide complex $M(NR_2)_4$ (R = Me, Et) with 4 equiv of $HOSi(O^tBu)_3$ [67, 68] (Eq. 3). All three precursors can be purified by crystallization from nonpolar solvents (e.g., pentane) and are isolated in good yields (> 75%). The structures of $Zr[OSi(O^tBu)_3]_4$ and $Hf[OSi(O^tBu)_3]_4$ were determined by single-crystal X-ray structure analysis, and both have 5-coordinate metal atoms with one bidentate (through a datively bound O^tBu group) and 3 monodentate $-OSi(O^tBu)_3$ ligands. Additionally, ^{29}Si NMR spectroscopy revealed one resonance for the siloxy ligands of $Ti[OSi(O^tBu)_3]_4$, $Zr[OSi(O^tBu)_3]_4$, and $Hf[OSi(O^tBu)_3]_4$ centered at – 103.24, – 100.50, and – 97.06 ppm, respectively. Related species have been synthesized previously, including $(O^tBu)_3TiOSi(O^tBu)_3$ [69] and $^iPrOTi[OSi(O^tBu)_3]_3$ [70]. A dimeric molecular precursor $[(^tBuO)_2Ti\{\mu - O_2Si[OSi(O^tBu)_3]_2\}]_2$ was synthesized in 75% yield by reaction of $Ti(O^tBu)_4$ with $(HO)_2Si[OSi(O^tBu)_3]_2$ (1 equiv) [61] (Eq. 4). The dimeric structure of $[(^tBuO)_2Ti\{\mu - O_2Si[OSi(O^tBu)_3]_2\}]_2$ was confirmed by single-crystal X-ray structure analysis (Fig. 1). The titanium (III) tris(*tert*-butoxy)siloxy complexes $Ti[OSi(O^tBu)_3]_3 \cdot 2THF$ and $LiTi[OSi(O^tBu)_3]_4$ were synthesized in high yields (> 75%) by reaction of $TiCl_3 \cdot 3THF$ with 3 or 4 equiv of $LiOSi(O^tBu)_3$ in THF [71].

Given the Ti – O – Si linkages in the above titania-silica molecular precursors, these compounds serve as excellent models for isolated 4-coordinate Ti(IV) centers in a silica matrix. Such molecular models are valuable for the identification of active species in titania-silica catalytic materials. For example, for such materials FTIR spectroscopy has been extensively used to identify Ti – O – Si linkages, which give rise to a band in the region of 980–920 cm^{-1} [72–74]. The IR spectrum of $Ti[OSi(O^tBu)_3]_4$ exhibits a band centered at 925 cm^{-1} and that of $[(^tBuO)_2Ti\{\mu - O_2Si[OSi(O^tBu)_3]_2\}]_2$ exhibits a strong band centered at 974 cm^{-1} for the asymmetric Ti – O – Si stretch. UV-vis spectroscopy is a useful corroborative tool used in conjunction with FTIR spectroscopy to suggest the presence of tetrahedral Ti(IV) sites. Generally, absorption in the range of ca. 210–225 nm is thought to stem from a LMCT for tetrahedral Ti(IV) in a silica environment [75, 76].

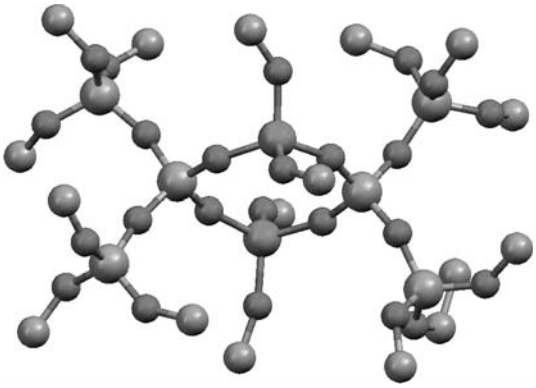

Fig. 1 The molecular structure of $[(^tBuO)_2Ti\{\mu-O_2Si[OSi(O^tBu)_3]_2\}]_2$ generated from crystallographic data, with all hydrogen atoms and *tert*-butyl methyl groups omitted for clarity

By UV-vis spectroscopy, a strong absorption at $\lambda_{max} = 227$ nm is observed for the oxygen to tetrahedral Ti(IV) charge transfer band (LMCT) for $Ti[OSi(O^tBu)_3]_4$. Likewise, a strong absorption at $\lambda_{max} = 216$ nm is observed for $[(^tBuO)_2Ti\{\mu-O_2Si[OSi(O^tBu)_3]_2\}]_2$. These titanium siloxide molecular precursors were also analyzed by X-ray photoelectron spectroscopy (XPS) to probe the chemical environment of titanium. The binding energies of the Ti $2p_{3/2}$ peaks are centered at approximately 461 eV, which is ca. 2 eV higher than the binding energy reported for titanium in an octahedral oxygen environment [77, 78].

2.2.3 Group 5

$$Al_2Me_6 + 2HO(O)P(O^tBu)_2 \xrightarrow[25\,^\circ C]{\text{pentane}} [Me_2AlO_2P(O^tBu)_2]_2 + 2CH_4 \qquad (5)$$

Tris(*tert*-butoxy)siloxide molecular precursors of V(IV) and V(V) can be prepared via simple silanolysis reactions. For example, $OV[OSi(O^tBu)_3]_3$ was obtained in 85% yield by reaction of $OVCl_3$ with excess $HOSi(O^tBu)_3$ in the presence of pyridine [79]. Although crystals of sufficient quality for an X-ray structural analysis of $OV[OSi(O^tBu)_3]_3$ were not obtained, its identity was confirmed by various spectroscopic and analytical techniques. Additionally, $(^tBuO)_3VOSi(O^tBu)_3$ and $(^tBuO)_2V[OSi(O^tBu)_3]_2$ were obtained via reaction of $V(O^tBu)_4$ with 1 and 2 equiv of $HOSi(O^tBu)_3$, respectively, in toluene at 80 °C [80] (Eq. 5). Both $(^tBuO)_3VOSi(O^tBu)_3$ and $(^tBuO)_2V[OSi(O^tBu)_3]_2$ are monomeric in the solid state, and possess only monodentate siloxide ligands

(Fig. 2). Attempts to obtain ^{t}BuOV[OSi(O^{t}Bu)$_3$]$_3$ and V[OSi(O^{t}Bu)$_3$]$_4$ have thus far been unsuccessful [80].

As with other molecular precursors containing the tris(*tert*-butoxy)-siloxide ligand, these vanadium complexes serve as useful models for silica-supported vanadium materials. For example, OV[OSi(O^{t}Bu)$_3$]$_3$ is an excellent structural model for isolated, pseudotetrahedral V(V) centers supported on silica, which are often cited as the active species in a number of partial oxidation reactions [81]. Utilizing FTIR and Raman spectroscopies, it is possible to characterize the V – O, V = O, V – O – Si vibrations to provide useful spectroscopic handles for isolated V(V)/SiO_2 sites. For example, Raman bands have been identified for V = O (1038 cm^{-1}) and V – O (651, 674, 705 cm^{-1}) vibrational transitions in OV[OSi(O^{t}Bu)$_3$]$_3$. Additionally, FTIR spectroscopy was useful in the assignment of the V – O – Si asymmetric stretch as a broad band centered at 910–920 cm^{-1}. Finally, the UV-vis spectrum of OV[OSi(O^{t}Bu)$_3$]$_3$ contains a broad absorption centered at 250 nm assigned to LMCT from oxygen to vanadium. For comparison, supported $O_3V = O$ surface species on silica are generally reported to have $\lambda_{max} < 350$ nm [82].

The Nb(V) and Ta(V) complexes (^{i}PrO)$_2$M[OSi(O^{t}Bu)$_3$]$_3$ were prepared by reaction of the appropriate pentakis(*iso*-propoxide) complex, M(O^{i}Pr)$_5$, with excess HOSi(O^{t}Bu)$_3$ in pentane [71, 83]. Crystals of sufficient quality for an X-ray structure analysis of (^{i}PrO)$_2$Ta[OSi(O^{t}Bu)$_3$]$_3$ could not be obtained, but an analogous complex, (EtO)$_2$Ta[OSi(O^{t}Bu)$_3$]$_3$, was crystallographically characterized. Interestingly, one of the – OSi(O^{t}Bu)$_3$ ligands exhibits dative coordination of a *tert*-butoxide group to the Ta center and a slightly distorted octahedral coordination environment. It does not appear possible to add further bulky siloxide ligands to these species. Similarly, Wolczanski has reported tantalum complexes containing never more than three silox

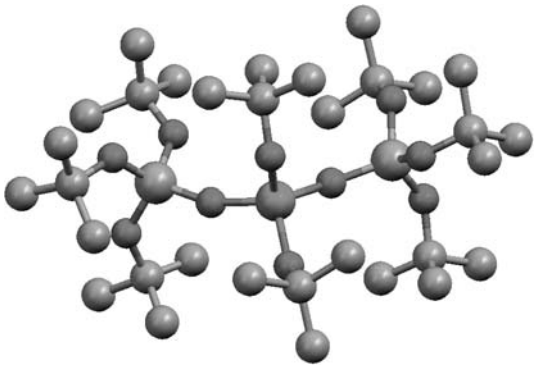

Fig. 2 The molecular structure of (^{t}BuO)$_2$V[OSi(O^{t}Bu)$_3$]$_2$ generated from crystallographic data, with all hydrogen atoms omitted for clarity

(– OSi^tBu_3) ligands [84]. However, Bradley has reported the less sterically hindered, homoleptic siloxide $Ta(OSiMe_3)_5$ [85].

2.2.4 Group 6

Tris(*tert*-butoxy)siloxide complexes of Cr in several oxidation states have been synthesized. Surprisingly, reaction of $Cr(NEt_2)_4$ with 4 equiv of $HOSi(O^tBu)_3$ led to isolation of only reduced Cr species, $(HNEt_2)_2Cr[OSi(O^tBu)_3]_2$ and $(HNEt_2)_2Cr[OSi(O^tBu)_3]_3$, in low to moderate yields [86]. Reaction of $Cr(O^tBu)_4$ with 1 or 2 equiv of $HOSi(O^tBu)_3$ (solvent-free) led to the formation of $(^tBuO)_3CrOSi(O^tBu)_3$ and $(^tBuO)_2Cr[OSi(O^tBu)_3]_2$, respectively [87]. Interestingly, use of solvent leads to significantly lower yields and formation of reduced Cr species. The monosiloxide can be reproducibly obtained in > 80% yield via crystallization from a mixture of toluene and acetonitrile. It is worth noting that $(^tBuO)_3CrOSi(O^tBu)_3$ can also be sublimed at 80 °C under reduced pressure (0.001 mm Hg), making it potentially useful in CVD applications. Both complexes are monomeric in the solid state and possess only monodentate siloxide ligands. As with the vanadium analogs, Cr(IV) complexes with three or four – $OSi(O^tBu)_3$ ligands could not be synthesized, perhaps due to steric factors and/or redox processes [87]. In related work, Bradley and Chisholm reported the synthesis of $Cr(OSiEt_3)_4$ via reaction of $Cr(O^tBu)_4$ with the less sterically encumbered $HOSiEt_3$ [88].

Formation of molybdenum and tungsten molecular precursors was obtained via simple silanolysis reactions. The first such complexes were formed via reactions of $(HO)_2Si(O^tBu)_2$ with $Mo_2(NMe_2)_6$ or $W_2(NMe_2)_6$ [89], to give the novel siloxide complexes $Mo_2[O_2Si(O^tBu)_2]_3$ and $W_2(NHMe_2)_2[O_2Si(O^tBu)_2]_2[OSi(OH)(O^tBu)_2]_2$. The complex $Mo_2[O_2Si(O^tBu)_2]_3$ was found to adopt an eclipsed structure, with three di(*tert*-butoxy)silanediolato ligands bridging the molybdenum centers in a symmetrical fashion. The structure of $W_2(NHMe_2)_2[O_2Si(O^tBu)_2]_2[OSi(OH)(O^tBu)_2]_2$ involves two – $O_2Si(O^tBu)_2$ ligands that bridge the W ≡ W bond in an η^1, η^1 fashion, and one – $OSi(OH)(O^tBu)_2$ ligand coordinated to each W center. This molecule also adopts an eclipsed conformation and has a 2-fold axis of symmetry that perpendicularly bisects the W ≡ W bond.

Reactions of $Mo_2(NMe_2)_6$ and $Mo_2(O^tBu)_6$ with 2 *equiv* of $HOSi(O^tBu)_3$ in pentane provide $Mo_2(NMe_2)_4[OSi(O^tBu)_3]_2$ and $Mo_2(O^tBu)_4[OSi(O^tBu)_3]_2$ (yields of 76% and 59%, respectively) after crystallization from pentane [90]. Crystallographic analyses of both complexes revealed that the – $OSi(O^tBu)_3$ ligands are arranged in a staggered fashion about the Mo ≡ Mo bond (Fig. 3). In a similar manner, the tungsten complex $W_2(NMe_2)_4[OSi(O^tBu)_3]_2$ was synthesized in 55% yield via reaction of $W_2(NMe_2)_6$ with 2 equiv of $HOSi(O^tBu)_3$ in pentane [91].

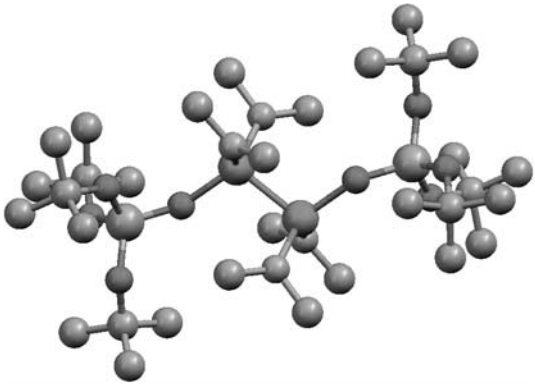

Fig. 3 The molecular structure of $Mo_2(NMe_2)_4[OSi(O^tBu)_3]_2$ generated from crystallographic data, with all hydrogen atoms omitted for clarity

Molybdenum and tungsten complexes containing metal-oxo fragments and the tris(*tert*-butoxy)siloxide ligand have also been prepared. Complexes of the form $MO[OSi(O^tBu)_3]_4$ (M = Mo and W) can be synthesized from the reaction of $MOCl_4$ and 4 equiv of $LiOSi(O^tBu)_3$ in Et_2O in low isolated yields (10–40%) after precipitation from pentane [92]. Similarly, reactions of $MO_2Cl_2(DME)$ with 2 equiv of $LiOSi(O^tBu)_3$ in Et_2O afforded the siloxide complexes $MO_2[OSi(O^tBu)_3]_2$ (M = Mo and W) in low to moderate yields (30–50%) [92]. These complexes are thermally unstable and decompose within hours of isolation under an inert atmosphere. These oxo-containing molybdenum and tungsten siloxides serve as valuable structural models for catalytic sites containing M = O moieties supported on silica, and they have provided valuable NMR (including ^{95}Mo, ^{29}Si, and ^{183}W), IR, Raman, and UV-vis data [92]. Other oxo-molybdenum and -tungsten complexes with supporting siloxide ligands have been reported, primarily as proposed models for active sites in oxo-transfer catalysts. For example, $MoO_2(OSiPh_3)_2$ [93], $MoO_2(OSiMe_2{}^tBu)_2(py)$ [94], $[O_2Mo(O_2Si^tBu_2)]_2$ [95], $WO[O(Ph_2SiO)_3]_2(THF)$ [96], and $WO_2(OSiPh_3)_2(OSC_4H_8)_2$ [96] have been synthesized by various research groups.

2.2.5 Group 8

$$FeCl_3 + 3NaOSi(O^tBu)_3 \xrightarrow[\text{reflux}]{\text{THF}} Fe[OSi(O^tBu)_3]_3 \cdot THF + 3NaCl \quad (6)$$

The only group 8 tris(*tert*-butoxy)siloxide molecular precursor that has been reported thus far is the iron(III) complex $Fe[OSi(O^tBu)_3]_3 \cdot THF$, synthesized via the reaction of $FeCl_3$ with $NaOSi(O^tBu)_3$ in THF (74%) [71, 97] (Eq. 6). An

X-ray crystallographic analysis of $Fe[OSi(O^tBu)_3]_3THF$ revealed a distorted tetrahedral geometry (toward a trigonal pyramid) at the Fe center. Related alkyl siloxide complexes of Fe(III) with dimeric structures, $[Fe(OSiMe_3)_3]_2$ and $[Fe(OSiEt_3)_3]_2$, have been reported by Schmidbaur and Richter [98].

2.2.6 Group 9

The only examples of tris(*tert*-butoxy)siloxide compounds from this group are the dimeric Rh diene complexes $\{(cod)Rh[\mu - OSi(O^tBu)_3]\}_2$ and $\{(nbd)Rh[\mu - OSi(O^tBu)_3]\}_2$, where cod = 1,5-cyclooctadiene and nbd = norborna-2,5-diene [99]. Both complexes are formed via reaction of $KOSi(O^tBu)_3$ with the respective $[(diene)RhCl]_2$ starting material in Et_2O. Although crystals of sufficient quality for X-ray structure analyses were not obtained, solution molecular weight determinations and spectroscopic evidence suggest folded, dimeric structures. Similar structures were found for the related siloxides $[(cod)RhOSiMe_3]_2$ and $[(cod)RhOSiPh_3]_2$ [100].

2.2.7 Group 10

Two tris(*tert*-butoxy)siloxy complexes of nickel were obtained and structurally characterized by single-crystal X-ray crystallography. The first was prepared via reaction of $NiI_2(THF)_2$ with $NaOSi(O^tBu)_3$ in refluxing THF to yield $Na_3(\mu_3 - I)\{Ni[\mu_3 - OSi(O^tBu)_3]_3I\} \cdot 0.5THF \cdot 0.5C_5H_{12}$ [101]. The molecule forms a cube-like structure, with vertices defined by a Ni(II) center, three sodium ions, three silanolate oxygens, and an iodide atom. The second complex was obtained via reaction of bis(allyl)nickel with $HOSi(O^tBu)_3$ to give the dimeric $[(\eta^3 - allyl)NiOSi(O^tBu)_3]_2$ complex [101]. The Ni_2O_2 core of the dimer is bent in a butterfly fashion along the O – O vector resulting in a fold angle of ca. 135°.

2.2.8 Group 11

The Cu(II) tris(*tert*-butoxy)siloxide complex $Cu[OSi(O^tBu)_3]_2(py)_2$ was prepared via addition of $NaOSi(O^tBu)_3$ to $CuBr_2$ in a THF and pyridine mixture [102]. Unfortunately, this complex was isolated with average yields of 14%. This complex is unusual in that Cu(II) alkoxides are generally highly associated and insoluble [103, 104]. An X-ray crystallographic analysis of $Cu[OSi(O^tBu)_3]_2(py)_2$ revealed well-separated monomeric units, and a coordination environment about Cu that can be described as a severely distorted tetrahedron. In an effort to synthesize a molecular precursor featuring Cu in a higher isolated yield, the Cu(I) siloxy complex $[CuOSi(O^tBu)_3]_4$ was

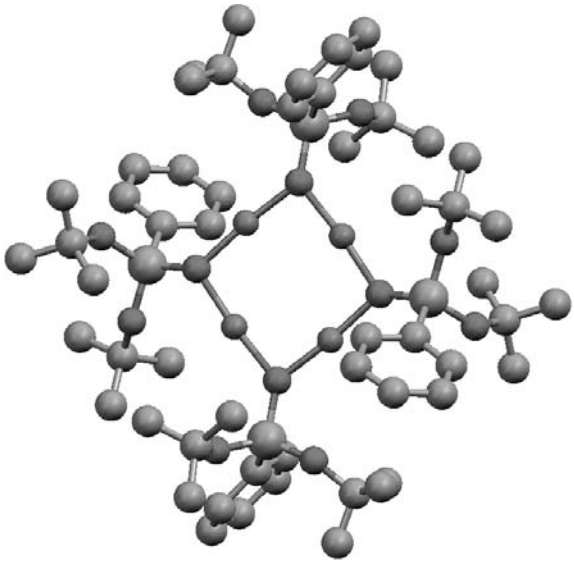

Fig. 4 The molecular structure of $[CuOSiPh(O^tBu)_2]_4$ generated from crystallographic data, with all hydrogen atoms omitted for clarity

prepared by silanolysis of $[CuO^tBu]_4$ with $HOSi(O^tBu)_3$ (58%) [105]. Attempts to structurally characterize the complex by single crystal X-ray analysis were unsuccessful; however, an analogous complex $[CuOSiPh(O^tBu)_2]_4$ was prepared and structurally characterized (Fig. 4). The structure of $[CuOSiPh(O^tBu)_2]_4$ resembles that of $[CuO^tBu]_4$ in possessing a planar Cu_4O_4 core with noninteracting, oxygen-bridged Cu centers [106].

2.2.9 Group 12

The zinc tris(*tert*-butoxy)siloxide complex $\{Zn[OSi(O^tBu)_3]_2\}_2$ was prepared from the reaction of $ZnMe_2$ with $HOSi(O^tBu)_3$ [107]. This complex was structurally characterized as an asymmetric dimer with four $-OSi(O^tBu)_3$ ligands, each exhibiting a unique coordination mode (η^1; η^2; $\mu-\eta^1$, η^1; $\mu-\eta^1$, η^2). A molecular weight determination for the complex supports a monomeric structure in solution. Reaction of $ZnMe_2$ with $(HO)_2Si(O^tBu)_2$ leads to the formation of polymeric species, $[ZnOSi(O^tBu)_2O]_n$, that are soluble in organic solvents [107]. For comparison, the zinc siloxane polymer $[ZnOSiPh_2O]_n$ reported by Hornbraker and Conrad is an insoluble material contaminated with ZnO [108].

2.2.10 Group 13

Reaction of 2 equiv of $HOSi(O^tBu)_3$ with $B(O^tBu)_3$ as a neat mixture at 80 °C results in the formation of $^tBuOB[OSi(O^tBu)_3]_2$, which can be readily isolated in crystalline form (79%) [64]. X-ray crystallography revealed that $^tBuOB[OSi(O^tBu)_3]_2$ is monomeric in the solid state, with a trigonal planar coordination geometry about boron (Fig. 5). Similarly, $B[OSi(O^tBu)_3]_3$ can be formed by reaction of $B(O^tBu)_3$ with 3 equiv of $HOSi(O^tBu)_3$ in toluene [64]. The related triphenylsiloxide compound $B(OSiPh_3)_3$ had been previously reported [109].

Several aluminum tris(*tert*-butoxy)siloxides have been synthesized, including $[Me_2AlOSi(O^tBu)_3]_2$ and $[Me(^tBuO)AlOSi(O^tBu)_3]_3$ [110]. Additionally, $Al[OSi(O^tBu)_3]_3 \cdot THF$ was formed via reaction of $[Al(O^iPr)_3]_4$ with 12 equiv of $HOSi(O^tBu)_3$ in THF (72%) [111]. The latter precursor is not stable at room temperature, and decomposes to insoluble Al/Si/O materials upon storage under inert conditions. Barron et al. reported synthesis of the analogous, but stable, $Al(OSiPh_3)_3 \cdot THF$ [112]. Interestingly, when 12 equiv of $HOSi(O^tBu)_3$ reacted with $[Al(O^iPr)_3]_4$ in hexanes, an $Al[OSi(O^tBu)_3]_3 \cdot HO^iPr$ adduct formed, which cocrystallizes with $1/2[Al(O^iPr)_3]_4$ [111]. The related, dimeric complex $[(^iPrO)_2AlOSi(O^tBu)_3]_2$ was formed via reaction of 4 equiv of $HOSi(O^tBu)_3$ with $[Al(O^iPr)_3]_4$ in toluene at 80 °C; however, the isolated yield was low (30%) [111]. With similar methods, Abe et al. prepared $\{^iPrOAl[OSi(O^tBu)_3]_2\}_2$ [113]. Other workers have reported $(^iPrO)_2AlOSiMe_3$ and $(^nBuO)_2AlOSi(OEt)_3$ as molecular precursors [114, 115].

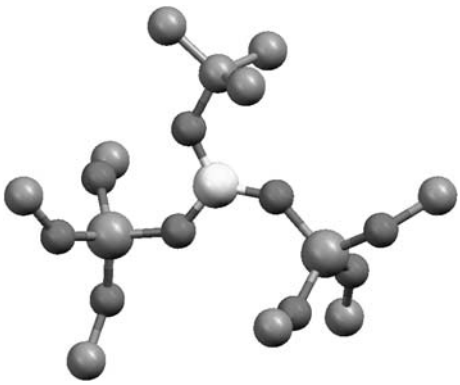

Fig. 5 The molecular structure of $^tBuOB[OSi(O^tBu)_3]_2$ generated from crystallographic data, with all hydrogen atoms and the siloxide ligand methyl groups omitted for clarity

2.2.11 Groups 14–15

Reaction of $PbCl_2$ with 3 equiv of $NaOSi(O^tBu)_3$ produced the "ate" complex $NaPb[OSi(O^tBu)_3]_3$ in 66% isolated yield. Similarly, the analogous tin complex, $KSn[OSi(O^tBu)_3]_3$, was formed by reaction of $SnCl_2$ with $KOSi(O^tBu)_3$ in 81% yield [116]. The single crystal X-ray structures of $NaPb[OSi(O^tBu)_3]_3$ and $KSn[OSi(O^tBu)_3]_3$ revealed isomorphic structures containing a 3-coordinate, trigonal prismatic metal center and a 6-coordinate alkali metal (Na or K) atom encapsulated in an oxygen matrix formed by the bridging siloxy and *tert*-butoxy groups of the $-OSi(O^tBu)_3$ ligands. The molecular precursor $Bi[OSi(O^tBu)_3]_3$ was synthesized by reaction of $BiCl_3$ with $KOSi(O^tBu)_3$ in low isolated yield (30%) [116].

2.3 $L_nM[O_2P(O^tBu)_2]_x$ Molecular Precursors

Successful strategies for generating complexes of the di(*tert*-butyl)phosphate ligand primarily focus on the use of $HOP(O)(O^tBu)_2$ as a reagent. As with the related siloxide species, all synthetic manipulations must be performed under inert conditions to avoid hydrolysis of the M – O – P linkages. Complexes of the $-O_2P(O^tBu)_2$ ligand are useful precursors to M/P/O oxide materials.

2.3.1 Group 4

Although potassium titanyl phosphate ($KTiOPO_4$) has been studied extensively as a nonlinear optical material [117, 118], the chemistry of molecular precursors to titanium phosphate materials remains fairly undeveloped. Notably, Thorn and Harlow reported a series of well-defined molecular titanium phosphate complexes derived from titanium halides, amides, and siloxides [119]. Given the general need for efficient molecular precursors to titanium phosphates, several di(*tert*-butyl)phosphate complexes were targeted. Reaction of 1 equiv of $HOP(O)(O^tBu)_2$ with $Ti(OR)_4$ (R = Et, ^{i}Pr) in pentane resulted in the formation of $[Ti(OR)_3O_2P(O^tBu)_2]_2$ species in yields in excess of 80% after crystallization [120]. In the solid-state, $[Ti(O^iPr)_3O_2P(O^tBu)_2]_n$ was found to be a centrosymmetric dimer. Combination of ethanol solutions of KOEt (2 equiv) and $[Ti(OEt)_3O_2P(O^tBu)_2]_n$ led to isolation of a new potassium titanium di(*tert*-butyl)phosphate complex $[Ti_2K(OEt)_8O_2P(O^tBu)_2]_2$, identified by combustion analysis and X-ray crystallography [120]. A structural analysis revealed that this complex is a centrosymmetric dimer in the solid state.

The zirconium di(*tert*-butyl) phosphate complex $Zr_2(O^tBu)_5(HO^tBu)[O_2P(O^tBu)_2]_3$ was generated (74% isolated) by the reaction of $HOP(O)(O^tBu)_2$

with $Zr(O^tBu)_4$ in pentane [71]. This complex features three bridging phosphate ligands, and five terminal $-O^tBu$ ligands. Addition of $Zr_2(O^tBu)_5(HO^tBu)[O_2P(O^tBu)_2]_3$ to KH in toluene led to the formation of $Zr_2(O^tBu)_6[O_2P(O^tBu)_2]_2$ in 54% isolated yield after crystallization from toluene [71]. An X-ray crystallographic analysis revealed that both phosphate ligands bridge the Zr atoms, and the $-O^tBu$ ligands are all terminal (3 per Zr atom).

2.3.2 Group 5

The niobium phosphate complex $\{(^iPrO)_4Nb[O_2P(O^tBu)_2]\}_2$ was produced by the reaction of $Nb(O^iPr)_5$ with $HOP(O)(O^tBu)_2$ in pentane [71]. Although crystals of sufficient quality for an X-ray crystallographic analysis were not obtained, spectroscopic evidence suggests that the phosphate ligands bridge the two Nb centers.

2.3.3 Group 6

From the triply bonded $M_2(NMe_2)_6$ (M = Mo and W) starting materials, the new complexes $M_2(NMe_2)_2[\mu-O_2P(O^tBu)_2]_2[OP(O)(O^tBu)_2]_2$ were obtained [90, 91]. Interestingly, 2 isomers (*cis* and *trans*) of $Mo_2(NMe_2)_2[\mu-O_2P(O^tBu)_2]_2[OP(O)(O^tBu)_2]_2$ were isolated. X-ray crystallographic analyses of both isomers of $Mo_2(NMe_2)_2[\mu-O_2P(O^tBu)_2]_2[OP(O)(O^tBu)_2]_2$ determined that two of the di(*tert*-butyl)phosphate ligands bridge the Mo atoms, and the other two phosphate ligands are terminal (Figs. 6, 7).

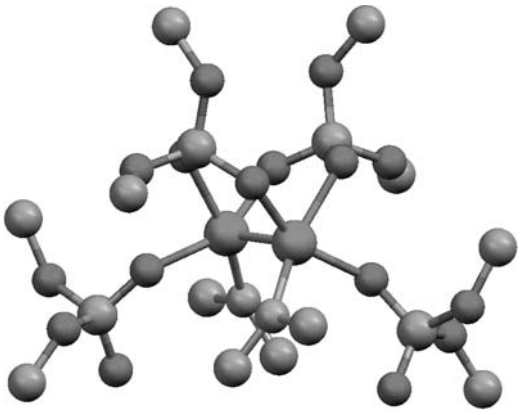

Fig. 6 The molecular structure of *cis*-$Mo_2(NMe_2)_2[O_2P(O^tBu)_2]_4$ generated from crystallographic data, with all hydrogen atoms and *tert*-butyl methyl groups omitted for clarity

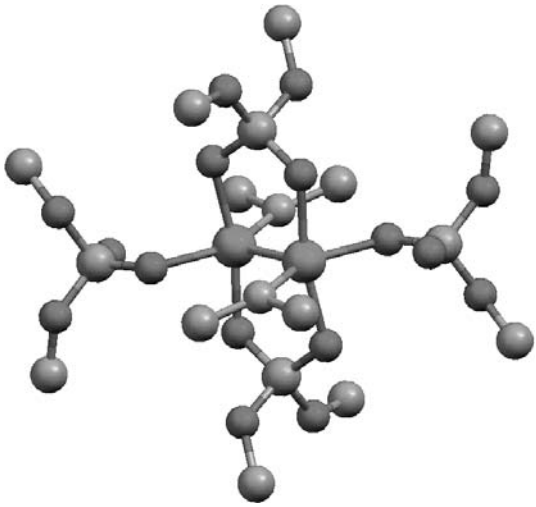

Fig. 7 The molecular structure of *trans*-$Mo_2(NMe_2)_2[O_2P(O^tBu)_2]_4$ generated from crystallographic data, with all hydrogen atoms and *tert*-butyl methyl groups omitted for clarity

2.3.4 Group 12

Attempts to prepare $Zn[O_2P(O^tBu)_2]_2$ via the reaction of 2 equiv of $HO(O)P(O^tBu)_2$ with $ZnEt_2$ gave an insoluble polymeric material $\{Zn[O_2P(O^tBu)_2]_2\}_n$ in 50% yield [121]. One soluble product of the reaction was fractionally crystallized and identified as an oxo-centered tetranuclear cluster $Zn_4(\mu_4-O)[O_2P(O^tBu)_2]_6$. This complex was independently synthesized by reaction of 4 equiv of $ZnEt_2$, 6 equiv of $HO(O)P(O^tBu)_2$, and 1 equiv of water (66% yield) [121].

2.3.5 Group 13

$$Al_2Me_6 + 2HO(O)P(O^tBu)_2 \xrightarrow[25\,^\circ C]{\text{pentane}} [Me_2AlO_2P(O^tBu)_2]_2 + 2CH_4 \qquad (7)$$

Reactions of $HOP(O)(O^tBu)_2$ with Al_2Me_6 and $[Al(O^iPr)_3]_4$ gave the molecular precursors $[Me_2AlO_2P(O^tBu)_2]_2$ and $[Al(O^iPr)_2O_2P(O^tBu)_2]_4$, respectively (> 90% yield) [122] (Eq. 7). In the solid state, $[Me_2AlO_2P(O^tBu)_2]_2$ exists as a centrosymmetric dimer consisting of two four-coordinate Al centers bridged by di(*tert*-butyl)phosphate groups. In contrast, $[Al(O^iPr)_2O_2P(O^tBu)_2]_4$ exists as a centrosymmetric tetramer in which the unique half of the tetramer consists of two aluminum atoms bridged by two $-O_2P(O^tBu)_2$

groups. The central part of the molecule contains a planer Al_2O_2 four-membered ring containing two symmetry-related Al atoms bridged by two $-O^iPr$ ligands.

2.4
$L_nM\{OB[OSi(O^tBu)_3]_2\}_x$ Molecular Precursors

The recent discovery of $HOB[OSi(O^tBu)_3]_2$ has allowed access to potential single-source molecular precursors to M/B/Si/O materials.

2.4.1
Group 4

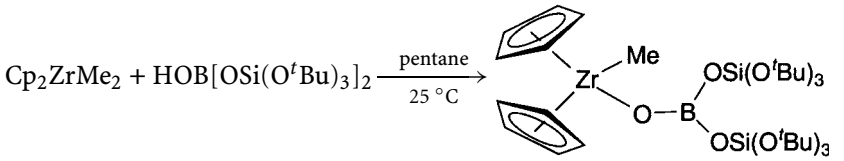

(8)

The first reported complex containing this (siloxy)boryloxide ligand, $Cp_2Zr(Me)OB[OSi(O^tBu)_3]_2$, was synthesized by reaction of Cp_2ZrMe_2 with 1 equiv of $HOB[OSi(O^tBu)_3]_2$ in pentane (90% yield) [64] (Eq. 8). Although not an effective molecular precursor to materials due to formation of $Cp_2Zr[OSi(O^tBu)_3]_2$ upon heating (via presumed methide abstraction by boron), $Cp_2Zr(Me)OB[OSi(O^tBu)_3]_2$ serves as a molecular model for surface-

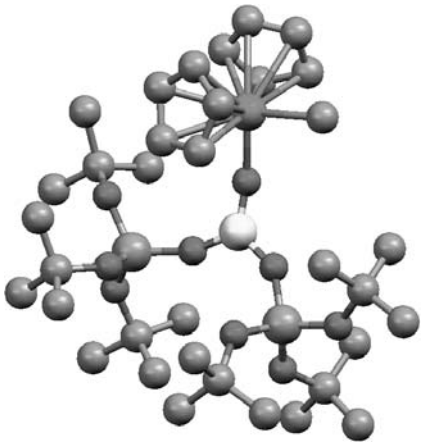

Fig. 8 The molecular structure of $Cp_2Zr(Me)OB[OSi(O^tBu)_3]_2$ generated from the crystallographic data of 1 of the 18 independent molecules from the asymmetric unit, with all hydrogen atoms omitted for clarity

bound metallocene catalysts [64]. The single crystal X-ray crystallographic analysis of $Cp_2Zr(Me)OB[OSi(O^tBu)_3]_2$ confirmed the monomeric nature of the complex and revealed a trigonal planar geometry about the boron center (Fig. 8). Interestingly, the asymmetric unit of the crystal structure contained 18 unique molecules.

Reaction of excess $HOB[OSi(O^tBu)_3]_2$ with $M(NEt_2)_4$ (M = Zr, Hf) in pentane afforded $Et_2NM\{OB[OSi(O^tBu)_3]_2\}_3$ complexes in moderate yields (50 and 46% for M = Zr and Hf, respectively) [91]. Single crystal X-ray structural analysis of $Et_2NZr\{OB[OSi(O^tBu)_3]_2\}_3$ confirmed that its structure contains three monodentate $-OB[OSi(O^tBu)_3]_2$ ligands with nearly linear Zr – O – B linkages.

2.4.2 Group 6

Reaction of $Mo_2(NMe_2)_6$ with $HOB[OSi(O^tBu)_3]_2$ in pentane afforded $Mo_2(NMe_2)_4\{OB[OSi(O^tBu)_3]_2\}_2$ in 73% yield after crystallization [90]. A single crystal structural analysis revealed a trigonal planar geometry about the boron atoms and a significantly bent Mo – O – B bond angle (121.8°). Interestingly, reaction of $Mo_2(NMe_2)_4\{OB[OSi(O^tBu)_3]_2\}_2$ with 4 equiv of HO^tBu leads to substitution of the NMe_2 ligands with O^tBu groups, accompanied by transfer of a single $-OSi(O^tBu)_3$ ligand from boron to molybdenum to give $Mo_2(O^tBu)_4[OSi(O^tBu)_3]_2$.

2.5 Molecular Precursors Containing Combinations of $-OSi(O^tBu)_3$, $-O_2P(O^tBu)_2$, and $-OB[OSi(O^tBu)_3]_2$ Ligands

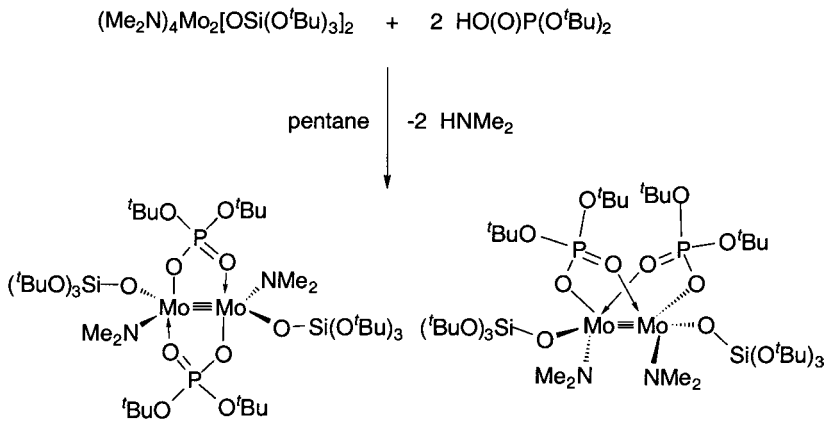

(9)

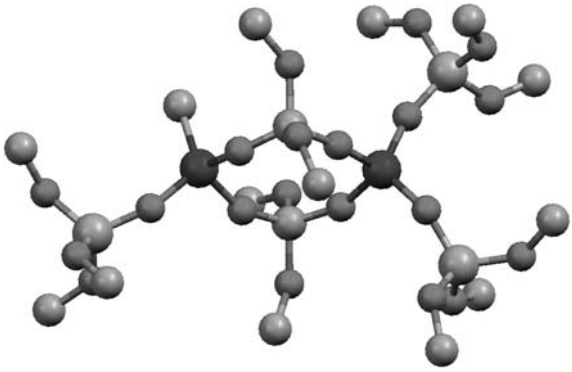

Fig. 9 The molecular structure of $[(^t\mathrm{BuO})_3\mathrm{SiO}]_2\mathrm{Al}[(\mu-\mathrm{O})_2\mathrm{P}(\mathrm{O}^t\mathrm{Bu})_2]_2\mathrm{Al}(\mathrm{Me})\mathrm{OSi}(\mathrm{O}^t\mathrm{Bu})_3$ generated from crystallographic data, with all hydrogen atoms and *tert*-butyl methyl groups omitted for clarity

More recent efforts have focused on the incorporation of multiple ligand types to allow access to new materials with three or more components from a single source. Although the potential for a huge library of precursors exists, synthetic access to the desired species has proven to be a significant challenge. The typical approach has involved further derivitization of known species in a stepwise manner. The first molecular precursor fitting the above description, $[(^t\mathrm{BuO})_3\mathrm{SiO}]_2\mathrm{Al}[(\mu-\mathrm{O})_2\mathrm{P}(\mathrm{O}^t\mathrm{Bu})_2]_2\mathrm{Al}(\mathrm{Me})\mathrm{OSi}(\mathrm{O}^t\mathrm{Bu})_3$, was reported in 2001 [123]. Reaction of excess $\mathrm{HOSi}(\mathrm{O}^t\mathrm{Bu})_3$ with $[\mathrm{Me}_2\mathrm{AlO}_2\mathrm{P}(\mathrm{O}^t\mathrm{Bu})_2]_2$ in toluene led to isolation of this silicoaluminophosphate precursor in 62% yield. A single crystal X-ray structural analysis revealed that the di(*tert*-butyl)phosphate ligands bridge the two aluminum centers (Fig. 9). Interestingly, the O – Si – O – Al – O – P – O – Al – O – Si – O linkages and the ring structure are similar to those in well-ordered microporous silicoaluminophosphates, making this molecular precursor a good model compound for these materials [123].

Further efforts to prepare complexes with multiple ligand types focused on the reactions of $\mathrm{Mo}_2(\mathrm{NMe}_2)_4[\mathrm{OSi}(\mathrm{O}^t\mathrm{Bu})_3]_2$ or $\mathrm{Mo}_2(\mathrm{NMe}_2)_4\{\mathrm{OB}[\mathrm{OSi}(\mathrm{O}^t\mathrm{Bu})_3]_2\}_2$ with 2 equiv of $\mathrm{HOP(O)}(\mathrm{O}^t\mathrm{Bu})_2$, which led to the formation of $\mathrm{Mo}_2(\mathrm{NMe}_2)_2[\mathrm{OSi}(\mathrm{O}^t\mathrm{Bu})_3]_2[\mu-\mathrm{O}_2\mathrm{P}(\mathrm{O}^t\mathrm{Bu})_2]_2$ (60% yield) and $\mathrm{Mo}_2(\mathrm{NMe}_2)_2\{\mathrm{OB}[\mathrm{OSi}(\mathrm{O}^t\mathrm{Bu})_3]_2\}_2[\mu-\mathrm{O}_2\mathrm{P}(\mathrm{O}^t\mathrm{Bu})_2]_2$ (22% yield), respectively [90]. As observed with the molybdenum phosphate precursor, *cis* and *trans* isomers of $\mathrm{Mo}_2(\mathrm{NMe}_2)_2[\mathrm{OSi}(\mathrm{O}^t\mathrm{Bu})_3]_2[\mu-\mathrm{O}_2\mathrm{P}(\mathrm{O}^t\mathrm{Bu})_2]_2$ were isolated and characterized (Eq. 9). Crystallographic studies of all three of these complexes confirmed the bridging nature of the di(*tert*-butyl)phosphate ligands, as shown for $\mathrm{Mo}_2(\mathrm{NMe}_2)_2\{\mathrm{OB}[\mathrm{OSi}(\mathrm{O}^t\mathrm{Bu})_3]_2\}_2[\mu-\mathrm{O}_2\mathrm{P}(\mathrm{O}^t\mathrm{Bu})_2]_2$ in Fig. 10.

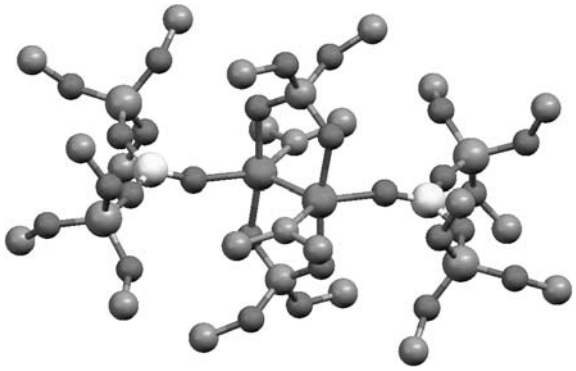

Fig. 10 The molecular structure of $Mo_2(NMe_2)_2[O_2P(O^tBu)_2]_2\{OB[OSi(O^tBu)_3]_2\}_2$ generated from crystallographic data, with all hydrogen atoms and *tert*-butyl methyl groups omitted for clarity

3 Mechanistic Insight into the Decomposition of Oxygen-Rich Molecular Precursors

Typical characterization of the thermal conversion process for a given molecular precursor involves the use of thermogravimetric analysis (TGA) to obtain ceramic yields, and solution NMR spectroscopy to identify soluble decomposition products. Analyses of the volatile species given off during solid phase decompositions have also been employed. The thermal conversions of complexes containing $M-OSi(O^tBu)_3$ and $M-O_2P(O^tBu)_2$ moieties invariably proceed via elimination of isobutylene and the formation of M – O – Si – OH and M – O – P – OH linkages that immediately undergo condensation processes (via elimination of H_2O), with subsequent formation of insoluble multi-component oxide materials. For example, thermolysis of $Zr[OSi(O^tBu)_3]_4$ in toluene at 413 K results in elimination of 12 equiv of isobutylene and formation of a transparent gel [67, 68].

The thermal decompositions are catalyzed by Brønsted and Lewis acids [68]. In general, when M is electron poor and Lewis acidic, the thermal decompositions occur efficiently and at low temperatures (typically between 100 and 200 °C, but sometimes at lower temperature). The addition of a catalytic amount of a Lewis or Brønsted acid (i.e., $AlCl_3$ or HCl) has been observed to accelerate the elimination of isobutylene and the formation of three-dimensional network structures [64, 124–126]. Pioneering studies on pyrolyses of various metal alkoxides by Bradley and others have also shown that alkene eliminations represent a primary decomposition pathway [104].

The mechanism by which electron-rich late transition metal complexes decompose is distinct from those involving more electropositive metals

such as Al and Zr. The formation of significant amounts of $HOSi(O^tBu)_3$ and Cu^0 upon thermolysis of $[CuOSi(O^tBu)_3]_4$ in the solid phase suggests that the homolytic cleavage of Cu – O bonds may be involved [105]. Similar homolytic processes have been proposed by Caulton and coworkers for related electron rich $[CuOSiR]_4$ (R = alkyl and aryl) species [127] and by our group for the recently synthesized $\{(cod)Rh[\mu - OSi(O^tBu)_3]\}_2$ and $\{(nbd)Rh[\mu - OSi(O^tBu)_3]\}_2$ species [99].

4
Solid Phase and Solution TMP Methods

Over the past 15 years, numerous studies have shown that transition-metal and main-group element complexes of $-O_nSi(OR)_{(4-n)}$ (n = 1, R = ^{t}Bu; n = 2, R = ^{t}Bu or $Si(O^tBu)_3$), $-O_2P(O^tBu)_2$, and $-OB[OSi(O^tBu)_3]_2$ ligands are convenient precursors to homogeneous (well-dispersed), metal oxide-silica, metal phosphate, and metal borosilicate materials (and combinations thereof). Thermogravimetric analyses (TGA) typically reveal a precipitous weight loss during the decomposition event, suggesting rapid and uniform conversion to largely carbon-free materials. Thermolyses of molecular precursors in nonpolar media provide high surface area xerogels upon air-drying of the resulting gels.

An expansion of the solution TMP approach involves a cothermolytic strategy, whereby two or more molecular species that thermally convert to materials under mild heating are converted simultaneously in the same solution [83, 128–130]. This cothermolysis method allows the composition of the final material to be tuned to variable stoichiometries, and has proven useful in the generation of catalytic materials where even small variations in elemental content can lead to dramatic performance changes. The remainder of this section serves to provide examples of the materials that can be formed via simple solid phase or solution TMP routes.

4.1.1
Thermolytic Conversion of Group 2 Siloxide Precursors

Although the extreme moisture sensitivity of $Mg[OSi(O^tBu)_3]_2$ complicated attempts to obtain meaningful thermogravimetric analysis (TGA) data for its solid phase decomposition, solution thermolyses in toluene produced $MgO \cdot 2SiO_2$ gels that formed high surface area (ca. 250 $m^2\,g^{-1}$) xerogels upon drying in air [66]. Supercritical CO_2 drying of the wet gel resulted in a dramatic increase in the surface area to ca. 650 $m^2\,g^{-1}$. Both types of $MgO \cdot 2SiO_2$ materials were amorphous (by PXRD), and only after calcination at 1200 °C under flowing oxygen was crystalline enstatite ($MgSiO_3$) detected. Predictions and experimental evidence for high SiO_2 content magnesia-silica

materials suggested that more acidic sites would be present for more homogeneous materials [131]. Poorly dispersed $MgOSiO_2$ materials (containing large SiO_2 and MgO domains) are known to have increased basicity [132]. The $MgO \cdot 2SiO_2$ xerogels made from $Mg[OSi(O^tBu)_3]_2$ have high acid site concentrations (from NH_3 TPD: 2.7 sites nm^{-2}) and a negligible basicity (from CO_2 TPD: 0.13 sites nm^{-2}), suggesting significant amounts of Mg – O – Si heterolinkages and hence a high degree of homogeneity.

4.1.2 Thermolytic Conversion of Group 4 Siloxide Precursors

The solid-state decomposition temperature for group 4 siloxide molecular precursors (as determined by TGA) ranges from ca. 140 °C for $Zr[OSi(O^tBu)_3]_4$, $Hf[OSi(O^tBu)_3]_4$, and $[(^tBuO)_2Ti\{\mu - O_2Si[OSi(O^tBu)_3]_2\}]_2$ to ca. 250 °C for $Ti[OSi(O^tBu)_3]_4$. Solid phase decompositions of $Zr[OSi(O^tBu)_3]_4$ and $Hf[OSi(O^tBu)_3]_4$ at 200 °C give materials with a BET surface area of ca. 100 $m^2\,g^{-1}$, whereas pyrolysis of $Ti[OSi(O^tBu)_3]_4$ provides a material with a much lower surface area (ca. 20 $m^2\,g^{-1}$) [67, 68]. Domains of crystalline anatase-TiO_2, tetragonal-ZrO_2, and cubic/tetragonal-HfO_2 were not observed by PXRD until heating the $TiO_2 \cdot 4SiO_2$, $ZrO_2 \cdot 4SiO_2$, and $HfO_2 \cdot 4SiO_2$ materials to temperatures in excess of 1000 °C under flowing oxygen, suggesting a high degree of initial homogeneity [68]. The crystallization of anatase in the $TiO_2 \cdot 3SiO_2$ material from $[(^tBuO)_2Ti\{\mu - O_2Si[OSi(O^tBu)_3]_2\}]_2$ occurred at a slightly lower temperature (800 °C), which is to be expected as the Ti/Si ratio is higher for this material [61]. Related work by Abe and co-workers on the thermolyses of $(^iPrO)Ti[OSi(O^tBu)_3]_3$ and $(^iPrO)_2Ti[OSi(O^tBu)_3]_2$ revealed crystallizations of anatase at 700–750 °C and 800–800 °C, respectively [133].

The relatively low decomposition temperatures of these group 4 siloxide-based molecular precursors allow the thermal conversions to take place in hydrocarbon solution (typically toluene or *n*-octane). The BET surface areas of the xerogels obtained after air-drying the resulting gels ranged from ca. 300 $m^2\,g^{-1}$ (for $TiO_2 \cdot 3SiO_2$) to 500 $m^2\,g^{-1}$ (for $ZrO_2 \cdot 4SiO_2$ and $HfO_2 \cdot 4SiO_2$) to 550 $m^2\,g^{-1}$ (for $TiO_2 \cdot 4SiO_2$) [61, 68]. Supercritical CO_2 drying of the wet $TiO_2 \cdot 4SiO_2$ gel yielded an aerogel with a moderately higher surface area of 675 $m^2\,g^{-1}$. The similarity of the surface areas suggests that use of the solution TMP method can provide xerogels (from conventional drying) with surface areas approaching those of aerogels (dried via supercritical methods) with similar compositions. Solid state ^{29}Si MAS NMR studies of the $ZrO_2 \cdot 4SiO_2$ xerogels show that the majority of the Si atoms are in Q^2 and Q^3 environments, which are attributed to the presence of $(ZrO)_2Si(OSi)_2$ and $ZrOSi(OSi)_3$ sites, respectively. This suggests a high degree of homogeneity [68]. The presence of a large number of M – O – Si heterolinkages would be expected to give rise to a highly acidic material [50]. Hammet acidity measurements [134] of these

xerogels determined a Hammet acidity function (H_o) to be between – 5.6 and – 8.2, which is consistent with high acidity and homogeneity [68].

Many useful gas and liquid phase oxidation reactions are catalyzed by Ti(IV)/SiO_2 materials, and therefore these materials have been extensively studied [135, 136]. Of particular interest are titania-silica gels studied by Hutter and Baiker as catalysts for various oxidation reactions [137]. Thus, we elected to examine Ti(IV)/SiO_2 materials produced by TMP methods in alkene partial oxidation reactions. The $TiO_2 \cdot 4SiO_2$ xerogel formed from $Ti[OSi(O^tBu)_3]_4$ is an active catalyst for the epoxidation of cyclohexene using cumene hydroperoxide (CHP) or *tert*-butyl hydroperoxide (TBHP) as the oxidant [126]. After 2 h in toluene at 65 °C, the yields of cyclohexene oxide were 37.8% (CHP) and 16.2% (TBHP) relative to the initial concentration of peroxide. The titanium-rich $TiO_2 \cdot 3SiO_2$ xerogel is also an active oxidation catalyst, yielding 14.1% (CHP) and 8.6% (TBHP) of cyclohexene oxide after 2 h [61]. The lower activity of the $TiO_2 \cdot 3SiO_2$ xerogel can be attributed to a greater degree of polymeric and octahedral Ti(IV) environments, which are known to be less active in the catalytic oxidation of alkenes [138–140]. Another interesting use of molecular precursors of the type described here was reported by Narula et al., whereby $(^tBuO)_3TiOSi(O^tBu)_3$ was employed in CVD processes to generate anti-reflective coatings for glass [69].

Recently, Murugavel et al. have reported the use of cubic titanosiloxanes of the type $[RSiO_3Ti(O^iPr)]_4$ (R = 2,6 – $^iPr_2C_6H_3NSiMe_3$) as precursors to titanosilicate materials [141]. Interestingly, the reaction of $[RSiO_3Ti(O^iPr)]_4$ with $HOSi(O^tBu)_3$ did not yield the expected $[RSiO_3Ti(OSi(O^tBu)_3)]_4$, but rather the transesterification product $[RSiO_3Ti(O^tBu)]_4$. Thermolytic conversions to the $TiO_2 \cdot SiO_2$ materials were shown to begin at 140 °C (by TGA) and continue until 650 °C. Bulk conversion at 600–800 °C led to heterogeneous catalysts that gave ca. 11% yield of cyclohexene oxide (based on oxidant) after 24 h. These authors speculate that the low conversions result from the presence of small amounts of octahedral titanium centers (i.e., TiO_2) or catalytic decomposition of the peroxide.

4.1.3
Thermolytic Conversion of Group 5 Siloxide Precursors

The solid-state decomposition of $OV[OSi(O^tBu)_3]_3$ occurs with a precipitous weight loss at ca. 200 °C (as observed by TGA) and a final ceramic yield that is 10% less than the expected ceramic yield [79]. This discrepancy results from volatilization and loss of $HOSi(O^tBu)_3$. However, solution thermolyses of $OV[OSi(O^tBu)_3]_3$ in *n*-octane produce xerogels with an approximate composition of $V_2O_5 \cdot 6SiO_2$ (after drying) with a quantitative ceramic yield (i.e., with no loss of $HOSi(O^tBu)_3$) that have a BET surface area of 320 $m^2\ g^{-1}$.

The onset temperatures for decompositions of $(^tBuO)_3VOSi(O^tBu)_3$ and $(^tBuO)_2V[OSi(O^tBu)_3]_2$ are ca. 100 °C, with ceramic yields corresponding

closely to the predicted values [80]. Vanadia-silica materials formed via solid phase decompositions of $(^tBuO)_3VOSi(O^tBu)_3$ and $(^tBuO)_2V[OSi(O^tBu)_3]_2$ had surface areas of 30 and 170 $m^2 g^{-1}$, respectively, while xerogels formed via solution decompositions (toluene) had surface areas of 40 and 70 $m^2 g^{-1}$. The synthesis of V/Si/O single-source precursors with various oxidation states and silicon contents provided an opportunity to examine how these properties influence the nature of the final material [80]. Vanadia-silica xerogels generated by thermolysis of $OV[OSi(O^tBu)_3]_3$ in *n*-octane exhibited phase separation and formation of V_2O_5 nanocrystals at low temperatures (300 °C, in O_2). By comparison, vanadia-silica xerogels derived from solution thermolyses of the V(IV) precursors, $(^tBuO)_3VOSi(O^tBu)_3$ and $(^tBuO)_2V[OSi(O^tBu)_3]_2$, produced smaller nanocrystals of V_2O_5 at a reduced rate (requiring 400 °C, in O_2). This suggests that the initial materials derived from the V(IV) precursors are more homogeneous (by PXRD and TEM).

It is well known that VO_x/SiO_2 materials have important catalytic uses, often associated with partial oxidations. Conventional dehydrogenation of light alkanes proceeds only at high temperatures, where cracking and the deposition of carbon present serious problems. Alternatively, oxidative dehydrogenation (ODH) is thermodynamically favored at lower temperatures and does not suffer from coking, which decreases catalyst performance [142]. Given the high demand for propene in the production of polypropylene, acrylonitrile, and propene oxide, ODH has generated considerable attention as an alternative source of this valuable molecule [143]. Utilizing $OV[OSi(O^tBu)_3]_3$ and $Zr[OCMe_2Et]_4$, or $OV(O^tBu)_3$ and $Zr[OCMe_2Et]_4$, in cothermolytic TMP processes, a series of catalysts with varying vanadium content (2–33%) were prepared and tested for their catalytic efficiency for propane ODH [128, 130]. These new catalysts were compared to catalysts of similar stoichiometry that were prepared by conventional aqueous impregnation methods. The surface areas of the V/Zr/Si/O and V/Zr/O catalysts prepared via the cothermolytic route were high (up to 465 $m^2 g^{-1}$) and the intrinsic selectivities for propene reached values in excess of 95% at 400 °C. The presence of oligomeric tetrahedral vanadium sites appears to be critical for the more active compositions (10–18% vanadia). The V/Zr/O catalysts with 18–23% vanadia are as efficient as the most selective and active catalysts thus far reported for propane ODH, and are superior to other vanadium-based systems. Significantly, the impressive catalytic results and novel features for these vanadium-containing catalysts suggest that molecular-level control over structure evolution during calcination is possible, and can provide new generations of catalysts with enhanced performance.

The molecular precursors $(^iPrO)_2Ta[OSi(O^tBu)_3]_3$ and $(^iPrO)_2Nb[OSi(O^tBu)_3]_3$ decompose in the solid phase with a precipitous weight loss at ca. 200 °C [71, 83]. Solution thermolyses of these precursors in hydrocarbon solvents yield xerogels with compositions corresponding to $Nb_2O_5 \cdot 6SiO_2$ and $Ta_2O_5 \cdot 6SiO_2$ having BET surface areas of 500 and 450 $m^2 g^{-1}$, respec-

tively. Interestingly, co-thermolyses of $(^{i}PrO)_2Ta[OSi(O^{t}Bu)_3]_3$ with excess $HOSi(O^{t}Bu)_3$ readily yields more silica-rich tantala-silica materials with quantitative loss of isobutylene from both molecular precursors. This clearly suggests that Ta species catalyze the decomposition of $HOSi(O^{t}Bu)_3$ which is normally inert under the conditions employed. Calcination of the Nb/Si/O xerogel at 900 °C under flowing oxygen led to formation of domains of T – Nb_2O_5. Interestingly, domains of L – Ta_2O_5 were not observed by PXRD until after calcination of the Ta/Si/O materials at temperatures in excess of 1000 °C.

4.1.4
Thermolytic Conversion of Group 6 Siloxide Precursors

Chromia-silica materials are important catalysts for several reactions, including alkene polymerizations and alkane dehydrogenations [144–148]. In addition, several molybdenum-based materials are efficient catalysts for partial oxidation reactions of alkanes and alkenes [149–153]. Hence, the development of molecular precursors to well-defined chromia- and molybdena-silica materials represents an important goal in solid-state synthesis. Thermogravimetric analysis of $(^{t}BuO)_3CrOSi(O^{t}Bu)_3$ reveals a sharp mass loss initiated at ca. 100 °C, concurrent with a melting transition. A high surface area Cr/Si/O xerogel ($\sim 300\ m^2\ g^{-1}$) derived from the solution thermolysis of $(^{t}BuO)_3CrOSi(O^{t}Bu)_3$ exhibits higher activity (by a factor of 3) and selectivity (by 5%) for propane ODH than a Cr/Si/O material with a slightly higher surface area that is derived from the solid phase thermolysis of $(^{t}BuO)_3CrOSi(O^{t}Bu)_3$ [87]. Thus, specific conditions for the thermolyses play an important role in determining the properties of the final material.

Combinations of $(^{t}BuO)_3CrOSi(O^{t}Bu)_3$ and $Zr[OCMe_2Et]_4$ or $[Al(O^{t}Bu)_3]_2$ in cothermolytic TMP routes provides high surface area (from 150 to $450\ m^2\ g^{-1}$), amorphous Cr/Si/Zr/O or Cr/Si/Al/O xerogels with well-dispersed Cr centers, even after calcinations at 500 °C [129]. Some of these Cr/Si/M/O materials exhibit high intrinsic activities (among the highest known) for propylene formation in catalytic propane oxidative dehydrogenation reactions; however, their selectivities are low due to high rates of propylene combustion. In contrast, the Cr/Si/M/O materials were efficient catalysts for the dehydrogenation of propane (nonoxidative), some of which provide excellent selectivities for propylene formation (ca. 95%) at high propane conversions (ca. 35%). Observed differences in the nature of the Cr species in the various Cr/Si/M/O materials support the notion that chromate clusters are more effective for propane ODH while isolated sites are preferred for propane DH [129].

The solid phase decomposition of $Mo_2[O_2Si(O^{t}Bu)_2]_3$ occurs with an initial precipitous weight loss at ca. 200 °C (as observed by TGA) and a second event occurring gradually from 700 to 1050 °C attributed to the sublimation of MoO_3 [89]. The theoretical yield for the anticipated Mo(III)/Si/O ma-

terial (51.8%), is slightly lower than that observed experimentally after the first weight loss event (55.4%), suggesting oxidation of some Mo to form MoO_2 and/or MoO_3. The material is amorphous after heating under argon at 500 °C (by PXRD); however, heating at 1200 °C leads to formation of crystalline MoO_2 domains. Calcination of the Mo/Si/O material under flowing air results in loss of nearly all the Mo as MoO_3. The solid phase decomposition of $W_2(NHMe_2)_2[O_2Si(O^tBu)_2]_2[OSi(OH)(O^tBu)_2]_2$ occurs with an initial weight loss beginning at 50 °C followed by a precipitous loss at ca. 150 °C (by TGA) giving a ceramic yield of 53%, in agreement with that expected [89]. Powder X-ray diffraction analysis of the material after heating at 1200 °C under argon reveals the presence of crystalline W and WO_2.

The solid phase thermal decomposition of $Mo_2(O^tBu)_4[OSi(O^tBu)_3]_2$ initiates at ca. 100 °C [90]. As observed with $Mo_2[O_2Si(O^tBu)_2]_3$, heating the material formed from the solid phase decomposition of $Mo_2(O^tBu)_4[OSi(O^tBu)_3]_2$ at temperatures above 700 °C results in loss of all Mo as MoO_3.

The TGA trace for $MoO[OSi(O^tBu)_3]_4$ exhibits an initial weight loss starting at 50 °C and a precipitous loss at 80 °C. It is interesting to note that sublimation of MoO_3 was not observed, which suggests that $MoO[OSi(O^tBu)_3]_4$ may provide access to materials with enhanced thermal stability [92]. The TGA trace of $MoO_2[OSi(O^tBu)_3]_2$ exhibits a precipitous weight loss at ca. 70 °C and a ceramic yield at 400 °C (37.6%) that corresponds closely to formation of $MoO_3 \cdot 2SiO_2$ (36.3%) [92]. Unlike the mono-oxo complex, there is a second weight loss event between 650 and 1000 °C that appears to correspond to the sublimation of nearly all of the Mo as MoO_3. The differences in high temperature behavior of the various Mo/Si/O materials discussed here are not well understood at this time. Solution thermolyses of these oxo-containing Mo molecular precursors provide xerogels with surface areas ranging from 6 to 270 $m^2 g^{-1}$, depending upon the precursor employed [92]. The materials derived from these complexes do not contain well-dispersed metal centers, but instead exhibit phase-separated nanodomains of MoO_3. These Mo/Si/O xerogels were highly selective in the epoxidation of cyclohexene (> 95% for cyclohexene oxide) when TBHP was used as the oxidant; however, use of aqueous H_2O_2 as the oxidant drastically lowers the cyclohexene oxide selectivity. In related work with oxo-containing Mo and W species, Neumann and coworkers generated Mo/Si/O and W/Si/O materials via the synthetic intermediates $MO[OSi(O^tBu)_3]_4$ (M = Mo and W), which were not isolated or characterized [154].

4.1.5
Thermolytic Conversion of Group 8 Siloxide Precursors

Thermal decomposition of $Fe[OSi(O^tBu)_3]_3(THF)$ occurs at ca. 140 °C (by TGA) to provide a material with a lower ceramic yield (25.9%) than that calculated for $FeO_{1.5} \cdot 3SiO_2$ (30.7%), suggesting potential loss of $HOSi(O^tBu)_3$

as described earlier [71, 97]. Thermolysis of a toluene solution of Fe[OSi$(O^tBu)_3]_3$(THF) leads to formation of a gel. Drying and calcination of the gel under oxygen at 600 °C provides a high surface area (660 $m^2\ g^{-1}$) xerogel with a composition approaching $FeO_{1.5} \cdot 3SiO_2$. The xerogel remains amorphous (by PXRD) after calcination at 800 °C; however, calcination at 1000 °C leads to formation and phase separation of cristobalite (SiO_2) and hematite ($\alpha - Fe_2O_3$) [71].

4.1.6
Thermolytic Conversion of Siloxide Precursors of Groups 9–12

The Rh complexes $\{(cod)Rh[\mu - OSi(O^tBu)_3]\}_2$ and $\{(nbd)Rh[\mu - OSi(O^tBu)_3]\}_2$ thermally decompose primarily via loss of $HOSi(O^tBu)_3$ and formation of Rh metal particles, rendering them ineffective for use as precursors to Rh/Si/O materials; however, these complexes are potentially useful as sources of Rh nanoparticles or site-isolated Rh species via grafting methods [99].

Thermal decomposition of $[CuOSi(O^tBu)_3]_4$ in the solid phase begins at ca. 100 °C under argon (by TGA) and results in formation of an amorphous material until roughly 600 °C, at which temperature Cu metal was detected (by PXRD) [105]. Conversely, decomposition under oxygen led initially to a material with Cu^0 crystallites and small amounts of Cu_2O and CuO, and subsequent heating beyond 800 °C resulted in oxidation of all the copper to CuO.

The molecular precursor $\{Zn[OSi(O^tBu)_3]_2\}_2$ readily undergoes thermolysis to give zinc orthosilicate-silica composite materials ($Zn_2SiO_4 \cdot SiO_2$) with a facile weight loss beginning at 100 °C [107]. After the polymer was heated at 850 °C for 2 h, partial crystallization of Zn_2SiO_4 was observed, with complete crystallization occurring at 1100 °C. Interestingly, the TMP route offers a significant advantage over sol-gel processes for formation of Zn_2SiO_4, as sol-gel methods tend to form domains of ZnO as a side-product [155, 156].

As a result of its high luminescence efficiency, manganese-doped zinc orthosilicate has been widely used as a green-emitting phosphor in the display industry [157, 158]. Emission from this material is attributed to a d-level spin-forbidden transition for isolated Mn^{2+} ions. Traditionally, appropriate Zn_2SiO_4 : Mn materials are made through mechanical processing or high-temperature solid state reactions; however, it is difficult to obtain reliable emission intensities by such methods. In an effort to provide access to these materials via a more reliable route, cothermolyses of $[ZnOSiPh_2O]_n/[Mn(CH_2SiMe_3)_2]_m$ mixtures that provide manganese-doped Zn_2SiO_4 materials were employed. The resulting materials exhibit two photoluminescence emission bands centered at 535 (major) and 605 nm (minor). The observed photoluminescence decay lifetime of ca. 5 ms is typical for Zn_2SiO_4 : Mn phosphors [159].

4.1.7
Thermolytic Conversion of Group 13 Siloxide Precursors

Borosilicate materials with stoichiometries corresponding to $BO_{1.5} \cdot 2SiO_2$ and $BO_{1.5} \cdot 3SiO_2$ are formed from ^{t}BuOB[OSi(O^{t}Bu)$_3$]$_2$ and B[OSi(O^{t}Bu)$_3$]$_3$, respectively, in solution TMP methods [64]. However, in contrast to other tris(*tert*-butoxy)siloxide species, these boron-containing precursors exhibit melting and subsequent boiling behavior prior to thermolysis. Solution thermolyses proceed efficiently (via elimination of CH_2CMe_2 in the usual way) in the presence of a catalytic amount of $AlCl_3$ to form the appropriate $BO_{1.5} \cdot 2SiO_2$ and $BO_{1.5} \cdot 3SiO_2$ xerogels (upon drying) with surface areas of 48 and 590 $m^2\ g^{-1}$, respectively.

The aluminum tris(*tert*butoxy)siloxide species Al[OSi(O^{t}Bu)$_3$]$_3$(HO^{i}Pr) 1/2[Al(O^{i}Pr)$_3$]$_4$ and[(^{i}PrO)$_2$AlOSi(O^{t}Bu)$_3$]$_2$ readily decompose at low temperatures in the solid phase to form materials with stoichiometries corresponding to $Al_2O_3 \cdot 2SiO_2$ [111]. Solid phase decomposition of Al[OSi (O^{t}Bu)$_3$]$_3 \cdot$ THF also occurs at ca. 100 °C, giving a material corresponding to $1/2Al_2O_3 \cdot 3SiO_2$ [111]. Solution thermolyses of these precursors provide xerogels (after drying) exhibiting surface areas that range from 200–600 $m^2\ g^{-1}$. As previously noted, the TMP method has been used for generating several types of solid acid materials. For amorphous aluminosilicates, the chemical nature of the molecular precursor has a profound influence on the properties of the resultant solid. This is illustrated by studies of the $Al_2O_3 \cdot 2SiO_2$ xerogels derived from Al[OSi(O^{t}Bu)$_3$]$_3$(HO^{i}Pr)1/2[Al(O^{i}Pr)$_3$]$_4$ and [(^{i}PrO)$_2$AlOSi(O^{t}Bu)$_3$]$_2$ (both with Al/Si = 1) via solution thermolyses [111]. These two types of materials have very different microstructures and surface acidities, with the primary differences being that xerogels derived from Al[OSi(O^{t}Bu)$_3$]$_3$(HO^{i}Pr) $\cdot$ 1/2[Al(O^{i}Pr)$_3$]$_4$ have lower Brønsted acid site concentrations (0.8 ± 0.2 vs 2.3 ± 0.2 sites nm^{-2}), higher Lewis/Brønsted site ratios (1.6 vs. 1.0), and microstructures that more closely resemble that of mullite. The preexistence of only Al – O – Si linkages in [(^{i}PrO)$_2$AlOSi(O^{t}Bu)$_3$]$_2$ gives rise to more Brønsted acid sites, whereas the Al – O – Al linkages in the [Al(O^{i}Pr)$_3$]$_4$ component of Al[OSi(O^{t}Bu)$_3$]$_3$ (HO^{i}Pr) $\cdot$ 1/2[Al(O^{i}Pr)$_3$]$_4$ lead to lower Brønsted acidity and increased mullite character.

4.2
Thermolytic Conversion of Di(*tert*-butyl)phosphates

The following examples describing the thermolytic behavior of di(*tert*-butyl)phosphate complexes serve to demonstrate the utility of the TMP approach for synthesis of various phosphate materials.

Zinc phosphate networks based on ZnO_4 and PO_4 tetrahedra display a large structural diversity, and there have been reports of zincophosphate

frameworks that are microporous [160], layered [161], or 1-dimensional [162]. Our initial efforts in this area focused on the development of molecular precursors to Zn/P/O materials that would transform via low energy pathways to provide a versatile approach for the formation of novel zinc phosphate network materials. Upon heating $Zn_4(\mu_4-O)[O_2P(O^tBu)_2]_6$, this complex readily loses its hydrocarbon moieties in the usual manner (via elimination of CH_2CMe_2) at a low temperature (ca. 135 °C) to give a material corresponding to $Zn_4P_6O_{19}$ in quantitative yield [121]. Additional heating of the material at 300 °C gives one crystalline component (an unindexed phase of $Zn_2P_2O_7$), as observed by PXRD. Subsequent heating at 600 °C gives rise to domains of α– $Zn_2P_2O_7$ and β– $Zn(PO_3)_2$. The TGA trace for polymeric $\{Zn[O_2P(O^tBu)_2]_2\}_n$ reveals an abrupt weight loss at 125 °C, with the ceramic yield at 1000 °C within 0.1% of that expected for a material with the formula ZnP_2O_6. Heating this material at 800 °C produced domains of β– $Zn(PO_3)_2$ as the only crystalline phase (by PXRD).

Aluminophosphates ($AlPO_4$) and related materials are useful in a number of applications, including as catalysts and catalyst supports, abrasion resistant coatings, and materials with a low index of refraction [163, 164]. Considerable attention has been devoted to the development of methods for the generation of $AlPO_4$ materials, including the sol-gel route and the reaction of $AlCl_3$ with H_3PO_4 [165]. The TGA trace of $[Me_2AlO_2P(O^tBu)_2]_2$ revealed a precipitous weight loss at ca. 150 °C, and only isobutylene and methane were detected as volatile decomposition products by NMR spectroscopy [122]. Amorphous aluminophosphate xerogels derived from solution thermolyses of $[Me_2AlO_2P(O^tBu)_2]_2$ have BET surface areas approaching 320 $m^2\,g^{-1}$ after calcination at 600 °C. These xerogels remained amorphous until calcinations at 1200 °C, when the tridymite form of $AlPO_4$ was observed by PXRD. The TGA trace of $[Al(O^iPr)_2O_2P(O^tBu)_2]_4$ reveals a weight loss beginning near room temperature that continues gradually until 140 °C, after which it becomes precipitous [122]. Xerogels from solution thermolyses of $[Al(O^iPr)_2O_2P(O^tBu)_2]_4$ also have relatively high BET surface areas (290 $m^2\,g^{-1}$) after calcination at 600 °C. As with xerogels derived from $[Me_2AlO_2P(O^tBu)_2]_2$, those from $[Al(O^iPr)_2O_2P(O^tBu)_2]_4$ remain amorphous until the tridymite form of $AlPO_4$ is observed by PXRD at 1200 °C.

Thermolyses of the $Mo_2(NMe_2)_2[\mu-O_2P(O^tBu)_2]_2[OP(O)(O^tBu)_2]_2$ isomers in the solid phase are similar and are characterized by a precipitous mass loss starting at ca. 150 °C and leading to a ceramic yield at 1000 °C (ca. 44%) that approaches that of $2MoO_{1.5}\cdot 2P_2O_5$ (46.9%) and more closely than that for $2MoO_3\cdot 2P_2O_5$ (51.2%), suggesting that the molybdenum exists in a reduced state [90]. Thermolysis of a toluene solution of $Mo_2(NMe_2)_2[\mu-O_2P(O^tBu)_2]_2[OP(O)(O^tBu)_2]_2$ results in formation of a xerogel (upon drying) with a surface area of 165 $m^2\,g^{-1}$ [90]. Interestingly, the uncalcined Mo/P/O xerogel exhibits IR, ^{31}P MAS NMR, and DRUV-vis features that are indicative of retention of the bridging phos-

phate groups, suggesting that structural features of the molecular precursor are transferred to the final material. Propane ODH studies using this Mo/P/O xerogel as the catalyst led to moderate activity, but poor selectivity. Use of $Bi[OSi(O^tBu)_3]_3$ in solution cothermolytic TMP methods with $Mo_2(NMe_2)_2[\mu - O_2P(O^tBu)_2]_2[OP(O)(O^tBu)_2]_2$ gives rise to Bi/Mo/P/Si/O xerogels (upon drying) that have high surface areas ($380–500\ m^2\ g^{-1}$), even after calcinations at 300 °C (up to $360\ m^2\ g^{-1}$) [90]. The Bi/Mo/P/Si/O materials with moderate amounts of Bi exhibit significantly increased selectivity for propylene in propane ODH reactions versus the Mo/P/O xerogels; however, larger quantities of Bi lead to no appreciable reaction [90].

Murugavel and co-workers have recently reported a series of copper, manganese, and cadmium di(*tert*-butyl)phosphates that have been used as molecular precursors to metal phosphate materials. For example, monomeric, tetrameric, and polymeric Cu di(*tert*-butyl)phosphate complexes with ancillary pyridine ligands have been prepared [166]. Regardless of which precursor is employed, heating at 500 °C gives mainly the pyrophosphate $Cu_2P_2O_7$ and small amounts of the metaphosphate $Cu(PO_3)_2$ (by PXRD). Other di(*tert*-butyl)phosphate species generated by the Murugavel group include the single coordination polymers $[M(O_2P(O^tBu)_2)_2]_n$ (M = Mn, Cu) and $[M(O_2P(O^tBu)_2)_2(H_2O)]_n$ (M = Cd) from the reaction of $M(OAc)\cdot xH_2O$ with $HOP(O)(O^tBu)_2$ [167]. Interestingly, for formation of the manganese phosphate precursor, if the reaction is not carried out in the presence of a base, an oxo-centered tetranuclear cluster $Mn_4(\mu_4 - O)[O_2P(O^tBu)_2]_6$, analogous to $Zn_4(\mu_4 - O)[O_2P(O^tBu)_2]_6$, is formed. Thermal decompositions of the $[M(O_2P(O^tBu)_2)_2]_n$ (M = Mn, Cu) polymers occur at ca. 150–200 °C, whereas decomposition of $[Cd(O_2P(O^tBu)_2)_2(H_2O)]_n$ begins at 40–70 °C (with loss of water) and then continues at 140–170 °C.

4.3 Thermolytic Conversion of $L_nM\{OB[OSi(O^tBu)_3]_2\}_x$ Molecular Precursors

The $-OB[OSi(O^tBu)_3]_2$ ligand has provided species of the form $L_nM\{OB[OSi(O^tBu)_3]_2\}_x$ that are viable molecular precursors to M/B/Si/O materials. However, the chemistry of this ligand appears to be sensitive to the ancillary ligands on the associated metal, with ligand transfer to the boron center (sometimes accompanied by siloxide transfer from boron to the metal) being a primary pathway for decomposition [64, 90].

For example, the initial stages of the solid phase decompositions of $Et_2NM\{OB[OSi(O^tBu)_3]_2\}_3$ (M = Zr, Hf) complexes are quite similar, with mass loss beginning at ca. 100 °C and a maximum rate of loss occurring at ca. 165 °C [91]. The ceramic yields for $Et_2NZr\{OB[OSi(O^tBu)_3]_2\}_3$ closely correspond to that calculated for a material with the composition $3BO_{1.5}\cdot 6SiO_2\cdot ZrO_2$ (32.2%). In contrast, the ceramic yield after solid phase decomposition of $Et_2NHf\{OB[OSi(O^tBu)_3]_2\}_3$ is 23.0% at 500 °C, which is significantly lower

than that calculated for $3BO_{1.5} \cdot 6SiO_2 \cdot HfO_2$ (35.3%) and suggests that the conversion may be complicated by other processes.

4.4
Thermolytic Conversion of Mixed Ligand Species

Silicoaluminophosphates (SAPOs) are a class of primarily microporous solid acids that have been explored for use in a variety of catalytic applications, the most prominent being the transformation of methanol to olefins [168]. Typical SAPO preparations involve hydrothermal methods employing organic templates. The TMP method would seem to be well-suited for the preparation of new types of SAPO materials with potentially unique properties. Toward that end, the decomposition of the first molecule to contain Si – O – Al – O – P – O – Al – O – Si linkages, $[(^tBuO)_3SiO]_2Al[(\mu - O)_2P(O^tBu)_2]_2Al(Me)OSi(O^tBu)_3$, proceeds as expected with elimination of CH_2CMe_2 and CH_4, as shown by solution NMR analysis [123]. The TGA trace of this SAPO single source molecular precursor reveals a ceramic yield of 32.3%, which corresponds closely to that expected for $Al_2P_2Si_2O_{14}$ (33.2%). Solution thermolyses (toluene) lead to formation of gels that form high surface area SAPO xerogels ($> 500\,m^2\,g^{-1}$) upon drying. The surface acidity of this material was determined to correspond to 5.3 ± 0.2 total sites nm^{-2} ($2.0 \pm 0.2\,nm^{-2}$ of "OH" sites and $3.3 \pm 0.3\,nm^{-2}$ of Lewis acid sites), using a combination of NH_3 temperature programmed desorption and titration of the material with $Mg(CH_2Ph)_2 \cdot 2THF$ [123].

Other single source molecular precursors containing multiple oxygen-rich ligand types are based upon the triply-bonded dimolybdenum fragment, $Mo_2(NMe_2)_2[OSi(O^tBu)_3]_2[\mu - O_2P(O^tBu)_2]_2$ and $Mo_2(NMe_2)_2OB[OSi\{(O^tBu)_3\}_2]_2[\mu - O_2P(O^tBu)_2]_2$. Unfortunately, $Mo_2(NMe_2)_2OB[OSi\{(O^tBu)_3\}_2]_2[\mu - O_2P(O^tBu)_2]_2$ exhibits a complicated decomposition, both in solution and in the solid phase, and does not appear to be well suited as a precursor to bulk materials [90]. On the other hand, this complex may be used as a molecular model for Mo – O – P and Mo – O – B oxide materials, and as a source of isolated Mo_2 fragments via grafting reactions. In contrast, the $Mo_2(NMe_2)_2[OSi(O^tBu)_3]_2[\mu - O_2P(O^tBu)_2]_2$ species are very effective as molecular precursors with solid phase decompositions initiating at ca. 150 °C [90]. Solution phase conversions to form xerogels (upon drying) provide materials that exhibit high surface areas ($> 250\,m^2\,g^{-1}$) and interesting structural features, resembling those of the starting precursor. Calcination of the xerogel at 300 °C leads to pore collapse and a significant reduction in the surface area (to $< 5\,m^2\,g^{-1}$).

5
TMP Routes to Mesoporous, Multicomponent Oxides

Synthetic control over the nanostructure of advanced materials is an important objective in materials research [169]. This challenge has been met with intense research efforts in the template-directed synthesis of mesoporous materials, initially sparked by scientists at Mobil Corp by their preparation of MCM materials [170]. The synthesis of this class of silica-based materials, having well-defined hexagonal pore structures (1–5 nm pore radii), was achieved using long chain quaternary ammonium surfactants as structure-directing agents under aqueous conditions. In another groundbreaking report, Stucky and co-workers described the preparation of mesoporous SBA silicas via a templating strategy employing nonionic poly(alkylene oxide) block copolymers in conjunction with sol-gel hydrolyses of silicon alkoxides [171]. Although a wide variety of template-directed mesoporous silicas have been isolated, relatively few non-silica oxides with mesoporous structures have been reported. Pinnavaia and co-workers were able to achieve some structural control over a non-silica material via hydrolysis of aluminum alkoxide precursors in the presence of nonionic block copolymers under neutral solvent conditions, to obtain mesoporous alumina with a worm-hole type pore structure [172]. Additionally, Stucky et al. have used the hydrolyses of metal chlorides in ethanolic solvents in the presence of block copolymer templates to produce a variety of large-pore metal oxides (TiO_2, ZrO_2, WO_3) with semicrystalline frameworks [173, 174]. The Stucky group also used this method to synthesize a few mixed-metal oxides by combining two metal chlorides (e.g., $SiCl_4$ and $TiCl_4$) with an ethanol solution of the block copolymer. Unfortunately, the use of independent precursors in cohydrolysis methods leads to formation of M – O – M homolinkages, as discussed previously.

The use of poly(alkylene oxide) block copolymer templates as structure-directing agents is readily incorporated into the TMP method for the preparation of new mesoporous materials with complex compositions. For example, the use of block copolymer templates with molecular precursors in nonpolar solvents has yielded a series of mesoporous, multicomponent oxides with the following compositions: $ZrO_2 \cdot 4SiO_2$, $Ta_2O_5 \cdot 6SiO_2$, $Fe_2O_3 \cdot 6SiO_2$, $AlPO_4$, $BO_{1.5} \cdot 2SiO_2$, $BO_{1.5} \cdot 3SiO_2$, and $Si_2Al_2P_2O_{14}$ [64, 123–125]. These materials have high surface areas, homogeneous dispersions of elements, and thick framework walls. The pore structures tend to be of the "worm-hole" type, similar to those observed by Pinnavaia [172]. Notably, the relatively narrow pore size distributions and PXRD data clearly indicate the presence of long-range nanostructural ordering. Figure 11 compares the pore size distributions and the transmission electron microscopy (TEM) images for a xerogel formed via solution decomposition of $Zr[OSi(O^tBu)_3]_4$, and a mesostructured material formed from $Zr[OSi(O^tBu)_3]_4$ in the presence of an organic

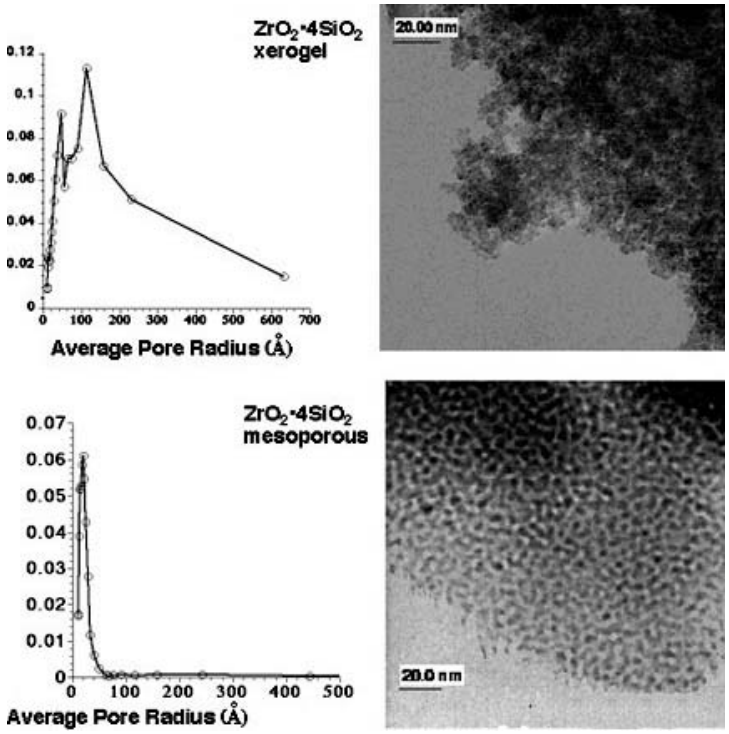

Fig. 11 Pore size distributions and TEM images of $ZrO_2 \cdot 4SiO_2$ materials formed from $Zr[OSi(O^tBu)_3]_4$. The *upper portion* shows a xerogel and the *bottom portion* shows a mesostructured material

block copolymer template [125]. Further evidence for the high degree of homogeneity was obtained via an EDX HR-TEM study of the mesoporous $ZrO_2 \cdot 4SiO_2$ material. This study revealed that the mesoporous material has a constant 4 : 1 Si/Zr ratio throughout, using a 10 Å probe scanning at 35 Å intervals [125]. The templating mechanism for these mesoporous materials is unknown, since little is understood concerning the phase behavior of poly(alkylene oxide) block copolymers in nonaqueous solvents. This variation of the TMP route to form mesoporous materials allows access to materials with a wide-range of compositions and potential catalytic applications.

6
TMP Routes to Hybrid Inorganic/Organic Materials

Hybrid inorganic/organic materials have unique properties that result from a combination of the inorganic and organic components [175–178]. Much effort has gone into the development of hybrid inorganic/organic materials via

the sol-gel route. For example, Sanchez and co-workers have made hybrid materials derived from combinations of polydimethylsiloxanes and various metal alkoxides (Al, Ge, Sn, Ti, Zr, Nb, Ta, etc.) [179]. In addition, Wilkes et al. have used various oligomers of poly(tetramethylene oxide), poly(arylene ether phosphine oxide), poly(arylene ether ketone), and poly(arylene ether sulfone) with alkoxides of titanium, zirconium, and aluminum to generate hybrid inorganic/organic materials [180–183]. Many of these examples involve the entrapment of organic or siloxane polymers by a growing inorganic network upon hydrolysis. Ideally, covalent linkages between the organic and inorganic fragments would be formed. As with the formation of mixed oxides via hydrolytic sol-gel methods, an inherent problem for the generation of covalently linked hybrids stems from the different rates of hydrolysis for the various precursors employed. Common solutions to this problem which allow for improved homogeneity involve pre-hydrolysis of the slower reacting component or lowering the activity of the faster reacting component by altering its structure (usually increasing the bulk of ligands). Another viable option for the generation of hybrid materials with improved homogeneity is the use single-source precursors, as demonstrated by Schubert et al. for the synthesis of hybrid inorganic/organic titania-silica materials [184].

The TMP cothermolytic method has been modified to create new metal oxide-silica hybrid inorganic/organic materials. For example, the molecular precursor $Zr[OSi(O^tBu)_3]_4$ was co-thermolyzed with $(EtO)_3Si(CH_2)_nSi(OEt)_3$ ($n = 1,\ 2$) or $(EtO)_3Si(C_6H_4)_nSi(OEt)_3$ ($n = 1,\ 2$; C_6H_4 = 1,4-phenylene) in nonpolar media [185]. The resulting gels form amorphous xerogels (upon drying) that are homogeneous and exhibit high surface areas (up to 750 $m^2\ g^{-1}$). Additionally, the organic bridging groups were spectroscopically determined to remain intact (using ^{13}C and ^{29}Si MAS NMR and DRUV-vis techniques). Perhaps the most interesting feature of these materials is their unique surface properties, as examined by atomic force microscopy (AFM).

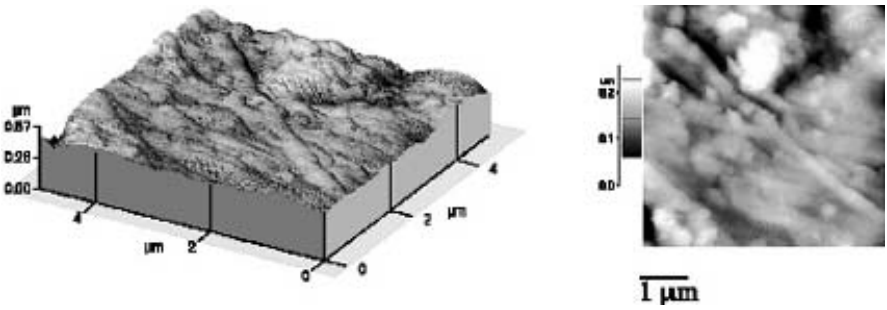

Fig. 12 AFM images of a hybrid inorganic-organic xerogel formed via cothermolytic TMP methods using $Zr[OSi(O^tBu)_3]_4$ and $(EtO)_3SiCH_2Si(OEt)_3$. The *left image* shows a topographical view while that on *the right* is a top view

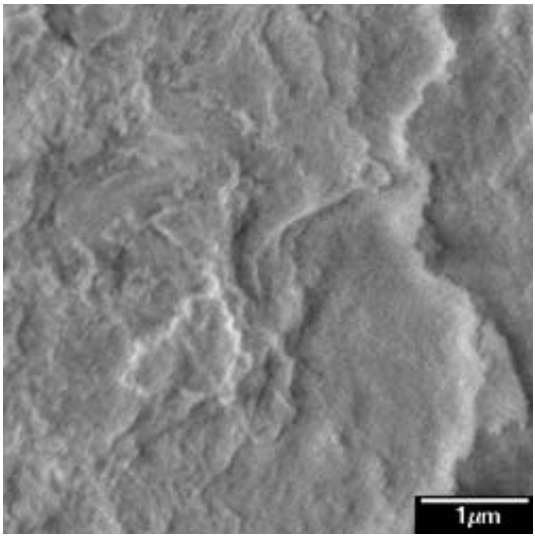

Fig. 13 SEM image of a hybrid inorganic-organic xerogel formed via cothermolytic TMP methods using $Zr[OSi(O^tBu)_3]_4$ and $(EtO)_3SiCH_2Si(OEt)_3$

The surface properties were probed by examining the adhesive forces between the silicon nitride AFM tip and the surface of the hybrid materials (Fig. 12). A uniformly high adhesion force was observed for the parent $ZrO_2 \cdot 4SiO_2$ xerogel, which indicates the presence of a surface water layer on this hydrophilic support. Conversely, the surface adhesive properties of the hybrid materials are substantially lower, a result of the increased hydrophobicity imparted by their organic-rich nature. Scanning electron microscopy (SEM) was also used to examine the surface morphology of these new hybrid materials (Fig. 13).

7
CVD Applications of Single-Source Molecular Precursors

Some of the tris(*tert*-butoxy)siloxide complexes can be sublimed, suggesting that they may be appropriate for use in CVD studies. For example, $[CuOSi(O^tBu)_3]_4$ sublimes at 120–140 °C (0.001 mm Hg), which makes it a suitable candidate for MOCVD applications. Vapor transport of this molecular precursor was accomplished by sublimation under vacuum onto a glass slide preheated at 450 °C. After 30 min, the slide was covered with a smooth, copper-colored film [105]. By varying the deposition time, the film thicknesses ranged from 200 nm to 6 μm. Rapid heating of the sample to 300 °C caused complete decomposition, and further heating to 600 °C produced a film containing both Cu^0 and Cu_2O (by PXRD).

The volatility of $[Me_2AlO_2P(O^tBu)_2]_2$ and $[Al(O^iPr)_2O_2P(O^tBu)_2]_4$ make these complexes good reagents for CVD routes to $AlPO_4$ thin films. Indeed, thin films (< 1 μm) can be prepared from these complexes at 200 °C using a simple CVD process [122]. The homogenous films that form are smooth, dense, and transparent. Previously, $AlPO_4$ thin films were prepared from solutions of $AlCl_3$ and H_3PO_4; however, the CVD route using thermolytic molecular precursors is more versatile, as it can be used to form films on substrates that are acid-sensitive [122].

Many of the molecular precursors described in this review are not suitable as precursors for CVD methods (due to their thermal sensitivity and lack of volatility). Gordon and co-workers have recently developed a simple method for the deposition of metal silicate films using chemistry related to that described above [186]. The key aspect of Gordon's approach is that volatile species (essentially reagents for the formation of appropriate siloxide complexes) are simultaneously introduced onto a heated substrate. For example, $Hf(NMe_2)_4$ vapor was allowed to react with $HOSi(O^tBu)_3$ vapor at substrate temperatures from 250 °C to 350 °C, to form films of hafnium silicate glass with silicon/hafnium ratios ranging from 2 : 1 to 3 : 1, depending on deposition conditions [186]. It is likely that M – O – Si linkages are formed via elimination of the appropriate amine and that the tris(*tert*-butoxy)siloxide ligands subsequently decompose in the usual manner, thus giving rise to the observed M/Si/O films. It is believed that this CVD method could be adapted for many volatile metal alkylamides.

8
Molecular Precursor Grafting Methods

An exciting area of research has emerged in recent years, which involves the grafting of organometallic or inorganic molecular species onto the surface of an oxide support to form well-defined catalytic sites [40–47, 187–189]. Along these lines, the TMP route may be used to introduce site-isolated metal centers onto the surface of an oxide support (e.g., aluminosilicates, silica, etc.) via a grafting reaction. The general grafting method is illustrated in Scheme 2. The first step involves reaction of the precursor with surface Si – OH sites via a protonolysis reaction. For alkoxy(siloxy) precursors of the type $M[OSi(O^tBu)_3]_n$, the protonolysis reaction can proceed via loss of HO^tBu and/or (more commonly) $HOSi(O^tBu)_3$ to yield species bound to the surface through Si – O-(surface) and/or M – O-(surface) linkages, respectively. Calcination (< 200 °C) then converts these species into $MO_x \cdot nSiO_2$ or $MO_x(n-1)SiO_2$ surface-supported sites after loss of isobutylene in the usual way. Upon loss of CH_2CMe_2 additional Si – OH sites are formed, allowing formation of additional M – O – Si – O-surface linkages that provide a stable anchor for the metal center.

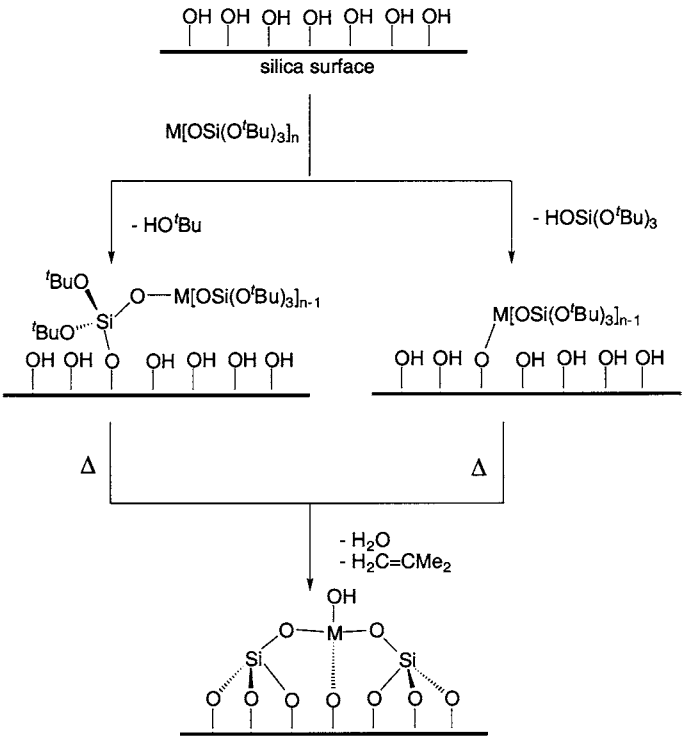

Scheme 2

This TMP grafting method offers the potential for molecular-level control over the structure of the catalytic site via the generation of site-isolated catalysts. The grafting reactions may be easily monitored by solution NMR and IR spectroscopies to provide information about the nature of the grafted species. Also, since the thermolytic conversion occurs through a kinetically controlled, low-temperature pathway, the oxygen-rich molecular precursors can introduce reactive (high-energy) metal centers onto the substrate (e.g., site-isolated, unusual oxidation states, etc.).

8.1 Site-Isolated Ti(IV) Centers

The method outlined above was initially investigated for the introduction of isolated Ti(IV) sites onto a silica substrate for use in selective oxidation catalysis. Since the development of a silica-supported Ti(IV) epoxidation catalyst by Shell in the 1970s, titania-silica materials have attracted considerable attention [135, 136]. Many other titania-silica materials have been studied in this context including, but not limited to, TS1 and TS2 (titanium-substituted molecular sieves), Ti-β (titanium-substituted zeolite),

and TiSBA – 15 and TiMCM – 41 (titanium substituted into or grafted onto mesoporous silica) [190–193]. Use of $Ti[OSi(O^tBu)_3]_4$ as a source of Ti(IV) for the introduction of site-isolated metal centers provides catalysts that are highly active and selective in the oxidation of cyclohexene to cyclohexene oxide using cumene hydroperoxide as the oxidant [126, 194]. These catalysts are more active than the Shell catalyst derived from treatment of silica with $Ti(O^iPr)_4$.

Further investigations of the Ti(IV) system focused on the influence of the siloxy ligands on the grafting chemistry and catalytic performance of the resulting catalysts. These studies involved use of $Ti[OSi(O^tBu)_3]_4$, $^iPrOTi[OSi(O^tBu)_3]_3$, and $(^tBuO)_3TiOSi(O^tBu)_3$ with mesoporous silica materials, and showed that fewer siloxide ligands in the precursor generally lead to higher Ti(IV) loadings (presumably a result of the steric bulk of the siloxy ligand) [195]. However, the tris(*tert*-butoxy)siloxide ligands provide an enhancement of the catalytic selectivity and activity, such that the optimum precursor was $(^iPrO)Ti[OSi(O^tBu)_3]_3$. In a further study of this system, the effect of the nuclearity of the molecular precursor was evaluated by grafting the dimeric molecular precursor $[(^tBuO)_2Ti\{\mu - O_2Si[OSi(O^tBu)_3]_2\}]_2$ onto a mesoporous silica surface [61]. The resultant catalyst exhibited a comparable activity, and a slightly better selectivity, than the catalysts derived from grafting monomeric $(^iPrO)Ti[OSi(O^tBu)_3]_3$.

The viability of using site-isolated Ta(V) centers for cyclohexene epoxidation was explored by grafting $(^iPrO)_2Ta[OSi(O^tBu)_3]_3$ onto a mesoporous silica material [83]. After calcinations, the material formed is less active and selective in the oxidation of cyclohexene than the surface-supported Ti(IV) catalysts using organic peroxides; however, the site-isolated Ta(V) catalysts are more active under aqueous conditions.

8.2 Site-Isolated Fe(III) Centers

The iron-containing zeolite FeZSM-5 has attracted considerable attention as a catalyst for the oxidation of hydrocarbons [196, 197]. The active site of this catalyst has been hypothesized by some to be isolated Fe(III) centers substituted in the aluminosilicate framework. Using the TMP grafting approach, $Fe[OSi(O^tBu)_3]_3(THF)$ can be grafted onto the surface of a mesoporous silica (SBA-15) [97]. Spectroscopic evidence (DRUV-vis and EPR) suggests that the pseudotetrahedral Fe(III) centers remain mononuclear and site-isolated, even after calcination. These catalysts exhibited high selectivity for the oxidation of alkanes, alkenes, and arenes using hydrogen peroxide.

8.3
Site-Isolated Cu(I) Centers and Cu Nanoparticles

The molecular precursor $[CuOSi(O^tBu)_3]_4$ was grafted onto a mesoporous silica support (SBA-15) to study the generation of tailored Cu sites for industrially relevant catalytic applications (e.g., the partial oxidation of MeOH) [198]. For comparison, $[CuO^tBu]_4$ was also grafted onto the SBA-15 support. The resulting surface structures were characterized using detailed XAS (XANES and EXAFS) analyses, with the starting molecular precursors being among the models used to identify the Cu sites. Use of $[CuOSi(O^tBu)_3]_4$ as the Cu source gives only isolated Cu(I) sites (100% of the Cu detected) for the uncalcined materials, with site isolation being maintained after heating at 400 °C (up to 88% of the detected Cu). In contrast, use of $[CuO^tBu]_4$ in identical grafting and heating procedures provides isolated tetrameric Cu(I) species (with Cu – O – Si linkages) in uncalcined samples (100% of the Cu detected) and Cu metal nanoparticles after heating (100% of the Cu detected). The differences in the surface structures after thermal treatment can be primarily attributed to the presence of the remaining $-OSi(O^tBu)_3$ ligands in the material from $[CuOSi(O^tBu)_3]_4$ and the extra stabilization that they provide by formation of Cu – O – Si – O-surface linkages. Thus, proper selection of the metal source and treatment conditions can lead to sites with tailored structures [198].

9
Summary and Future Directions

This contribution provides an overview of the TMP method and its various applications. The synthetic methods described here offer some advantages over more established routes for the generation of multi-component oxide materials for use as (for example) heterogeneous catalysts, refractory materials, catalyst supports, and electronic materials. The well-defined molecular precursors allow control over the stoichiometry, nanostructure, elemental dispersion, and surface structure, depending upon the experimental parameters employed. The preexisting M – O – E linkages in these single-source precursors promote maximum homogeneity and elemental dispersion in the final materials. Use of nonaqueous solvents for the generation of materials is often beneficial, in that the presence of excess water can have a strong influence over the structures that form, causing pore collapse and redistribution of elements to form inhomogeneous materials. The molecular precursors may serve as excellent molecular models for oxide-supported catalytic sites, given their M – O – E heterolinkages and their oxygen-rich nature. A wide range of stoichiometries can be accessed via the cothermolytic TMP approach, whereby two or more molecular precursors are simultaneously utilized.

The continued development of new single-source molecular precursors should lead to increasingly complex mixed-element oxides with novel properties. Continued work with grafting methods will provide access to novel surface structures that may prove useful for catalytic applications. Use of molecular precursors for the generation of metal nanoparticles supported on various oxide supports is another area that shows promise. We expect that the thermolytic molecular precursor methods outlined here will contribute significantly to the development of new generations of advanced materials with tailored properties, and that it will continue to provide access to catalytic materials with improved performance.

Acknowledgements The authors are extremely grateful for the support of this work by the Office of Basic Energy Sciences, Chemical Sciences Division, of the U. S. Department of Energy under Contract No. DE-AC03-76SF00098, and for the enthusiastic efforts of the many coworkers who have contributed to this research. The contributions of our collaborator, Professor A.T. Bell of the Chemical Engineering Department at the University of California, Berkeley, are also appreciated [79, 81, 97, 130, 198].

References

1. Uhlmann DR, Ulrich DR (1992) (eds) Ultrastructure Processing of Advanced Materials. Wiley, New York
2. Narula CK (1995) Ceramic Precursor Technology and Its Applications. Marcel Dekker, New York
3. Jolivet J-P (2000) Metal Oxide Chemistry and Synthesis. From Solution to Solid State. Wiley, Chichester
4. Bowes CL, Ozin GA (1996) Adv Mater 8:13
5. Amabilino DB, Stoddart JF (1995) Chem Rev 95:2725
6. Stein A, Keller SW, Mallouk TE (1993) Science 259:1558
7. Cowley AH, Jones RA (1989) Angew Chem Intl Ed Engl 28:1208
8. Chaput F, Lecomte A, Dauger A, Boilot JP (1989) Chem Mater 1:199
9. Apblett AW, Warren AC, Barron AR (1992) Chem Mater 4:167
10. Chandler CD, Roger C, Hampden-Smith MJ (1993) Chem Rev 93:1205
11. Bradley DC (1994) Polyhedron 13:1111
12. Klabunde KJ (2001) (ed) Nanoscale Materials in Chemistry. Wiley, New York
13. Corma A (1997) Chem Rev 97:2373
14. Thomas JM (2001) Stud Surf Sci Catal 140:1
15. Arakawa H, Aresta M, Armor JN, Barteau MA, Beckman EJ, Bell AT, Bercaw JE, Creutz C, Dinjus E, Dixon DA, Domen K, DuBois DL, Eckert J, Fujita E, Gibson DH, Goddard WA, Goodman DW, Keller J, Kubas GJ, Kung HH, Lyons JE, Manzer LE, Marks TJ, Morokuma K, Nicholas KM, Periana R, Que L, Rostrup-Nielson J, Sachtler WHM, Schmidt LD, Sen A, Somorjai GA, Stair PC, Stults BR, Tumas W (2001) Chem Rev 101:953
16. Thomas JM, Terasaki O, Gai PL, Zhou W, Gonzalez-Calbet J (2001) Acc Chem Res 34:583
17. Bazin D, Mottet C, Treglia G (2000) Appl Catal A 200:47

18. Bowker M (1998) The Basis and Applications of Heterogeneous Catalysis. Oxford University Press, New York
19. Somorjai GA, Yang MX (1997) J Mol Catal A 115:389
20. He X, Antonelli D (2002) Angew Chem Intl Ed Engl 41:214
21. Trindade T, O'Brien P, Pickett NL (2001) Chem Mater 13:3843
22. Rolison DR, Dunn B (2001) J Mater Chem 11:963
23. Schueth F (2001) Chem Mater 13:3184
24. Ma Y, Tong W, Zhou H, Suib SL (2000) Microporous Mesoporous Mater 37:243
25. Ying JY, Mehnert CP, Wong MS (1999) Angew Chem Intl Ed Engl 38:56
26. Huo Q, Zhao D, Feng J, Weston K, Buratto SK, Stucky GD, Schacht S, Schüth F (1997) Adv Mater 9:974
27. Murray CB, Kagan CR, Bawendi MG (2000) Annu Rev Mater Sci 30:545
28. Aiken JD III, Finke RG (1999) J Molec Catal A: Chem 145:1
29. Alivisatos AP (1996) Science 271:933
30. Aiken JD III, Lin Y, Finke RG (1996) J Molec Catal A: Chem 114:29
31. Thomas JM (1999) Angew Chem Intl Ed Engl 38:3588
32. Thomas JM (2001) Top Catal 15:85
33. Volta J-C (2001) Top Catal 15:121
34. Grasselli RK (2001) Top Catal 15:93
35. Millet J-MM, Védrine JC (2001) Top Catal 15:139
36. Thomas JM, Sankar G, Klunduk MC, Attfield MP, Maschmeyer T, Johnson BFG, Bell RG (1999) J Phys Chem B 103:8809
37. Brinker CJ, Scherer GW (1990) Sol-Gel Science. Academic Press, Boston
38. Corriu RJP, Leclercq D (1996) Angew Chem Int Ed Engl 35:1421
39. Schubert U (1996) J Chem Soc, Dalton Trans 3343
40. Basset J-M, Lefebvre F, Santini C (1998) Coord Chem Rev 178:1703
41. Scott SL, Basset J-M (1994) J Mol Catal 86:5
42. Coperet C, Chabanas M, Petroff Saint-Arroman R, Basset J-M (2003) Angew Chem Intl Ed Engl 42:156
43. Coperet C, Maury O, Thivolle-Cazat J, Bassett J-M (2001) Angew Chem Intl Ed Engl 40:2331
44. Chabanas M, Baudouin A, Coperet C, Basset J-M (2001) J Am Chem Soc 123:2062
45. Rosier C, Niccolai GP, Basset J-M (1997) J Am Chem Soc 119:12408
46. Chabanas M, Vidal V, Coperet C, Thivolle-Cazat J, Basset J-M (2000) Angew Chem Intl Ed Engl 39:1962
47. Vidal V, Theolier A, Thivolle-Cazat J, Basset J-M (1997) Science 276:99
48. Gao X, Wachs IE (1999) Catal Today 51:233
49. Hutter R, Mallat T, Dutoit DCM, Baiker A (1996) Top Catal 3:421
50. Miller JB, Ko EI (1996) J Catal 159:58
51. Dutoit DCM, Schneider M, Baiker A (1995) J Catal 153:165
52. Miller JB, Johnston ST, Ko EI (1994) J Catal 150:311
53. Tanabe KJ (1970) Solid Acids and Bases; Their Catalytic Properties. Academic Press, New York
54. Grzybowska-Swierkosz B (2000) Top Catal 11:23
55. Trifirò F (1998) Catal Today 41:21
56. Bettahar MM, Costentin G, Savary L, Lavalley JC (1996) Appl Catal A 145:1
57. Jansen M, Guenther E (1995) Chem Mater 7:2110
58. Vioux A (1997) Chem Mater 9:2292
59. Abe Y, Kijima I (1969) Bull Chem Soc Jpn 42:1118
60. Miner CS Jr, Bryan LA, Hoylsz RP, Pedlow GW Jr (1947) Ind Eng Chem 39:1368

61. Brutchey RL, Mork BV, Sirbuly DJ, Yang P, Tilley TD (2005) J Mol Catal A 238:1
62. Goldwhite H, Saunders BC (1957) J Chem Soc 2409
63. Zwierzak A, Kluba M (1971) Tetrahedron 27:3163
64. Fujdala KL, Tilley TD (2003) Inorg Chem 42:1140
65. Terry KW (1993) PhD Thesis, University of California, San Diego
66. Kriesel JW, Tilley TD (2001) J Mater Chem 11:1081
67. Terry KW, Tilley TD (1991) Chem Mater 3:1001
68. Terry KW, Lugmair CG, Tilley TD (1997) J Am Chem Soc 119:9745
69. Narula CK, Varshney A, Riaz U (1996) Chem Vap Deposition 2:13
70. Gunji T, Kasahara T, Abe Y (1998) J Sol-Gel Sci Technol 13:975
71. Lugmair CG (1997) PhD Thesis, University of California, Berkeley
72. Ugina MA, Ovejero G, van Grieken R, Serrano DP, Camacho M (1994) J Chem Soc, Chem Commun 27
73. Liu Z, Davis R (1994) J Phys Chem 98:1253
74. Shraml-Marth M, Walther KL, Wokaun A, Handy BE, Baiker A (1992) J Non-Cryst Solids 143:93
75. Klein S, Weckhuysen BM, Martens JA, Majer WF, Jacobs PA (1996) J Catal 163:489
76. Klaas J, Schulz-Ekloff G, Jaeger NI (1997) J Phys Chem B 101:1305
77. Blasco T, Camblor MA, Fierro JLG, Perez-Pariente J (1994) Microporous Mater 3:259
78. Capel-Sanchez MC, Campos-Martin JM, Fierro JLG, de Frutos MP, Padilla Polo A (2000) Chem Commun 855
79. Rulkens R, Male JL, Terry KW, Olthof B, Khodakov A, Bell AT, Iglesia E, Tilley TD (1999) Chem Mater 11:2966
80. Fujdala KL, Tilley TD (2002) Chem Mater 14:1376
81. Rulkens R, Male JL, Terry KW, Olthof B, Khodakov A, Bell AT, Iglesia E, Tilley TD (1999) Chem Mater 11:2966
82. Morey M, Davidson A, Eckert H, Stucky G (1996) Chem Mater 8:486
83. Brutchey RL, Lugmair CG, Schebaum LO, Tilley TD (2005) J Catal 229:72
84. Wolczanski PT (1995) Polyhedron 14:3335
85. Bradley DC, Thomas IM (1959) J Chem Soc 3404
86. Terry KW, Gantzel PK, Tilley TD (1993) Inorg Chem 32:5402
87. Fujdala KL, Tilley TD (2001) Chem Mater 13:1817
88. Alyea EC, Basi JS, Bradley DC, Chisholm MH (1971) J Chem Soc A 772
89. Su K, Tilley TD (1997) Chem Mater 9:588
90. Fujdala KL, Tilley TD (2004) Chem Mater 16:1035
91. Fujdala KL (2003) PhD Thesis, University of California, Berkeley
92. Jarupatrakorn J, Tilley TD (2005) Chem Mater 17:1818
93. Huang M, DeKock CW (1993) Inorg Chem 32:2287
94. Kim G-S, Huffman D, DeKock CW (1989) Inorg Chem 28:1279
95. Gosink H-J, Roesky HW, Noltemeyer M, Schmidt H-G, Freire-Erdbrugger C, Sheldrick GM (1993) Chem Ber 126:279
96. Brisdon BJ, Mahon MF, Rainford CC (1998) J Chem Soc Dalton Trans 19:3295
97. Nozaki C, Lugmair CG, Bell AT, Tilley TD (2002) J Am Chem Soc 124:13194
98. Schmidbauer H, Richter W (1974) Chem Ber 107:2427
99. Jarupatrakorn J, Tilley TD (2004) Dalton Trans 17:2808
100. Vizi-Orosz A, Ugo R, Psaro R, Sironi A, Moret M, Zucchi C, Ghelfi F, Palyi G (1994) Inorg Chem 33:4600
101. McMullen AK, Tilley TD, Rheingold AL, Geib SJ (1990) Inorg Chem 29:2228
102. McMullen AK, Tilley TD, Rheingold AL, Geib SJ (1989) Inorg Chem 28:3772
103. Mehrotra RC (1983) Adv Inorg Chem Radiochem 26:269

104. Bradley DC, Mehrotra RC, Gaur DP (1978) Metal Alkoxides. Academic Press, London
105. Terry KW, Lugmair CG, Gantzel PK, Tilley TD (1996) Chem Mater 8:274
106. Greiser T, Weiss E (1976) Chem Ber 109:3142
107. Su K, Tilley TD, Sailor MJ (1996) J Am Chem Soc 118:3459
108. Hornbaker ED, Conrad F (1959) J Org Chem 24:1858
109. Murphy D, Sheehan JP, Spalding TR, Ferguson G, Lough AJ, Gallagher JF (1993) J Mater Chem 3:1275
110. Terry KW, Gantzel PK, Tilley TD (1992) Chem Mater 4:1290
111. Lugmair CG, Fujdala KL, Tilley TD (2002) Chem Mater 14:888
112. Apblett AW, Warren AC, Barron AR (1992) Can J Chem 70:771
113. Kijima I, Yamamoto T, Abe Y (1971) Bull Chem Soc Jpn 44:3193
114. Pouxviel JC, Boilot JP, Poncelet O, Hubert-Pfalzgraf LG, Lecomte A, Dauger A, Beloeil JC (1987) J Non-Cryst Solids 93:277
115. Chaput F, Lecomte A, Dauger A, Boilot JP (1989) Chem Mater 1:199
116. Terry KW, Su K, Tilley TD, Rheingold AL (1998) Polyhedron 17:891
117. Munowitz M, Jarman RH, Harrison JF (1992) Chem Mater 4:1296
118. Stucky GD, Phillips MLF, Gier TE (1989) Chem Mater 1:492
119. Thorn DL, Harlow RL (1992) Inorg Chem 31:3917
120. Lugmair CG, Tilley TD (1998) Inorg Chem 37:1821
121. Lugmair CG, Tilley TD, Rheingold AL (1997) Chem Mater 9:339
122. Lugmair CG, Tilley TD, Rheingold AL (1999) Chem Mater 11:1615
123. Fujdala KL, Tilley TD (2001) J Am Chem Soc 123:10133
124. Kriesel JW, Sander MS, Tilley TD (2001) Adv Mater 13:331
125. Kriesel JW, Sander MS, Tilley TD (2001) Chem Mater 13:3554
126. Coles MP, Lugmair CG, Terry KW, Tilley TD (2000) Chem Mater 12:122
127. McGeary MJ, Wedlich RC, Coan PS, Folting K, Caulton KG (1992) Polyhedron 11:2459
128. Rulkens R, Tilley TD (1998) J Am Chem Soc 120:9959
129. Fujdala KL, Tilley TD (2003) J Catal 218:123
130. Male JL, Niessen HG, Bell AT, Tilley TD (2000) J Catal 194:431
131. Tanabe KJ, Misono M, Ono Y, Hattori H (1989) New Solid Acids and Bases: Their Catalytic Properties. In: Delmon B, Yates JT (eds) Studies in Surface Science and Catalysis, Vol. 51. Elsevier, New York
132. Llanos ME, Lopez T, Gomez R (1997) Langmuir 13:974
133. Gunji T, Kasahara T, Abe Y (1998) J Sol-Gel Sci Tech 13:975
134. Bosman HJM, Kruissink EC, van der Spoel J, van der Brink F (1994) J Catal 148:660
135. Sheldon RA (1980) J Mol Catal 7:107
136. Shell Oil GB Patent 1249079
137. Hutter R, Mallat T, Baiker A (1995) J Catal 153:177
138. Sinclair PE, Sankar G, Catlow CRA, Thomas JM, Maschmeyer T (1997) J Phys Chem B 101:4232
139. Sinclair PE, Catlow CRA (1999) J Phys Chem B 103:1084
140. Marchese L, Gianotti E, Dellarocca V, Maschmeyer T, Rey F, Collucia S, Thomas JM (1999) Phys Chem Chem Phys 1:585
141. Murugavel R, Davis P, Shete VS (2003) Inorg Chem 42:4696
142. Kung HH (1994) Adv Catal 40:1
143. Thayer AM (1997) Chem Eng News 75:20
144. Clark A (1970) Catal Rev 3:145
145. McDaniel MP, Leigh CH, Wharry SM (1989) J Catal 120:170
146. Badayal JPS, Ruddick VJ (1998) J Phys Chem B 102:2991

147. Gorriz OF, Cadus LE (1999) Appl Catal A-General 180:247
148. Weckhuysen BM, Schoonheydt RA (1999) Catal Today 51:223
149. Liu HF, Liu RS, Liew KY, Johnson RE, Lunsford JH (1984) J Am Chem Soc 106:4117
150. Zhen KJ, Khan MM, Mak CH, Lewis KB, Somarjai GA (1985) J Catal 94:501
151. Ruth K, Burch R, Kieffer R (1998) J Catal 175:27
152. Neumann R, LevinElad M (1997) J Catal 166:206
153. Dallmann K, Buffon R, Loh W (2002) J Mol Catal A 178:43
154. Juwiler D, Blum J, Neumann R (1998) Chem Commun 1123
155. Morimo R, Matae K (1989) Mat Res Bull 24:175
156. Lin C-C, Shen P (1994) J Non-Cryst Solids 171:281
157. Minami T, Miyata T, Takata S, Fukuda I (1990) Japanese J Appl Phys, Part 2–Letters 30:L117
158. Miyata T, Minami T, Saikai K, Takata S (1994) J Luminescence 60&61:926
159. Franz KA, Kehr WG, Siggel A, Wieczoreck J, Adam W (1990) In: Ullmann's Encyclopedia of Industrial Chemistry, 5th ed. VCH, Weinheim
160. Feng P, Bu X, Stucky GD (1995) Angew Chem Int Ed Engl 34:1745
161. Ortiz-Avila CY, Squattrito PJ, Shieh M, Clearfield A (1989) Inorg Chem 28:2608
162. Harrison WTA, Nenoff TM, Gier TE, Stucky GD (1994) J Mater Chem 4:1111
163. Mostafa MR, Youssef AM (1998) Mater Lett 34:405
164. Rothon RN (1981) Thin Solid Films 77:149
165. Birchall JD (1984) Brit Ceram Trans J 83:158
166. Murugavel R, Sathiyendiran M, Pothiraja R, Walawalkar MG, Mallah T, Riviere E (2004) Inorg Chem 43:945
167. Sathiyendiran M, Murugavel R (2002) Inorg Chem 41:6404
168. Hartman M, Kevan L (1999) Chem Rev 99:635
169. Stupp SI, LeBonheur V, Walker K, Li LS, Huggins KE, Keser M, Amstutz A (1997) Science 276:384
170. Kresge CT, Leonowicz ME, Roth WJ, Vartuli JC, Beck JS (1992) Nature 359:710
171. Zhao D, Huo W, Feng J, Chmelka BF, Stucky GD (1998) J Am Chem Soc 120:6024
172. Bagshaw SA, Prouzet E, Pinnavaia TJ (1995) Science 269:1242
173. Yang P, Zhao D, Margolese DI, Chmelka BF, Stucky GD (1998) Nature 396:512
174. Yang P, Zhao D, Margolese DI, Chmelka BF, Stucky GD (1999) Chem Mater 11:2813
175. Loy DA (2001) MRS Bull 26:364
176. Judenstein P, Sanchez C (1996) J Mater Chem 6:511
177. Lichtenhan JD (1995) Comments Inorg Chem 17:115
178. Laine RM, Zhang C, Sellinger A, Viculis L (1998) Appl Organomet Chem 12:715
179. Julian B, Gervais C, Cordoncillo E, Escribano P, Babonneau F, Sanchez C (2003) Chem Mater 15:3026
180. Wang B, Brennan AB, Huang H, Wilkes GL (1990) J Macromol Sci-Chem A27:1447
181. Wang B, Wilkes GL, Smith CD, McGrath JE (1991) Polym Commun 32:400
182. Wang B, Wilkes GL (1991) J Polym Sci A 29:905
183. Wang B, Wilkes GL, Hedrick JC, Liptak SC, McGrath JE (1991) Macromolecules 24:3449
184. Schubert U, Volkel T, Moszner N (2001) Chem Mater 13:3811
185. Brutchey RL, Goldberger JE, Koffas TS, Tilley TD (2003) Chem Mater 15:1040
186. Gordon RG, Becker J, Hausmann D, Sug S (2001) Chem Mater 13:2464
187. Beaudoin M, Scott SL (2001) Organometallics 20:237
188. Richmond MK, Scott SL, Alper H (2001) J Am Chem Soc 123:10521
189. Amor Nait Ajjou J, Scott SL (2000) J Am Chem Soc 122:8968
190. Clerici MG, Ingallina P (1993) J Catal 140:71

191. van der Waal JC, Rigutto MS, van Bekkum H (1996) Appl Catal A 167:331
192. Luan Z, Maes EM, van der Heide PA, Zhao D, Czernuszewicz RS, Kevan L (1999) Chem Mater 11:3680
193. Blasco T, Corma A, Navarro MT, Perez-Pariente J (1995) J Catal 156:65
194. Kriesel JW, Tilley TD (2001) Adv Mater 13:1645
195. Jarupatrakorn J, Tilley TD (2002) J Am Chem Soc 124:8380
196. Panov GI, Uriaete AK, Rodkim MA, Sobolov VI (1998) Catal Today 41:365
197. Sobolev VI, Dubkov KA, Panna OV, Panov GI (1995) Catal Today 24:251
198. Fujdala KL, Drake IJ, Bell AT, Tilley TD (2004) J Am Chem Soc 126:10864

Top Organomet Chem (2005) 16: 117–149
DOI 10.1007/b138075

Published online: 10 September 2005

Spectroscopic Characterization of Organometallic Centers on Insulator Single Crystal Surfaces: From Metal Carbonyls to Ziegler–Natta Catalysts

T. Risse (✉) · H.-J. Freund

Fritz-Haber-Institut der Max-Planck Gesellschaft, Abteilung Chemische Physik, Faradayweg 4–6, 14195 Berlin, Germany
risse@fhi-berlin.mpg.de

Abstract A detailed knowledge of the microscopic properties is one of the prerequisites for an understanding of heterogeneous catalysts. A strategy which has proven to be valuable in this respect is the use of model systems prepared under well-defined conditions and a subsequent characterization of these systems under both ultrahigh vacuum as well as ambient pressures. In the following review we focus on two systems where organometallic species play an important role. The first class of systems under consideration is metal carbonyls prepared under ultrahigh vacuum conditions. In particular, we will discuss the prospects of these species for use as probes for the environment of the deposited metal atom. In the second part we will discuss experiments on Ziegler–Natta model catalysts. In particular, we will describe how surface science studies of these systems can help to elucidate atomistic properties of surface sites involved in polymerization reactions.

Keywords Oxide surfaces · Metal carbonyls · Ziegler–Natta catalyst · IR spectroscopy · EPR spectroscopy

Abbreviations
CESR Conduction band electron spin resonance
ESR Electron spin resonance
EPR Electron paramagnetic resonance

ISS Ion scattering spectroscopy
IRAS Infrared absorption spectroscopy
1 L (Langmuir) = 10^{-6} Torr s
LEED Low energy electron diffraction
LRI Laser reflection interferometry
ML Monolayer
NMR Nuclear magnetic resonance
STM Scanning tunneling microscopy
TMA Trimethylaluminum
TEA Triethylaluminum
TPD Temperature programmed desorption
XPS X-ray photoelectron spectroscopy

1 Introduction

A common property of working heterogeneous catalysts is their complexity with respect to structure, chemical stoichiometry, and reaction kinetics [1]. This complexity often hampers a detailed microscopic understanding of the systems due to a lack of appropriate methodology. Therefore, strong efforts have been made to develop model systems which retain some degrees of complexity of real systems and investigate their influence on the catalytic properties of system under both ideal ultrahigh vacuum conditions, as well as ambient pressures [2–8]. One strategy, which might be classified as a bottom-up approach, is to prepare model catalysts starting from an ideal single crystal surface, under well-defined ultrahigh vacuum conditions. From this starting point, reaction centers are added to the surface in a controlled manner. A variety of methods are employed to prepare reactive centers, depending on the nature of the catalytic site. For the preparation of deposited metal particles, an important class of heterogeneous catalysts, atomic vapor deposition or cluster beam methods are used, which may be considered physical methods (e.g., [9–13]). On the other hand, grafting of catalytically active sites can be achieved by specific reactions of organometallic compounds with functional groups on the surface, ultimately aiming at a single-site catalyst (e.g., [14]).

In the following review we will focus on two classes of systems: dispersed metal particles on oxide supports as used for a large variety of catalytic reactions and a model Ziegler–Natta catalyst for low pressure olefin polymerization. The discussion of the first system will focus on the characterization of the environment of deposited metal atoms. To this end, we will discuss the prospects of metal carbonyls, which may be formed during the reaction of metal deposits with a CO gas phase, as probes for mapping the environment of deposited metal atoms [15–19].

The second part of the review will describe results on a model Ziegler–Natta catalyst [20, 21]. This investigation was inspired by the pioneering work of the Somorjai group [22], who have investigated these systems with a variety of surface science methods [23]. This review is not meant to survey the current state of knowledge in heterogeneous Ziegler–Natta catalysis. Instead, we will focus on experiments performed on model systems prepared under well-defined ultrahigh vacuum conditions and review the current state of knowledge based on these results.

2
Metal Carbonyls on a Well Defined Alumina Surface

Small supported metal particles may exhibit properties fundamentally different from the corresponding bulk materials (e.g., [24, 25]). This becomes increasingly important for decreasing particle sizes. For such particles the geometric structure, their electronic properties, and their reactivity are closely correlated. In fact, it has been shown that even changes in the size of the particles by a single atom may alter their properties drastically [12, 26]. The situation may be complicated further by the fact that different structural isomers and/or different interactions of deposited atoms with the substrate may change the catalytic properties of a particle of given size considerably. Therefore, a detailed knowledge of the environment of a deposited atom, e.g., its nucleation site or its coordination is a prerequisite for a comprehensive understanding of the deposition system. However, gathering this kind of detailed information is still challenging even for well-defined model systems. In this context, vibrational properties of metal carbonyls can give additional insight into the environment of deposited atoms.

In the present study we have used a thin, well-ordered atomically flat alumina film grown on a NiAl(110) single crystal surface as a model support [27]. The atomic arrangement within line defects of this film have recently been investigated [28]. In addition, there exists a proposed structure of the film based on X-ray diffraction data which is controversially debated at the moment [29]. The structure and size of the oxide-supported metal particles were controlled utilizing nucleation and growth of vapor deposited metal atoms under ultrahigh vacuum conditions.

In previous work on nucleation and growth of a variety of metals on this alumina film, three different nucleation sites were identified:

(i) Line defects, which show the strongest interaction with metal atoms. These are most notably antiphase domain boundaries with a characteristic distance of 100–200 Å, whose structure has recently been investigated in detail by low temperature scanning tunneling microcopy (STM) [28]. Reflection domain boundaries and substrate steps also have to be considered [30, 31].

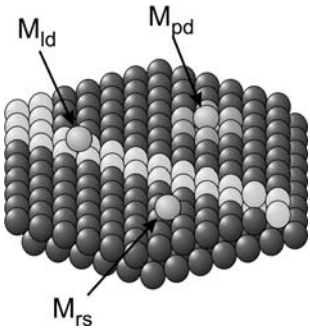

Fig. 1 Schematic representation of the different nucleation sites on the alumina film: M_{ld} nucleation at line defects, M_{pd} nucleation at point defects, M_{rs} nucleation at regular surface sites

(ii) Point defects [16, 32], which have a number density of about 10^{13} cm^{-2}.
(iii) Regular oxide sites, which exert the weakest interaction on metal atoms [16].

The adsorption sites are schematically shown in Fig. 1. However, it should be emphasized at this point that this is a schematic picture. The precise atomic positions for these species are not known at present.

The nucleation behavior of transition metal particles is determined by the ratio between the thermal energy of the diffusing atoms and the interaction of the metal atoms at the various nucleation sites. To create very small particles or even single atoms, low temperatures and metal exposures have to be used. The metal was deposited as metal atoms impinging on the surface. The metal exposure is given as the thickness (in monolayer ML) of a hypothetical, uniform, close-packed metal layer. The interaction strength of the metals discussed here was found to rise in the series from Pd < Rh < Co ($\approx$ Ir) < V [17, 32]. Whereas Pd and Rh nucleate preferentially at line defects at 300 K and decorate the point defects at 90 K, point defects are the predominant nucleation center for Co and V at 300 K. At 60 K, Rh nucleates at surface sites between point defects [16, 33].

In the following we shall see that a more detailed picture of the structural properties of small metal deposits and their electronic interaction with the substrate can be obtained from the infrared spectra of metal carbonyls created in situ by reaction with CO from the gas phase.

2.1
Small Metal Particles and Single Metal Atoms

Figure 2 shows infrared spectra (IR or IRAS) of low Pd, Rh, and V exposures at a sample temperature of 60 K (Rh, Pd) and 90 K (V) with respect to the CO dosage [15, 17]. The spectra in the CO stretching region are characterized

by broad bands as well as very narrow peaks with a half width below 4 cm^{-1}. First, we will discuss the results obtained for Rh particles, and afterwards move on to the results for V and Pd.

At low CO dosage a small amount of rhodium deposited at 60 K shows two bands at 2000/1994 and 1966 cm^{-1} (see Fig. 2a). With increasing CO coverage a new peak at 2116 cm^{-1} evolves. Later, additional bands appear at 2172, 2087, and around 2037 cm^{-1}. While the latter signals grow in, the peak at 1966 cm^{-1} vanishes. With increasing coverage the oscillator strength around 2000 cm^{-1} is redistributed in a complicated manner. However, at saturation the spectrum simplifies again, and a single line at 1999 cm^{-1} is observed. Despite the large number of lines in the spectrum it is important to emphasize that the small line width of the peaks at constant frequency indicates structurally uniform, well-defined surface species containing only few CO ligands.

The situation becomes less complicated in case of Rh deposition at 90 K. For low coverage only one peak at 1994 cm^{-1} is observed while at high coverage (see Fig. 3a) a broad band centered around 2075 cm^{-1} and a sharp, prominent peak at 2117 cm^{-1}, also observed at 60 K, is found [15]. In addition, the spectrum shows a sharp band of lower intensity at 2097 cm^{-1}. Since all bands are located above 1950 cm^{-1} the CO molecules are predominantly bound terminally in all cases. The broad line, which changes somewhat in shape upon annealing to 300 K (see Fig. 3a), is due to CO on larger Rh particles [33, 34] in line with observations on technical catalysts [35–40].

The band at 1994 cm^{-1}, observed at low CO coverage, was assigned to a monocarbonyl Rh(CO) species. The nature of the species observed at 2117 cm^{-1} has been elucidated using mixtures of different CO isotopes. As shown in Fig. 4, the band splits into three bands after adsorption of $^{12}CO/^{13}CO$ mixtures proving the presence of a dicarbonyl species

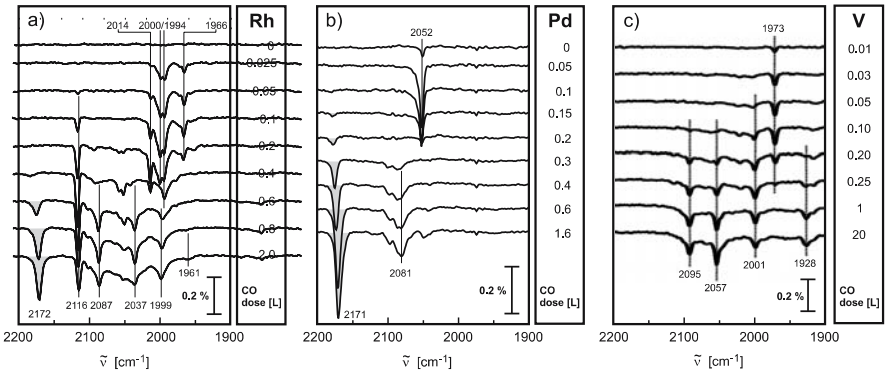

Fig. 2 Infrared spectra taken after metal deposition and exposure to increasing amounts of CO at a constant temperature: **a** 0.02 ML Rh, 60 K; **b** 0.013 ML Pd, 60 K; **c** 0.2ML V, 90 K. CO bands present on nominally clean surfaces are due to CO adsorption from the background during sample preparation

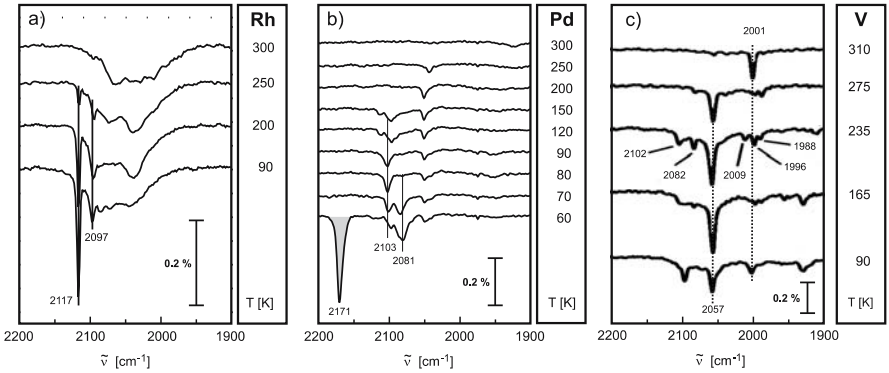

Fig. 3 Infrared spectra taken after metal deposition and CO saturation as a function of substrate temperature: **a** 0.024 ML Rh, T_{dep} = 90 K; **b** 0.013 ML Pd, T_{dep} = 60 K; **c** 0.2 ML V, T_{dep} = 90 K

$Rh(CO)_2$ [16]. Such a dicarbonyl should possess two vibration modes. However, only the symmetric mode is observable in the IR spectrum. The asymmetric mode is inaccessible to an IR experiment on a metal surface due to the so-called metal surface selection rule, which prohibits the observation of dipole excitation if the transition dipole moment is oriented parallel to the surface. It should be noted that the observed frequencies fit well to values observed for $Rh(CO)_2$ on technical Rh/Al_2O_3 catalysts [35–40] ($\sim 2100\ cm^{-1}$) and $Rh(CO)_2$ on planar $TiO_2(110)$ surfaces [41] ($2112\ cm^{-1}$).

From combination with IR results at room temperature and STM investigations it was concluded that the dicarbonyls are located at point defects of

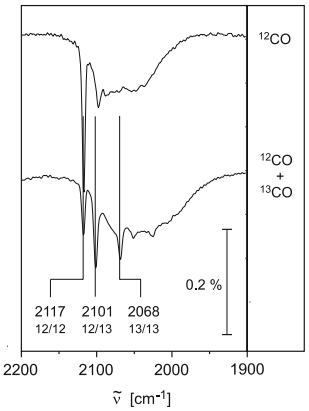

Fig. 4 Infrared spectra taken after deposition of 0.028 ML of Rh at 90 K and subsequent saturation with CO. *Top* pure ^{12}CO; *bottom* approximately equimolar mixture of ^{12}CO and ^{13}CO

the alumina film [16]. Hence, the species are formed directly from a heterogeneously nucleated Rh atom at this defect site. The species are fairly stable and start to decompose above 200 K as indicated in Fig. 3a.

The band at 2172 cm^{-1} observed in spectrum of the 60 K deposit is remarkably different from the others in the sense that it is blue shifted with respect to the gas phase value of CO (2143 cm^{-1}). This peak can be attributed to CO adsorption on the alumina film [27].

In comparison to the 90 K situation, two additional peaks at 2000 and 1966 cm^{-1} were found. Due to the reduced diffusion length of the metal atoms at lower temperatures the new peaks should be due to monocarbonyls attached to the additionally populated sites. Therefore, both species were tentatively assigned to monocarbonyls at "regular" oxide sites [15]. Investigations of the electronic structure of single Pd atoms on this surface have shown that a large variety of different adsorption sites exist, which leads to considerably different electronic structures of adsorbed Pd atoms as probed by scanning tunneling spectroscopy [42]. Thus, it is conceivable to propose metal carbonyls with different stretching frequencies nucleated at sites that were classified as "regular" adsorption sites based on their population with respect to temperature.

The intensity of the dicarbonyl at 2116 cm^{-1} is considerably reduced as compared to the 90 K deposit, indicating that the amount of metal atoms trapped at point defects is reduced for growth at 60 K. The difference in the nucleation sites is also reflected by the lower thermal stability of the systems, which decompose between 80 and 150 K as compared to 200 to 250 K for the 90 K deposits. With isotope mixing experiments the peak at 2087 cm^{-1} was assigned to a carbonyl with three or more CO ligands, while the peak at 1999 cm^{-1} is associated to a monocarbonyl [32].

It is remarkable that the feature at 2097 cm^{-1} which was observed for a preparation at 90 K is missing at 60 K. The peak shows the characteristics of a monocarbonyl in mixing experiments. Furthermore, thermal treatment of the deposit as shown in Fig. 3a reveals a slightly increased thermal stability of this species as compared to the dicarbonyl at point defects. From this information it was suggested that the monocarbonyl is located at line defects of the alumina film [15].

Moving now from Rh to Pd, the IR spectrum of Pd deposits at 60 K exhibits a single narrow line at 2052 cm^{-1} in the low CO coverage regime as shown in Fig. 2b [15]. With increasing coverage a signal at 2081 cm^{-1} grows, accompanied by the peak at 2171 cm^{-1} associated with CO adsorption on the alumina film. This behavior is markedly different to the behavior observed at 90 K where stretching features due to on-top bound CO(μ^1 – CO) at 2098 cm^{-1} and multiply coordinated molecules ($\sim$ 1940 cm^{-1}) are observed [15]. These broad signals with a large fraction of on-top bound CO are typical for adsorption on small, disordered Pd particles as observed on technical catalysts [43–45], as well as on corresponding model systems [46].

For vanadium deposits the IR spectrum (Fig. 2c) taken after saturation at 90 K is characterized by four peaks at 2095, 2057, 2001, and 1928 cm^{-1} [17]. However, at low CO dosage a single vibration at 1973 cm^{-1} is observed that first gains intensity with increasing CO amounts and vanishes for saturation coverage. It is important to note that the IR spectra of vanadium grown at 300 K are also characterized by several sharp lines indicative of well-defined surface species [17]. This is in contrast to Rh and Pd deposits, which show only broad lines characteristic for adsorbates on larger metal particles [33, 47, 48]. It is a consequence of the enhanced metal-support interaction of vanadium, which reduces the diffusion length of adatoms considerably. The two bands at 2057 and 2001 cm^{-1} observed at 90 K are also present at 300 K. However, the spectrum taken at 300 K shows several additional bands at 2116, 2034, 2019, and 1988 cm^{-1}, which are missing in the spectra of the 90 K deposits. This is remarkable since the overall morphology, as probed by STM, is essentially independent of the preparation temperature [17]. Upon annealing, the peak at 2057 cm^{-1} quickly grows at the expense of most of the other species (see Fig. 3c). In the course of the treatment new features develop. Two of them are close to species observed for 300 K deposits. Interestingly, the species at 2001 cm^{-1} is the most stable species for this preparation condition, while for the deposits prepared at 300 K the band at 2034 cm^{-1}, missing for the 90 K deposits, is the most stable species. The latter band is the one being observed exclusively for small CO doses at 300 K.

Due to the complexity of the spectra the use of isotopic CO mixtures does not allow an unambiguous determination of the stoichiometry. However, some of the features can be prepared such that the interference with other spectral components is negligible. From these experiments it was possible to assign the peak at 2057 cm^{-1} to a tricarbonyl $V(CO)_3$ and the one at 2001 cm^{-1} to a dicarbonyl $V(CO)_2$. In addition, the two peaks observed at low coverage, namely at 1973 cm^{-1} observed at 90 K and at 2034 cm^{-1} observed at 300 K, were assigned to monocabonyls V(CO) [17]. A summary of the different stoichiometries, corresponding stretching frequencies and nucleation sites is given in Table 1.

The frequencies of the carbonyl species anchored to oxide surfaces are blue shifted with respect to their matrix isolated counterparts. The main reason for these frequency shifts are charge-transfer processes between the metal center and the oxide support. This interaction modifies the extent of metal-to-CO-π-back-donation [49]. Andrews et al. were among the first to use the correlation between charge and IR frequency to measure the charge state of the metal carbonyl [50]. However, one has to include the partial charge localized at the metal center to establish the proper charge-frequency correlation [51]. It is therefore necessary to correct for the difference between the charge state of the whole carbonyl and the charge at the metal center. In addition, the geometry as well as the electronic state of the carbonyl influences the stretching frequency considerably (e.g., [52]). In order to correlate these

Table 1 Stoichiometry and corresponding IR stretching frequencies of different metal carbonyls. Charges for monocarbonyls were estimated from the correlation between IR stretching frequency and charge of the metal center as inferred from theoretical calculations (for details see [15, 17])

	T [K]	$\tilde{\nu}$ [cm^{-1}]	Charge	Adsorption site
RhCO/alumina	90 K	1994	$-0.2to + 0.2$	Point defects
	60 K	2097	$0.6to + 0.7$	Line defects
	60 K	2000/1966	$-0.3to + 0.2$	Regular surface sites
$Rh(CO)_2$/alumina	90 K, 60 K	2117	–	Not known
PdCO/alumina	60 K	2052	~ 0	Point defects
VCO/alumina	90 K	1973	+ 0.2	Regular surface sites
	300 K	2034	+ 0.5	Point defects
$V(CO)_2$/alumina	90 K, 300 K	2001	–	Not known
$V(CO)_3$/alumina	90 K, 300 K	2057	–	Not known
VCO/silica	90 K	2016	$+ 0.3to + 0.4$	Not known

quantities, precise values of the stretching frequency mostly taken from data acquired in Ne matrices and ab-initio calculations are needed for the ground state as well as for both charged states. For the cases studied so far almost linear charge frequency relations have been found [15, 17], although it should be kept in mind that these values can only serve as estimates for the charge of the metal center.

From these linear relationships the charges of the two V(CO) carbonyls at 1973 cm^{-1} and 2034 cm^{-1} were determined to be + 0.2 and + 0.5 electrons. The positive sign means that electrons are transferred from the carbonyl to the substrate. The corresponding charges for Rh(CO) located around 2000 cm^{-1} is close to zero between – 0.2 and + 0.2 electrons. However, the monocarbonyl at 2097 cm^{-1}, which was tentatively assigned to a monocarbonyl at a line defect, shows a significant charge of about + 0.6 – + 0.7 electrons. This value fits well with one measured for vanadium at 300 K. Yet, it is not clear why the two vanadium monocarbonyls observed at different temperatures show such distinctly different stretching frequencies.

Two different explanations may be given to account for this behavior:

(i) The two types of monocarbonyls are located at different sites of the alumina support. In this case the degree of charge transfer must depend on the nucleation site.

(ii) The carbonyls nucleated at the same site for both temperatures. However, the charge transfer between substrate and carbonyl is a function of the temperature. For example, an activated process which would be more effective at 300 K than at 90 K may explain this behavior.

It was possible to discriminate between the two situations by an experiment at intermediate temperature. At 120 K both species, the one at 2037 cm^{-1} (together with its ^{13}CO counterpart at 1988 cm^{-1}) and the one at 1973 cm^{-1} with its ^{13}CO satellite, were observed simultaneously. This proves that the first explanation is correct, indicating the variation of the metal support interaction for the various nucleation sites [17].

Despite the uncertainties regarding the absolute values of the charge transfer the following conclusions can be drawn:

(i) The extent of charge transfer depends on the metal nucleation site. It is larger for adsorption on point defects as compared to regular terrace sites. The metal to oxide charge transfer is also theoretically predicted for regular terrace sites [53]. The situation is much more complex for adsorption on defect sites such as anion vacancies. The result depends on the charge of the vacancy, and opposite effects are expected, e.g., for singly positive charge (F^+) and neutral (F^0) oxygen vacancies, usually called color centers because of their optical absorption in the visible [12, 54–56].

(ii) The extent of charge transfer depends on the reactivity of the metal towards oxygen. Rh monocarbonyls prepared at 90 K have been shown to nucleate at point defects, yet they are almost neutral whereas the corresponding vanadium particles seem to be charged. The latter result is confirmed by XPS (X-ray photoelectron spectroscopy) and XAS (X-ray absorption spectroscopy) [17].

Finally, it is interesting to note that the carbonyl chemistry can be tuned to some extent by the choice of the substrate under consideration. Figure 5 shows the IR spectra of CO adsorbed to 0.03 ML of vanadium deposited at 90 K to a well-ordered silica film [17]. At low CO coverage a single sharp line at 2016 cm^{-1}, most probably due to a monocarbonyl, is observed which is transformed into another sharp feature at 2075 cm^{-1}. The latter is tentatively assigned to a higher carbonyl $V(CO)_x$ with $x \geq 2$. However, most of the IR intensity is located in the broad feature from 1900–2200 cm^{-1}, which is due to CO molecules adsorbed to larger vanadium particles. This is distinctly different to the alumina case where sharp narrow lines indicative of well-defined carbonyl species dominate the spectrum even at 300 K. It can be interpreted as a smaller metal support interaction which results in an increased diffusion length of the atoms on the surface. However, the position of the signal at 2016 cm^{-1}, which is associated with a monocarbonyl species, points towards a charge transfer from the carbonyl to the surface by approximately (+)0.3–0.4 electrons. This is in line with the observation on the alumina surface, but the relative amount of these sites is distinctly smaller on silica than on alumina. This indicates that not only the reactivity of the metal towards oxygen, but also the chemistry of the substrate surface, is very important for the properties of the deposited metal particles. In the future we need to explore the chemistry of these single site systems.

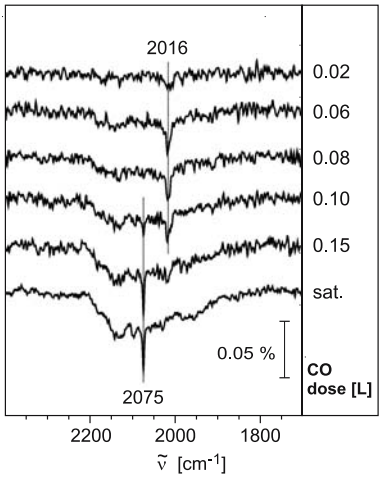

Fig. 5 Infrared spectra of 0.03 ML vanadium deposited on silica as a function of CO exposure. Preparation and measurements were done at 90 K

2.2 Carbonyl Species on Metal Particles

We have shown in the preceding section that the IR spectra of well-defined metal carbonyls provide valuable information of the environment of the deposited metal atom. However, IR signals of CO molecules adsorbed on larger particles suffer from broad lines, which hamper a more detailed analysis of the data. In the forthcoming section we will present results on cobalt particles where carbonyl species are formed on larger particles containing hundreds of atoms.

Figure 6 shows IR spectra of CO adsorbed at 44 K on Co particles grown on the alumina film at 300 K [19]. An average thickness of 1 ML Co was deposited, which corresponds to a mean particle diameter of ~ 1.6 nm (170 atoms). At low coverage, an absorption band appears at 1967 cm^{-1}, attributable to atop-bound CO [57]; this peak gradually shifts to higher energy with increasing coverage. Just after the adsorption band at 1967 cm^{-1} forms, another band at 2060 cm^{-1} also begins to grow in intensity; this second feature shifts only slightly to 2068 cm^{-1} at saturation coverage and is much stronger than the band due to atop-bound CO(μ^1 – CO) at this point. As the absorption band due to atop adsorption shifts to higher energy, it melds into a tail of the absorption feature at 2068 cm^{-1}, making it difficult to quantify the stretching frequency for atop-bound CO at the saturation limit. After annealing to 300 K, the peak attributable to atop-bound CO remains at about 2000 cm^{-1} and the feature at 2068 cm^{-1} vanishes (data not shown).

The adsorption band at 2068 cm^{-1} has no counterpart on surfaces of smooth single crystals. There, only red shifted bands (1900–1967 cm^{-1}) were

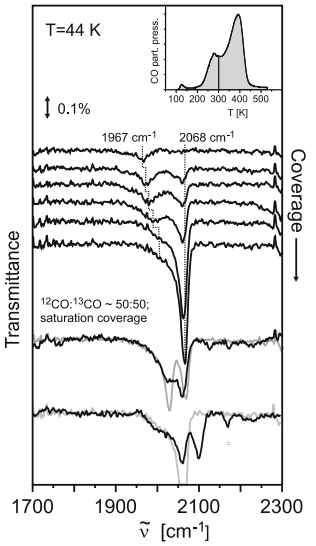

Fig. 6 IR spectra of adsorbed CO on 1 ML Co deposited at room temperature on the alumina film as a function of CO coverage. Spectra were taken at 44 K. *Black trace second up from the bottom* shows the spectrum resulting from saturation coverage of a 50 : 50 mixture of $^{13}CO : ^{12}CO$. *Overlaid gray trace* is artificially created by adding the saturation coverage spectra ^{12}CO and ^{13}CO scaled by a factor 1/2. *Lowest black trace* shows the spectrum of CO saturation coverage on particles grown by 1 MLCo + 0.05 MLPd. *Corresponding grey trace* is the pure Co spectrum for comparison. *Right inset* shows TPD spectrum of 1 ML Co [64]

observed which have been assigned to bridge bound (μ^2 – CO) species [57, 58]. Adsorption bands at 2080 cm^{-1} and 2040 cm^{-1} have been observed for CO adsorbed on sputtered Co(0001) [58] and un-annealed films [59]; in the former case this was attributed to CO adsorption at defect sites [58], and in the latter case it was attributed to carbonyl formation [59]. An adsorption band near 2068 cm^{-1} has also been observed on supported Co particles [60–62], and has been attributed to an $M(CO)_n$ species [60]. The assignment as a single-centered carbonyl is based on analogy with metal carbonyls, which suggests the following categorizations [63]: on-top (μ^1 – CO) 2000–2130 cm^{-1}, twofold bridge (μ^2 – CO) 1860–2000 cm^{-1}, and threefold bridge (μ^3 – CO) 1800–1920 cm^{-1}. Given these categories, it seems reasonable to attribute the band at 2068 cm^{-1} to a $M(CO)_n$ species. However, as compared to the sharp signals observed for carbonyls formed on single atoms the band seen here is rather broad. This is in line with expectations due to the much more heterogeneous environment in such particles.

The stoichiometry of the compound was investigated by isotope exchange experiments along the lines described in the preceding section. The pure

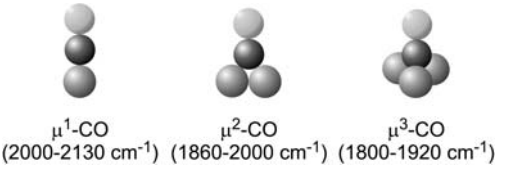

Scheme 1

^{13}CO case shows a peak at 2022 cm^{-1}, as expected from simple mass consideration. It is evident from the spectrum of an equimolar mixture of ^{13}CO and ^{12}CO at saturation coverage (shown as the black trace in the second to bottom panel of Fig. 6) that the species responsible for this band consists of strongly coupled oscillators (the light trace, second to bottom panel of Fig. 6 visualized the expectation for a decoupled system). From a careful analysis of combined annealing and isotope exchange experiments it was concluded that the observed intensity pattern is due to the formation of cobalt carbonyls $Co(CO)_x$ with $x \geq 3$ [19]. The formation of a carbonyl species is further corroborated by the intensity behavior of the system. A quantitative evaluation of the IR intensities in correlation with the corresponding TPD results (see inset Fig. 6) reveals a dynamic dipole moment of the species at 2068 cm^{-1}, being at least a factor of two higher than for the regular on-top sites [18]. In combination with theoretical calculations, it could be shown that this intensity enhancement of the carbonyl species is due to a decoupling of the CO bond to a low coordinated metal from those atoms embedded in the metal surface. Such species can only exist on metal atoms with a low metal–metal coordination based on simple chemical considerations. Thus, IR intensity, rather than the position of the band, might be a more reliable reporter on the chemical nature of the species.

The presence of a site with a low metal–metal coordination is compatible with the non-crystalline nature of the cobalt deposits [64]. It is to be expected that these sites exhibit different chemical reactivity than the usual adsorption sites. This can be verified by subsequent deposition of a small amount (0.1 Å) of Pd atoms, which are known to nucleate exclusively on the cobalt particles [64]. The corresponding IR spectrum is shown as the bottom trace in Fig. 6. It is seen that an additional peak appears at 2105 cm^{-1}, which is readily assigned to CO bound terminally to Pd. More importantly, the growth of this Pd feature is completely at the expense of the carbonyl species, indicating that Pd nucleates almost exclusively at these low coordinated sites and prevents the formation of the carbonyl species.

In summary, we have shown that metal carbonyls formed in situ by adsorption of CO under ultrahigh vacuum condition can serve as a very sensitive tool for monitoring the nucleation site as well as the environment of the metal atom. It was shown that low coordinated metal atoms, in particular

single atoms, show distinct chemical properties that depend upon the metal and may be altered by the substrate. The specific reactivity of low coordinated sites being present on small metal particles was demonstrated by subsequent evaporation of a second metal that exclusively decorates this adsorption site.

3 Ziegler–Natta Model Catalyst

The polymerization of α-olefins with so-called Ziegler–Natta catalysts is one of the most important industrial processes based on an organometallic catalyst. Since the early work by Ziegler [65] and Natta [66, 67] transition metal (in particular titanium) halides and organoaluminum compounds have been used [68, 69]. The development of industrial processes has increased the activity and efficiency of the catalysts by orders of magnitudes as compared to the first generation of (homogeneous) Ziegler–Natta catalysts [69]. One breakthrough in the development of more efficient catalysts was achieved by the so-called third generation of Ziegler–Natta catalysts introduced in the mid 1970s. These systems represent supported catalysts where inorganic chlorides, such as $MgCl_2$ and $CoCl_2$ are used as supports to increase the amount of active Ti [70]. The high activity of these catalysts has allowed use of low catalyst concentrations and, therefore, catalyst residues can remain in the polymer [69]. The literature on "classical" Ziegler–Natta catalysis is huge (e.g., [69, 71–79] and references therein). In addition, new developments such as metallocenes/methylaluminoxane catalysts have recently increased the interest in this field substantially [68, 80].

Despite this large body of work most of the experimental characterization of supported third generation Ziegler–Natta catalysts has been indirectly done via polymer product analysis. However, as has been frequently stated in the literature [69, 71–79], knowledge of surface properties of such systems is of fundamental importance to describe the process and its mechanism in detail. Recently, theoretical studies have given interesting and important contributions to our understanding of the surface sites (e.g., [81–84]). From an experimental point of view, surface science studies of model systems can offer a valuable strategy for investigating the nature of the active surface species. However, such studies on polymerization catalysts have been rather scarce. Model studies on the Phillips catalyst have been performed [85, 86] and more importantly, Somorjai and coworkers [22, 23, 87–91] have developed model systems for supported Ziegler–Natta catalysts, which allow a characterization of surface species in the course of the preparation. The procedure is sketched in Fig. 7, which may also serve as an outline for the forthcoming sections.

First, we will briefly discuss the growth properties of epitaxially grown $MgCl_2$ films used as support for the Ti centers. $TiCl_4$ was anchored on these

substrates as the active component. The anchoring process has been studied by several techniques including electron spectroscopy [89] and, recently in our group, by electron spin resonance (ESR) spectroscopy. It will be shown that surface defects in the $MgCl_2$ film are crucial in this process. The subsequent activation of the catalyst by adding a co-catalyst, namely an alkyl aluminum compound (trimethylaluminum, TMA, or triethylaluminum ,TEA) lowers the oxidation state of Ti (e.g., [23]). It will be shown how EPR spectroscopy as an in-situ technique can be used to elucidate the mechanism of the activation step. Finally, the polymerization of ethylene and propylene was monitored using several techniques such as IR spectroscopy, Raman spectroscopy or laser reflectance interferometry (LRI).

3.1 $MgCl_2$ Thin Film as a Model Support

$MgCl_2$ is used as support for heterogeneous Ziegler–Natta catalysts, therefore preparation of a well-defined epitaxial $MgCl_2$ film is an important prerequisite for the subsequent steps of the preparation procedure. $MgCl_2$ films were grown on a variety of different metal surfaces. Among them polycrystalline Au, and single crystalline Pd(111), Pd(100), Pt(111), and Rh(111) were

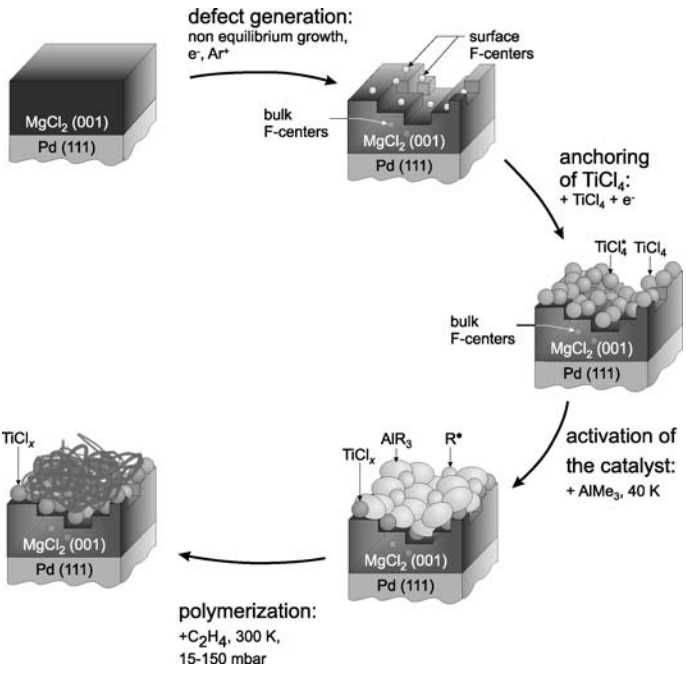

Fig. 7 Schematic representation of the preparation of a Ziegler–Natta model catalyst

used [21, 88, 92–94]. $MgCl_2$ was thermally evaporated under ultrahigh vacuum conditions as molecular $MgCl_2$ [92]. Thick films grown on Pt(111) and Pd(111) at elevated temperatures (610–630 K) show a hexagonal LEED pattern of a $MgCl_2$ film as shown in Fig. 8c. Due to the small escape depth of low energy electrons the diffraction pattern is purely determined by diffraction spots of the $MgCl_2$ film. The size of the unit cell was determined to be 3.6–3.7 Å, consistent with the unit cell parameters of α-$MgCl_2$ grown along the (001) direction. A quantitative analysis of the LEED spot intensity as a function of the electron energy (I–V analysis) (e.g., [95–97]) confirms the formation of films with α-$MgCl_2$ structure [94]. In the monolayer regime a (4×4) superstructure is observed by LEED (Fig. 8b). Such a film can be prepared either by heating the multilayer film above the multilayer desorption temperature at 680 K or by preparation of the film around 700–710 K [21, 93]. The term monolayer refers here to a Cl – Mg – Cl trilayer with a height of nominally 5.9 Å. For this thickness the diffraction experiment will probe both the film as well as the substrate, therefore the (4×4) pattern is due to the 4 : 3 coincidence of substrate and adsorbate lattice as schematically shown in Fig. 8d. It is clear that, even though the surface is polar, the system is stable due to the $MgCl_2$ structure, which is a case B structure according to Tasker's rules [98]. Analysis of the temperature programmed desorption experiments reveals an activation energy for $MgCl_2$ desorption of 224 kJ/mol for several single crystal surfaces [93], which is in good agreement with the heat of sublimation of bulk magnesium chloride, 238 kJ/mol [99]. A similar value (201 kJ/mol) was observed for $MgCl_2$ films on polycrystalline gold [88].

The growth direction of $MgCl_2$ is independent of the substrate symmetry [93]. Growth on a cubic crystal, namely Pd(100), leads to hexagonal LEED pattern. However, the structure of the films is much more complex due to the

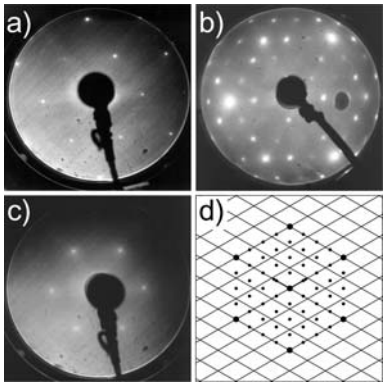

Fig. 8 LEED pattern as observed during preparation of a $MgCl_2$-film. **a** Pd(111), **b** 1 ML $MgCl_2(001)$/Pd(111), **c** multilayer $MgCl_2(001)$/Pd(111). **d** Schematic real space representation of **b**; the *mesh* represents the Cl lattice and *spots* the underlying Pd lattice

existence of symmetry equivalent rotation domains that give rise to 12 LEED spots on top of a ring of diffuse intensity, indicating a strong perturbation of the structure [93]. This is a direct consequence of the layered structure of the $MgCl_2$ and surface energies of surfaces other than (001) [100].

It is important to study whether the prepared $MgCl_2$ film exhibits pinholes. This can be done by temperature programmed desorption experiments of probe molecules. On Pd, CO is a suitable probe. The only signals observed are in the range of 70 K, which is compatible with desorption from the $MgCl_2$ film [21]. There were no signals in the range where CO desorbs from Pd(111) [101]. The same result was achieved by Magni and coworkers for $MgCl_2$ films on gold using *n*-hexane as a probe molecule [88].

3.2
Adsorption of $TiCl_4$

On a well-ordered $MgCl_2$ film prepared at high temperatures $TiCl_4$ does not adsorb at 300 K. This result is independent of the substrate used, namely it was found for gold as well as palladium substrates [21, 88]. $TiCl_4$ can of course be condensed on the surface at low temperatures, but by elevating the temperature all $TiCl_4$ desorbs well below room temperature. Magni and Somorjai in their $TiCl_4$ pioneering work had already realized the necessity of producing defects in the film to bind the $TiCl_4$ precursor [22]. The idea goes back even further (e.g., [102, 103]), however. Early on it was noted that low coordinated edge and corner sites on $MgCl_2$ crystallites serve as binding sites for $TiCl_4$ [68, 70, 104]. Recent model calculations strongly support this picture [81–84, 105].

Several routes have been used to produce defect sites on $MgCl_2$ surfaces: One way is to grow the $MgCl_2$ film at low temperatures so that the mobility of the $MgCl_2$ is too low to allow for the formation of a fully epitaxial film. However, a major problem of this procedure is the tendency to produce films containing pinholes, which change the reactivity of the system [21]. Another option is to bombard the surface either with electrons or ions [22, 87–90, 106, 107].

How do these treatments change the structure of the surface? Growth of the film at lower temperatures leads to more diffuse LEED spots, indicating a higher degree of disorder on the surface. This is corroborated by the fact that these films exhibit a sharp EPR signal at $g = 2.004$ as shown in Fig. 9a, which indicates the formation of paramagnetic chlorine vacancies in these films. This is in contrast to a film grown at elevated temperatures which is free of paramagnetic resonance signals.

Starting from a stoichiometric, well-ordered $MgCl_2$ film, an increasing dosage of sputtered ions leads to increasing background intensity of the LEED picture, which finally results in a complete loss of all diffraction spots [108]. Even though the process removes material from the surface, the surface

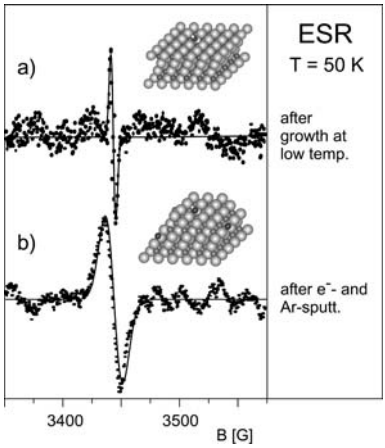

Fig. 9 EPR spectra of color center in $MgCl_2$ films for two different preparation conditions: **a** film grown at lower temperature; **b** initially well-ordered film after bombardment with electrons and argon ions

composition remains almost constant [106]. In contrast, electron bombardment leads to an electron-stimulated desorption of chlorine atoms from the surface. For low dosage this results in the formation of chlorine vacancies. Higher electron dosages reduce the $MgCl_2$ further and the formation of metallic magnesium could be observed by electron spectroscopy [106]. It should be noted that the surface of the film is always chlorine terminated, as revealed by ion scattering spectroscopy (ISS), indicating that metallic magnesium tend to diffuse to the metal substrate interface [106]. However, neither of these two processes alone is sufficient to produce paramagnetic defects on the surface. Subsequent argon ion bombardment (150 eV, 1 $\mu A/cm^2$, 3 min) of a sample initially exposed to electrons does produce an EPR signal, as shown in Fig. 9b. As compared to the spectra created by growth at lower temperatures, the signal is shifted slightly to higher g-value ($g = 2.007$). Additionally, an increase of the line width from 4 G to 14 G is observed.

Obviously, only parts of the defects created on the surface are paramagnetic, and thus EPR active. Nonetheless subsequent $TiCl_4$ deposition on samples covered with a non-epitaxial $MgCl_2$ film quenches the EPR signal by 40% [21]. This can be taken as a clear indication that some of the defects are localized on the surface of the $MgCl_2$ film, while most of the defects are bulk defects not influenced by adsorbed $TiCl_4$.

What is the nature of the defects seen in the EPR spectra? For alkali and alkali earth halogenides it is well known that irradiation with X-ray, neutrons, gamma-radiation, or electrons produce paramagnetic color centers (F-center) [109–111]. If these centers are created in large amounts, they can be stabilized by the formation of metal clusters as observed for $MgCl_2$ films after prolonged electron radiation [106]. From the temperature dependence

as well as the intensity of the signal it was concluded that the signal is due to the presence of color centers. The difference in line width between the two preparation procedures (4 versus 14 G) might be explained by the dependence of the *g*-values on the local coordination of the low coordinated sites. Thus, the more defected sample should show a broader line due to an increased heterogeneity of the defect sites. A schematic view of the situation is shown as insets in Fig. 9.

$TiCl_4$ was exposed to the surfaces by vapor deposition under electron bombardment on the surface. After this procedure Ti was found on the surface. Detailed analysis of the adsorbed Ti species by XPS measurements have shown that Ti exists as Ti^{2+} and Ti^{4+}. However, Ti^{3+} centers were not observed using XPS [87]. EPR spectroscopy offers the possibility to test this result, because Ti^{3+} as a d^1 system is a paramagnetic system. Thus, it should be EPR active, at least in its monomeric form. Figure 10 shows two distinctly different EPR spectra attributed to Ti^{3+} species which have been observed after deposition of $TiCl_4$ to differently prepared samples. The relatively sharp signal b (ΔH_{pp} = 14 G) centered at g = 1.96 was observed after deposition of $TiCl_4$ in the presence of electrons on a surface free of paramagnetic defects, followed by subsequent electron bombardment. It should be noted that systems not exposed to additional electrons after deposition of the $TiCl_4$ lack this signal. This is in line with the observations by Magni who found only Ti^{2+} and Ti^{4+} for electron-assisted deposition of $TiCl_4$ [87]. However, further electron irradiation leads to electron-stimulated desorption of chlorine, which results in a reduction of Ti^{4+} centers to Ti^{3+}. The XPS spectrum observed after this treatment showed an increase of the Ti^{2+} species at the expense of the Ti^{4+} lines. In addition, the spectral features broadened, which can be due to an additional Ti^{3+} component. However, Magni et al. did not interpret the

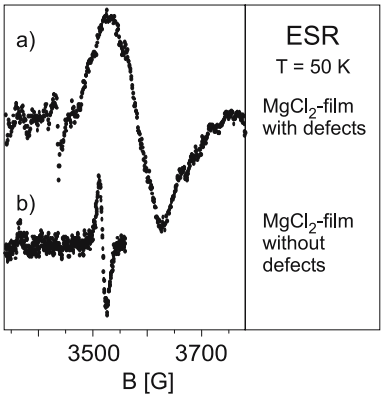

Fig. 10 EPR spectra of Ti^{3+} centers at 40 K after electron stimulated $TiCl_4$ deposition and subsequent electron bombardment. *Top* defective $MgCl_2$ film; *bottom* defect-free $MgCl_2$ film

broadening at this point due to the lack of an independent verification for the presence of Ti^{3+} species.

Upon aluminum alkyl exposure the intensity of the EPR signals is reduced by 10–60% depending on the preparation condition. This can be interpreted as a further reduction of the Ti^{3+} centers in agreement with other experiments (see next section); however, the surface concentration of these sites varies considerably with preparation conditions.

The other signal shown in Fig. 10a was observed after adsorption of $TiCl_4$ under electron bombardment and subsequent treatment with electrons on $MgCl_2$ substrates, which show paramagnetic defect states. In this case the signal intensity is increased by more than an order of magnitude as compared to the former case. In addition, the signal is shifted up-field, now located at $g = 1.93$, with a peak-to-peak width of 50–90 G, depending on the preparation.

The g-values found are situated among values reported for $TiCl_3$ in octahedral ($g = 1.94$) and tetrahedral ($g = 1.96$) environments [112–114]. These values were found for Ziegler–Natta catalysts. While the signal observed on the less defected surface is close to the value observed for tetrahedral environments, the signal of the surface showing paramagnetic defects is centered at the value for octahedral environments. Comparing the line width of the signals measured here with the ones in the literature, the general trend of the signal at $g = 1.94$ to be broader than those at $g = 1.96$ also holds true for these measurements; however, the line width of the resonance at $g = 1.93$ is considerably broader than in the literature. Considering the stronger disorder of these systems it is more likely that isolated Ti^{3+} centers are formed in this case, which may comprise different local environments. The increase in line width would thus be caused by inhomogeneous line broadening.

However, there is no indication that the presence of the observed signals correlates with the polymerization efficiency of the catalyst. In fact, systems which exhibit these signals are less effective catalysts and in some cases do not even polymerize ethylene under the chosen conditions. In contrast, systems without EPR signals correlated to Ti^{3+} species are found to be catalytically active. It has to be emphasized at this point that the lack of an ESR signal associated to Ti^{3+} ions, in cases where no additional argon or electron bombardment has been applied, cannot be interpreted as an indication of the absence of Ti^{3+} centers at the surface. It has been discussed in the literature that small spin-lattice-relaxation times, dipole coupling, and super exchange may leave a very small fraction of Ti^{3+} that is detectable in an EPR experiment [115, 116]. From a combination of XPS and EPR results it unlikely that Ti^{3+} centers play an important role in the catalytic activity of the catalysts.

A second class of catalysts was prepared by deposition of $TiCl_4$ and Mg metal on gold surfaces [91, 117]. Mg deposition and subsequent $TiCl_4$ exposure results in a complex structure with Mg metal being located at the gold interface and covered by a $MgCl_2$ layer. On top of that $TiCl_x$ species of differ-

ent oxidation states were found. In contrast to deposition on the $MgCl_2$ films, not only Ti^{4+} and Ti^{2+} but also Ti^{3+} centers were found under these preparation conditions. However, the ratio of the different oxidation states changes significantly with the preparation condition [91, 117]. For simultaneous deposition of $TiCl_4$ and Mg the situation is different. In this case Mg is completely oxidized to $MgCl_2$. The $MgCl_2$ film is covered by $TiCl_x$ species of different oxidation states. Similar to the sequential deposition, all three oxidations are present and the precise composition depends on the relative concentration of $TiCl_4$ and Mg atoms at the surface during growth [91]. Mesitylene (1,3,5 trimethyl-benzene) was used as a probe molecule to titrate different adsorption sites on these systems. The mesitylene TPD from these films are characterized by two desorption peaks around 200 K and 250 K. The desorption temperatures are virtually identical to the ones observed on the pure $MgCl_2$ film. This was attributed to the fact that both systems are chorine terminated, thus the adsorption energy is mostly determined by the local configuration of chlorine atoms, which was considered to be similar for both cases. The two peaks were assigned to mesitylene desorbing from coordinatively saturated sites at 200 K and desorption from low coordinated sites or defect sites at 250 K [118].

A third class of catalysts was prepared by electron beam induced deposition of $TiCl_4$ on a polycrystalline Au foil. Deposition of $TiCl_4$ at 300 K leads to films which comprise Ti^{4+} and Ti^{2+} species as inferred from XPS measurements [90]. Depending on the experimental parameters (background pressure of $TiCl_4$, electron flux, electron energy) different composition of Ti oxidation states are observed [23]. From angular-dependent measurements it was concluded that the Ti^{4+} centers are more prominent at the surface of the titanium chloride film, while the Ti^{2+} centers are located in the bulk [90].

Temperature-programmed desorption of mesitylene shows a marked difference to the catalysts prepared on $MgCl_2$ surfaces. The spectrum contains only one desorption peak at around 250 K. Due to the similar desorption temperature to the peak observed for $MgCl_2$-based films, this peak was assigned to desorption from low coordinated or defect sites [118].

3.3
Activation of the Catalyst

Activation of the catalyst is usually performed by exposure to a co-catalyst, namely an aluminum alkyl. The model catalysts were successfully activated by trimethylaluminum (TMA) and triethylaluminum (TEA), commonly used for this purpose. The compounds were dosed from the gas phase either at room temperature for a prolonged time or for a much shorter time at a surface temperature of 40 K. Nominal 3400 L of TMA or TEA were exposed at room temperature. The chemical integrity of the co-catalyst was verified by IR spectroscopy of condensed films grown at low temperature on the substrates. The spectra were typical for condensed and matrix isolated species [119].

Figure 11a shows a typical ESR spectrum after deposition of TMA on the $TiCl_4/MgCl_2/Pd(1111)$ system at 50 K [20]. The $TiCl_4/MgCl_2$ system was prepared by subsequent deposition of $TiCl_4$ onto an epitaxial $MgCl_2$ film. The intensity of the observed signal scales with the amount of Ti on the surface, which suggests that the observed signal is due to a surface reaction of the TMA with the Ti centers on the surface. This interpretation is corroborated by the fact that the intensity of the EPR signal saturates for increasing dosage of TMA. Additionally, adsorption of TMA on smooth as well as defected $MgCl_2$ gives no signal.

According to XPS investigations by the Somorjai group, interaction of TEA with Ti centers grafted on $MgCl_2$ leads to a reduction of Ti^{4+} center to Ti^{2+} [107]. No indications for the formation of Ti^{3+} centers were found. As indicated in the preceding section, the amount of Ti^{3+} centers present after deposition depends on the preparation conditions. However, for all situations investigated the amount of Ti^{3+} is slightly reduced by the activation process [118, 120]. The mesitylene desorption temperature from the low coordinated sites is reduced by about 15 K whereas the desorption temperature from the regular sites at 200 K is virtually unchanged (small reduction by 2–5 K depending on the preparation) [118]. Thus, it can be concluded that the alkylation takes place at the low coordinated sites. The situation is less obvious for the regular sites due to the small changes observed there.

The EPR spectrum shows, in accordance with the XPS results, no feature that can be attributed to Ti^{3+} centers. What is the nature of the radical observed in the EPR spectrum? It might be thought that methyl radicals are the most natural products in the reduction of a mixed titanium-chlorine-methyl species according to the following simple reaction scheme:

$$AlMe_3 + TiCl_4 \rightarrow AlMe_2Cl + TiCl_3Me \quad (1a)$$

$$TiCl_3Me \rightarrow TiCl_3 + Me^{\cdot} \quad (1b)$$

However, a comparison of the line shape of the observed spectra with spectra of methyl radicals (Fig. 11b) clearly proves that the species present here are not methyl radicals. The EPR spectrum of a methyl radical is a quartet of lines. However, the observed spectrum, though dominated by a quartet structure, shows a couple of additional lines pointing to additional interactions of the unpaired electron. By comparing the observed line shape to other alkyl radicals it turned out that the present spectrum can be attributed to ethyl radicals. Figure 11c shows the EPR spectrum of ethyl radicals created in an ethylchloride matrix generated by photolysis for comparison [121].

How have the C_2H_5 radicals been created?

It has already been shown above that the radicals are most probably produced at the TMA – $TiCl_4/MgCl_2$ interface, where an alkylation of the $TiCl_4$ by ligand exchange is supposed to happen (see reaction scheme above). Assuming this ligand exchange occurs, the primary radical would be a methyl

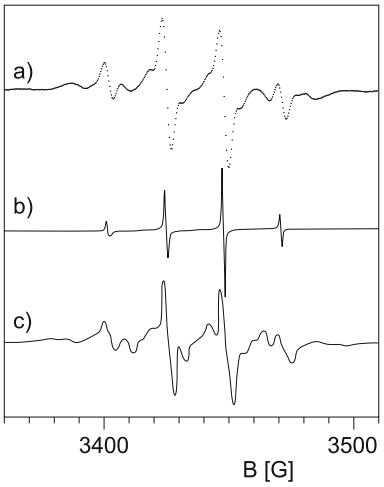

Fig. 11 *a* EPR spectrum of the model catalyst after adsorption of TMA at 50 K; *b* EPR spectrum of methyl radicals [151]; *c* EPR spectrum of ethyl radicals [121]

radical. Methyl radicals have a high mobility, even at low temperature, in the solid state, which makes consecutive reactions likely [122]. A simple reaction yielding ethyl radicals is:

$$CH_3^{\cdot} + Al(CH_3)_3 \rightarrow H_3C - H_2C^{\cdot} + AlH(CH_3)_2 \quad (2)$$

Even though this reaction has not been reported in the literature so far, it can be crudely estimated that it is energetically possible. An alternative reaction may be proposed by analogy to the known chemistry of titanocenes. Here reaction of Cp_2TiCl_2($Cp = \eta^5 - C_5H_5$) with $AlMe_3$ yields the Tebbe reagent $Cp_2Ti(\mu^2 - Cl)(\mu^2 - CH_2)AlMe_2$, which is a protected methylidene carbene [123]. It is possible that an analogous surface complex $Ti_S(\mu^2 - Cl)(\mu^2 - CH_2)AlMe_2$ may serve as a source of methylidene to produce ethyl radicals.

The EPR intensity of the ethyl radicals is irreversibly attenuated above 50 K and falls below the detection limit above 80 K. This can be explained by assuming the ethyl radicals to diffuse and recombine at these temperatures, as has been observed for methyl radicals above 45 K [124] and for NO_2 radicals on an oxide surface above 75 K [125].

At 300 K TMA has desorbed from the surface. However, carbon is found on the surface indicating a successful alkylation of the $TiCl_4$. Exposure of the surface to 3400 L at room temperature leads to a similar amount of carbon. This is in contrast to observations by Magni et al. who report on a minimal dosage of 10 000 L to observe carbon on the surface [107]. It is important to note that additional dosage of TMA at low temperature does not produce further radical signals. However, removing the reacted $TiCl_x$ moieties from the

surface, e.g., by soft argon sputtering, and redosing with TMA creates new C_2H_5 radicals, as observed by their EPR spectrum.

A different behavior is observed if TMA is replaced by TEA. Even though the final catalysts are equally active for ethylene polymerization, radicals have never been observed. This is in line with expectations based on indirect evidence [126–128] proposing a disproportionation reaction for the activation with TEA according to:

$$AlEt_3 + TiCl_4 \rightarrow AlEt_2Cl + TiCl_3Et \quad (3a)$$

$$2TiCl_3Et \rightarrow 2TiCl_3 + C_2H_4 + C_2H_6 \quad (3b)$$

Because ethyl radicals have been observed in the preceding experiment, which also suggest that these radicals are stable at 50 K, the initial formation of ethyl radicals would undoubtedly lead to the observation of the radicals. A possible mechanism may be proposed by analogy to molecular organometallic chemistry. Negishi et al. have shown that the reaction of zirconocene dichloride with $AlEt_3$ liberates ethane and forms a coordinated ethylene according to [129]:

$$Cp_2ZrCl_2 + AlEt_3 \leftrightarrow (Cp_2Zr(Cl)(\mu^2 - Cl)(\mu^2 - Et)AlEt_2 \leftrightarrow Cp_2Zr(Et)(\mu^2 - Cl)_2AlEt_2) \quad (4a)$$

$$Cp_2ZrCl_2 + 2AlEt_3 \rightarrow Cp_2Zr(\mu^2 - Cl)(\mu^2 - \eta^2 - C_2H_4)AlEt_2 + EtH + Et_2AlCl \quad (4b)$$

Thus it seems possible that analogous titanium-based complexes play a role in the activation of the catalyst with $AlEt_3$ according to:

$$Ti_SCl_2 + AlEt_3 \leftrightarrow (Ti_S(Cl)(\mu^2 - Cl)(\mu^2 - Et)AlEt_2 \leftrightarrow Ti_S(Et)(\mu^2 - Cl)_2AlEt_2) \quad (5a)$$

$$Ti_SCl_2 + 2AlEt_3 \rightarrow Ti_S(\mu^2 - Cl)(\mu^2 - \eta^2 - C_2H_4)AlEt_2 + EtH + Et_2AlCl \quad (5b)$$

It should be emphasized that no spectroscopic evidence exists for either of the proposed species; however, the lack of an EPR signal can be taken as strong evidence that no radicals are produced during activation of the catalyst with $AlEt_3$, thus favoring a kind of disproportionation mechanism.

3.4 Polymerization of Ethylene and Propylene

The model catalysts prepared according to the above-mentioned procedures were active for ethylene and propylene polymerization without additional cocatalyst present in the gas phase [21, 23]. The $TiCl_x/MgCl_2$-based catalysts have been proven catalytically active at 300 K and an ethylene pressure above

15 mbar. The polymer films have been characterized by a variety of methods including XPS, IRAS, LRI, and Raman spectroscopy.

We have used IRAS to investigate the polymerization of ethylene on a $TiCl_x/MgCl_2/Pd(111)$ catalyst activated with TEA or TMA. The catalysts were exposed at 300 K to 15–150 mbar ethylene. Polyethylene is produced on this catalyst, as shown by the IR spectrum in Fig. 12. Characteristic vibrations are the stretching modes at 2852/2924 cm^{-1}, the doublet of the deformation modes at 1473/1463 cm^{-1}, and the split rocking modes at 730/720 cm^{-1} (see Table 2). The observed frequencies of the stretching modes are situated at positions that indicate a large percentage of *trans* configurations [130–132]. This was taken as an indication that the polymer chains have long range order in *trans* configurations but also contain some *gauche* defects. Similar results were also obtained in other work. Polyethylene formed via diazo methane reactions on Au(111) films showed similar behavior [131]. Also, *n*-$C_{44}H_{90}$ adsorbed on Au surfaces yielded analogous results. Here the authors found *gauche* defects only in the second layer, while the first represented a flat lying chain [133].

This analysis is corroborated by the signature of the bands in the fingerprint and low frequency regime. A sharp doublet of the scissoring mode at 1473/1463 cm^{-1} is indicative for crystalline polyethylene, while a broad resonance at 1468 cm^{-1} is found for amorphous polyethylene [134–137]. The doublet is caused by a Davidov splitting due to the presence of two polyethylene chains in the unit cell [133, 138]. In this case the relative small half width of the two peaks is a good indication for a rather well-developed crystallinity. Another feature typical for crystalline polyethylene is a doublet in the region of the rocking mode at 730/720 cm^{-1} [135]. In addition, bands in the region between 1300 and 1380 cm^{-1}, which have been observed for disordered polyethylene, are not present these samples [134]. A lower limit for the chain length of the polymer can be estimated from the fact that vibrations in the

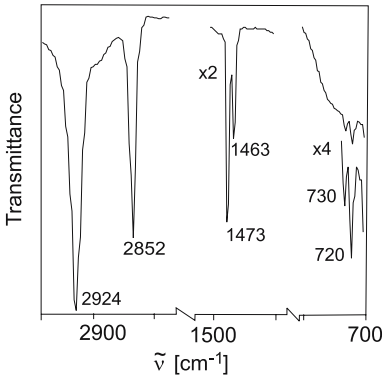

Fig. 12 Infrared spectrum of polyethylene film grown on the model catalyst

Table 2 Comparison of IR frequencies between the model catalyst and data for literature as well as the assignment of the frequencies taken from the literature

ν_{obs} [cm^{-1}]	ν_{ref} [cm^{-1}]	Assignment
2924	2922–2926 Without 2915–2920	CH_2 asymmetric stretching mode d^-: crystalline PE with gauche-defect [131, 133, 146]
2852	2852–2856 Without 2846–2850	CH_2 symmetric stretching mode d^+: crystalline PE with gauche-defect [131, 133, 146, 147]
1473	1470–1473	CH_2 deformation mode orthorombic PE *a*-axis [136, 137, 146–148]
1463	1463	CH_2 deformation mode orthorombic PE *b*-axis [136, 137, 146–148]
730	730–731	CH_2 rocking mode orthorombic PE *a*-axis [135, 149]
720	720	CH_2 rocking mode orthorombic PE *b*-axis [135, 149, 150]

range between 720 and 1300 cm^{-1} are completely missing. For alkanes with a chain length above 20 units the vibrations in this frequency range become so broad that they cannot be observed, which renders this value the lower limit of the chain length in our case [133, 139, 140]. In addition, the line corresponding to terminal methyl groups is very small, which serves as another hint for the polymeric nature of the material produced. It is important to notice that the absence of a line in an IRAS experiment performed under grazing incidence on a metal surface might be due to the so-called metal surface selection rule.

Polymerization of ethylene and propylene has also been monitored by XPS, IR, and Raman spectroscopy [89, 91, 120, 141]. The valence band XPS spectra of polyethylene and polypropylene are characterized by two and three lines between 13 and 19 eV binding energy, respectively. The two outer lines of the polypropylene are due to excitations in methylene groups while the central peak corresponds to methyl group excitations. Subsequent polymerization of propylene and ethylene results in a layered polymer film with polypropylene being at the polymer gas interface and polyethylene being located underneath. From this result in combination with the observation that XPS shows Ti and Cl signals only at the substrate/polymer interface (measured after peeling off the polymer film) it was concluded that polymerization occurs at the solid support [141]. Even though the active site remains at the substrate surface during polymerization, the chemical environment at the catalyst changes during the course of the polymerization.

After polymerization took place an additional EPR signal located at $g = 2.002$ was observed. This signal can be assigned to Ti^{3+} centers within an organic environment [142, 143]. This result points towards a change of the chemical environment of the Ti center at the interface during polymerization. The signal intensity and width varies considerably from preparation to preparation, but there is no simple correlation of these quantities with the activity.

An important characteristic of polypropylene is the tacticity of the material. Kim and Somorjai have investigated the tacticity of the polymer by means of the different solubilities of iso- and atactic polypropylene in boiling *n*-alkanes [120]. The soluble fractions were dried on glass surfaces and investigated by AFM. Based on these results a significant enhancement of isotactic polypropylene was found for catalysts prepared by $TiCl_4$ adsorption on Au as compared to a $MgCl_2$-based system. In fact, Kim et al. claim that the $TiCl_y$/Au catalyst produces exclusively isotactic polypropylene whereas the other catalyst produces a mixture of iso- and atactic polypropylene. It should be noted that an analysis of IR spectra of the grown polymer is not as conclusive. The isotactic index based on the intensity ratio of vibrations at 998 and 973 cm^{-1}, which is used in literature to estimate the amount of isotactic polypropylene (e.g., [144]), is much lower than expected based on the extraction results [120]. The IR analysis might be hampered by amorphous fractions of the polymer. However, values of the isotactic index measured after high temperature treatment to increase the crystallinity of the sample, or independent measurements such as NMR are not available.

Kim and Somorjai have associated the different tacticity of the polymer with the variation of adsorption sites for the two systems as titrated by mesitylene TPD experiments. As discussed above, the $TiCl_y$/Au system shows just one mesitylene desorption peak which was associated with desorption from low coordinated sites, while the $TiCl_x/MgCl_x$ exhibits two peaks assigned to regular and low coordinated sites, respectively [23]. Based on this coincidence, Kim and Somorjai claim that isotactic polymer is produced at the low-coordinated site while atactic polymer is produced at the regular surface site. One has to bear in mind, however, that a variety of assumptions enter this interpretation, which may or may not be valid. Nonetheless it is an interesting and important observation which should be confirmed by further experiments, e.g., structural investigations of the activated catalyst. From these experiments it is clear that the degree of tacticity depends on catalyst preparation and most probably on the surface structure of the catalyst; however, the atomistic correlation between structure and tacticity remains to be clarified.

The kinetics of the reaction has been studied by IR as well as laser reflection interferometry (LRI) [21, 145]. The amount of polymer grown on the surface was measured from the LRI signal as a function of time. It was shown that propylene polymerization was about 30 times slower than ethylene polymerization [145]. In addition, Kim et al. estimated the polymerization ac-

tivity of the model catalyst to be 2–8 times lower that that of commercial catalysts. The observed kinetic was analyzed in terms of a 1st and 2nd order deactivation process, as often used in Ziegler–Natta catalysis [70]. However, transport properties, namely diffusion of the monomers towards the reaction center, can also be responsible for the decrease of the polymerization rate as pointed out by the authors [141].

The course of the reaction has also been studied by evaluating the IR band at 2852 cm^{-1}, which is the one least influenced by the presence of gaseous ethylene [21]. The polymerization has been followed for 12–150 h.

Two different kinds of behavior have been observed. Typical results are given in Fig. 13. The behavior is determined by the degree of disorder in the surface of the model catalyst. While a catalyst with a high degree of disorder shows a monotonous increase of the polyethylene amount with time, catalysts prepared on a smooth and less defected surface show a self-terminating reaction after approximately 50 h leading to a considerably less thick film than in the former case. This can be explained in a straightforward way by considering that on a smooth surface a rather smooth polymer film forms, which becomes impermeable for ethylene from the gas phase in a relatively short period of time so that the reaction is self-limiting. In the other case, the growing film possibly has a sufficient number of pores so that the monomer can continue to reach the catalyst and the reaction keeps going. This assumes that the polymerization reaction takes place at the interface of the polymer and the magnesium chloride support, which has been corroborated experimentally [145]. In the light of these results it seems appropriate to model the kinetic data by assuming diffusion-limited transported of monomer to the interface. The amount of polymer n_e increases with reaction time t according to:

$$n_e = \delta\sqrt{t} \tag{6}$$

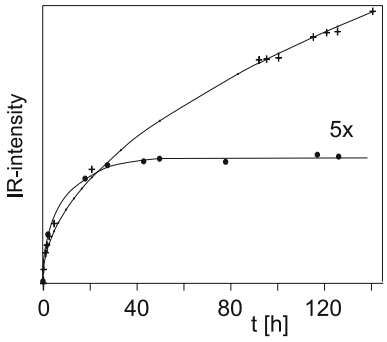

Fig. 13 Amount of polymer as measured by the IR absorption at 2852 cm^{-1} with respect to time. The kinetics observed on a rough catalyst is represented by *crosses*. The *line* through these points is a fit to the kinetic model given in the text. Kinetics observed for smooth catalysts is given by *full circles*. The line is a guide for the eye

where the constant δ is a function of the diffusion coefficient, the surface area, the molar volume of the polymer, and the concentration at infinite time t. Therefore, we expect the IR intensity to increase as $\sqrt{t}$. With $\delta = 4.6 \times 10^{-2} \text{mol s}^{-1/2}$ the fit given in Fig. 13 has been obtained.

In conclusion, we have shown that the combination of several surface science methods allows a detailed understanding of the properties of surface sites as well as of reactions taking place at the catalyst surface. In particular, EPR spectroscopy has proven useful for elucidating mechanistic details of the activation process of these catalysts.

4 Conclusions

We have reviewed experiments on two classes of systems, namely small metal particles and atoms on oxide surfaces, and Ziegler–Natta model catalysts. We have shown that metal carbonyls prepared in situ by reaction of deposited metal atoms with CO from the gas phase are suitable probes for the environment of the adsorbed metal atoms and thus for the properties of the nucleation site. In addition, examples of the distinct chemical and physical properties of low coordinated metal atoms as compared to regular metal adsorption sites were demonstrated. For the Ziegler–Natta model catalysts it was demonstrated how combination of different surface science methods can help to gain insight into a variety of microscopic properties of surface sites involved in the polymerization reaction.

Acknowledgements We are grateful to all coworkers who have contributed to the results presented here. Their names may be taken from the list of references given below. We would also like to acknowledge support by the Deutsche Forschungsgemeinschaft (SFB 290 and SFB 546), Fond der chemischen Industrie and EU through the TMR project "Oxide surfaces; reactivity of clean and modified oxide surfaces". We are grateful to Dr. Christophe Coperet and Dr. Bruno Chaudret for bringing the work of Negishi et al. to our attention.

References

1. Ertl G, Knözinger H, Weitkamp J (eds) (1997) Handbook of heterogeneous catalysis. Wiley-VCH, Weinheim
2. Gunter PLJ, Niemantsverdriet JWH, Ribeiro FH, Somorjai GA (1997) Catal Rev Sci Eng 39:77
3. Henry CR (1998) Surf Sci Rep 31:235
4. Campbell CT (1997) Surf Sci Rep 27:1
5. Freund H-J (2002) Surf Sci 500:271
6. Libuda J, Freund HJ (2002) J Phys Chem B 106:4901

7. Diebold U (2003) Surf Sci Rep 48:53
8. Freund HJ, Libuda J, Bäumer M, Risse T, Carlsson A (2003) Chem Rec 3:181
9. Poppa H (1993) Catal Rev-Sci Eng 35:359
10. Bäumer M, Freund H-J (1999) Progr Surf Sci 61:127
11. Heiz U, Vanolli F, Trento L, Schneider WD (1997) Rev Sci Inst 68:1986
12. Heiz U, Schneider WD (2000) J Phys D 33:R85
13. Binns C (2001) Surf Sci Rep 44:1
14. Coperet C, Chabanas M, Petroff Saint-Arroman R, Basset JM (2003) Angew Chem Int Ed 42:156
15. Frank M, Bäumer M, Kühnemuth R, Freund H-J (2001) J Phys Chem B 105:8569
16. Frank M, Kühnemuth R, Bäumer M, Freund H-J (2000) Surf Sci 454:968
17. Magg N, Giorgi JB, Frank MM, Immaraporn B, Schroeder T, Bäumer M, Freund H-J (2004) J Am Chem Soc 126:3616
18. Risse T, Carlsson A, Bäumer M, Klüner T, Freund H-J (2003) Surf Sci 546:L829
19. Carlsson AF, Bäumer M, Risse T, Freund H-J (2003) J Chem Phys 119:10885
20. Risse T, Schmidt J, Hamann H, Freund H-J (2002) Angew Chem Intern Ed 41:1517
21. Schmidt J, Risse T, Hamann H, Freund HJ (2002) J Chem Phys 116:10861
22. Magni E, Somorjai GA (1995) Catal Lett 35:205
23. Kim SH, Somorjai GA (2001) Surf Interface Anal 31:701
24. Cox AJ, Louderback JG, Apsel SE, Bloomfield LA (1994) Phys Rev B 49:12295
25. Haruta M (1997) Catal Today 36:153
26. Heiz U, Sanchez A, Abbet S, Schneider W-D (1999) J Am Chem Soc 121:3214
27. Jaeger RM, Kuhlenbeck H, Freund H-J, Wuttig M, Hoffmann W, Franchy R, Ibach H (1991) Surf Sci 259:235
28. Kulawik M, Nilius N, Rust HP, Freund HJ (2003) Phys Rev Lett 91:6101
29. Stierle A, Renner F, Streitel R, Dosch H, Drube W, Cowie BC (2004) Science 303:1652
30. Bäumer M, Frank M, Libuda J, Stempel S, Freund H-J (1997) Surf Sci 391:204
31. Bäumer M, Libuda J, Sandell A, Freund H-J, Graw G, Bertrams T, Neddermeyer H (1995) Ber Bunsenges Phys Chem 99:1381
32. Bäumer M, Frank M, Heemeier M, Kühnemuth R, Stempel S, Freund H-J (2000) Surf Sci 454–456:957
33. Frank M, Bäumer M (2000) Phys Chem Chem Phys 2:3723
34. Frank M, Kühnemuth R, Bäumer M, Freund HJ (1999) Surf Sci 427–428:88
35. Yang AC, Garland CW (1957) J Phys Chem 61:1504
36. Yates JT Jr, Duncan TM, Worley SD, Vaughan RW (1979) J Chem Phys 70:1219
37. Rice CA, Worley SD, Curtis CW, Guin JA, Tarrer AR (1981) J Chem Phys 74:6487
38. Solymosi F, Knoezinger H (1990) J Chem Soc Faraday Trans 86:389
39. Basu P, Panayotov D, Yates JT (1987) J Phys Chem 91:3133
40. Solymosi F, Bansagi T (1993) J Phys Chem 97:10133
41. Hayden BE, King A, Newton MA (1998) Surf Sci 397:306
42. Nilius N, Wallis TM, Ho W (2003) Phys Rev Lett 90:6808
43. Dulaurent O, Chandes K, Bouly C, Bianchi D (1999) J Catal 188:237
44. Tessier D, Rakai A, Bozonverduraz F (1992) J Chem Soc Faraday Trans 88:741
45. Hicks RF, Qi HH, Kooh AB, Fischel LB (1990) J Catal 124:488
46. Rainer DR, Wu MC, Mahon DI, Goodman DW (1996) J Vac Sci Techn A 14:1184
47. Wolter K, Seiferth O, Libuda J, Kuhlenbeck H, Bäumer M, Freund HJ (1998) Surf Sci 402–404:428
48. Wolter K, Seiferth O, Kuhlenbeck H, Bäumer M, Freund H-J (1998) Surf Sci 399:190
49. Papai I, Goursot A, Stamant A, Salahub DR (1992) Theor Chim Acta 84:217
50. Zhou MF, Andrews L, Bauschlicher CW (2001) Chem Rev 101:1931

51. Zhou MF, Andrews L (1999) J Am Chem Soc 121:9171
52. Mineva T, Russo N, Freund HJ (2001) J Phys Chem A 105:10723
53. Bogicevic A, Jennison DR (1999) Phys Rev Lett 82:4050
54. Abbet S, Riedo E, Brune H, Heiz U, Ferrari AM, Giordano L, Pacchioni G (2001) J Am Chem Soc 123:6172
55. Abbet S, Ferrari AM, Giordano L, Pacchioni G, Hakkinen H, Landman U, Heiz U (2002) Surf Sci 514:249
56. Bogicevic A, Jennison DR (2002) Surf Sci 515:L481
57. Toomes RL, King DA (1996) Surf Sci 349:1
58. Beitel GA, Laskov A, Oosterbeek H, Kuipers EW (1996) J Phys Chem 100:12494
59. Bradshaw AM, Pritchard J (1970) Proc Roy Soc Lond A 316:169
60. Heal MJ, Leisegang EC, Torrington RG (1978) J Catal 51:314
61. Gardner RA, Petrucci RH (1960) J Am Chem Soc 82:5051
62. Kavtaradze NN, Sokolova NP (1964) Russ J Phys Chem 38:548
63. Sheppard N, Nguyen TT (1978) In: Hester RE, Clark RJH (eds) Advances in infrared and Raman spectroscopy, vol 5. Heyden, p 67
64. Heemeier M, Carlsson AF, Naschitzki M, Schmal M, Bäumer M, Freund H-J (2002) Angew Chem Intern Ed 41:4073
65. Ziegler K, Holzkamp E, Breil H, Martin H (1955) Angew Chem Int Ed 67:541
66. Natta G, Pino P, Mazzanti P U.S. Patent 3 715 344
67. Natta G (1955) J Polym Sci 16:143
68. Barbé PC, Cecchin G, Noristi L (1987) Adv Polym Sci 81:1
69. Kaminsky W, Arndt M (1997) In: Ertl G, Knözinger H, Weitkamp J (eds) Handbook of heterogeneous catalysis, vol 5. Wiley-VCH, Weinheim, p 2405
70. Dusseault JJA, Hsu CC (1993) J Macromol Sci C 33:103
71. Fink G, Mühlhaupt R, Brintzinger HH (eds) (1995) Ziegler catalysts: recent scientific innovations and technological improvements. Springer, Berlin Heidelberg New York
72. Boor J (1979) Ziegler–Natta catalysts and polymerization. Academic, New York
73. Keii T (1982) Kinetics of Ziegler–Natta polymerization. Chapman & Hall, London
74. Kissin YV (1985) Isospecific polymerization of olefins. Springer, Berlin Heidelberg New York
75. Sinn H, Kaminsky W (1980) Adv Organomet Chem 18:99
76. Pasquon I, Giannini U (1984) In: Anderson JR, Boudart M (eds) Catalysis, science and technology. Springer, Berlin Heidelberg New York, p 65
77. Chien JCW (ed) (1975) Coordination polymerization. Academic, New York
78. Quirk RP (ed) (1988) Transition metal catalyzed polymerization: Ziegler–Natta and metathesis polymerizations. Cambridge University Press, Cambridge
79. Kaminsky W, Sinn H (eds) (1988) Transition metals and organometallics as catalysts for olefin polymerization. Springer, Berlin Heidelberg New York
80. Sinn H (1995) Marcomol Symp 97:27
81. Weiss H, Boero M, Parrinello M (2001) Marcomol Symp 173:137
82. Boero M, Parrinello M, Weiss H, Hüffer S (2001) J Phys Chem 105:5096
83. Martinsky C, Minot C, Ricart JM (2001) Surf Sci 490:237
84. Seth M, Margl PM, Ziegler T (2002) Macromolecules 35:7815
85. Hemmerich I, Rohr F, Seiferth O, Dillmann B, Freund H-J (1997) Z Phys Chem 202:31
86. Thüne PC, Loos J Lemstra PJ, Niemantsverdriet JW (1999) J Catal 183:1
87. Magni E, Somorjai GA (1996) Surf Sci 345:1
88. Magni E, Somorjai GA (1995) Appl Surf Sci 89:187
89. Koranyi TI, Magni E, Somorjai GA (1999) Topics Catal 7:179

90. Magni E, Somorjai GA (1996) J Phys Chem 100:14786
91. Kim SH, Somorjai GA (2000) J Phys Chem B 104:5519
92. Fairbrother DH, Roberts JG, Rizzi S, Somorjai GA (1997) Langmuir 13:2090
93. Fairbrother DH, Roberts JG, Somorjai GA (1998) Surf Sci 399:109
94. Roberts JG, Gierer M, Fairbrother DH, van Hove MA, Somorjai GA (1998) Surf Sci 399:123
95. Rous PJ (1992) Prog Surf Sci 39:3
96. van Hove MA (1997) Surf Rev Lett 4:479
97. Heinz K, Hammer L (1998) Z Kristall 213:615
98. Tasker PW (1984) Adv Ceram 10:176
99. Pankratz LB (1984) Thermodynamic properties of halides. US Dept. of Interior Bureau of Mines, Washington DC
100. Lin JS, Catlow CRA (1993) J Mater Chem 3:1217
101. Guo XC, Hoffman A, Yates JT (1989) J Chem Phys 90:5787
102. Galli P, Barbe P, Guidetti G, Zannetti R, Martorana A, Marigo A, Bergozza M, Fichera A (1983) Eur Polym J 19:19
103. Gerbasi R, Marigo A, Martorana A, Zannetti R, Guidetti GP, Baruzzi G (1984) Eur Polym J 20:967
104. Corradini P, Barone V, Fusco R, Guerra G (1979) Eur Polym J 15:1133
105. Costuas K, Parrinello M (2002) J Phys Chem B 106:4477
106. Magni E, Somorjai GA (1995) Surf Sci 341:L1078
107. Magni E, Somorjai GA (1997) Surf Sci 377:824
108. Schmidt J (2001) Charakterisierung eines Ziegler–Natta-Modellkatalysators für die Polyethylen-Herstellung – Untersuchung mit ESR und IRAS bei der Präparation und Ethylen-Polymerisierung. PhD, Ruhr-Universität Bochum
109. Kinno S, Onaka R (1983) J Phys Soc Jpn 52:267
110. Fryburg GC, Lad RA (1975) Surf Sci 48:353
111. Den Hartog HW, Mollema P, Schaafsma TJ (1973) Phys Status Solidi B 55:721
112. Peyroche J, Girard Y, Laputte R, Guyot A (1969) Makromol Chem 129:215
113. Soga K, Terano M (1981) Macromol Chem Phys 182:2439
114. Zakharov VA, Makhtarulin SI, Poluboyarov VA, Anufrienko VF (1984) Macromol Chem Phys 185:1781
115. Chien JCW, Wu JC (1982) J Polym Sci, Polym Chem Ed 20:2461
116. Fuhrmann H, Herrmann W (1994) Macromol Chem Phys 195:3509
117. Magni E, Somorjai GA (1998) J Phys Chem B 102:8788
118. Kim SH, Tewell CR, Somorjai GA (2000) Langmuir 16:9414
119. Kvisle S, Rytter E (1984) Spectroc Acta Pt A-Molec Biomolec Spectr 40:939
120. Kim SH, Somorjai GA (2001) J Phys Chem B 105:3922
121. Ayscough PB, Thomson C (1962) Trans Faraday Soc 58:1477
122. Morehouse RL, Christiansen JJ, Gordy W (1966) J Chem Phys 45(5):1751
123. Tebbe FN, Parshall GW, Reddy GS (1978) J Am Chem Soc 100:3611
124. Toriyama K, Iwasaki M, Nunome K (1979) J Chem Phys 71(4):1698
125. Schlienz H, Beckendorf M, Katter UJ, Risse T, Freund H-J (1995) Phys Rev Lett 74:761
126. Beermann C, Bestian H (1959) Angew Chem Int Ed 71:618
127. D'yachowvskii FS, Khrushch NE, Shilov AE (1968) Kin Catal (USSR) 9:831
128. de Vries H (1961) Recl Trav Chim Pays-Bas 80:866
129. Negishi E, Kondakov DY, VanHorn DE (1997) Organometallics 16:951
130. Painter PC, Runt J, Coleman MM, Harrison IR (1977) J Polym Sci – Polym Phys Ed 15:1647

131. Seshadri K, Atre SV, Tao Y-T, Lee M-T, Allara DL (1997) J Am Chem Soc 119
132. Snyder RG, Strauss HL, Elliger CA (1982) J Phys Chem 86:5145
133. Yamamoto M, Sakurai Y, Hosoi Y, Ishii H, Kajikawa K, Ouchi Y, Seki K (2000) J Phys Chem B 104:7363
134. Hagemann H, Snyder RG, Peacock AJ, Mandelkern L (1989) Macromolecules 22:3600
135. Snyder RG (1961) J Mol Spec 7:116
136. Tasumi M, Shimanouchi T (1965) J Chem Phys 43(4):1245
137. Tobin MC, Carrano MJ (1956) J Chem Phys 25(5)
138. Krimm S, Liang CY, Sutherland GBB (1956) J Chem Phys 25(3)
139. Snyder RG (1992) J Chem Soc, Faraday Trans 88(13):1823
140. Nielsen JR, Holland RF (1961) J Mol Spec 6:394
141. Kim SH, Somorjai GA (2000) Catal Lett 68:7
142. Bartelink HJM, Bos H, Smidt J, Vrinssen CH, Adema EH (1962) Recl Trav Chim Pays-Bas 81:225
143. Sergeev SA, Poluboyarov VA, Zakharov VA, Anufrienko VF, Bukatov GD (1985) Makromol Chem 186:243
144. Paukkeri R, Lehtinen A (1993) Polymer 34:4075
145. Kim SH, Vurens G, Somorjai GA (2000) J Catal 193:171
146. Zielinski P, Dalla Lana IG (1992) J Catal 137:368
147. Scarano D, Spoto G, Bordiga S, Carnelli L, Ricchiardi G, Zecchina A (1994) Langmuir 10:3094
148. Rebenstorf B (1988) J Mol Catal 45:263
149. Zerbi G, Gallino G (1989) Polym 30:2324
150. Snyder RG, Schachtschneider JH (1963) Spectrochim Acta 19:85
151. Shiga T, Yamaoka H, Lund A (1974) Z Naturforsch A 29:653

Top Organomet Chem (2005) 16: 151–210
DOI 10.1007/b138076

Published online: 14 September 2005

Analogy between Surface and Molecular Organometallic Chemistry

Jean-Pierre Candy · Christophe Copéret (✉) · Jean-Marie Basset

Laboratoire de Chimie Organometallique de Surface, UMR 9986 CPE Lyon—CNRS,
43 Bd du 11 Novembre 1918, 69616 Villeurbanne Cedex, France
coperet@cpe.fr

Abstract Homogeneous and heterogeneous catalysis traditionally pertains to different communities, and it is thought that they are directed by different rules. In contrast, surface organometallic chemistry has been developed on the basis that chemical bonds are formed and cleaved in both cases, and therefore that common features between these two fields exist, and that they are based on similar molecular phenomena. In this review, the reaction of organometallic reagents with oxides or metallic particles, the method of characterization of these solids and their reactivity are discussed. This approach, named surface organometallic chemistry, leads to better defined heterogeneous catalysts, which can be understood at a molecular level, and therefore allowing structure-activity relationships to be obtained. Analogies and differences between molecular and surface organometallic chemistry will also be addressed.

Keywords Elementary steps · Homogeneous and heterogeneous catalysis · Metal particles · Oxide supports · Surface organometallic chemistry

1 Surface Organometallic Chemistry

Catalysis has been traditionally divided into three fields: enzymatic, heterogeneous, and homogeneous catalysis. While heterogeneous catalysts offer great advantages in terms of process designs (especially in continuous flow systems), regeneration and separation of the products from the catalyst, it usually suffers from a lack of understanding of the so-called "active sites" or "active phases", which impedes the rational development of these systems. On the contrary, homogeneous catalysts can be designed in a more rational way, and their properties easily tuned through ligand designs and an understanding of elementary steps, yet they often require a lot of technical advances to be competitive with heterogeneous catalysts. It is therefore clear that these two fields are complementary, and if it were possible to combine the advantages of both sub-disciplines, it should greatly help the development of better catalysts. This is exactly the goal of surface organometallic chemistry, which tries to design prepare heterogeneous catalysts with molecularly defined active sites.

In this review, we will specifically discuss the similarities and the differences between the chemistry on surfaces and molecular chemistry. In Sect. 2, we will first describe how to generate well-dispersed monoatomic transition metal systems on oxide supports and understand their reactivity. Then, the chemistry of metal surfaces, their modification and the impact on their reactivity will be discussed in Sect. 3. Finally, in Sect. 4, molecular chemistry and surface organometallic chemistry will be compared.

2
Surface Organometallic Chemistry on Oxide Supports

2.1
Reaction of Organometallic Complexes with Oxide Supports: the Controlled Formation of Surface Organometallic Complexes

Within the goal to generate well-defined systems, a key parameter is to understand the interaction/reaction of the molecular organometallic complex and the surface of an oxide support. This is achieved by using the following methodology: Step (1) characterization of the support; Step (2) mass balance analysis and mechanistic studies on the grafting step; Step (3) characterization of the grafted species through spectroscopy; and (Step 4) chemical reactivity studies. Each of these steps will be detailed hereafter.

2.1.1
Step 1: Characterization of the Support

In order to understand the support, it is necessary to probe its structure at the macro-, micro-, meso-, and atomic scale level. In the case of silica and more specifically Aerosil "flame" silica, it is composed of regular 50 nm spheres, free of metal and carbon traces, which have a high surface area (200–300 m^2/g) as measured by BET. Silica is a neutral support with a surface covered with siloxane bridges (of various sizes) and silanols (of various types: isolated, vicinal, and gem). The concentration and relative composition can be controlled by the thermal pre-treatment. When a thermal treatment at high temperatures (above 600–700 °C) under vacuum is applied, the surface is mainly composed of isolated silanols ($0.7 \pm 10\%$ OH/nm^2) besides siloxane bridges. At lower temperatures, the concentration of silanols is higher ($1.4 \pm 10\%$ OH/nm^2 at 500 °C and $3.5 \pm 10\%$ OH/nm^2 at 200 °C) and favours the presence of vicinal and gem silanols [2–4]. The use of higher temperatures will lower the concentration of surface silanols, but also favours the formation of strained siloxane bridges, which can become reactive (Scheme 1).

While our discussion will mainly focus on silica, other oxide materials can also be used, and they need to be characterized with the same rigorous approach. For example, in the case of meso- and microporous materials such as zeolites, SBA-15, or MCM materials, the pore size, pore distribution, surface composition, and the inner and outer surface areas need to be measured since they can affect the grafting step (and the chemistry thereafter) [5–7]. Some oxides such as alumina or silica-alumina contain Lewis acid centres/sites, which can also participate in the reactivity of the support and the grafted species. These sites need to be characterized and quantified: this is typically carried out by using molecular probes (Lewis bases) such as pyridine [8, 9],

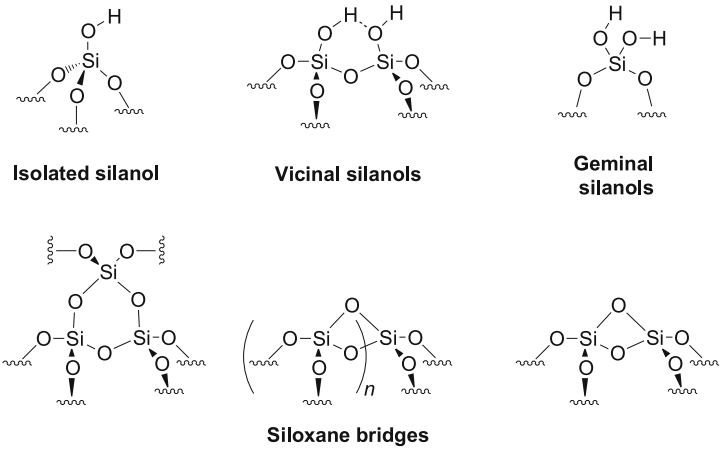

Scheme 1

phosphine or phosphine oxide [10, 11], which give characteristic signals in IR or solid state NMR spectroscopies, and which can thereby serve to quantify and/or give the strength of these sites.

2.1.2 Step 2: Mass Balance Analysis and Mechanistic Studies on the Grafting Step

After the preparation of the support (calcination and dehydroxylation) and its characterization have been completed, the second step is to study its reaction with the "molecular" organometallic complex. The grafting strategy in SOMC is based in general on the formation of a covalent bond between the support and the metal through the reaction of "reactive" functional groups at the surface of the support, a silanol in the case of silica [≡ SiO – H], and a reactive bond of the molecular complex, typically a metal-carbon bond (L_nM – R). This reaction generates the corresponding alkane (R – H) and a solid on which the metal is attached via a [≡ SiO – ML_n] bond (mechanism 1). Metal hydrides can also be used in principle for the grafting step, but it has been applied so far to Sn and Si, e.g. R_3SnH (mechanism 2) [12]. Note that several strategies have been undertaken in order to generate cationic species starting with silica by adding activators [13, 14].

$$[\equiv \mathrm{SiOH}] + [L_nM - R] \rightarrow [\equiv \mathrm{SiO} - ML_n] + R - H \quad (1)$$

$$[\equiv \mathrm{SiOH}] + [L_nM - H] \rightarrow [\equiv \mathrm{SiO} - ML_n] + H_2 \quad (2)$$

The reaction can be easily monitored by IR spectroscopy since surface silanols give a characteristic peak at 3747 cm^{-1}. In order to establish the mass balance, it is necessary to obtain an elemental analysis of the solid (M, C, H, N ...) and to measure the amount of alkane evolved during grafting.

For example, we have shown that the thermal treatment of silica is key to controlling the grafting step. Therefore, when a silica is partially dehydroxylated at 200 °C, its reaction (at room temperature) with [Ta(= CH*t*Bu) (CH_2tBu)$_3$] yields [(≡ SiO)$_2$Ta(= CH*t*Bu)(CH_2tBu)] and 2 equiv. of CH_3tBu/grafted Ta, while [(≡ SiO)Ta(= CH*t*Bu)(CH_2tBu)$_2$] is obtained along with 1 equiv. of CH_3tBu/grafted Ta when silica is partially dehydroxylated at 700 °C
(Scheme 2, vide infra for characterization of these structures) [15]. At an intermediate temperature of 500 °C, a 65/35 mixture of these two complexes is obtained [16]. The proposed structure is further confirmed by the mass balance analysis since hydrolysis or ethanolysis of the resulting solid yields the complementary amounts of neopentane, these are 2 and 3 equiv. of neopentane/Ta for [(≡ SiO)$_2$Ta(= CH*t*Bu)(CH_2tBu)] and [(≡ SiO)Ta(= CH*t*Bu)(CH_2tBu)$_2$], respectively. Moreover, elemental analysis provides further information: indeed, 4.2 wt % of Ta grafted onto silica partially dehydroxylated at 700 °C corresponds to 0.22 mmol of Ta/g of solid [17, 18]. This is comparable to the amount of silanol present on this support (0.26 mmol OH/g), which shows that most of them have reacted during grafting (as observed by IR spectroscopy).

These observations are very general, and typically on a silica pre-treated at 200 °C, bissiloxy complexes are obtained (Scheme 3) [15, 19, 20]. Conversely, a silica treated at 700 °C will yield monosiloxy complexes.

Yet, mass balance analysis should be checked thoroughly since there can be some deviations/exceptions depending on the support and the metal. For instance, while the reaction of [Zr(CH_2tBu)$_4$] with $SiO_{2-(500)}$ generates a monosiloxy species, its reaction with a MCM-41 material partially dehydroxylated at 500 °C yields a bissiloxy surface complex [21], and the reaction

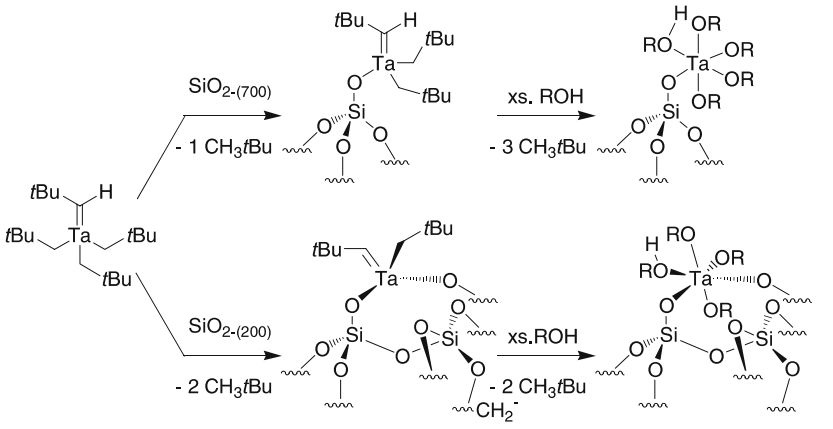

Scheme 2

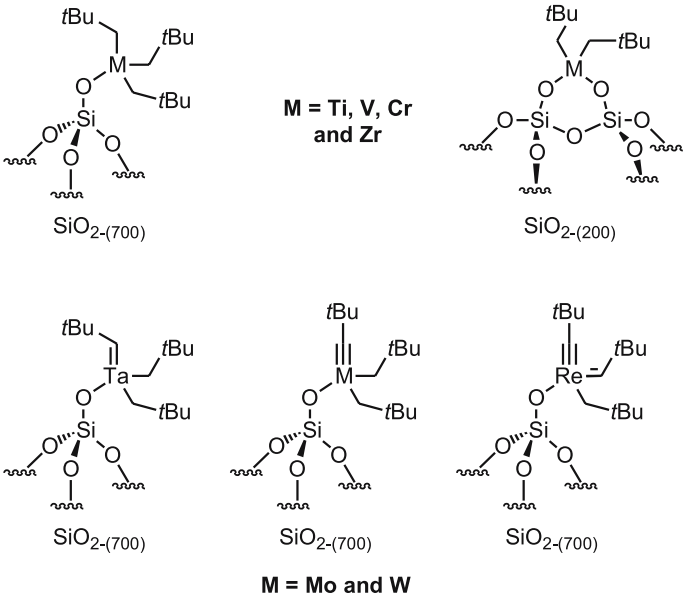

Scheme 3

of [Ta(= CH*t*Bu)(CH_2*t*Bu)$_3$] with $SiO_{2-(500)}$ generates a mixture of mono- and bissiloxy species (vide supra) [15, 16].

Mass balance analysis is easily performed on organometallic reagents since the molecule released, an alkane, does not react with the support. However, the use of alkoxide and amide metal complexes as molecular precursors can generate some difficulty. In these cases, alcohols and amines are formed upon grafting, and they can remain coordinated to the metal or further react with the surface of the oxide, and can give rise to complex reactions on surfaces [22–25]. In the specific case of $[\{(t\mathrm{BuO})_3\mathrm{SiO}\}_x\mathrm{M}]$ complexes, grafting occurs mainly via cleavage of the (O – M) bonds, thus liberating [*t*Bu_3SiOH] and providing the corresponding complexes $[(\equiv \mathrm{SiO})\mathrm{M}\{\mathrm{OSi}(O t\mathrm{BuO})_3\}_{x-1}]$, and in some cases a small amount of *t*BuOH is formed consistent with a grafting via cleavage of the (Si – O) bond. This approach has been used to support Ti^{IV} and Fe^{III} complexes on MCM-41 and SBA-15 materials. Grafting $[\mathrm{Fe}\{\mathrm{OSi}(O t\mathrm{BuO})_3\}_3 \bullet \mathrm{THF}]$ yields selectively the mononuclear surface complex $[(\equiv \mathrm{SiO})\mathrm{Fe}\{\mathrm{OSi}(O t\mathrm{BuO})_3\}_2]$ [26], while grafting of $[\mathrm{Ti}\{\mathrm{OSi}(O t\mathrm{BuO})_3\}_4]$ is less selective, giving $[(\equiv \mathrm{SiO})\mathrm{Ti}\ \{\mathrm{OSi}(O t\mathrm{BuO})_3\}_3]$ and $[\{(\equiv \mathrm{SiO})(t\mathrm{BuO})_2\mathrm{SiO}\}\mathrm{Ti}\{\mathrm{OSi}(O t\mathrm{BuO})_3\}_3]$ [27]. It is noteworthy that by replacing one of the bulky siloxy by an *i*PrO ligand, grafting on SBA-15 (a large pore mesoporous silica) occurs selectively to give a mononuclear Ti centre, $[(\equiv \mathrm{SiO})\mathrm{Ti}(O i\mathrm{Pr})\{\mathrm{OSi}(O t\mathrm{BuO})_3\}_2]$ and [*t*Bu_3SiOH] in contrast to $[\{\mathrm{Ti}[(O i\mathrm{Pr})_4\}_2]$, which gives polynuclear species (Scheme 4) [23]. Mononuclear $[(\equiv \mathrm{SiO})\mathrm{Ti}(O i\mathrm{Pr})_3]$ and $[(\equiv \mathrm{SiO})_2\mathrm{Ti}(O i\mathrm{Pr})_2]$ seems accessi-

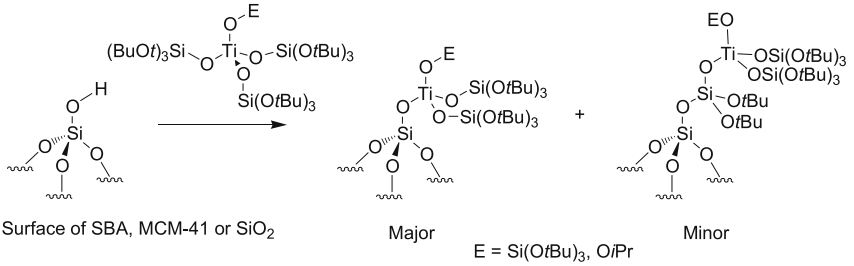
(BuOt)3Si
Si(OtBu)3
Surface of SBA, MCM-41 or SiO2
Major
Minor
E = Si(OtBu)3, OiPr

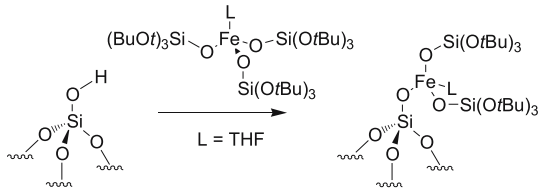
(BuOt)3Si
Si(OtBu)3
L = THF
Surface of SBA

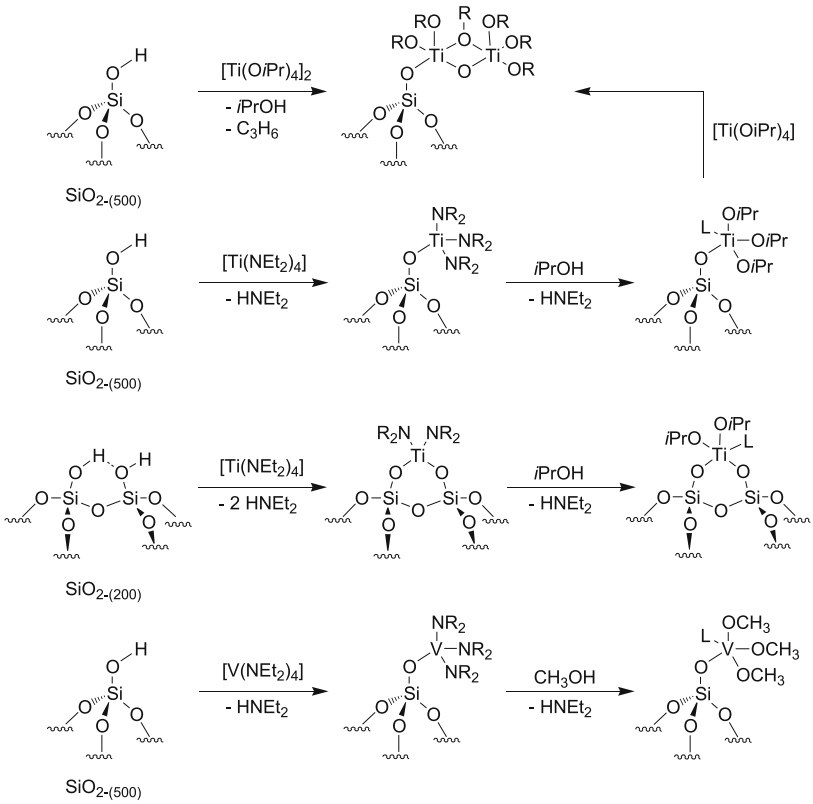
[Ti(OiPr)4]2
- iPrOH
- C3H6
[Ti(OiPr)4]
SiO2-(500)
[Ti(NEt2)4]
- HNEt2
iPrOH
- HNEt2
SiO2-(500)
[Ti(NEt2)4]
- 2 HNEt2
iPrOH
- HNEt2
SiO2-(200)
[V(NEt2)4]
- HNEt2
CH3OH
- HNEt2
SiO2-(500)

Scheme 4

ble through the alcoholysis of the corresponding surface amido complexes $[(\equiv SiO)Ti(NEt_2)_3]$ and $[(\equiv SiO)_2Ti(NEt_2)_2]$.

The grafting step can also provide further information on the reactivity of the organometallic complex. Tetraneopentylmetal complexes such as $[Ti(CH_2tBu)_4]$ and $[Zr(CH_2tBu)_4]$ react with the silanols of SiO_2 via a simple electrophilic cleavage of the M – C bond as shown by the formation of monodeuterated neopentane (D-CH_2tBu) when deuterated silica is used (mechanism 3) [28, 29].

$$[\equiv SiOD] + [M(CH_2R)_4] \rightarrow [\equiv SiOM(CH_2R)_3] + RCH_2 - D \quad (3)$$

On the other hand, in the case of $[Ta(=CHtBu)(CH_2tBu)_3]$ and $[Re(\equiv CtBu)(=CHtBu)(CH_2tBu)_2]$, which contain different types of metal-carbon bonds, the grafting mechanism can be more complex then one imagines. In the first example, during grafting of $[Ta(=CHtBu)(CH_2tBu)_3]$ on deuterated silica, both non- and monodeuterated neopentanes are formed [16]. This leads us to propose that grafting occurs through two concomitant mechanisms: (1) a simple electrophilic cleavage of the Ta – C bond, which forms 1 DCH_2tBu/Ta; and (2) an addition of the silanol onto the carbene yielding a pentacoordinated complex $[(\equiv SiO)Ta(CH_2tBu)_3(CHXtBu)]$ (X = D when silica is deuterated), which upon decomposition into $[(\equiv SiO)Ta(=CHtBu)(CH_2tBu)_2]$ gives mono- and non-deuterated neopentane only with a 3/8 and 5/8 probability, respectively (Scheme 5).

The formation of the pentacoordinated intermediate was confirmed later by performing the reaction at low temperature and by using a poly-

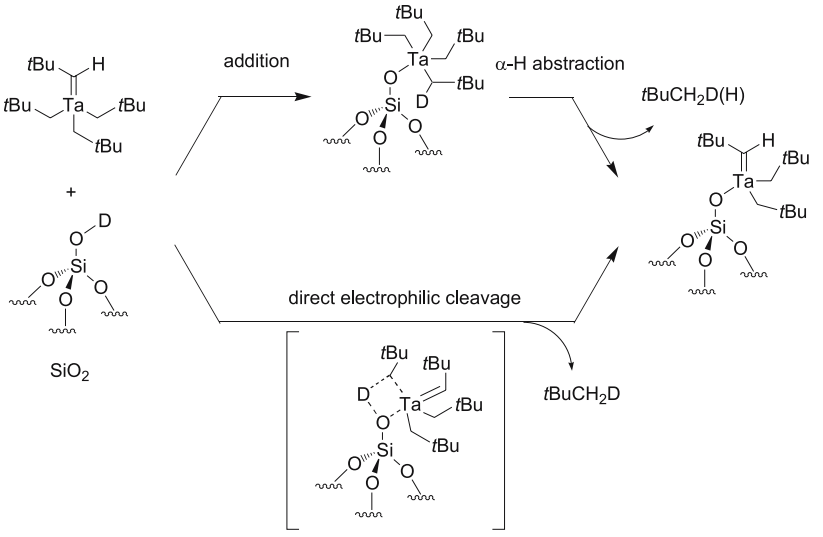

Scheme 5

oligomeric silsesquisioxane $[(c\text{-}C_5H_9)_7Si_7O_{12}Si-OH]$ as a soluble model of silica (Scheme 6) [17], whose reaction can be easily monitored by solution NMR. Upon the addition of $[(c\text{-}C_5H_9)_7Si_7O_{12}Si-OH]$ in a red solution of $[Ta(=CHtBu)(CH_2tBu)_3]$ in C_6D_6, the reaction mixture turns pale yellow and displays a peak at 108.7 ppm in the ^{13}C NMR spectrum, which has been assigned to the methylene of the neopentyl of $[((c\text{-}C_5H_9)_7Si_7O_{12}Si\text{-}O)Ta(CH_2tBu)_4]$. Then, the reaction mixture slowly turns orange, and this signal is replaced by two signals at 245.4 and 95.7 ppm corresponding respectively to the methine (=CH*t*Bu) and the methylene (CH_2tBu) carbons in $[(c\text{-}C_5H_9)_7Si_7O_{12}Si-O)Ta(=CHtBu)(CH_2tBu)_2]$. Similar solid state NMR data have been obtained while studying the reaction of $[Ta(=CHtBu)(CH_2tBu)_3]$

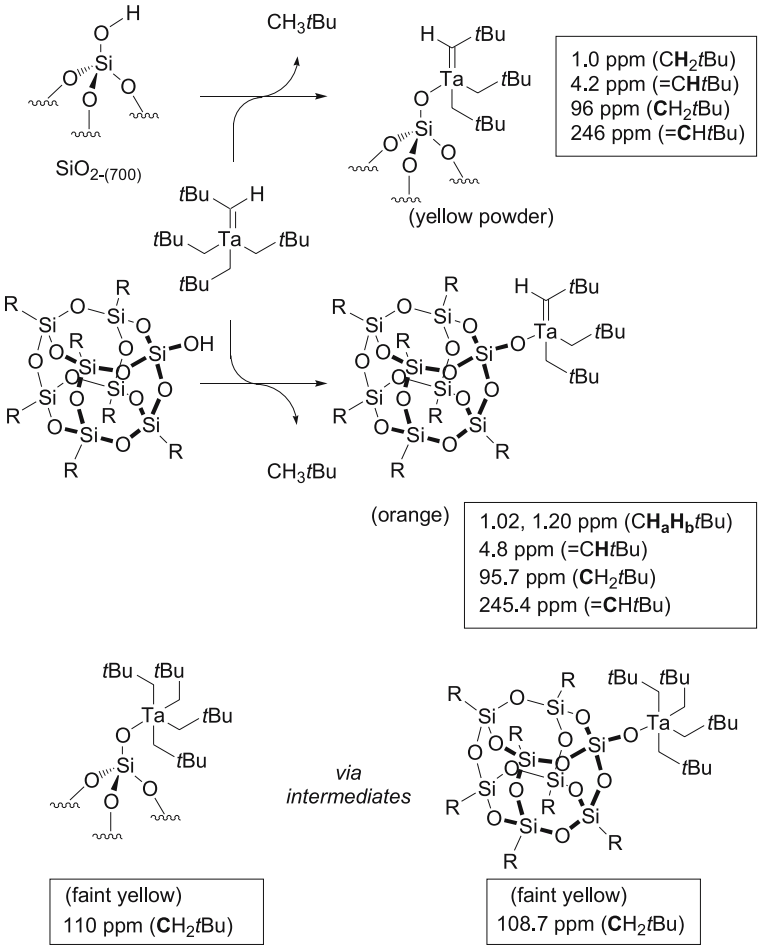

Scheme 6

with silica at low temperatures, confirming the formation of the intermediate $[(\equiv.\,SiO)Ta(CH_2tBu)_4]$.

In the second example, three types of perhydrocarbyl ligands are present in the molecular precursor $[Re(\equiv CtBu)(=CHtBu)(CH_2tBu)_2]$: neopentyl, neopentylidene, and neopentylidyne ligands [30]. Therefore, three mechanisms of grafting can be possible (Scheme 7): (mechanism 1) direct cleavage of the Re – C bond of the neopentyl ligand by a silanol O – H bond (electrophilic cleavage); (mechanism 2) addition of a silanol O – H bond onto the neopentylidene moiety followed by α-H abstraction; and/or (mechanism 3) addition of a silanol O – H bond onto the neopentylidyne moiety followed by α-H abstraction. Grafting the $[Re(\equiv CtBu)(=CHtBu)(CH_2tBu)_2]$ on $SiO_{2-(700)}$ selectively ^{13}C labelled on the CH and CH_2 carbons gives a surface complex having no carbynic resonance in its ^{13}C solid state NMR spectrum, which rules out grafting through protonation of the alkylidyne ligand (mechanism 3).

When grafting is performed with a deuterated silica (92% deuterated), it yields neopentane on average $74 \pm 5\%$ mono-deuterated and $26 \pm 5\%$ non-deuterated according to mass spectrometry, which shows that grafting occurs via the mechanisms (mechanism 1) and (mechanism 2) in 61 and $39 \pm 10\%$, respectively (Scheme 8). Since $[(\equiv SiO)Re(\equiv CtBu)(=CHtBu)(CH_2tBu)]$ contains two alkyl ligands for one alkylidene ligand, the reactivity ratio between alkylidene and alkyl ligands is 1.3 ± 0.6, showing that in this case, alkyl and alkylidene moieties have in fact a similar reactivity towards silanols.

In molecular chemistry, the reaction of $[Re(\equiv CtBu)(=CHtBu)(CH_2tBu)_2]$ with Brönsted acids (HX, X = Cl, OC_6F_5, BF_4, OTf…) gives $[Re(\equiv CtBu)(CH_2tBu)_3X]$ as a stable product resulting exclusively from the protonation

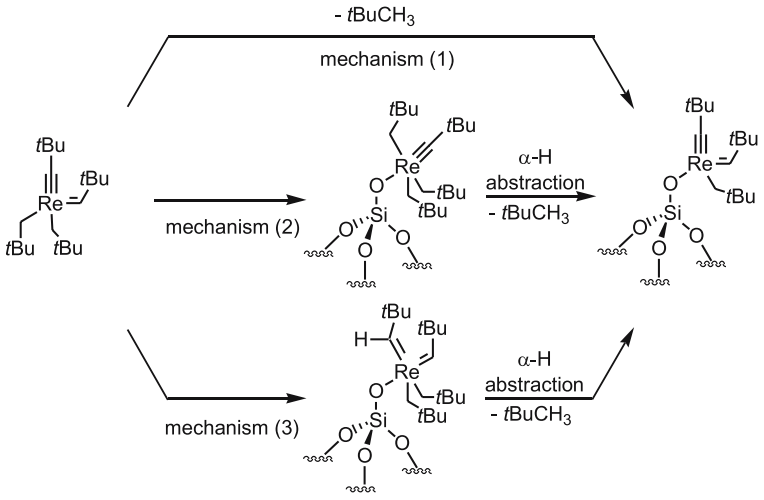

Scheme 7

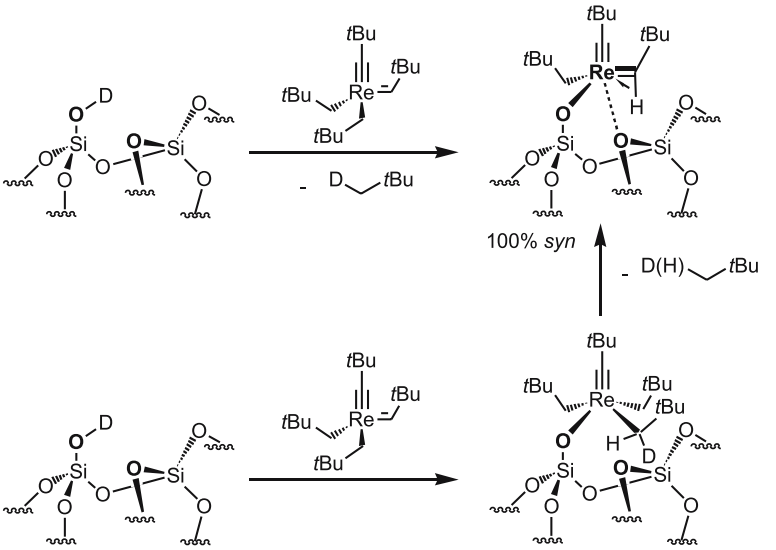

Scheme 8

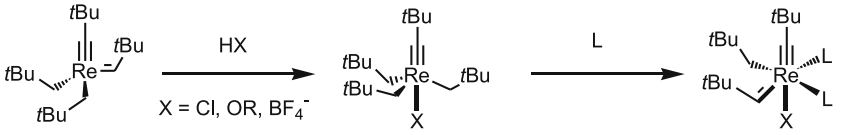

Scheme 9

onto the alkylidene moiety (Scheme 9) [31]. These compounds are transformed into the corresponding alkylidene complexes only upon adding donor ligands such as pyridine or acetonitrile. The presence of siloxane bridges in surface complexes as evidenced by EXAFS (vide infra) can probably explain this difference of reactivity.

2.1.3 Step 3: Characterization of the Grafted Species Through Advanced Spectroscopic Techniques

Generality

One key aspect of SOMC is the determination of the structure of surface complexes at a molecular level; one of the reasons being that our goal is to assess structure-activity relationships in heterogeneous catalysis, which requires a firm characterization of active sites or more exactly active site precursors. While elemental analysis is an essential first step to understand how the organometallic complex reacts with the support, it is necessary to gather spectroscopic data in order to understand what are the ligands and

how they are interacting with the grafted metal (including those of the surface). IR spectroscopy is an important tool, especially in the study of the grafting step: the disappearance of silanol bands (3747 cm^{-1}) upon contacting an organometallic complex provides the first evidence for the formation of a bond between the metal and the support. This technique also allows other surface reactions to be rapidly evaluated. The modification of the structure of the surface complex upon addition of a reagent or thermal treatments can indeed be easily monitored.

Since molecular and surface organometallic complexes have more and more complex structures, IR spectroscopy or any other single technique is not sufficient to understand the structure of a system. It is therefore necessary to combine data from several techniques. In molecular chemistry, X-ray crystallography, NMR, and ESR spectroscopies provide a detailed picture of the coordination sphere around a metal centre. In *surface organometallic chemistry*, we use the corresponding techniques for amorphous solids. Advanced solid state NMR (1D and 2D) is probably the most powerful method for structure determination when applicable. In some cases, ESR and XANES can be used to determine the oxidation state and geometry of the metal complex. Extended X-ray fine structure spectroscopy (EXAFS) can replace X-ray crystallography to afford distances (with a high accuracy) and average coordination numbers around the metal (with some uncertainty). The combined use of these techniques along with the accumulated knowledge of molecular chemistry including model reactions between an organometallic reagent and a soluble silica analogue will be critical to an accurate description of the structure of a surface complex (vide supra).

Examples of Structure Determination Through the Combined Use of Advanced Spectroscopic Techniques

One exemplary case is the grafting of [Re(≡ C*t*Bu)(= CH*t*Bu)(CH_2*t*Bu)$_2$] on silica partially dehydroxylated at 700 °C [30, 32]. During grafting, silanols are consumed according to IR spectroscopy and about 1.06 ± 0.13 equiv. of CH_3*t*Bu is evolved. The corresponding solid contains 15.5 ± 0.8 carbons per grafted Re. Therefore, the data are consistent with the loss of approximately one equivalent of neopentane during grafting, leaving an average of three "neopentyl-like" ligands around the metal centre. The complexity of the structure led us to undertake advance solid state NMR spectroscopy. The ^{1}H solid state NMR spectrum of [(≡ SiO)Re(≡ C*t*Bu)(= CH*t*Bu)(CH_2*t*Bu)] displays signals at 11.0, 3.0, 2.6, 1.5, 1.3 and 1.1 ppm, which can be assigned to the carbene proton (= CH), the two diastereotopic protons (CH_aH_b) and the methyl groups of the three different *t*Bu groups (Fig. 1 and Scheme 10). While the ^{13}C CP/MAS spectrum of the natural abundance sample gives little information (no peak above 100 ppm), a H-decoupled ^{13}C solid state NMR spectrum of a 10% ^{13}C-enriched sample is in agreement with the

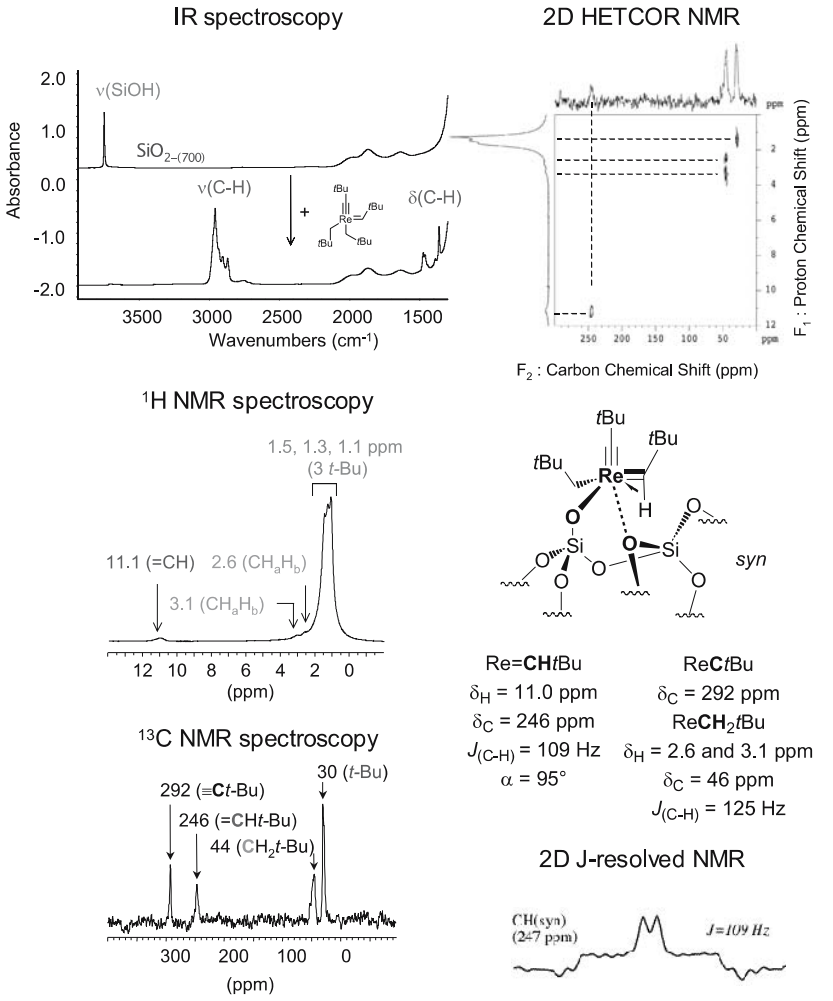

Fig. 1 Structural determination through the combined use of spectroscopic techniques

presence of three types of hydrocarbyl ligands around Re: a neopentyl (46 ppm, CH_2tBu), a neopentylidene (246 ppm, =CH*t*Bu), and a neopentylidyne (292 ppm, ≡C*t*Bu). These assignments are fully confirmed by 2D HETCOR (heteronuclear correlation) solid state NMR using magic angle spinning (MAS). By using short contact times during the pulse sequence, it is possible to selectively detect the protons directly linked to a carbon: firstly, the two signals at 2.6 and 3.0 ppm originally assigned to the two diastereotopic protons are indeed borne by the same carbon, and secondly the signal at 11 ppm in the H dimension correlates with that at 246 ppm in the C dimension in agreement with their assignments to the carbenic fragment (Fig. 1). Using longer contact times (> 1 ms), extra correlation peaks appear, and they arise

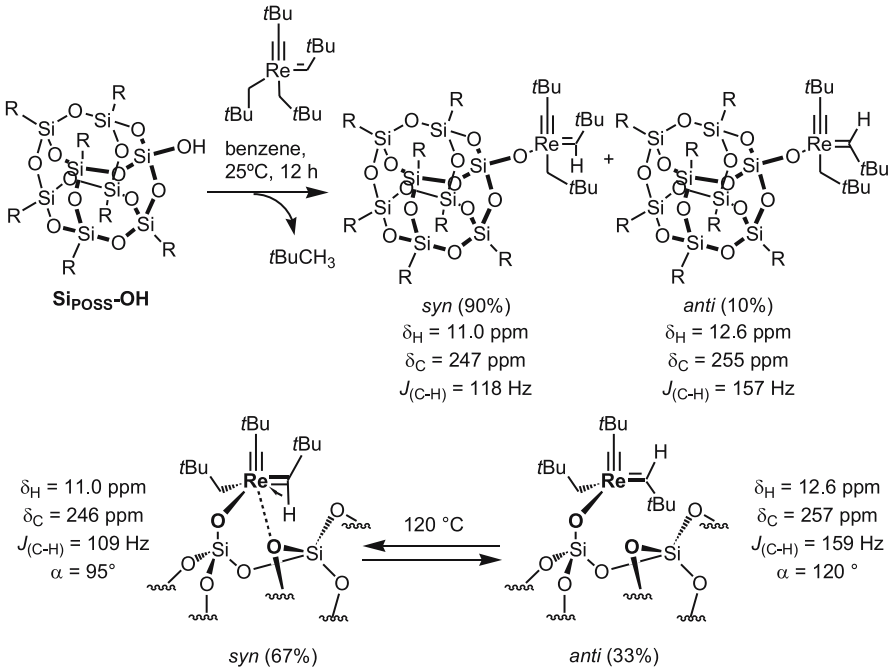

Scheme 10

from longer range dipolar through-space interactions, which allow the full ^{13}C NMR spectrum of [(≡SiO)Re(≡C*t*Bu)(= CH*t*Bu)(CH_2*t*Bu)] (including all quaternary carbons) to be reconstituted (Table 1).

EXAFS data are in agreement with the structure determined by NMR with two carbons at relatively short distances (not resolved at 1.79 Å), corresponding to the (= **C**H*t*Bu) and (≡ **C***t*Bu) ligands, another carbon and an

Table 1 Chemical shift assignments for *syn*-[(≡SiO)Re(≡C*t*Bu)(= CH*t*Bu)(CH_2*t*Bu)] through the combined use of 1D and 2D HETCOR NMR data

^{1}H NMR, δ/ppm		^{13}C NMR, δ/ppm[a]	
Resonances	Assignments	Resonances	Assignments
1.1	{C(C**H**$_3$)$_3$}	28	{≡CC(**C**H$_3$)$_3$)}
1.3	{C(C**H**$_3$)$_3$}	30	{C(**C**H$_3$)$_3$)}
1.5	{≡CC(C**H**$_3$)$_3$}	30	{CH$_2$C(**C**H$_3$)$_3$)}
2.6	{C**H**$_A$H$_B$*t*Bu}	44	{= CH**C**(CH$_3$)$_3$)}
3.1	{CH$_A$**H**$_B$*t*Bu}	46	{**C**H$_2$*t*Bu}
11.1	{= C**H***t*Bu}	53	{≡**C**C(CH$_3$)$_3$)}
		246	{= **C**H*t*Bu}
		292	{≡ **C***t*Bu}

oxygen atom at larger distances (not resolved at 2.01 Å), corresponding to the ($\mathbf{C}H_2t$Bu) and ($\equiv$ Si **O**) ligands. Nonetheless, EXAFS data fit best when an extra ligand, an oxygen at 2.42 Å, is added to the model. It suggests that there is a dative bond from a siloxane bridge to the rhenium centre.

This structure can be further refined by using 2D *J*-resolved 2D solid state NMR spectroscopy, which allows multiplicities and J(C – H) coupling constants to be obtained. Noteworthy is the low coupling constant measured for the carbene ligand: the = C**H***t*Bu (246 ppm) appears as a doublet with a low $J_{\text{C-H}}$ coupling of 110 Hz [33]. This low $J_{\text{C-H}}$ value indicates that this C – H bond is probably elongated, which is consistent with a 3 centre-2 electron bond, also called agostic interaction [34]. The (Re – C – H) bond angle is distorted from the typical 120° value, and it is possible to evaluate the (Re – C – H) bond angle to about $95 \pm 10°$ since $J_{\text{C-H}}$ values have been correlated to that angle [35]. Such types of interaction points towards a *syn* configuration of the carbene ligands (Fig. 1 and Scheme 10) [31, 36].

Soluble molecular models of silica like alkyl silanols or polyoligomeric silsesquisioxanes (POSS) can also help to assign surface structures [37–40]. For example, the reaction of the molecular complex with either [Ph_3SiO – H] or [(*c*-$C_5H_9)_7Si_7O_{12}SiO$ – H] in benzene solution (Scheme 10) yields the corresponding monosiloxy complexes [Ph_3SiO – Re($\equiv$ C*t*Bu)(= CH*t*Bu)(CH_2tBu)] and [[(*c*– $C_5H_9)_7Si_7O_{12}Si$ – O]– Re($\equiv$ C*t*Bu)(= CH*t*Bu)(CH_2tBu)]. In both cases however, they are obtained as a 10-to-1 mixture of the *syn*- and the *anti*-rotamers. The chemical shift data for the *syn*-rotamers of the molecular complex exactly match those obtained for the surface complex, while the NMR data of the *anti*-rotamers are quite different [30–32]. In fact, when the surface complex *syn*-[($\equiv$SiO)Re($\equiv$C*t*Bu)(= CH*t*Bu)(CH_2tBu)] is heated at 120 °C under Ar for 30 min, a 2 : 1 mixture of *syn*- and *anti*-isomers is formed. The new set of NMR signals in ^{1}H and ^{13}C NMR spectra is fully consistent with their assignments to those of the *anti* rotamers. 2D HETCOR and *J*-resolved solid state NMR spectroscopies on this mixture confirmed these assignments: the **CH***t*Bu (246 ppm) appears as a doublet with a $J_{\text{C-H}}$ coupling constant of 159 Hz as expected for an *anti* isomer [33].

The grafting of [Ta(= CH*t*Bu)(CH_2tBu)$_3$] on a silica partially dehydroxylated at 700 °C has also been studied in detail, and it shows similar structural characteristics: (1) formation of a monosiloxy complex; (2) grafting via both reaction of the carbene and the alkyl ligands in contrast to the soluble molecular model, which reacts exclusively through the carbene ligand; (3) the NMR chemical shift data sets of the model and the surface complex match; (4) interaction of the tantalum with an adjacent siloxane bridge; and (5) the presence of an agostic interaction of the C – H bond of carbene ($J_{\text{C-H}}$ = 80 Hz), which is quite comparable to that observed for similar molecular complexes (Scheme 11) [41, 42].

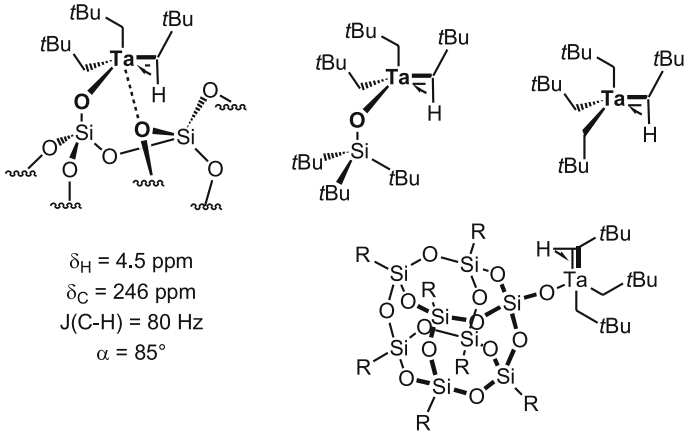

Scheme 11

2.1.4
Step 4: Chemical Reactivity of Surface Complexes

Reactivity with Alcohol and H_2O

These reactions have been mainly used to quantify the remaining perhydrocarbyl ligand attached to the metal after grafting in order to perform the mass balance analysis and to evaluate the structure of the surface complexes. This reaction is limited to early transition metals, and for example the reaction is not complete even at 200 °C for group 6 metals as evidenced by the remaining alkyl fragments in the IR spectrum, which is similar to what has been observed in molecular chemistry since the hydrolysis of $[W(\equiv CtBu)(CH_2tBu)_3]$ with an excess of H_2O gives a stable alkyl complex [43]. The use of D_2O or ROD can also allow us the nature of the metal-carbon bond to be understood, that is to differentiate between a single or a double bond. Moreover, it has been used in some cases to generate cleanly the corresponding alkoxide derivatives (vide infra) [44].

$$[\equiv SiOM(CH_2R)L_n] + R''OD(H) \rightarrow [\equiv SiOM(OR'')L_n] + RCH_2D(H) \quad (4)$$

$$[\equiv SiOM(= CHR)L_n] + R''OD(H) \rightarrow [\equiv SiOM(OR'')_2L_n] + RCHD_2(H) \quad (5)$$

$$[\equiv SiOM(\equiv CR)L_n] + R''OD(H) \rightarrow [\equiv SiOM(OR'')_3L_n] + RCHD_3(H) \quad (6)$$

2.1.4.1
Reactivity with Ketones

In molecular chemistry, ketones react cleanly with alkylidene ligands via a pseudo-Wittig reaction. This reaction yields a metalloxo complex and an

olefin, which can help to characterize and quantify the carbene ligands. For example, $[(\equiv SiO)Ta(=CHtBu)(CH_2tBu)_2]$ [16] and $[(\equiv SiO)Mo(=NH)(=CHtBu)(CH_2tBu)]$ [45] reacts with acetone to give one equivalent of $(Me_2C=CHtBu)/M$, which is consistent with the proposed structure.

$$[\equiv SiOM(=CHR)L_n] + (CH_3)_2C=O \rightarrow [\equiv SiOM(=O)L_n] + (CH_3)_2C=CHR \quad (7)$$

2.1.4.2 Reactivity with H_2

In the presence of H_2, perhydrocarbyl surface complexes loose their ligands through the hydrogenolysis of their metal carbon bonds to generate putative hydride complexes, which further react with the neighbouring surface ligands, the adjacent siloxane bridges (Eqs. 8–9) [46, 47].

$$[\equiv SiOM(CH_2R)L_n] + H_2 \rightarrow [\equiv SiOM(H)L_n] + RCH_3 \quad (8)$$

$$[\equiv SiOM(H)L_n] + (\equiv SiOSi\equiv) \rightarrow [(\equiv SiO)_2ML_n] + (\equiv SiH) \quad (9)$$

The parent surface complexes often show the presence of an oxygen atom of a siloxane bridge in the second coordination sphere of the metal, and when this organometallic fragment is transformed into a hydride, it reacts with the surface siloxane bridge to generate M – O and Si – H bonds. In the case of $[(\equiv SiO)Zr(CH_2tBu)_3]$, the treatment under H_2 generates two surface com-

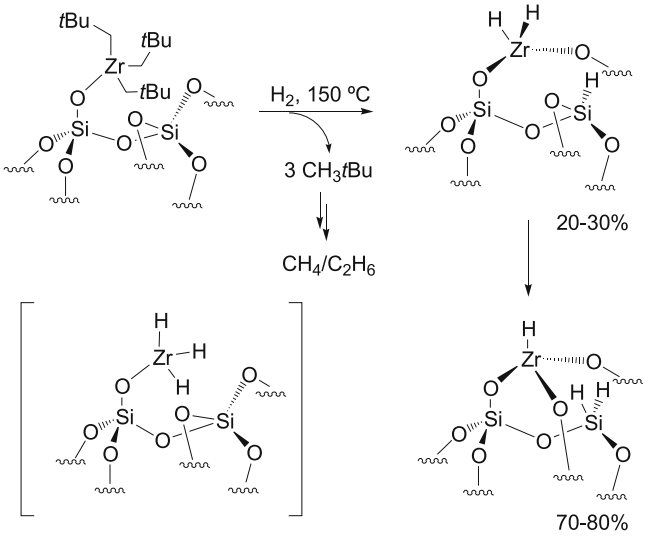

Scheme 12

plexes: $[(\equiv SiO)_2Zr(H)_2]$ and $[(\equiv SiO)_3Zr\text{-}H]$ along with $[(\equiv SiO)_3Si-H]$ and $[(\equiv SiO)_2Si(\text{-}H)_2]$, respectively (Scheme 12) [48–51].

The structures of these complexes and of the adjacent (SiH) fragments has been firmly established by using double quanta (DQ) 2D solid NMR spectroscopy [51], which can readily distinguish a pair of neighbouring protons from an isolated one. For example, the ^1H NMR chemical shift of the zirconium dihydride is 12 ppm, and it gives an autocorrelation peak at 24 ppm in the DQ 2D NMR spectra since two dipoles of the same chemical shifts interact with each other. On the other hand, the zirconium monohydride ($\delta = 10.4$ ppm) shows a correlation peak at 14.8 ppm (10.4 + 4.4) in agreement with the interaction of the monohydride ($\delta = 10.4$ ppm) and another dipole having a chemical shift of 4.4 ppm, (Si – H). It is therefore possible to characterize at the molecular level such types of systems. Note that the reaction of a single well-defined system with the surface yields two surface complexes. In fact, the well-defined mono-siloxy complex is probably surrounded by various different local environments since the surface of silica is heterogeneous (amorphous solid), and therefore its reaction with the surface can be translated into the formation of several species.

In the case of tantalum, the treatment under H_2 at 150 °C of a mixture of $[(\equiv SiO)Ta(=CHtBu)(CH_2tBu)_2]$ and $[(\equiv SiO)_2Ta(=CHtBu)(CH_2tBu)]$ is transformed into mainly one surface species: $[(\equiv SiO)_2Ta-H]$ (Scheme 13) [52]. However, when the temperature is increased step by step to 450 °C, this surface complex is gradually converted to $[(\equiv SiO)_3Ta]$ and (Si – H) [53]. The gradual reactivity of $[(\equiv SiO)_2Ta-H]$ with adjacent siloxane bridges also speaks for an heterogeneity of the silica surface.

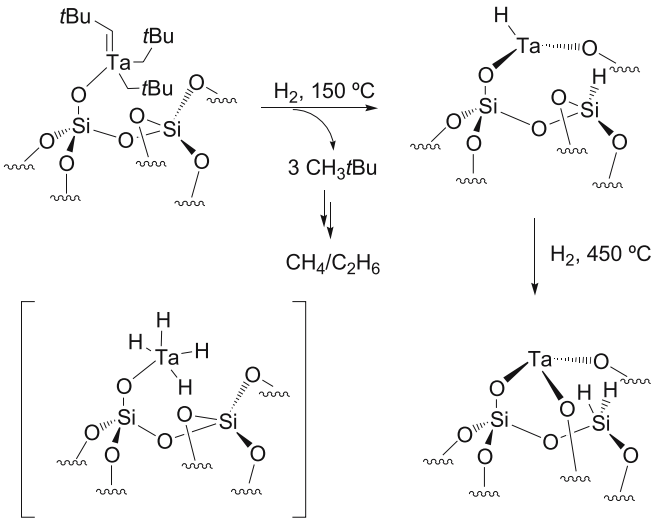

Scheme 13

2.1.5
Conclusion

It is therefore possible to control the number of bonds between the surface and the anchored metal by controlling the concentration of hydroxyls of the support. This can be readily achieved by selecting the right temperature of partial dehydroxylation of the support.

It is also possible to access trisgrafted species, but they are usually obtained upon further reaction of the grafted complex with the surface through the opening of adjacent siloxane bridges. This has typically been observed when group 4 surface complexes are heated under H_2, but unfortunately this reaction leads also to the bisgrafted species. Controlling this step is currently under investigation.

Since we are interested in evaluating structure-activity relationships (see Sect. 2.2), it is important to combine several analytical methods to allow a characterization at a molecular level: for example, elemental analysis, IR, and advanced NMR spectroscopies, EXAFS and chemical reactivity studies.

2.2
Catalytic Reactions and Elementary Steps

Pioneering works in this area started in the 1960s by polymer scientists like D. Ballard at ICI and Y. Yermakov at the Novosibirsk Institute of Catalysis [54, 55]. The need for polymers with better properties and for better technologies (gas phase processes) has led to the development of various strategies to obtain supported catalytic systems [56–58]. Here, we will concentrate on reactions leading to basic chemicals, and a comparison between homogeneous and heterogeneous catalysts will be performed when possible.

2.2.1
Oxidation, Transesterification and Related Reactions

In industry, one of the key epoxidation processes, the production of propene oxide from propene, uses a catalyst based on TiX_4 supported on SiO_2 [59]. After years of research, the nature of the active site is still not known. Model studies by using surface organometallic chemistry or soluble analogues have shown that the most active and selective site is probably the "tripodal" system (Scheme 14) [44, 60–62]. These properties probably correspond to a compromise between an accessible titanium centre and an increase of the electrophilicity of the metal centre through the presence of the right number of siloxy substituents. Moreover, Tilley et al. have observed a similar trend for their Ti-based catalyst systems, which are obtained by dispersing mononuclear Ti siloxide complexes on various silica supports [27]. The performance of the catalysts in the epoxidation of cyclohexene with cumyl-

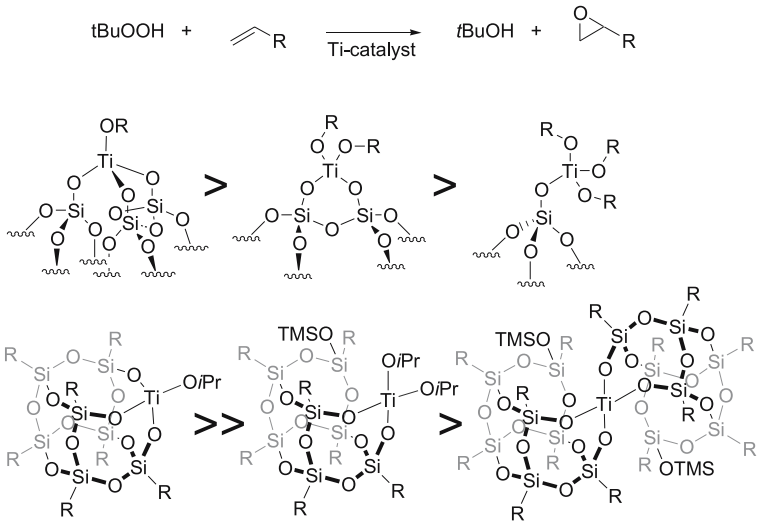

Scheme 14

hydroperoxide (CHP) can be ranked as follows: [Ti{OSi(O*t*BuO)$_3$}$_4$]/SBA-15 ≈ [Ti(O*i*Pr){OSi(O*t*BuO)$_3$}$_3$]/SBA-15 > [Ti(O*t*Bu)$_3${OSi(O*t*BuO)$_3$}]/SBA-15 ≫ [Ti(O*i*Pr)$_4$]/SBA-15. Moreover, they have also shown that, in the case of [(≡SiO)Ti(O*i*Pr){OSi(O*t*BuO)$_3$}$_2$], high surface area materials (SBA-15 > MCM-41 > SiO_2) and more importantly low loading of Ti, which assures a dispersion of the Ti centres, are critical to obtain good catalytic activities and selectivities in agreement with the necessity to have isolated sites as already shown in other studies [63].

Well-defined supported group 4 alkoxides also catalyze a variety of reaction, such as the reduction of ketone through hydrogen transfer [64, 65], the esterification of acids [66] or the transesterification of esters. In the case of the transesterification, the conversion of methyl methacrylate into its butyl derivative is efficiently catalyzed by [(≡SiO)$_3$Zr(acac)] (Scheme 15), and seems stable under the reaction conditions (no leaching) [67]. An advantage of a molecular approach to the preparation of heterogeneous catalysts is that it has been possible to correlate the loss of activity with the build-up of the corresponding *n*-butoxide derivatives, [(≡SiO)$_3$Zr(OBu)]. Therefore, a simple regeneration procedure has been developed through the addition of acetylacetone.

2.2.2 Olefin Metathesis

Olefin metathesis has been discovered on heterogeneous catalysts, which are typically transition-metal oxides supported on oxide supports, for example

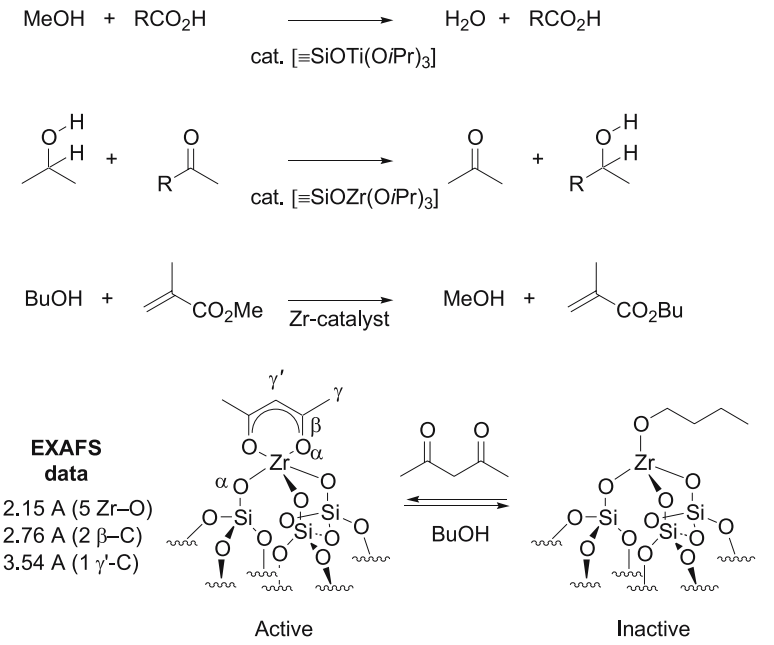

Scheme 15

MoO_3, WO_3, and Re_2O_7 supported on silica, silica-alumina or alumina. These systems usually work at high temperatures (150–450 °C), the exception being Re_2O_7/Al_2O_3, which can work at room temperatures [68–70]. In these cases, the active site(s) is not known because of the complexity of these systems, but it is now commonly accepted that metallocarbenes are probably formed and that they are the propagating species [71], even though the mechanism of formation of such types of intermediates is still a matter of debate. While they are used in industry to prepare basic chemicals, such as propylene from ethylene and 2-butenes, they are, however, not compatible with the usual functional groups, which prevents their use in the fine chemical industry [72, 73]. On the other hand, a variety of well-defined molecular complexes have been prepared, and their use in the polymer and in organic synthesis have started to emerge since they show good performances: good tolerance to functional groups, good turnovers and good selectivities (Scheme 16) [74–78].

One of the goals of surface organometallic chemistry is to combine the advantage of heterogeneous (simple processes, usually simple regeneration procedure) and homogeneous catalysis (well-defined systems, structure-activity relationship, compatibility with functionalized olefins). Therefore, a family of well-defined group 5–7 metallocarbenes and carbynes have been developed and fully characterized through surface organometallic chemistry (Scheme 17) [79, 80].

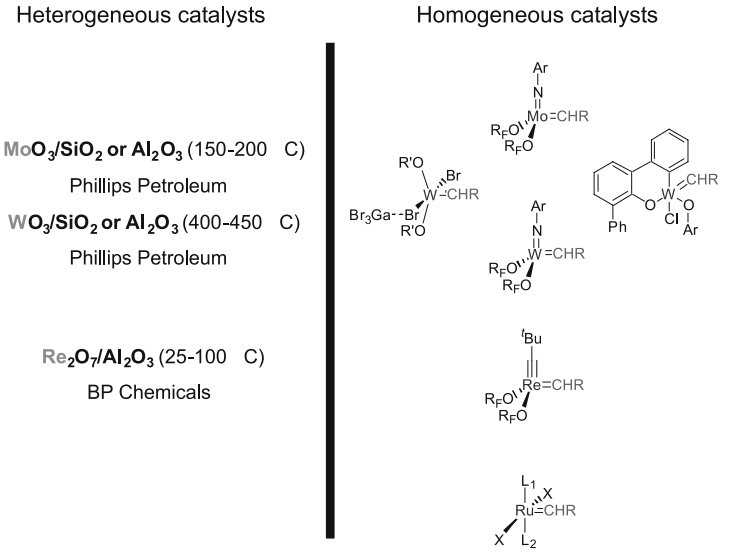

Scheme 16

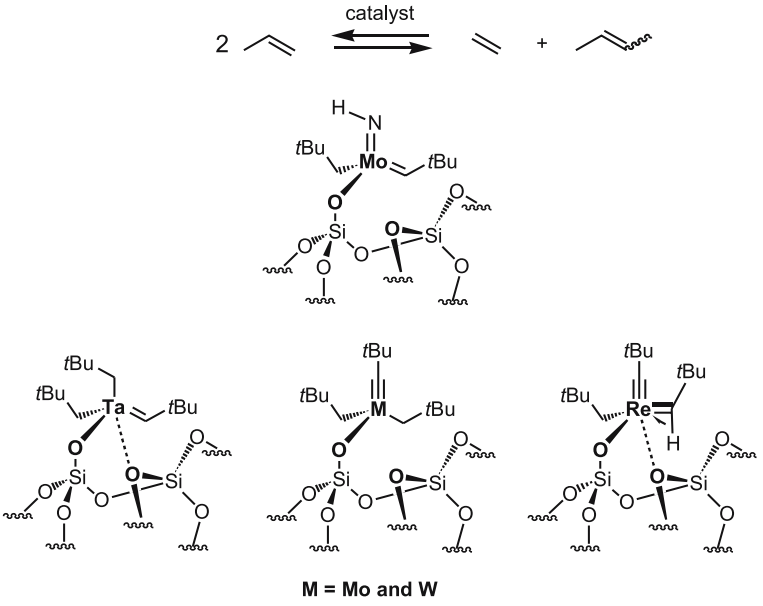

Scheme 17

Their activities (initial rates in mol/mol/s) in propene metathesis under identical experimental conditions (Table 1) are as follows: > Mo (0.53) ~ Mo = NH (0.49) > Re (0.25) ~ W (0.23) ≫ Ta (inactive). While there is not a significant difference between group 6 and 7 transition metals, Ta is not an

effective catalyst as already observed in homogeneous catalysis (Table 2). It is noteworthy that these catalyst precursors show much higher initial rates than their heterogeneous analogues, while they are comparable to their homogeneous ones. Note however that a direct comparison is difficult since classical heterogeneous catalysts are ill-defined and often contain less than 2% of active sites.

The initiation step for metallocarbyne catalyst precursors is not well-understood. But, in the case of Re, a well-defined metallocarbene, the initiation products have been detected: 0.7 equiv. of a 3/1 mixture of 3,3-dimethylbutene and 4,4-dimethyl-2-pentene (Fig. 2) [81, 82].

Table 2 Initial rates for the metathesis of propene with various heterogeneous catalysts

Catalyst	TOF[a]	R[b]
$[\equiv SiO - Ta(=CHtBu)(CH_2tBu)_2]$	Inactive$^{(25)}$	10^3
$[\equiv SiO - Mo(\equiv CtBu)(CH_2tBu)_2]$	$0.53^{(25)}$	500
$[\equiv SiO - Mo(=NH)(=CHtBu)(CH_2tBu)]$	$0.47^{(25)}$	870
$[\equiv SiO - W(\equiv CtBu)(CH_2tBu)_2]$	$0.23^{(25)}$	1700
$[\equiv SiO - Re(\equiv CtBu)(=CHtBu)(CH_2tBu)]$	$0.25^{(25)}$	500
MoO_3/SiO_2	$0.004^{(400)}$	–[c]
WO_3/SiO_2	–$^{(400)[c]}$	–[c]
Re_2O_7/SiO_2	$< 0.002^{(150)}$	–[c]
MoO_3/Al_2O_3	$0.05–0.5^{(200)}$	–[c]
WO_3/Al_2O_3	$0.1–1.0^{(300)}$	–[c]
Re_2O_7/Al_2O_3	$0.05–0.1^{(35)}$	–[c]

[a] Initial or steady state rates in mol/mol/s at the temperature indicated in parentheses
[b] Substrate to catalyst ratio, for which the reaction reaches at least the thermodynamic equilibrium
[c] Not readily calculated from the published data

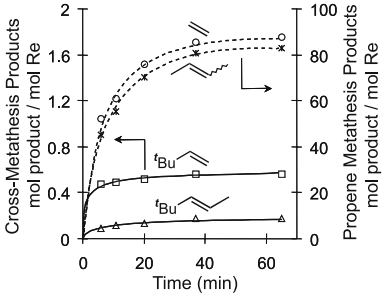

Fig. 2 Quantification in the gas phase of 3,3-dimethylbutene and *E* 4,4-dimethyl-2-pentene during propene metathesis (500 equiv.) catalyzed with 13 (1 equiv.) at 25 °C

They correspond to the cross-metathesis of propylene with the neopentylidene fragment (Scheme 18), and their relative ratio corresponds to a photograph of the active site as they are formed. Depending on how propylene will approach the carbene, it will generate different metallacyclobutanes, whose stabilities can direct the relative amounts of cross-metathesis (and self-metathesis) products. This model is based on the following: the favoured cross-metathesis product arises from the reaction pathway, in which [1,2]-interactions are avoided and [1,3]-interactions are minimized (here shown with both substituents in equatorial positions) [83].

It also explains the E/Z selectivity of products at low conversions (kinetic ratio, Scheme 19). In the case of propene, a terminal olefin, E 2-butene is usually favoured (E/Z = 2.5 Scheme 19), while Z 3-heptene is transformed into 3-hexene and 4-octene with E/Z ratios of 0.75 and 0.6, respectively, which shows that in this case Z-olefins are favoured (Scheme 20). At full conversion, the thermodynamic equilibriums are reached to give the E-olefins as the major isomers in both cases. For terminal olefins, the E olefin is the kinetic product because the favoured pathway involved intermediates in which the [1,2]-interactions are minimized, that is when both substituents (methyls) are least interacting. In the metathesis of Z-olefins, the metallacyclobutanes are trisubstituted, and Z-olefins are the kinetic products because they invoke reaction intermediates in which [1,2] and especially [1,3] interactions are minimized.

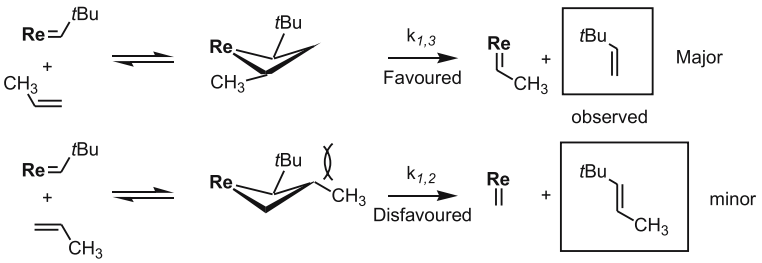

Scheme 18

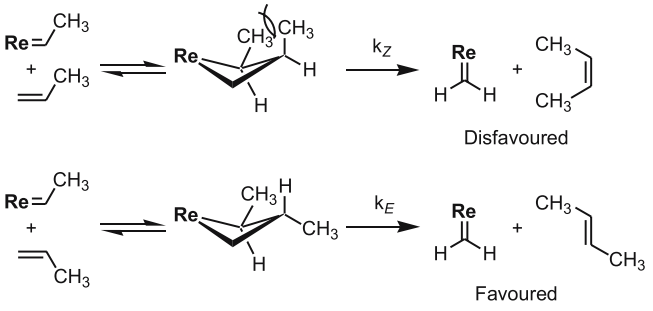

Scheme 19

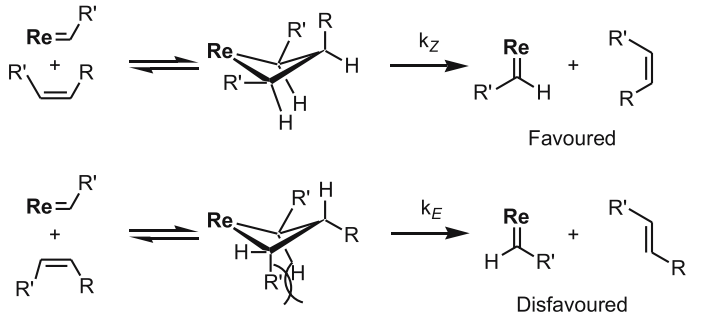

Scheme 20

In the case of functionalized olefins, heterogeneous catalysts have usually not performed well [84, 85]. Methyl oleate is the typical test substrate: the following order of stability towards the ester functional group for the different SOM catalysts has been observed (based on the number of turnovers): Re ∼ W > Mo, which is similar to what has been described for related homogeneous systems. In the specific case of Re, 900 TON can be reached, while TON for other Re-based heterogeneous catalysts do not exceed 200 [79, 84].

In conclusion, compared to classical heterogeneous catalysts, the catalysts prepared by surface organometallic chemistry can be understood at a molecular level. The initiation step, often unclear for classical heterogeneous catalysts is established. Moreover, they show a better tolerance towards functional groups, and their activities at room temperatures are much higher. Nonetheless, regeneration procedures are still to be developed. Secondly, the catalyst precursor $[(\equiv SiO)–Re(\equiv C\mathit{t}Bu)(= CH\mathit{t}Bu)(CH_2\mathit{t}Bu)]$ is as active and more robust than its Re-based homogeneous system. For example, $[Si_{POSS}O – Re(\equiv C\mathit{t}Bu)(= CH\mathit{t}Bu)(CH_2\mathit{t}Bu)]$ decomposed rapidly in the presence of olefins, and $[[R_{F6}O]_2Re(= CH\mathit{t}Bu)(\equiv C\mathit{t}Bu)]$ reaches 25 TON in the metathesis of methyl oleate [86]. Yet, it is still far from the current best homogeneous systems such as $[[RO]_2Mo(= CH\mathit{t}Bu)(= NAr)]$, which reaches initial rates of 2–8 mol/mol/s and TON of the order of 10 000 (terminal and internal olefins) [87, 88] or $[Cl_2Ru(= CHR)(PCy_3)L]$, with TON exceeding 1/2 million for various substrates (diallylmalonate, octene and methyl oleate) depending on the substitution on the heterocyclic carbene ligand L [89].

2.2.3 Alkane Hydrogenolysis

Supported metal hydrides of early transition metals catalyze the hydrogenolysis of alkanes at relatively low temperatures (50–150 °C) [29, 90–92]. Noteworthy are their differences in product selectivities. For example, the hydrogenolysis of propane in the presence of a large excess of H_2 gives a 1 : 1 mixture of ethane and methane in the case of zirconium hydride, a group 4

metal, and only methane in the case of tantalum hydride, a group 5 metal (Tables 3 and 4).

In the case of zirconium hydride, the hydrogenolysis of propane into a 1 : 1 mixture of methane and ethane is in good agreement with a β-alkyl transfer as a key step for carbon-carbon bond cleavage (Scheme 21) [90, 93].

This mechanism is general for all alkanes, and for example the hydrogenolysis of isobutane gives methane and propane as the primary products, and overall a 2 : 1 ratio of methane and ethane at 100% conversion of isobutane. Similarly, neopentane is transformed into a 3 : 1 methane/ethane mixture (Table 3 and Scheme 22).

The case of butane is noteworthy since the selectivity at low conversions indicates that there is no selectivity in the overall hydrogenolysis step between *n*- and *sec*-butyl zirconium surface intermediates, while earlier studies had shown that the *n*-alkyl zirconium complexes were more stable than *sec*-alkyl derivatives (Table 3 and Scheme 23) [94].

Finally, the reaction has also been applied to a wide range of paraffinic materials including polyolefins, which can transformed into lower alkanes

Table 3 Hydrogenolysis of alkanes catalyzed by zirconium hydride supported on silica

Zr–H	Activity (mol P/mol Zr/h)	Product selectivity at 0% conversion	Final product selectivity
Ethane	0	–	–
Propane	70	CH_4(50%)/C_2H_6(50%)	CH_4(50%)/C_2H_6(50%)
Isobutane	70	CH_4(52%)/C_3H_8(47%)[a]	CH_4(67%)/C_2H_6(33%)
Butane	66	CH_4(23%)/C_3H_8(20%)[b]	CH_4(60%)/C_2H_6(40%)
Neopentane	66	CH_4(54%)/C_4H_{10}(40%)[c]	CH_4(75%)/C_2H_6(25%)

[a] Ethane (1.5%)
[b] Ethane C_2H_6 (54%)
[c] Propane (5%) and ethane (1%)

Table 4 Hydrogenolysis of alkanes catalyzed by tantalum hydride supported on silica

Ta–H	Activity (mol P/mol Zr/h)	Product selectivity at 0% conversion	Final product selectivity
Ethane	30	CH_4(100%)	CH_4(100%)
Propane	12	CH_4(55%)/C_2H_6(45%)	CH_4(100%)
Isobutane	24	CH_4(55%)/C_2H_6(10%)/C_3H_8(35%)	CH_4(100%)
Butane	18	CH_4(42%)/C_2H_6(38%)/C_3H_8(20%)	CH_4(100%)
Neopentane	6	–[a]	CH_4(100%)

[a] Since isobutane is hydrogenolyzed faster than neopentane, selectivity at 0% conversion is difficult to measure in a batch reactor

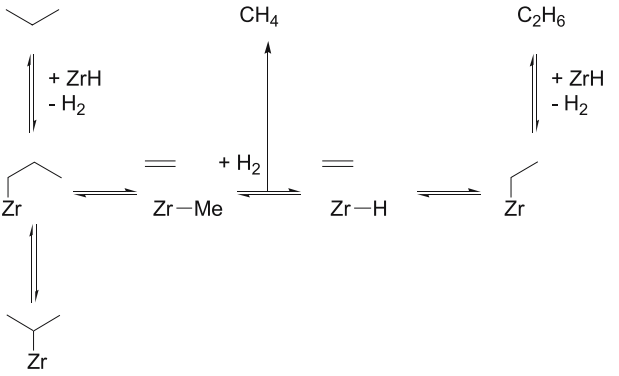

Scheme 21

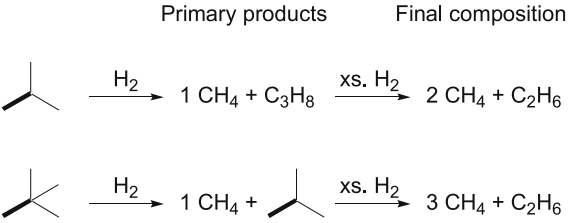

Scheme 22

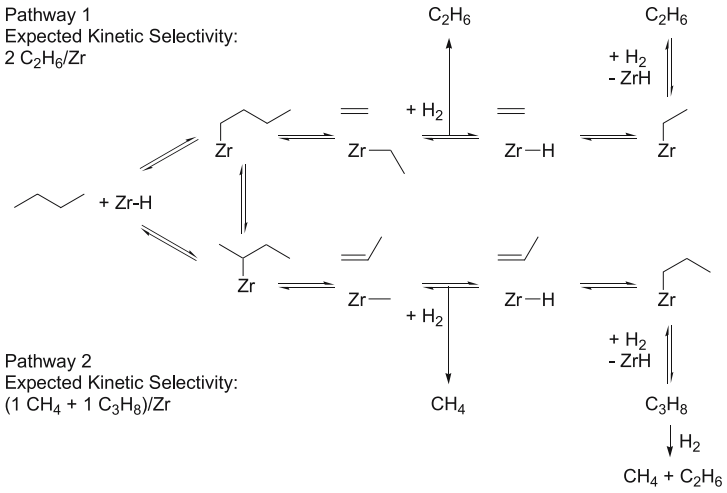

Scheme 23

under mild conditions, thus illustrating the Ziegler Natta depolymerization (Scheme 24) [95].

In the case of tantalum, all alkanes including ethane are transformed into methane as the sole gaseous product, which is in sharp contrast to group 4

metal hydrides (Table 4). Carbon-carbon bond cleavage via a β-alkyl transfer cannot account for such an observation (Scheme 25).

Comparing the product selectivity at low conversion in the hydrogenolysis of 2,2-dimethylbutane for the two catalysts is noteworthy. Zirconium hydride supported on silica does not produce neopentane, but only isopentane (10%) as a C_5 product in agreement with a β-alkyl transfer as a key step for the carbon-carbon cleavage (no neopentane can be formed through this mechanism, Scheme 25).

In contrast, tantalum hydride supported on silica gives mainly neopentane (31%), which indicates that the mechanism of carbon-carbon bond cleavage must involve the removal of one carbon at a time (in contrast to β-alkyl transfer, which involves the removal of at least two carbons).

Note that the main difference between zirconium hydride and tantalum hydride is that tantalum hydride is formally a d^2 8-electron Ta^{III} complex. On the one hand, a direct oxidative addition of the carbon-carbon bond of ethane or other alkanes could explain the products; such a type of elementary step is rare and is usually a high energy process. On the other hand, formation of tantalum alkyl intermediates via C – H bond activation, a process already ob-

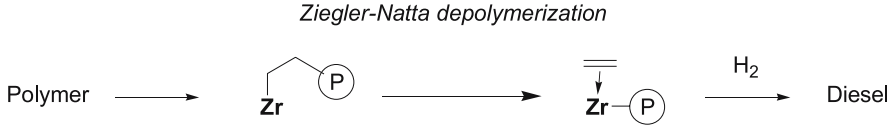

Scheme 24

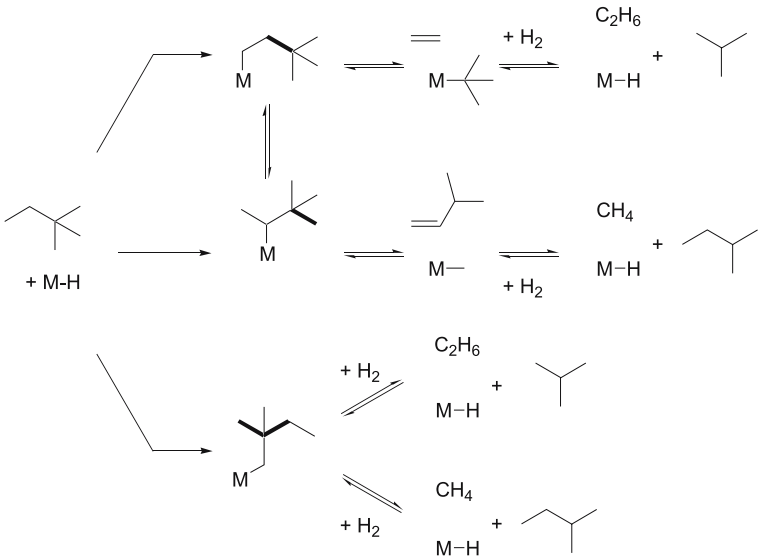

Scheme 25

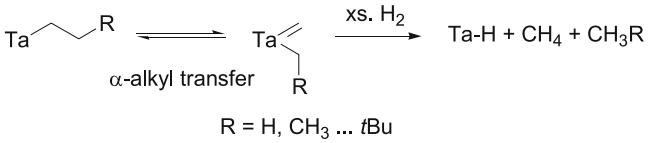

Scheme 26

served on such a system [96], followed by an α-alkyl transfer, a low energy process, can readily explain the results (Scheme 26). Note that the α-alkyl transfer step has not been observed in molecular organometallic chemistry, but that there are several examples of the reverse steps [97, 98].

2.2.4 Alkane Metathesis

In the absence of H_2 $[(\equiv SiO)_2Ta-H]$ activates alkanes (RH) at low temperatures to give the corresponding tantalum alkyl species, $[(\equiv SiO)_2Ta-R]$ [52, 96], and H_2 (vide supra), but above 80 °C acyclic alkanes are transformed into their lower and higher homologues (Fig. 3) [99].

This catalytic reaction has been named alkane σ-bond metathesis since alkyl fragments of alkane mixtures are exchanged. For example, propane is

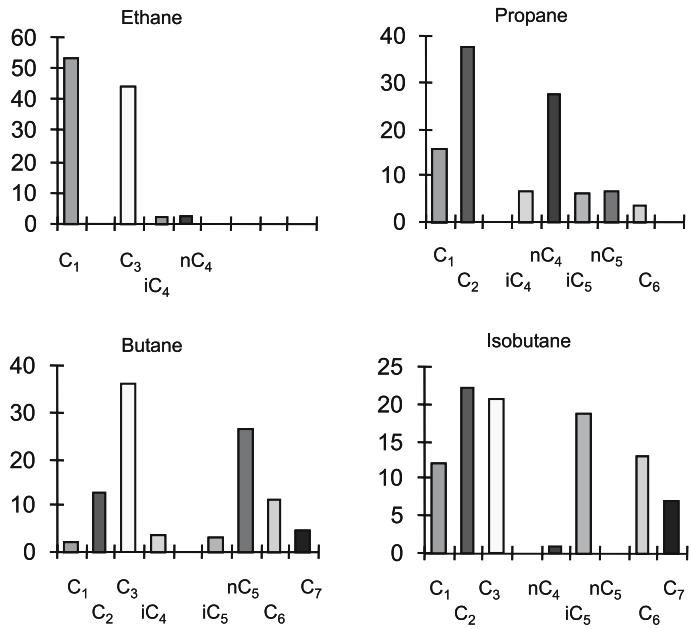

Fig. 3 Product selectivity in the metathesis of various acyclic alkanes

Table 5 Comparison of Ta^{III} and Ta^{V} catalyst precursors in the metathesis of propane at 150 °C for 120 h

Catalysts	TON	Selectivities/%				
		C_1	C_2	C_4^a	C_5^a	C_6
Ta – H[c]	60	10.0	46.0	30.6/6.0	4.8/2.2	0.4
Ta = CHR[d]	35	12.8	47.7	22.2/13.4	3.5/2.5[b]	0.9[b]

[a] The *n*/*i* selectivities are reported for butanes and pentanes

[b] 2,2-dimethylpropane (tBuCH$_3$, 1.05 equiv./Ta), 2,2-dimethylbutane (tBuCH$_2$CH$_3$, 0.30 equiv./Ta) and 2,2-dimethylpentane (tBuCH$_2$C$_2$H$_5$, 0.11 equiv./Ta) are also formed; no tBuCH$_2$C$_3$H$_7$ is detected (< 0.1%)

[c] $(SiO)_2Ta - H$

[d] $(SiO)Ta(=CHtBu)(CH_2tBu)_2$

mainly transformed into ethane and butanes along with smaller amounts of methane, pentanes, and hexanes (Table 5).

This reaction is also catalyzed by Ta^{V} d^0 catalyst precursors, such as $[(\equiv SiO)Ta(=CHtBu)(CH_2tBu)_2]$ and $[(\equiv SiO)_2Ta(=CHtBu)(CH_2tBu)]$ [100, 101]. In the case of propane, the following product selectivities are observed: methane, ethane, butanes, pentanes, and hexanes, and they are similar to those obtained with tantalum hydride. Moreover, in this case, 2,2-dimethylpropane (tBuCH$_2$–***H***, 1.05 equiv./Ta), 2,2-dimethylbutane (tBuCH$_2$–CH$_3$, 0.30 equiv./Ta), and 2,2-dimethylpentane (tBuCH$_2$-CH$_2$***CH***$_3$, 0.11 equiv./Ta) are also formed; no tBuCH$_2$-***CH***$_2$***CH***$_2$***CH***$_3$ is, however, detected (< 0.1%). Overall they correspond to the cross-metathesis products of propane and $[(\equiv SiO)Ta(=CHtBu)(CH_2tBu)_2]$ via C – H or C – C bond activation. Note that the ratio of initiation products arising from carbon-carbon bond activation tBuCH$_2$–CH$_3$/tBuCH$_2$–CH$_2$CH$_3$ is 2.5.

In olefin metathesis (vide supra), we have observed the initiation products of the reaction of propene and $[(\equiv SiO)Re(\equiv CtBu)(=CHtBu)(CH_2tBu)]$: tBuCH = CH$_2$and *trans*-tBuCH=CHCH$_3$(no *cis* tBuCH=CHCH$_3$ is detected), which are formed in a 3 : 1 ratio [32].

Note also that: (1) d^0 Ta^{V} alkylidene complexes are alkane metathesis catalyst precursors; (2) the cross-metathesis products in the metathesis of propane on Ta are similar to those obtained in the metathesis of propene on Re: they differ only by 2 protons; and (3) their ratio is similar to that observed for the initiation products in the metathesis of propane on $[(\equiv SiO)Ta(=CHtBu)(CH_2tBu)_2]$. Therefore, the key step in alkane metathesis could probably involve the same key step as in olefin metathesis (Scheme 27) [101].

In the case of olefin metathesis, the selectivity in initiation products can be understood in terms of minimization of the steric interactions in the metallacyclobutane intermediates (vide supra), which are governed by the relative position of the substituents: the metallacyclobutane with substituents in pos-

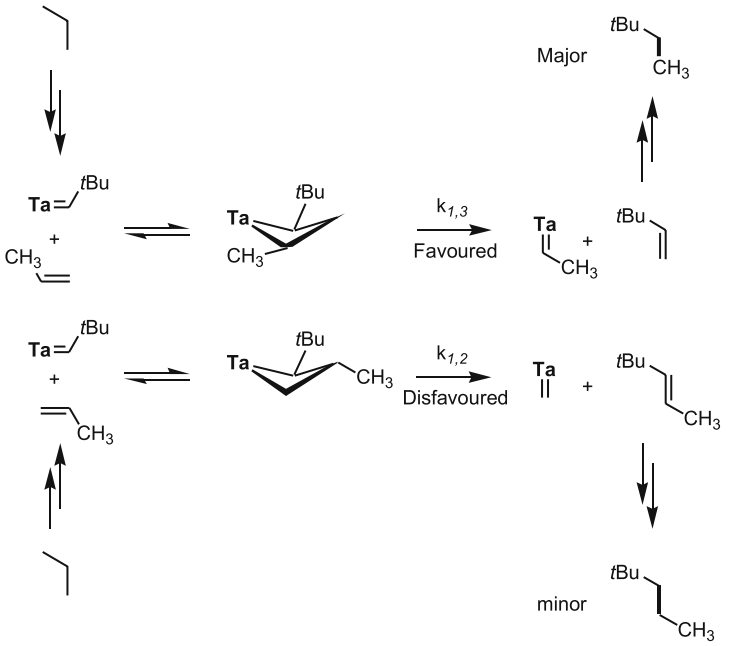

Scheme 27

itions [1e, 3e] are more favoured than those having their substituents in the [1e, 2e]-positions.

The product selectivities in propane metathesis can also be explained by using the same model in which [1,3]- and [1,2]-interactions determine the ratio of products. For instance, the butane/pentane ratios are 6.2 and 4.8 for $[(\equiv SiO)Ta(=CHtBu)(CH_2tBu)_2]$ and $[(\equiv SiO)_2Ta-H]$, respectively (Table 5). A similar trend is observed for the isobutane/isopentane ratio, which are 4.1 and 3.0, respectively. The higher selectivity in butanes (the transfer of one carbon via metallacyclobutanes involving [1,3]-interactions) than that of pentanes (the transfer of two carbons via metallacyclobutanes involving [1,2]-interactions) is consistent with this model (Scheme 28).

A key question remains: how is the olefin formed in the overall process? Molecular tantalum complexes are known to undergo facile α- and β-H transfer processes, leading to tantalumalkylidene and tantalum π-olefin complexes, respectively (mechanism 9, Scheme 29) [98]. Moreover, olefin polymerization with tantalum complexes belongs to the rare case in which the Green–Rooney mechanism seems to operate (Eq. 10, Scheme 29) [102]. Finally, intramolecular H-transfer between perhydrocarbyl ligands has been exemplified (Eq. 11, Scheme 29) [103, 104].

Several mechanisms are possible, based on known elementary steps of molecular chemistry: for example one involving two Ta sites or one involving a single tantalum site (Scheme 30).

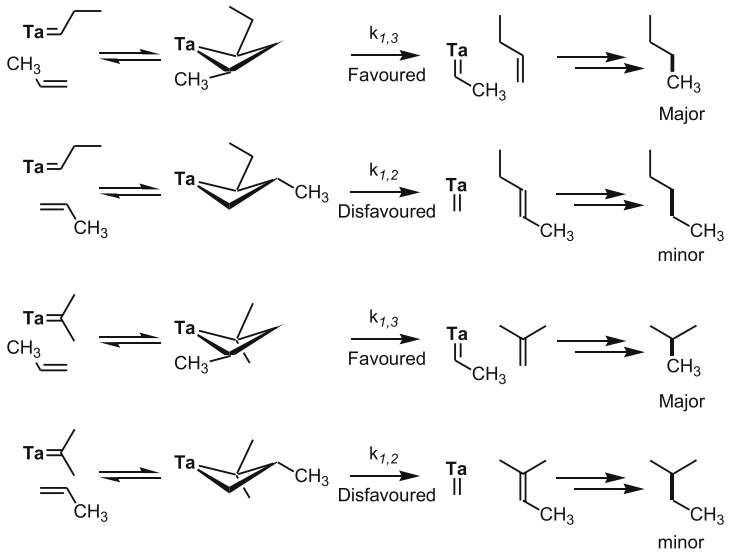

Scheme 28

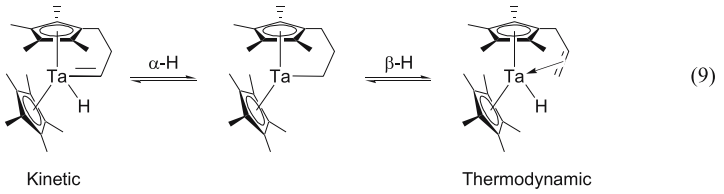

(9)

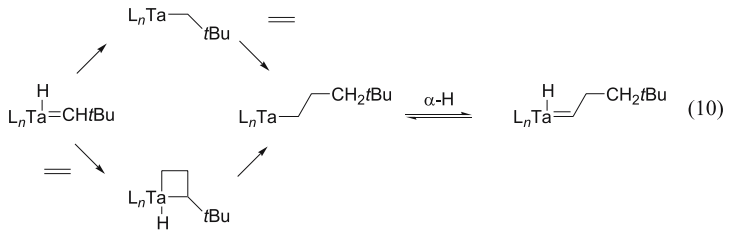

(10)

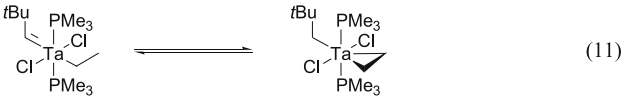

(11)

Scheme 29

Note that, while this reaction (as well as alkane hydrogenolysis) involves known elementary steps of molecular organometallic chemistry, it has not been discovered in homogeneous catalysis. One reason might be that highly

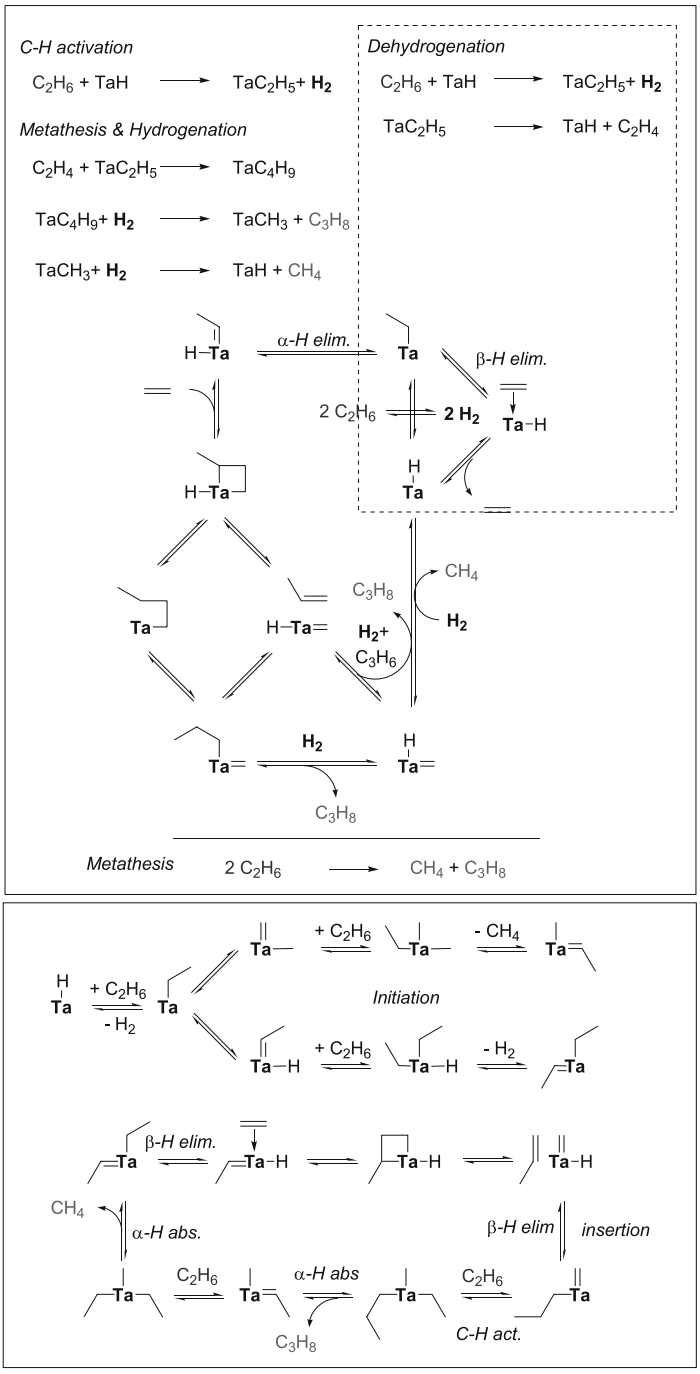
C-H activation
C2H6 + TaH → TaC2H5+ H2
Metathesis & Hydrogenation
C2H4 + TaC2H5 → TaC4H9
TaC4H9+ H2 → TaCH3 + C3H8
TaCH3+ H2 → TaH + CH4
Dehydrogenation
C2H6 + TaH → TaC2H5+ H2
TaC2H5 → TaH + C2H4
α-H elim.
β-H elim.
2 C2H6
2 H2
Ta-H
CH4
C3H8
H2+
C3H6
H2
Metathesis
2 C2H6 → CH4 + C3H8
Initiation
+ C2H6
- CH4
- H2
β-H elim.
α-H abs.
insertion
C-H act.

Scheme 30

reactive intermediates are involved, which would easily decompose in an homogeneous system, such as via bimolecular deactivation pathways.

2.2.5 The Cross-Metathesis of Propane and Methane

While alkane metathesis is noteworthy, it affords lower homologues and especially methane, which cannot be used easily as a building block for basic chemicals. The reverse reaction, however, which would incorporate methane, would be much more valuable. Nonetheless, the free energy of this reaction is positive, and it is 8.2 kJ/mol at 150 °C, which corresponds to an equilibrium conversion of 13%. On the other hand, thermodynamic calculation predicts that the conversion can be increased to 98% for a methane/propane ratio of 1250. The temperature and the contact time are also important parameters (kinetic), and optimal experimental conditions for a reaction carried in a continuous flow tubular reactor are as follows: 300 mg of $[(\equiv SiO)_2Ta-H]$, 1250/1 methane/propane mixture, Flow = 1.5 mL/min, P = 50 bars and T = 250 °C [105]. After 1000 min, the steady state is reached, and 1.88 moles of ethane are produced per mole of propane consumed, which corresponds to a selectivity of 96% selectivity in the cross-metathesis reaction (Fig. 4). The overall reaction provides a route to the direct transformation of methane into more valuable hydrocarbon materials.

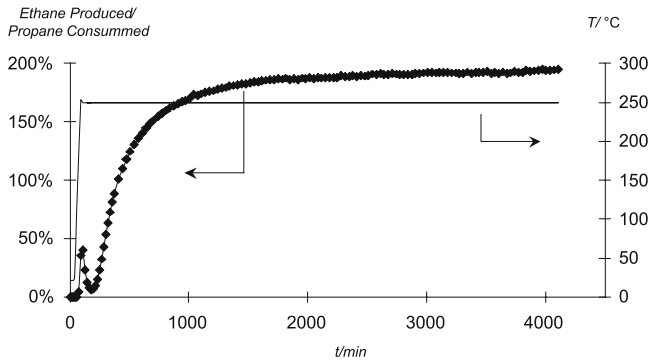

Fig. 4 Methane-propane cross-metathesis catalyzed by tantalum hydride supported on silica

2.2.6 Conclusion

This approach has allowed molecularly defined heterogeneous catalysts to be developed. It is the first step towards the development of rationally designed heterogeneous catalysts. While the performance of these catalysts are already

impressive, there is still room for improvements: it should be possible to: 1) simplify the preparation procedure, 2) investigate a larger variety of catalysts (high-throughput experiments) and 3) understand how they deactivate in order to implement rational regeneration strategies.

Additionally, grafting molecular entities on surfaces has already allowed to discover several reactions: the low temperature hydrogenolysis of alkanes including the depolymerization of polyolefins, the alkane metathesis and the cross-metathesis of methane and alkanes. These two latter reactions can allow higher molecular weight alkanes to be built.

Note that elementary steps involved in all these reactions are in fact quite similar to those observed in molecular systems, but the fact that these molecules are attached to a support often increases their reactivity and also allows highly reactive intermediates to be generated so that novel reactions can be discovered.

3
Surface Organometallic Chemistry on Metal Particles

3.1
Reaction of Organometallic Complexes with Particles of Transition Elements: The Stepwise Hydrogenolysis of Metal-Carbon Bonds

Before studying the reaction of organometallic complexes with the surface of metallic particles, it is necessary to define a metallic particle. Metallic particles with diameters in the nanometer range (nanoparticles) are key components of heterogeneous catalysis. Since, generally, only the surface metal atoms are active, it is necessary to have solids with high dispersion, which is the number of surface atoms against the total number of metal atoms ($= M_s/M_t$). This is achieved by decreasing the size of the particles. Note that, when reaching a critical size, the particles lose their activity in several catalytic reactions. In several cases, particles below 8 Å in diameter exhibit poor catalytic activity. Moreover, to avoid sintering, the particles are often supported on oxide supports (silica, alumina, ...).

The shape of the nanoparticles depends on numerous parameters such as the nature of the metal and the support, the metal loading.... Of the various models of polyhedral metal particles [106], the cubooctaedral structure can be used to represent small metallic particles (Scheme 31). Note that these idealized structures can vary with the nature of chemisorbed species (vide infra) and very subtle atomic rearrangements probably occur during catalytic events.

For these structures, the surface metallic atoms (M_s) are located on the (111) or (100) planes, on corners or on edges [107]. Note that the number of

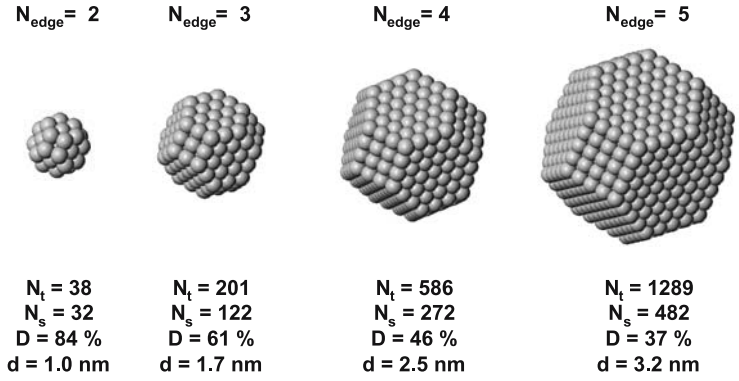

Scheme 31

atoms on each edge of a cuboctahedra (N_{edge}) is constant. In Scheme 31, examples of cubo-octahedral structures with 2, 3, 4, and 5 atoms per edge are given, with the corresponding particle diameters (d) and dispersions (D).

The number of surface atoms can be determined by chemisorption of probe molecules (H_2, O_2...), knowing the stoichiometry of the adsorbed species. As an example, in the case of Pt, the stoichiometry of irreversibly adsorbed hydrogen (H/Pt_s) and oxygen (O/Pt_s) at room temperature are both close to 1/1 [108–111]. Knowing the total number of atoms (elemental analysis) and the number of irreversibly adsorbed H and O, the dispersion of the particles ($D = Pt_s/Pt$) is then easily obtained. Note that the dispersion of these particles decreases when their size increases (Fig. 5).

These materials will be described by (i) the metal loading (elemental analysis); (ii) the surface area and porosity of the support (B.E.T. and

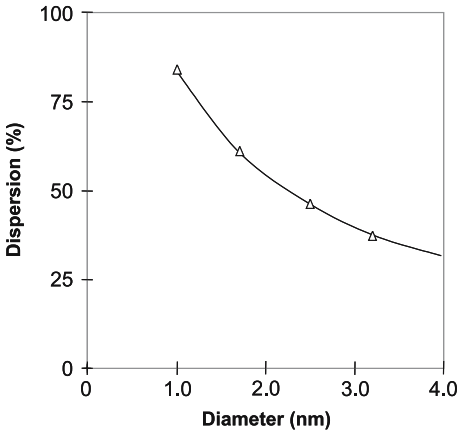

Fig. 5 Dispersion of a cubooctahedral particle as a function of diameter

B.J.H. methods); (iii) the average diameter (T.E.M.) and/or the dispersion (chemisorption of probe molecule) of the metallic particle. EXAFS will also provide average coordination numbers, which decrease sharply as the particle size decreases.

3.1.1 Tetraalkyl Compounds of the Group 14 Elements, the Case of $SnBu_4$

The reaction between organometallic compounds of group 14 (M = Sn Ge, Sn, Pb) and silica-supported transition metal particle M'/SiO_2 (M' = Rh, Ru, Ni, ...) in the presence of H_2 leads to the selective reaction of the metal particle with the organometallic complexes via the hydrogenolysis of the M – C bonds [112]. This yields the corresponding alkanes and the formation of organometallic fragments grafted on the "host" surface. (M'_s) represents a surface metal atom of the metallic particle, (mechanism 12).

$$M'_s + yMR_4 + \frac{4 - xy}{2} H_2 \rightarrow M'_s[MR_x]_y + xyRH \qquad (12)$$

The extent of the reaction (number of M – C bonds hydrogenolyzed/MR_4) depends on the temperature of the reaction, the nature of the metals (M and M'), the size of the "host" metal particle and the nature of the ligand. In the last few years, careful studies of the hydrogenolysis conditions, in particular, the selective hydrogenolysis of $SnBu_4$ on a silica supported Pt catalyst was carried out at different temperatures and for various $SnBu_4/M'_s$ ratio [113]. The reaction is performed in a volumetric apparatus, under H_2 (P = 50 mbar). The Pt particles of about 1.5 nm in diameter are supported on silica (Aerosil 200 m^2/g from Degussa) with a metal loading of 1.57 wt %. Analysis of the evolved gases during the reaction (Fig. 6) shows that only butane is formed and that the hydrogenolysis proceeds by a stepwise cleavage of the Sn-alkyl bonds.

Under 50 mbar of H_2 and 50 °C, $SnBu_4$ reacts selectively on the Pt surface to form surface complexes of average formula $Pt_s[SnBu_x]_y$. The empirical formula (values of x and y) depend on the reaction time and on the Sn_{int}/Pt_s ratio (Fig. 6). Note that under these conditions $SnBu_4$ does not chemically react with the silica surface, but it is fully physisorbed on the support [114]. In fact, when silica is contacted with $SnBu_4$, IR spectroscopy shows a shift of the ν(O – H) band of silica to lower wave numbers, i.e. from 3747 cm^{-1} to ca. 3700 cm^{-1}, which results from van der Waals interactions between the hydroxyl groups of the support and the butyl chains of adsorbed $SnBu_4$ (Scheme 32).

The first step of the grafting process is probably the physisorption of Bu_4Sn on the surface of the support (higher surface area), which then migrates from the support to the metal surface. Then, when the physisorbed complex interacts with the surface Pt atoms covered by hydrogen atoms (Pt_s-H_x), there is

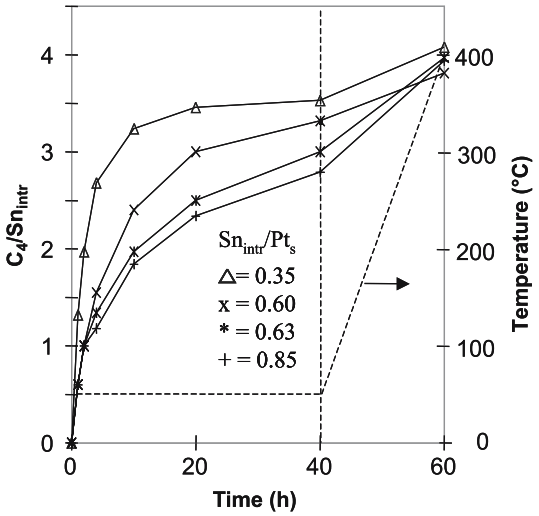

Fig. 6 Amount of butane evolved (C_4/Sn)during the reaction between $SnBu_4$ and Pt/SiO_2 at 50 °C and then at 400 °C, under 50 mbar of H_2. $SnBu_4$ introduced (Sn_{intr}) per platinum surface atom (Pt_s) were 0.35 (0.25); 0.60 (0.57); 0.63 (0.69) and 0.85 (0.73). The numbers in brackets are the quantity of Sn fixed per Pt_s, as measured by elemental analysis of the final solid

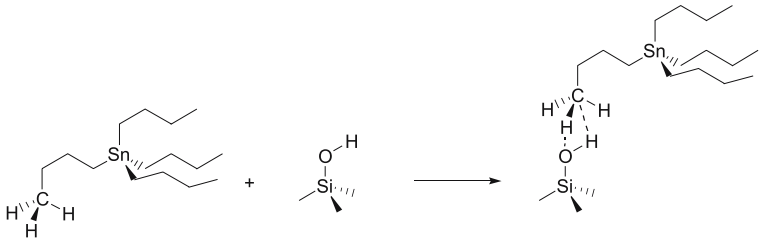

Scheme 32

a selective hydrogenolysis of the Sn – C bond, with butane evolution. The absence of hydrogenolysis products (lower homologues of butane) is consistent with the much lower bond dissociation energy of a Sn – C bond (201 kJ mol^{-1}) compared with a C – C bond (348 kJ mol^{-1}).

Simultaneous measurements of both the amount of butane evolved and the quantity of grafted organometallic fragments at increasing time of reaction allows the stoichiometry of the surface complexes $Pt_s[SnBu_x]_y$ to be determined (Fig. 7). Furthermore, extrapolation to a low amount of Sn grafted shows that a $[Bu_3Sn]_yPt_s$ species is formed, which then rapidly evolved towards more dealkylated species and finally to $Pt_s[SnBu]_y$.

In fact, the reaction of $SnEt_4$ on Pt surfaces covered by irreversibly adsorbed hydrogen (and in the absence of H_2) leads to the same type of species, $Pt_s[SnEt_3]_y$, which is stable under these conditions (mechanism 13) and has

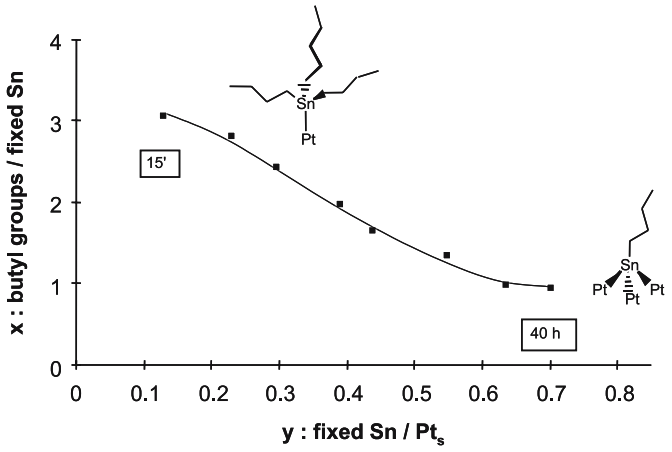

Fig. 7 Reaction of $SnBu_4$ on Pt particles supported on silica at 50 °C: evolution of the stoichiometry of surface organotin species as a function of coverage and reaction time (see time in *square boxes*)

been named a "primary surface complex" (PSC) [115, 116].

$$Pt_s - H + SnEt_4 \rightarrow Pt_sSnEt_3 + Et - H \quad (13)$$

It has been proposed that the formation of these species probably involves a coordination of SnR_4 to the Pt surface to form a pentacoordinated Sn intermediate (Scheme 33) [117]. This proposed step is based on a detailed study using SCF(CI) calculations [118] on the interaction between $Sn(CH_3)_4$ and a reduced $Rh_{13}H_{20}$ cluster. The formation of this intermediate induces the weakening of the Sn – C bond [119], which would facilitate the formation of the Sn – M_s bond.

When gaseous H_2 is present, the reaction does not end at the stage of the PSC formation, and $Pt_s[Sn(R)_3]_y$ undergoes further Sn – R hydrogenolysis (Scheme 34).

At 50 °C, for coverage ranging from 0.35 to 0.85 Sn/Pt_s and after about 40 h of reaction, the number of remaining butyl group per grafted fragment is close to one. There is formation of a rather stable monobutyl species with an average stoichiometry: $Pt_s[SnBu]_y$, $(0.35 < y < 0.85)$.

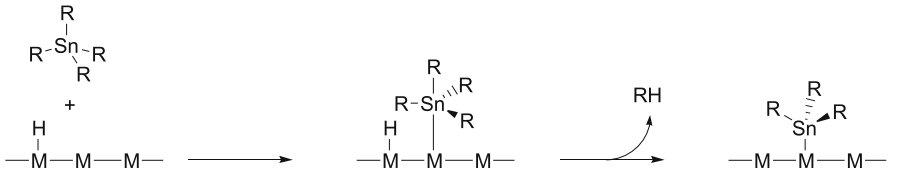

Scheme 33

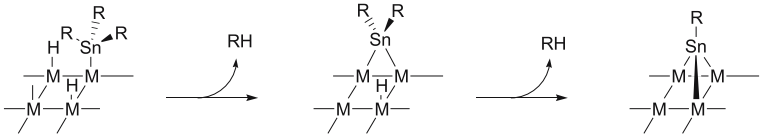

Scheme 34

The formation of a stable monobutyl species obtained at 50 °C is also further demonstrated by its hydrogenolysis at higher temperatures. Indeed, treatment under H_2 of the grafted surface organometallic complex, $Pt_s[SnBu]_y$, at 300 °C for 4 h generates about one butane per Sn along with traces amounts of propane, ethane, and methane.

After treatment under H_2 at 300 °C, naked Sn atoms are deposited on the top of the "host" Pt surface as adatoms. These adatoms can be located on specific sites of the "host" surface, such as faces, edges or corners. Increasing the reaction temperature, the naked M "adatoms" can migrate into the metallic particle lattice to form alloys (Scheme 35). These species were characterized by various physical techniques such as RGN, Infrared spectroscopy, TEM-EDAX, and EXAFS [113, 120–124]. Thus, EXAFS analysis at the Sn K-edge (Scheme 35) gives 3 heavy backscatterers (Pt) at 0.272 nm and 1 light atom (C) at 0.212 nm for the grafted fragment consistent with $Pt_s[SnBu]_y$. Four Pt atoms are found at 2.76 nm as first neighbours for the adatom and more than 5 Pt at 2.78 nm for the alloy. Moreover, TEM analysis showed that

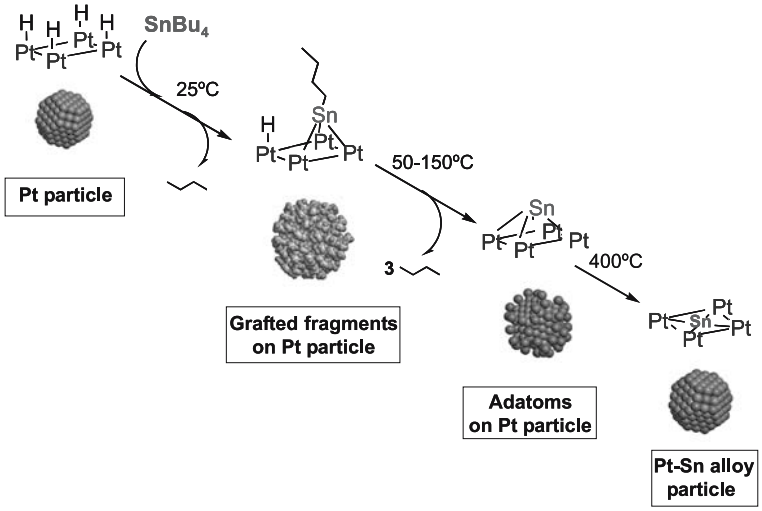

Scheme 35 Various steps observed during the hydrogenolysis of $SnBu_4$ at the surface of a Pt particle (sphere color-code: Pt brown, H blue, C white, Sn green)

the average diameter of the particles increased from 1.5 nm for the "host" Pt/SiO_2 to 2.0 nm for the $Pt-Sn/SiO_2$ (Sn/Pt = 0.3) alloy.

In summary, depending on the reaction temperature, it is possible under H_2 to obtain well-defined materials, in which a metal surface (the host) is covered with Sn atoms covalently bound. At low temperatures (50 °C), Sn conserves one of its alkyl fragments. At higher temperatures (300 °C), Sn adatoms are formed, but upon further increasing the reaction temperature (400 °C), it can migrate into the Pt lattice to form an alloy. The presence of this guest atom (Sn) and its ligand will affect the properties of the metal particles (as already observed by the absence of hydrogenolysis).

Moreover, the reaction observed during the hydrogenolysis of SnR_4 on a Pt catalyst is quite general and can be extended to group 14 molecules (SnR_4, SiR_4, GeR_4 ...) and to various transition metals particles (Ni, Ru, Rh, Pd, Pt ...).

They provide materials with considerable improved catalytic properties (vide infra) either by the presence of the organometallic fragment itself [120, 125–127], by the presence of the adatoms [128, 129] or by the formation of the surface alloys (vide infra) [116, 130–138].

3.1.2 Triphenyl Compound of Group 15 Elements, the Case of $AsPh_3$

Similarly, the reaction of $AsPh_3$, under H_2, on Ni surfaces can be monitored by measuring the variation of the arsine concentration with time at various temperatures [139]. In the presence of Ni/Al_2O_3 (alumina: 250 m^2/g; Ni loading: 25 wt %, average diameter of the metallic particles: 6 nm; 18% of dispersion) and H_2 (12 bars), $AsPh_3$ concentration decreases (Fig. 8a), and

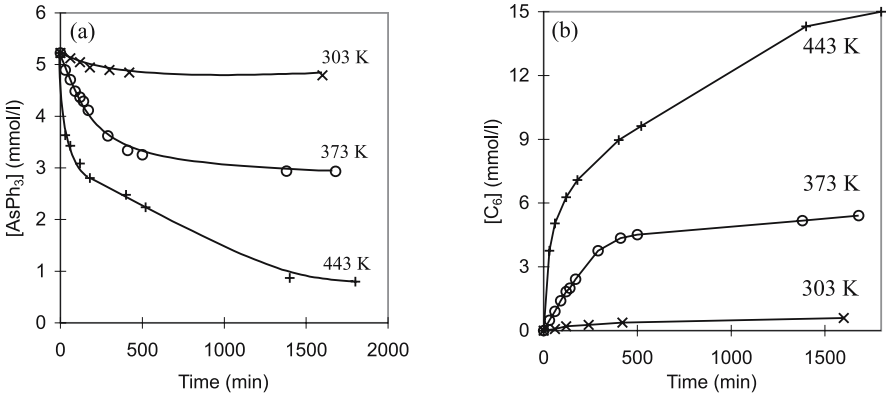

Fig. 8 Kinetics of $AsPh_3$ reaction at 303, 373 and 473 K under 12 bars of H_2 on Ni/Al_2O_3 (Ni loading: 25 wt %, dispersion: 18%). **a** triphenylarsine concentration; **b** benzene + cyclohexane evolution

Table 6 Quantity of $AsPh_3$ fixed (As_{fixed}) and ratio C_6/As_{fixed} at 303, 373 and 443 K, under 12 bars of H_2, after 3 h of reaction

T/K	As_{int}/Ni_t	As_{fixed}/Ni_t	As_{fixed}/Ni_s	C_6/As_{fixed}	XRD
303	1.21	0.10	0.56	1.4	Ni
373	1.21	0.53	2.94	2.4	–
443	1.21	1.02	5.67	3.0	NiAs

C_6 compounds (benzene + cyclohexane) are formed (Fig. 8b). Increasing the temperature increases the initial reaction rate, but also strongly enhances the amount of $AsPh_3$ having reacted (Fig. 8a) and the quantity of C_6 evolved (Fig. 8b).

At low temperatures, cyclohexane is the only product observed at the beginning of the reaction, but benzene becomes the only product formed after about 100 min of reaction, which shows that the aromatic hydrogenation ability of Ni is suppressed (poisoning), probably through the deposition of As on the Ni surface. At higher temperatures, benzene is the main compound formed, regardless of the reaction time.

The quantity of $AsPh_3$ fixed and C_6 evolved after 3 h of reaction at 303, 373, and 443 K, related to the amount of total Ni (As_{fixed}/Ni_t) or to the number of surface atoms (As_{fixed}/Ni_s) as reported in Table 6 indicates that the reaction of $AsPh_3$ with Ni under H_2 proceeds through a stepwise process, with a progressive hydrogenolysis of the As – Ph bonds. Moreover, after reaction at 443 K, the diffraction pattern of the solid presents clear lines at 33.6 and 50.5 2θ assigned to the NiAs phase (nickeline), thus showing that an alloy has been formed.

The overall reaction pathway is probably similar to what has been presented for the reaction of $SnBu_4$ with Pt particles, that is first hydrogenolysis of the As – C bond to form $Ni_s[AsPh_2]_y$ species, which rapidly evolves into $Ni_s[AsPh]_y$, $Ni_s[As]_y$ to give finally an alloy by migration of the As adatoms into the Ni lattice as evidenced by the formation of Nickeline (NiAs) according to XRD studies (Scheme 36).

The chemical events described above are the basis for the removal of arsines (R_3As) in crude oil or in raw gas condensates, which are known to cause major environmental pollution, equipment corrosion and reduction of catalyst life time (including automotive converters). It was recently demonstrated that these compounds can be completely removed by feedstock hydrotreatment on nickel-based catalysts under H_2 at 160–200 °C [140].

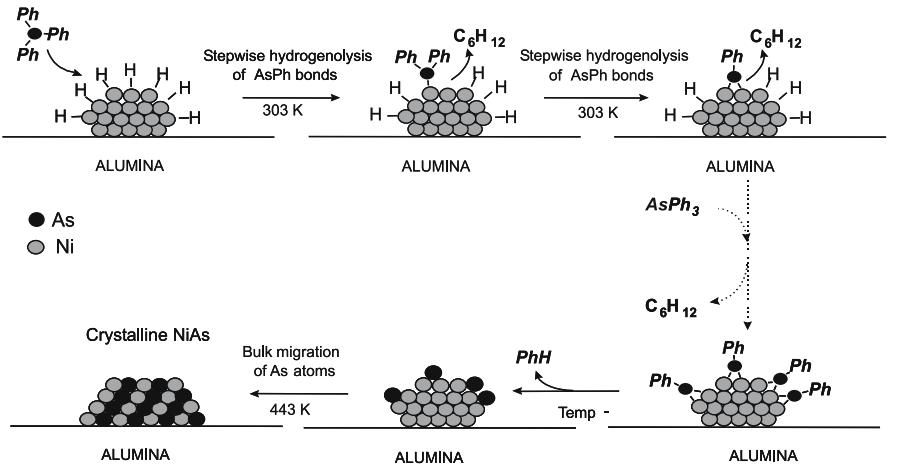

Scheme 36

3.1.3
Diphenyl Compound of a Group 12 Element, the Case of $HgPh_2$

At 300 K, $HgPh_2$ reacts with Ni/Al_2O_3 $\{HgPh_2/Ni = 1, (Hg/Ni_s = 6)\}$ in less than 0.5 h to give mostly biphenyl (Ph – Ph) (Table 7) along with small amounts of benzene (Bz), cyclohexane (Chxa), and phenylcyclohexane (Ph – Chxa), while, under the same conditions, alumina does not exhibit any

Table 7 Reaction of $HgPh_2$ with Ni/Al_2O_3 (50 mg, $Ni_t = 0.183$ mmol), H_2 (1 bar), T = 303 K, heptane (10 mL), reaction time of each run = 0.5 h[a]

Run	$HgPh_2$[a] (mmol)	Hg_i[b] Ni_t	$HgPh_2$[c] (%)	Ph-Ph[d] (mmol)	Ph-Chxa[d] (mmol)	C_6[d] (mmol)	Hg_f[e] (%)	Ph_f[e] (%)
1	0.182	1.0	0	0.165	0.001	0.0314	100	91
2	0.364	2.0	0	0.354	0.003	0.0148	100	98
3	0.728	4.0	0	0.717	0.004	0.0142	100	99
4	1.092	6.0	7	1.070	0.006	0.0140	93	99

[a] $HgPh_2$ corresponds to the cumulated amount of $HgPh_2$ introduced into the reactor 0.182 mmol of $HgPh_2$ were introduced in run 1, then, after 0.5 h of reaction, 0.182 were added in run 2, followed successively every 0.5 h by 0.364 mmol of $HgPh_2$ in run 3 and run 4.[b] Hg_i/Ni corresponds to the amount of Hg introduced initially per Ni. [c] $HgPh_2$ remaining after each run. [d] Cumulated amount of products at the end of each run; Ph – Ph, Ph – Chxa, C_6 designate biphenyl, phenylcyclohexane and the sum of benzene/cyclohexane respectively. [e] Hg_f and Ph_f correspond to the mass balance in Hg and organic compounds, respectively.

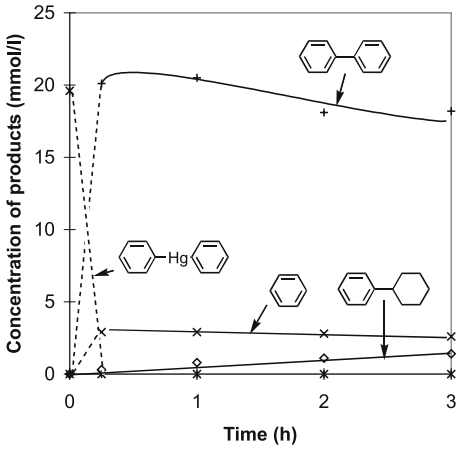

Fig. 9 Kinetic of the $HgPh_2$ hydrogenolysis on Ni/Al_2O_3 (0.1 g); heptane (10 mL), T = 20 °C, H_2 (1 bar), Hg/Ni = 0.54

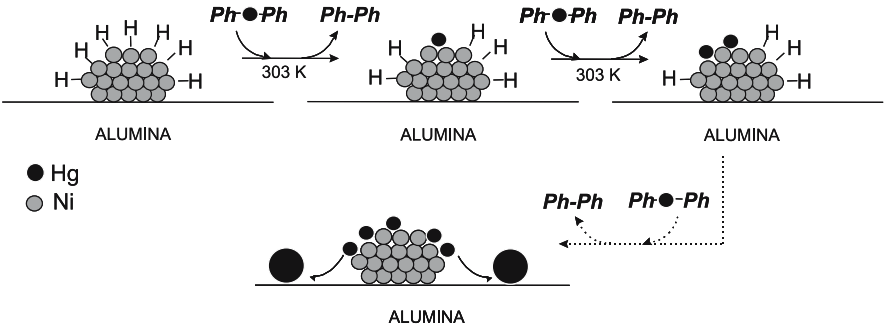

Scheme 37 C – C bond cleavage or formation – Gault mechanism

reaction with $HgPh_2$. The reaction is very fast as 0.182 mmol of $HgPh_2$ reacts in less than 0.5 h on 0.05 g of Ni/Al_2O_3 ($r_e > 7$ mmol h^{-1} g^{-1}; Fig. 9).

After four consecutive runs (Table 7), the total quantity of $HgPh_2$ introduced represents about 6 $HgPh_2$ per total Ni (Hg/Ni_t), that is 33 $HgPh_2/Ni_s$. There is a total decomposition of the $HgPh_2$ introduced with formation of mostly biphenyl along with a small amount of phenylcyclohexane (0.5%), benzene, and cyclohexane (0.6%). Since the quantity of $HgPh_2$ decomposed by the surface nickel atom is about 33, this reaction is catalytic. Moreover, at the end of the runs, 93% of the mercury introduced is recovered as metallic Hg in the bottom of the reactor.

While the thermal decomposition of $HgPh_2$ proceeds above 100 °C by simultaneous rupture of both Hg – C bonds with an activation energy of about 69 kcal/mole and formation of biphenyl as the primary product [141], the

same reaction is catalyzed on the nickel atoms at room temperature. In contrast to Ni and As, Hg and Ni do not give alloy or amalgam, and the Hg atoms adsorbed as "adatoms" on the surface are very mobile and can coalesce to give metallic Hg (Scheme 37).

3.1.4 Conclusion

The reactivity of organometallic reagents (R_xM) of group 12 and 14–15 with metal surfaces in the presence of H_2 have common features: the carbon-M bond undergoes hydrogenolysis on metal particles to generate well-defined species. At low temperatures, surface organometallic complexes are observed in which the organometallic reagent has formed a covalent bond with the metal surface, but has kept some of its alkyl ligands: $M'_s[MR_x]_y$. At higher temperatures, the organometallic fragment looses all its original ligands to form bonds exclusively with the surface of the metal to make adatoms, that can further migrate into the metal lattice to form alloys. In the specific case of Hg, this reaction is catalytic since it liberates a hydrocarbon and metallic mercury. In the case of $HgPh_2$ and $AsPh_3$, it is in fact the fundamental basis for a depollution process of crude oils. In the case of group 14 elements (Sn, Ge, and Si), this type of reaction generates a family of new materials, which have been used as catalysts since they display improved properties compared to the parent metal surfaces as will be discussed hereafter.

3.2 Catalytic Reactions and Elementary Steps on Metallic Surfaces

3.2.1 Carbon-Carbon Bond Cleavage on Metallic Surfaces

Many important catalytic reactions imply formation or cleavage of carbon-carbon bonds: for instance, the Fischer–Tropsch synthesis or the hydrogenolysis, the dehydrocyclization, and the skeletal isomerization of hydrocarbons. Some studies, in particular those of Basset [142–144], Garin, Gault and Maire [145–150], Maitlis [151, 152], Pettit [153], Rooney [154], Zaera [155–157] and Barteau [158, 159] suggested mechanistic relationships between different processes implicating carbon-carbon bond cleavage or formation. Many of these reports suggest elementary steps which are related or even identical to those already found in molecular organometallic chemistry.

From a general point of view, a monometallic catalyst can be considered as surface metal atoms linked together, forming an "ensemble" on the surface [160].

There is no clear consensus in the literature, regarding the elementary steps of carbon-carbon bond cleavage and formation on metallic surfaces.

Scheme 38 C – C bond cleavage or formation on metallic surfaces as proposed by Basset and Leconte

Gault and coworkers [149] have observed that the distribution of products obtained by hydrogenolysis and isomerization of methylcyclopentane was the same as those obtained with hexane. They proposed two competing mechanisms: a selective mechanism implying an $\alpha,\alpha,\beta,\beta$-tetra-adsorbed species and a non-selective mechanism implying coordinated olefin and bis-carbene intermediates (Scheme 38).

Leconte and Basset [161–166] proposed two other possible mechanisms (Scheme 39): the first one implies a 1,2 carbon-carbon activation which invokes the de-insertion of a methylidene fragment from a surface metal-alkyl species, and the second implies a 1,3 carbon-carbon bond activation in which the key steps are the formation of a dimetallacyle by γ-H activation from a metal-alkyl followed by carbon-carbon bond cleavage via a concerted electron transfer.

One should note that these mechanisms imply only well-known elementary steps of molecular organometallic chemistry [167].

The 1,3-carbon-carbon bond activation (also called γ-H activation pathway) has the advantage in that it explains several observations: (1) hexane undergoes hydrogenolysis on an Ir/SiO_2 catalyst at 200 °C (H_2/hexane = 50/1), while no hydrogenolysis of ethane is observed up to 270 °C under similar conditions; and (2) the hydrogenolysis of hexane and cyclohexane have common features (vide infra) [168].

Firstly, the difference between ethane and higher alkanes cannot be readily explained by mechanisms such as those proposed by Gault (Scheme 38) or 1,2-carbon-carbon activation mechanisms (Scheme 39), while the mechanism involving γ-H activation does fully account for this observation. Given

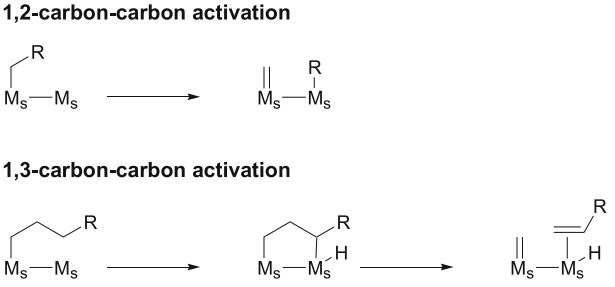

Scheme 39 Proposed mechanism for C – C bond cleavage of cyclohexane and hexane

Table 8 Distribution of C_1 to C_5 primary products in the hydrogenolysis of cyclohexane or *n*-hexane over Ir/SiO_2—Temp = 200 °C, H_2/Alkane ratio = 50

	CH_4	C_2H_6	C_3H_8	C_4H_8	C_5H_{10}
Hexane	9	18	47	16	9
Cyclohexane	30	8	24	12	26

this mechanism, ethane cannot undergo hydrogenolysis under mild conditions since formation of the necessary dimetallacyclopentane intermediate is not readily possible.

Secondly, this mechanism (1,3-carbon-carbon bond activation) applies to both acyclic and cyclic paraffins such as hexane and cyclohexane (Scheme 40 and Table 8). Kinetic studies on the hydrogenolysis of these alkanes are note-

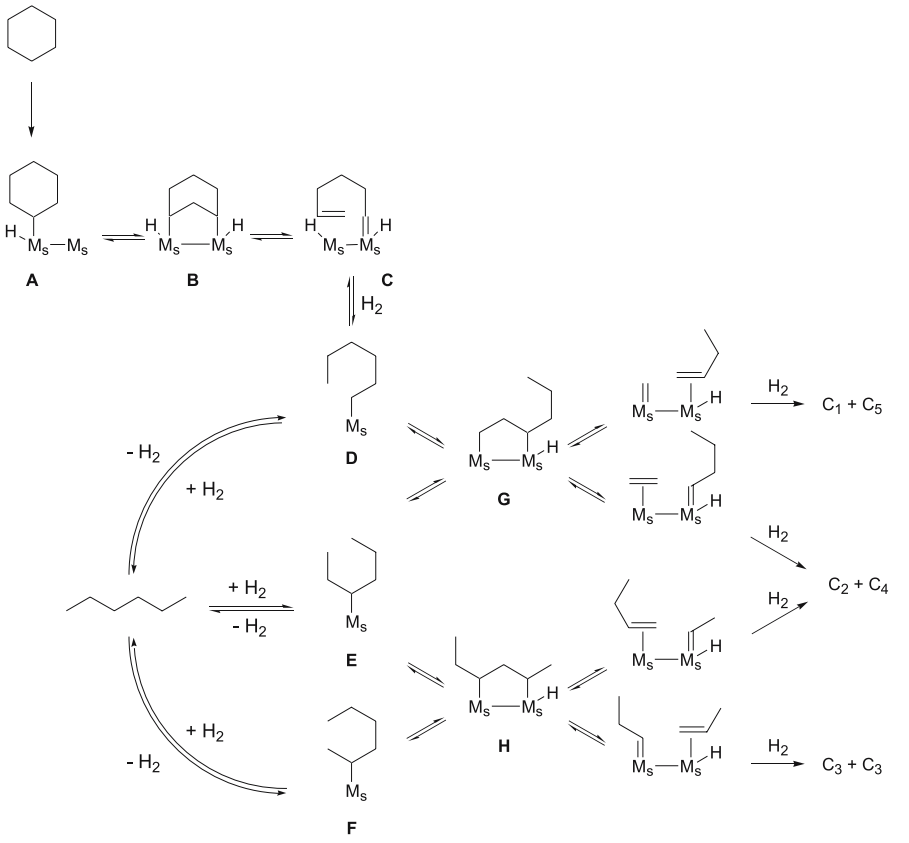

Scheme 40

worthy: when a mixture of a hydrocarbon and H_2 is passed at high temperatures through a catalytic bed (active sites of metal particles), there is formation of hydrogenolysis products, which arise from adsorption-reaction-desorption processes. By increasing the flow rate of the mixture through the fixed bed, the contact time of the mixture with the active sites decreases and thus, at very low contact time, only one process occurs leading to "primary" products (kinetic products), which can give mechanistic information.

As a case study, the hydrogenolysis of alkanes over Ir/SiO_2 will be studied in detail, and the product selectivities at zero contact time for the hydrogenolysis of hexane and cyclohexane are shown in Table 8.

From these data, some key information can be drawn: in both cases, the couple methane/pentane as well as the couple ethane/butane have similar selectivities. This implies that each couple of products (ethane/butane and methane/pentane) is probably formed via a common intermediate, which is probably related to the hexyl surface intermediate **D**, which is formed as follows: cyclohexane reacts first with the surface via C – H activation to produce a cyclohexyl intermediate **A**, which then undergoes a second C – H bond activation at the γ-position to give the key 1,3-dimetallacyclopentane intermediate **B**. Concerted electron transfer (a 2+2 retrocyclization) leads to a non-cyclic ω-alkenylidene metal surface complex, **C**, which under H_2 can evolve towards a surface hexyl intermediate **D**. Then, the surface hexyl species **D** can lead to all the observed products via the following elementary steps: (1) hydrogenolysis into hexane; (2) β-hydride elimination to form 1-hexene, followed by re-insertion to form various hexyl complexes (**E** and **F**); or (3) a second carbon-carbon bond cleavage, through a γ-C – H bond activation to the metallacyclic intermediate **G** or **H** (Scheme 40). Under H_2, intermediate **G** can lead either to pentane/methane or ethane/butane mixtures, while intermediate **H** would form ethane/butane or propane.

Moreover, while the change from cyclohexane to hexane as the reactant has produced a large change in the relative selectivity of the methane/pentane co-products with respect to other products, the ratio of propane to the ethane/butane couple is very close (46/30 or 1.5 for hexane and 24/20 or 1.2 for cyclohexane, Table 8). This small variation compared with the very large change in (methane + pentane) selectivity (18% for *n*-hexane, 56% for cyclohexane) suggests that the formation of ethane/butane is independent of the formation of methane/pentane, that is that intermediate **E** is not a major contributor to the formation of the ethane/butane couple.

Finally, the change in selectivity for the methane/pentane couple for the two different substrates (18% for hexane, 56% for cyclohexane) can be explained as follows: in the case of cyclohexane, the C_1 to C_5 products are formed through the second carbon-carbon bond cleavage via the hexyl surface intermediate **D** whereas in the case of hexane, the initial carbon-hydrogen bond activation step can lead to any of three alkyl surface intermediates (**D**, **E**, and **F**) before arriving at the key metallacyclic intermediates

G and **H**. This suggests that the isomerization of the surface alkyl fragments inter-converting **D**, **E**, and **F**, is slow with respect to the second carbon-hydrogen bond activation step and subsequent carbon-carbon bond cleavage.

Overall, this study shows that, like in molecular organometallic chemistry, the chemistry on metal surfaces follows similar elementary steps, and that it is possible to have a molecular understanding of catalytic phenomenon such as paraffin transformations on metal particles.

3.2.2 Taming Carbon-Carbon Bond Cleavage on Metallic Surfaces, the "Site Isolation" Effect

In some catalytic processes, it is necessary to avoid carbon-carbon bond cleavage. For example, isobutane is mainly transformed into its lower alkane homologues (hydrogenolysis products) on metal surfaces, while it can be converted more and more selectively into isobutene when the Pt catalysts contain an increasing amount of Sn (selective dehydrogenation process) [131].

Indeed, in the case of Pt particles, the first step involves a C – H bond activation of isobutane to generate a M-[*i* –Bu] fragment (Scheme 41). While this fragment can undergo β-H elimination to form isobutene and a metal hydride, it can also undergo a second C – H activation (γ-H) since the fragment is surrounded by other metal atoms to generate a dimetallacyclopentane. This metallacycle can rearrange to give a surface methylene fragment and a propylene molecule, which under H_2 can give methane and propane as observed experimentally. Alternatively, depending on the H_2 pressure, the methylene fragment may dehydrogenate further to a surface carbyne and eventually carbon adatom (carbide), leading to a coke deposit, which is one of the possible ageing phenomenon with time on stream.

In conclusion, hydrogenolysis processes and coke formation occur on large ensembles of surface platinum atoms [160], while dehydrogenation reactions would proceed on single (isolated) Pt atoms [169]. The presence of tin atoms regularly distributed on the metal surface diminishes the size of the ensemble [130, 170–173], the same is observed for copper atoms on nickel surfaces [174] or tin atoms on rhodium and nickel surfaces [137, 175–177], leading to "site isolation" and therefore to selectivity.

In the case of PtSn systems, the increasing amount of Sn decreases the probability of finding unaffected adjacent metal atoms, and it is therefore more difficult to generate the dimetallacyclopentane intermediate, necessary for the formation of the by-products (Scheme 42). Therefore, dehydrogenation becomes the major pathway, and up to 98% selectivity is achieved with catalysts containing a Sn/Pt_s ratio greater than ca. 0.8.

The effect of tin on the catalytic activity in terms of turn over frequencies (TOF) is more complex. When Sn/Pt_s increases from 0 to 0.85, the catalytic activity based both on the total number of Pt atoms or even on surface Pt

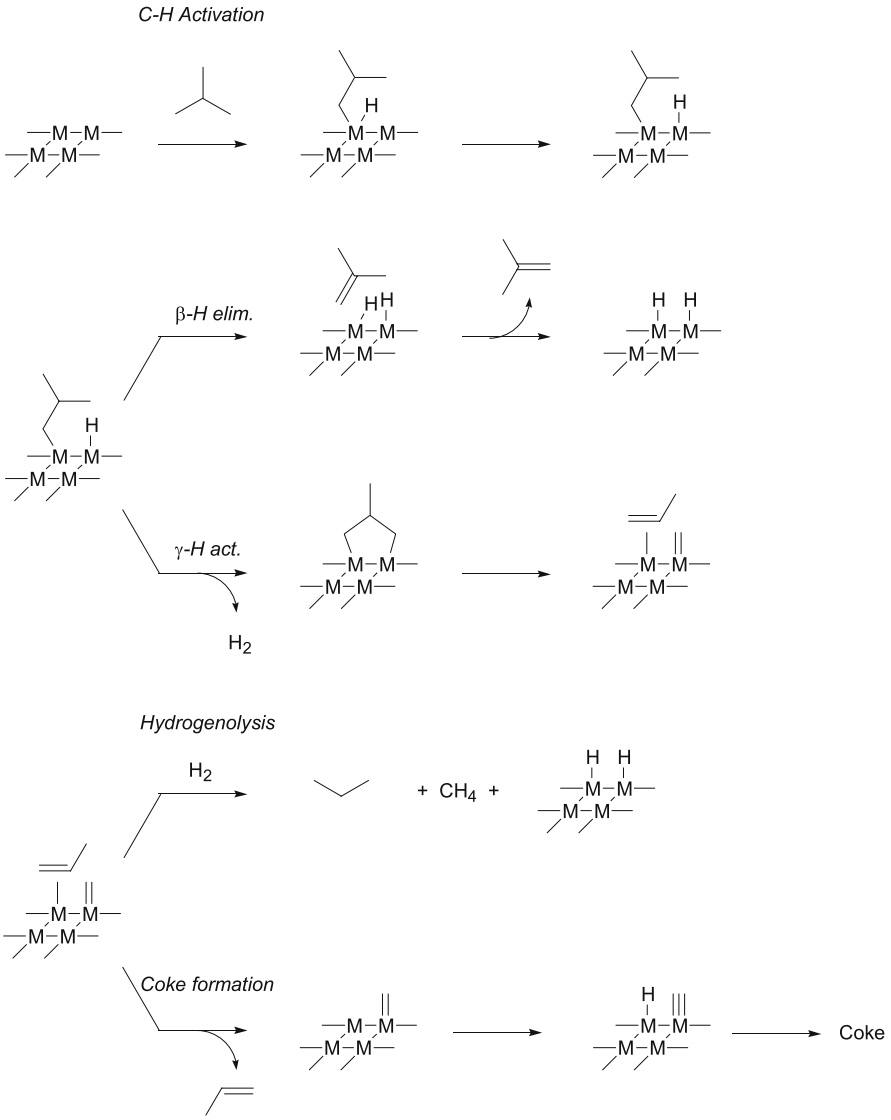

Scheme 41

atoms (Pt_s) first increases dramatically and then drops. The increase of activity with addition of tin (from $Sn/Pt_s = 0$ to 0.6) is probably due to a slower rate of coke formation, which poisons the active surface. Above a ratio of 0.6, the activity of the catalyst based on total Pt atoms begins to decrease but the activity based on surface Pt atoms, Pt_s, remains roughly constant. This result is consistent with a structure insensitive catalytic activity in alkane dehydrogenation [170, 178, 179], which is reasonable since all isolated Pt atoms

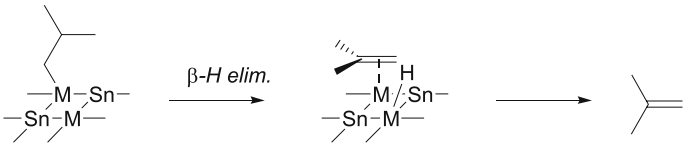

Scheme 42

can achieve in principle the C – H bond activation, leading to a Pt-isobutyl fragment, which upon β-H elimination generates isobutene.

3.2.3
Selective Reactions on Modified Metal Surfaces: the Ligand Effect

Hydrogenation of α-β Unsaturated Aldehydes

When the hydrogenation of citral (α,β-unsaturated aldehyde) is performed with a supported metal, for example Rh/SiO_2 under classical conditions (liquid phase, rhodium particles dimensions 1.8 nm, rhodium dispersion 80%, citral/Rh_s = 200, (PH_2) = 80 bars, T = 340 K) the catalytic activity is very high but the reaction is not selective, unsaturated alcohol, saturated aldehyde, and saturated alcohol are formed. On the other hand, when Rh/SiO_2 is modified by reaction with $SnBu_4$ (Sn/Rh_s = 0.95) to give Rh_sSnBu as a major surface species, the catalytic activity is only slightly decreased while 3,7-dimethyl-2,6-octenol, the unsaturated alcohol, is obtained with a selectivity greater than 95% [120]. This improvement in selectivity can be explained by the ligand effect of [SnBu] fragments as illustrated in Scheme 43.

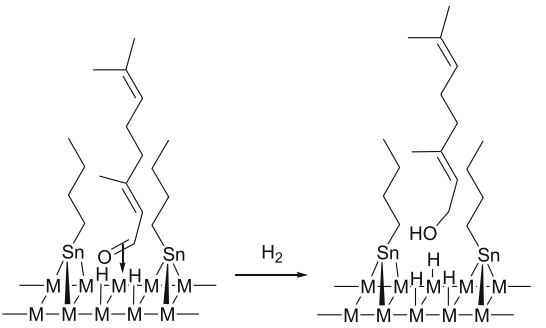

Scheme 43

3.2.4
Selective Reactions on Modified Metal Surfaces: Adatom Effect (Selective Site Poisoning)

Isomerization of 3-Carene into 2-Carene

Metals (Raney nickel or Ni/SiO_2, Pd/C, ...) can easily catalyze the isomerization of 3-carene into 2-carene (Scheme 44), but the selectivity is low, due to the hydrogenation of the two isomers into carane.

Addition of very small amounts of Bu_4Sn can completely transform the performance of these catalysts by poisoning the hydrogenation sites. For example, when a Ni^0/SiO_2 catalyst is used, the best result corresponds to a 2-carene yield of 30%, with at least 30% of the carenes transformed into by-products. Addition of 0.04 mole of Bu_4Sn/Ni_s results in an increase of the yield of 2-carene, up to 37%, and a decrease of the amount of by-products to less than 10%. In this case, tin is present as adatoms on the most hydrogenating sites (very likely those situated on the faces rather than on corners and edges).

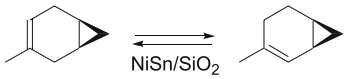

Scheme 44

Dehydrogenation of 2-Butanol into Butanone

The Raney nickel is a very efficient catalyst for the dehydrogenation of 2-butanol into butanone (Scheme 45) with a good selectivity (90%). But, for industrial applications selectivities as high as 99% are required. This can be achieved by poisoning some sites by reaction with Bu_4Sn (the best results are obtained with a Sn/Ni ratio of 0.02), which probably occurs first on the sites responsible for the side reactions. The consequence is a slight decrease of the catalytic activity and an increase of the selectivity in 2-butanone which can reach 99%. This catalyst, developed by IFP, has been used commercially in Japan for several years [180].

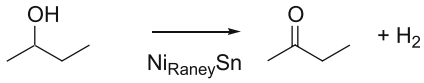

Scheme 45

3.2.5
Selective Reactions on Modified Metal Surfaces: The Case of Alloys

Selective Hydrogenolysis of Esters and Acids to Aldehydes and Alcohols

Hydrogenolysis of esters to aldehydes or alcohols needs high temperatures and high pressures. Moreover, it leads to the formation of acids, alcohols, and hydrocarbons. In contrast, bimetallic M – Sn alloys (M = Rh, Ru, Ni) supported on silica are very selective for the hydrogenolysis of ethyl acetate into ethanol [181]. For example while the selectivity to ethanol is 12% with Ru/SiO_2, it increases up to 90% for a Ru-Sn/SiO_2 catalyst with a Sn/Ru ratio of 2.5 [182]. In addition, the reaction proceeds at lower temperatures than with the classical catalysts (550 K instead of temperatures higher than 700 K). The first step is the coordination of the ester to the alloy (Scheme 46), and most probably onto the tin atoms. After insertion into the M – H bond, the acetal intermediate decomposes into acetaldehyde and an ethoxide intermediate, which are both transformed into ethanol under H_2.

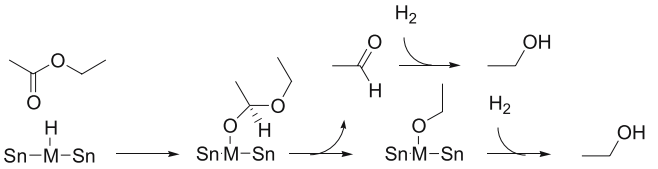

Scheme 46

3.2.6
Conclusion

It is clear that a molecular understanding of phenomena on surfaces, elementary steps, help to understand how to improve catalytic systems through a structure-activity relationship. While there is still room for improvement, it should lead, in the near future, to a more rational design of heterogeneous catalysts and to the application of metals modified by surface organometallic chemistry to a larger number of reactions.

4
General Conclusion

Structural Similarities and Differences between Molecular and Surface Organometallic Chemistry

It is first necessary to distinguish the surface organometallic chemistry on metals and on oxides since one deals with a large ensemble of metals, while the others generate dispersed metal atoms attached covalently onto the support.

In the latter case, grafting of molecular organometallic complexes provides well-defined surface structures when the pre-treatment of silica is controlled, that is the complex can be bound via one or two covalent bonds with the surface of the support. In fact, the oxide supports can be considered more like bulky ligands, typically η^1-X or η^2-X_2 ligands in the Green formalism, and in some cases as η^3-X_3 or even LX ligands. Therefore, the structures on oxide surfaces are not very different from those observed in molecular chemistry. In fact, the NMR data obtained in solution are usually very close to what is obtained for the corresponding surface complexes. Moreover, additional ligands can be observed by EXAFS such as oxygen of the surface (siloxane bridges); they could correspond to solvent molecules in the solution phase.

While structurally equivalent, they usually differ from a reactivity point of view. Firstly, the organometallic reagent, after reaction with the surface, readily extrudes extra ligands upon reaction with surface silanols, while they can give a stable adduct in solution.

Surface species are in general more stable than their molecular equivalents, and show unprecedented activities. By replacing an alkyl substituent by a siloxy group, a tremendous increase in the reactivity of the metal centre is seen: it changes inactive organometallics into highly active olefin metathesis catalysts for example. Additionally, alkane hydrogenolysis and metathesis are observed on supported complexes, while so far the corresponding hydrides or alkyl complexes have been quite unreactive towards alkanes [183, 184]. This is probably due to the use of solid ligands, which prevents dimerization deactivation pathways.

In the case of metallic particles, we have shown that the elementary steps are similar to those observed in standard organometallic chemistry, but it is governed by the presence of ensembles of atoms, which can allow multiple C – H bond activations. Moreover, since the metallic particles are electron reservoirs, they can easily participate further in electron transfer processes necessary for cleaving the carbon-carbon bond skeleton of molecules. It is possible to control their reactivity via controlling the coordination sphere of these metal surfaces through the reaction of organometallic reagents. By this method, it is possible to generate selectively: (1) grafted organometallics on

metallic particles; (2) adatoms; or (3) alloys, which show different selective catalytic properties compared to the original metal particles.

Acknowledgements We are grateful to the CNRS, CPE Lyon, the Minister of Research and Education, the Région Rhônes-Alpes district, BASF AG, BP Chemicals, Rhodia, Shell and IFP for financial support and helpful discussions. We also want to thank the numerous students and research associates who have participated over the years in this research effort.

References

1. Copéret C, Chabanas M, Saint-Arroman RP, Basset J-M (2003) Angew Chem Int Ed 42:156
2. Morrow BA (1990) Stud Surf Sci Catal 57:A161
3. Bartram ME, Michalske TA, Rogers JW Jr (1991) J Phys Chem 95:4453
4. Morrow BA, Gay ID (2000) Surfactant Science Series 90:9
5. Anwander R, Nagl I, Widenmeyer M, Engelhardt G, Groeger O, Palm C, Roeser T (2000) J Phys Chem B 104:3532
6. Anwander R (2001) Chem Mater 13:4419
7. Widenmeyer M, Anwander R (2002) Chem Mater 14:1827
8. Pichat P, Mathieu MV, Imelik B (1969) Bull Soc Chim Fr 2611
9. Zhang J, Nicholas JB, Haw JF (2000) Angew Chem Int Ed 39:3302
10. Osegovic JP, Drago RS (1999) J Catal 182:1
11. Osegovic JP, Drago RS (2000) J Phys Chem B 104:147
12. Nedez C, Theolier A, Lefebvre F, Choplin A, Basset JM, Joly JF (1993) J Am Chem Soc 115:722
13. Millot N, Cox A, Santini CC, Molard Y, Basset J-M (2002) J Chem 8:1438
14. Copéret C, Chabanas M, Petroff Saint-Arroman R, Basset J-M (2003) Angew Chem Int Ed 42:156
15. Lefort L, Chabanas M, Maury O, Meunier D, Copéret C, Thivolle-Cazat J, Basset J-M (2000) J Organomet Chem 593–594:96
16. Dufaud V, Niccolai GP, Thivolle-Cazat J, Basset J-M (1995) J Am Chem Soc 117:4288
17. Chabanas M, Quadrelli EA, Fenet B, Copéret C, Thivolle-Cazat J, Basset J-M, Lesage A, Emsley L (2001) Angew Chem Int Ed 40:4493
18. Meunier D, de Mallmann A, Basset J-M (2003) Topics in Catalysis 23:183
19. Ajjou JAN, Scott SL (1997) Organometallics 16:86
20. Ajjou JAN, Scott SL, Paquet V (1998) J Am Chem Soc 120:415
21. Wang X-X, Veyre L, Lefebvre F, Patarin J, Basset J-M (2003) Microporous and Mesoporous Materials 66:169
22. Anwander R, Roesky R (1997) J Chem Soc, Dalton Trans 137
23. Bouh AO, Rice GL, Scott SL (1999) J Am Chem Soc 121:7201
24. Wolke SI, Buffon R, Filho UPR (2001) J Organomet Chem 625:101
25. Grasser S, Haessner C, Koehler K, Lefebvre F, Basset J-M (2003) Phys Chem Chem Phys 5:1906
26. Nozaki C, Lugmair CG, Bell AT, Tilley TD (2002) J Am Chem Soc 124:13194
27. Jarupatrakorn J, Tilley TD (2002) J Am Chem Soc 124:8380
28. Quignard F, Lecuyer C, Bougault C, Lefebvre F, Choplin A, Olivier D, Basset JM (1992) Inorg Chem 31:928

29. Rosier C, Niccolai GP, Basset J-M (1997) J Am Chem Soc 119:12408
30. Chabanas M, Baudouin A, Copéret C, Basset J-M, Lukens W, Lesage A, Hediger S, Emsley L (2003) J Am Chem Soc 125:492
31. Toreki R, Schrock RR, Davis WM (1992) J Am Chem Soc 114:3367
32. Chabanas M, Baudouin A, Copéret C, Basset J-M (2001) J Am Chem Soc 123:2062
33. Lesage A, Emsley L, Chabanas M, Copéret C, Basset J-M (2002) Angew Chem Int Ed 41:4535
34. Brookhart M, Green MLH (1983) J Organomet Chem 250:395
35. Nugent WA, Mayer JM (1988) Metal-Ligand Multiple Bond. Wiley, New York
36. Schrock RR, Crowe WE, Bazan GC, DiMare M, O'Regan MB, Schofield MH (1991) Organometallics 10:1832
37. Feher FJ, Budzichowski TA (1995) Polyhedron 14:3239
38. Murugavel R, Voigt A, Walawalkar MG, Roesky HW (1996) Chem Rev 96:2205
39. Abbenhuis HCL, Krijnen S, van Santen RA (1997) Chem Commun 331
40. Duchateau R (2002) Chem Rev 102:3525
41. Schrock RR, Fellmann JD (1978) J Am Chem Soc 100:3359
42. LaPointe RE, Wolczanski PT, Van Duyne GD (1985) Organometallics 4:1810
43. Feinstein-Jaffe I, Gibson D, Lippard SJ, Schrock RR, Spool A (1984) J Am Chem Soc 106:6305
44. Rosier C (1999) Ph.D. Thesis, UCBL
45. Herrmann WA, Stumpt AW, Priermeier T, Bogdanovic S, Dufaud V, Basset J-M (1997) Angew Chem Int Ed Engl 35:2803
46. Zakharov VA, Dudchenko VK, Paukstis E, Karakchiev LG, Yermakov YI (1977) J Mol Catal 2:421
47. Yermakov YI, Ryndin YA, Alekseev OS, Kochubei DI, Shmachkov VA, Gergert NI (1989) J Mol Catal 49:121
48. Quignard F, Choplin A, Basset JM (1991) J Chem Soc, Chem Commun 1589
49. Quignard F, Lecuyer C, Choplin A, Olivier D, Basset JM (1992) J Mol Catal 74:353
50. Corker J, Lefebvre F, Lecuyer C, Dufaud V, Quignard F, Choplin A, Evans J, Basset J-M (1996) Science (Washington, DC) 271:966
51. Rataboul F, Thieuleux C, Baudouin A, Veyre L, Copéret C, Thivolle-Cazat J, Basset J-M, Lesage A, Emsley L (2004) J Am Chem Soc
52. Vidal V, Theolier A, Thivolle-Cazat J, Basset J-M, Corker J (1996) J Am Chem Soc 118:4595
53. Taoufik M, de Mallmann A, Prouzet E, Saggio G, Thivolle-Cazat J, Basset J-M (2001) Organometallics 20:5518
54. Ballard DGH, Heap N, Kilbourn BT, Wyatt RJ (1973) Makromol Chem 170:1
55. Yermakov YI, Kuznetsov BN, Zakharov VA (1981) Stud Surf Sci Catal 8:1
56. Chen EY-X, Marks TJ (2000) Chem Rev 100:1391
57. Hlatky GG (2000) Chem Rev 100:1347
58. Fink G, Steinmetz B, Zechlin J, Przybyla C, Tesche B (2000) Chem Rev 100:1377
59. Sheldon RA, Van Vliet MCA (2001) In: Sheldon RA, van Bekkum H (eds) Fine Chemicals through Heterogeneous Catalysis. Wiley-VCH, Weinheim, p 473
60. Crocker M, Herold RHM, Roosenbrand BG, Emeis KA, Wilson A (1998) Colloids and Surfaces, A: Physicochemical and Engineering Aspects 139:351
61. Crocker M, Herold RHM, Orpen AG, Overgaag MTA (1999) J Chem Soc, Dalton Trans 3791
62. Bini F (2004) Ph.D. Thesis, UCBL
63. Maschmeyer T, Klunduk MC, Martin CM, Shephard DS, Thomas JM, Johnson BFG (1997) Chem Commun 1847

64. Leyrit P, McGill C, Quignard F, Choplin A (1996) J Mol Catal A: Chem 112:395
65. Quignard F, Graziani O, Choplin A (1999) Appl Catal A: General 182:29
66. Blandy C, Pellegatta JL, Choukroun R, Gilot B, Guiraud R (1993) Can J Chem 71:34
67. Ferret N, Dufaud V, Salinier V, Basset J (1997) FR Patent 2747675
68. Ivin KJ, Mol IC (1996) Olefin Metathesis and Metathesis Polymerization. Academic Press, New York
69. Mol JC (1999) Catal Today 51:289
70. Mol JC (1999) Catal Today 52:377
71. Herisson JL, Chauvin Y (1971) Makromolekulare Chemie 141:161
72. Mol JC (2004) J Mol Catal A: Chem 213:39
73. Mol JC (2004) Topics in Catalysis 27:97
74. Schrock RR (1998) Top Organomet Chem 1:1
75. Trnka TM, Grubbs RH (2001) Accounts of Chemical Research 34:18
76. Hoveyda AH, Schrock RR (2001) J Chem 7:945
77. Couturier JL, Paillet C, Leconte M, Basset JM, Weiss K (1992) Angew Chem 104:622
78. Lefebvre F, Leconte M, Pagano S, Mutch A, Basset J-M (1995) Polyhedron 14:3209
79. Copéret C (2004) New J Chem 28:1
80. Copéret C, Lefebvre F, Basset JM (2003) In: Grubbs RH (ed) Handbook of Olefin Metathesis, vol 2. Wiley-VCH, Weinheim, p 190
81. Chabanas M, Baudouin A, Copéret C, Basset JM (2001)J Am Chem Soc 123:2062
82. Chabanas M, Copéret C, Basset J-M (2003) J Chem 9:971
83. Bilhou JL, Basset JM, Mutin R, Graydon WF (1977) J Am Chem Soc 99:4083
84. Mol JC (2002) Green Chem 4:5
85. Mol JC (2002) NATO Science Series, II: Mathematics, Physics and Chemistry 56:377
86. Toreki R, Vaughan GA, Schrock RR, Davis WM (1993) J Am Chem Soc 115:127
87. Schrock RR, Murdzek JS, Bazan GC, Robbins J, DiMare M, O'Regan M (1990) J Am Chem Soc 112:3875
88. Feher FJ, Tajima TL (1994) J Am Chem Soc 116:2145
89. Dinger MB, Mol JC (2003) Organometallics 22:1089
90. Lécuyer C, Quignard F, Choplin A, Olivier D, Basset JM (1991) Angew Chem Int Ed Engl 30:1660
91. d'Ornelas L, Reyes S, Quignard F, Choplin A, Basset JM (1993) Chem Lett 1931
92. Chabanas M, Vidal V, Copéret C, Thivolle-Cazat J, Basset J-M (2000) Angew Chem Int Ed 39:1962
93. Thieuleux C, Copéret C, Dufaud V, Marangelli C, Kuntz E, Basset JM (2004) J Mol Catal A: Chem 213:47
94. Niccolai GP, Basset J-M (1996) Appl Catal A: General 146:145
95. Dufaud V, Basset J-M (1998) Angew Chem Int Ed 37:806
96. Vidal V, Theolier A, Thivolle-Cazat J, Basset J-M (1995) J Chem Soc, Chem Commun 991
97. Sharp PR, Astruc D, Schrock RR (1979) J Organomet Chem 182:477
98. Parkin G, Bunel E, Burger BJ, Trimmer MS, Van Asselt A, Bercaw JE (1987) J Mol Catal 41:21
99. Vidal V, Theolier A, Thivolle-Cazat J, Basset J-M (1997) Science (Washington, DC) 276:99
100. Copéret C, Maury O, Thivolle-Cazat J, Basset J-M (2001) Angew Chem Int Ed 40:2331
101. Le Roux E, Chabanas M, Baudouin A, de Mallmann A, Copéret C, Thivolle-Cazat J, Basset J-M, Sunley GJ, Lesage A, Emsley L (2004) J Am Chem Soc (in press)
102. Turner HW, Schrock RR (1982) J Am Chem Soc 104:2331
103. Fellmann JD, Schrock RR, Traficante DD (1982) Organometallics 1:481

104. Fryzuk MD, Johnson SA, Rettig SJ (2001) J Am Chem Soc 123:1602
105. Soulivong D, Copéret C, Thivolle-Cazat J, Basset J-M, Pardy R, Sunley GJ (2004) Angew Chem Int Ed (in press)
106. Ascencio JA, Gutierrez-Wing C, Espinosa ME, Martin M, Techuacanero S, Zorrilla C, Jose-Yacaman M (1998) Surf Sci 396:349
107. Van Hardeveld R, Hartog F (1969) Surf Sci 15:189
108. Bond GC, Wells PB (1985) Appl Catal 18:225
109. Frennet A, Wells PB (1985) Appl Catal 18:243
110. Geus JW, Wells PB (1985) Appl Catal 18:231
111. Wells PB (1985) Appl Catal 18:259
112. Candy JP, Didillon B, Smith EL, Shay TB, Basset JM (1994) J Mol Catal 86:179
113. Humblot F, Didillon B, Le Peltier F, Candy JP, Corker J, Clause O, Bayard F, Basset JM (1998) J Am Chem Soc 120:137
114. Nédez C, Théolier A, Lefebvre F, Choplin A, Basset JM, Joly JF (1993) J Am Chem Soc 115:722
115. Margitfalvi J, Hegedüs M, Góbölös S, Kern-Tálas E, Szedlacsek P, Szabó S, Nagy F (1984) 8th Int Congr on Catalysis, vol IV. DECHEMA (Frankfurt am Main), Berlin, p 903
116. Margitfalvi JL, Tálas E, Gobolos S (1989) Catal Today 6:73
117. Dallaire C, Brook MA (1993) Organometallics 12:2332
118. Jubert AH, Michelini MC, Estiu GL, Ferretti OA (1997) Catalysis Letters 46:241
119. Chuit C, Corriu RJP, Reye C, Young JC (1993) Chem Rev 93:1371
120. Didillon B, El Mansour A, Candy JP, Basset JM, Le Peltier F, Boitiaux JP (1993) 10th Int Congr on Catalysis: New Frontiers in Catalysis 75:2370
121. Lesage P, Clause O, Moral P, Didillon B, Candy JP, Basset JM (1995) J Catal 155:238
122. Millet JM, Toyir J, Didillon B, Candy JP, Nédez C, Basset JM (1997) Hyperfine Interactions 108:477
123. Tena E, Spagnol M, Candy JP, de Mallmann A, Fiddy S, Corker J, Basset JM (2003) Chem Mater 15:1607
124. Vértes C, Tálas E, Czakó-Nagy I, Ryczkowski J, Göbölös S, Vértes A, Margitfalvi J (1991) Appl Catal 68:149
125. Chupin C, Candy JP, Basset JM (2003) Catal Today 79–80:15
126. Didillon B, El Mansour A, Candy JP, Bournonville JP, Basset JM (1991) Stud Surf Sci Catal 59:137
127. Margitfalvi M, Borbath I, Tompos A (1998) In: Delmon (ed) Preparation of Catalysts VII. Elsevier Science, Amsterdam, p 195
128. Lesage P, Candy JP, Hirigoyen C, Humblot F, Leconte M, Basset JM (1996) J Mol Catal A: Chem 112:303
129. Humblot F, Cordonnier MA, Santini C, Didillon B, Candy JP, Basset JM (1997) Stud Surf Sci Catal 108:289
130. Cortright RD, Dumesic JA (1994) J Catal 148:771
131. Humblot F, Candy JP, Le Peltier F, Didillon B, Basset JM (1998) J Catal 179:459
132. Balakrishnan K, Schwank J (1991) J Catal 132:451
133. Barias OA, Holmen A, Blekkan EA (1996) J Catal 158:1
134. Davis BH (1993) 10th Int Congr on Catalysis: New Frontiers in Catalysis A:889
135. Coq B, Figuéras F (1984) J Catal 85:197
136. Ferretti OA, Bournonville JP, Mabilon G, Martino G, Candy JP, Basset JM (1991) J Mol Cat 67:283
137. El Mansour A, Candy JP, Bournonville JP, Ferretti OA, Basset JM (1989) Angew Chem Int Ed Engl 28:347

138. Ferretti OA, Siri GJ, Humblot F, Candy JP, Didillon B, Basset JM (1998) React Kinet Catal Lett 63:115
139. Ryndin YA, Candy JP, Didillon B, Savary L, Basset JM (2001) J Catal 198:103
140. Didillon B, Savary L, Ryndin YA, Candy JP, Basset JM (2000) C R Acad Sci Paris, Série IIc, Chimie/Chemistry 3:413
141. Skinner HA (1964) In: Stone FGA, West R (eds) "Advances in Organometallic Chemistry", vol 2. Academic Press, New York, p 49
142. Hughes F, Besson B, Basset JM (1980) J Chem Soc, Chem Commun 719
143. Hughes F, Besson B, Bussière P, Dalmon JA, Basset JM, Olivier D (1981) Nouv J Chim 5:207
144. Commereuc D, Chauvin Y, Hughes F, Basset JM, Olivier D (1980) J Chem Soc, Chem Commun 154
145. Maire G, Garin F, Bernhard P, Girard P, Schmitt JL, Dartyge E, Dexpert H, Fontaine A, Lagarde P (1986) Appl Catal 26:305
146. Garin F, Gault FG (1975) J Am Chem Soc 97:4466
147. Garin F, Maire G, Gault FG (1981) Nouv J Chim 5:553
148. Garin F, Maire G, Gault FG (1981) Nouv J Chim 5:563
149. Gault FG (1981) Adv Catal 30:28
150. Weisang F, Gault FG (1979) J Chem Soc, Chem Commun:519
151. Maitlis PM, Long HC, Quyoum R, Turner ML, Wang Z-Q (1996) Chem Commun:1
152. Turner ML, Marsih N, Mann BE, Quyoum R, Long HC, Maitlis PM (2002) J Am Chem Soc 124:10456
153. Osterloh W, Cornell ME, Pettit R (1982) J Am Chem Soc 104:3759
154. O'Donohoe C, Clarck JKA, Rooney JJ (1980) J Chem Soc, Faraday Trans 76:345
155. Zaera F, Tjandra S (1996) J Am Chem Soc 118:12738
156. Zaera F, Tjandra S, Janssens TVW (1998) Langmuir 14:1320
157. Janssens VWT, Jin G, Zaera F (1997) J Am Chem Soc 119:1169
158. Idriss H, Pierce K, Barteau MA (1991) J Am Chem Soc 113:715
159. Idriss H, Libby M, Barteau MA (1992) Catal Lett 15:13
160. Biloen P, Helle JN, Verbeek H, Dautzenberg FM, Sachtler WMH (1980) J Catal 63:112
161. Rodriguez E, Leconte M (1991) J Catal 131:457
162. Rodriguez E, Leconte M, Basset JM (1989) J Catal 119:230
163. Rodriguez E, Leconte M, Basset JM (1991) J Catal 131:457
164. Rodriguez E, Leconte M, Basset JM (1991) J Catal 132:472
165. Rodriguez E, Leconte M, Basset JM, Tanaka K, Tanaka KI (1988) J Am Chem Soc 110:275
166. Leconte M (1994) J Mol Catal 86:205
167. Collman JP, Hegedus L (1980) Principles and Applications of Organotransition Metal Chemistry. University Science Book
168. Locatelli F, Candy JP, Niccolai G, Uzio D, Basset JM (2001) J Am Chem Soc 123:1658
169. Ribeiro FH, Bonivardi AL, Kim C, Somorjai GA (1994) J Catal 150:186
170. Biloen P, Dautzenberg FM, Sachtler WMH (1977) J Catal 50:77
171. Kappenstein C, Saouabe M, Guérin M, Marecot P, Uszkuruat I, Paal Z (1995) Catal Lett 31:9
172. Stagg SM, Querini CA, Alvarez WE, Resasco DE (1997) J Catal 168:75
173. Sachtler WMH, Van Santen RA (1977) Adv Catal 26:69
174. Martin GA, Dalmon JA (1980) J Catal 66:214
175. Agnelli M, Candy JP, Basset JM, Bournonville JP, Ferretti OA (1990) J Catal 121:236
176. Candy JP, Ferretti OA, Mabilon G, Bournonville JP, El Mansour A, Basset JM, Martino G (1988) J Catal 112:210

177. Didillon B, Candy JP, El Mansour A, Houtmann C, Basset JM (1992) J Mol Catal 74:43
178. Blakely DW, Somorjai GA (1976) J Catal 42:181
179. Guenin M, Breysse M, Frety R, Tifouti K, Marecot P, Barbier J (1987) J Catal 105:144
180. Snappe R, Bournonville JP, Miquel J, Martino G (1983) US Patent 4,380,673
181. Basset JM, Candy JP, Louessard P, Ferretti OA, Bournonville JP (1990) Wiss Zeitschr THLM 32:657
182. Louessard P, Candy JP, Bournonville JP, Basset JM (1989) Stud Surf Sci Cat 48:591
183. Wolczanski PT (1995) Polyhedron 14:3335
184. Turculet L, Tilley TD (2004) Organometallics 23:1542

Top Organomet Chem (2005) 16: 211–231
DOI 10.1007/b138078

Published online: 14 September 2005

Oxide- and Zeolite-supported "Molecular" Metal Clusters: Synthesis, Structure, Bonding, and Catalytic Properties

Bruce C. Gates

Department of Chemical Engineering and Materials Science, University of California, Davis, CA 95616, USA
bcgates@ucdavis.edu

Abstract This review is a summary of supported metal clusters with nearly molecular properties. These clusters are formed by adsorption or surface-mediated synthesis of metal carbonyl clusters, some of which may be decarbonylated with the metal frame essentially intact. The decarbonylated clusters are bonded to oxide or zeolite supports by metal–oxygen bonds, typically with distances of 2.1–2.2 Å; they are typically not free of ligands other than the support, and on oxide surfaces they are preferentially bonded at defect sites. The catalytic activities of supported metal clusters incorporating only a few atoms are distinct from those of larger particles that may approximate bulk metals.

Keywords Clusters · Clusters, metal · Clusters, supported metal · Clusters, ligands bonded to · Clusters reactivities and catalytic activities

Abbreviations
EXAFS Extended X-ray absorption fine structure
TEM Transmission electron microscopy
TOF Turnover frequency

1 Introduction

The typical solid catalyst used in technology consists of small catalytically active species, such as particles of metal, metal oxide, or metal sulfide, dispersed on a low-cost, high-area, nearly inert porous support such as a metal oxide or zeolite. The catalytic species are typically difficult to characterize in-

cisively because they are so small and nonuniform. The nonuniformity often corresponds to a low selectivity in catalysis.

In contrast to the typical supported catalyst, molecular catalysts such as organometallic complexes in solution offer the advantages of accessibility to reactants and uniqueness of structure that may confer high activity and selectivity. Organometallics anchored to solid supports may offer the same advantages if they are sufficiently accessible and nearly uniform (molecular analogues). Most supported organometallics are mononuclear metal complexes—but instead they may be polynuclear (metal clusters). The subject of this chapter is supported metal clusters that are molecular analogues.

Most successful catalysts present metal centers for bonding of reactant ligands. Attempts to prepare supported molecular catalysts incorporating metal centers have typically been made with organometallic precursors that react with a support to give anchored complexes. The support provides ligands, which may simply be those naturally present on the surface (e.g., oxygen and hydroxyl groups on metal oxides) or, alternatively, may be tethered groups such as phosphines. When the goal is precise synthesis to give a uniform, selective supported catalyst, the precursors of choice are those that react cleanly and uniquely with the support ligands. Organometallics are preferred over metal salts as precursors because they usually allow more easily controlled and better-characterized syntheses and give more uniform surface species than salts. However, preparation of uniform species on supports is difficult, whatever the precursor, because of the inherent nonuniformity of most surfaces, even those of single crystals.

The goal of precise synthesis of supported mononuclear and polynuclear metal complexes can be traced to the early work of Yermakov [1], Ballard [2], and others. Their work stimulated the lively field referred to as surface organometallic chemistry [3–6]. The success and importance of precise synthesis of supported "molecular" catalysts are illustrated by the application of supported metallocene catalysts for industrial alkene polymerization [7].

Most of the work on supported catalysts with nearly uniform structures has been dedicated to mononuclear metal complexes. Our focus is instead on polynuclear metal complexes, which have been much less thoroughly investigated. These clusters are important in catalysis, because, like metal surfaces, they offer neighboring metal sites for bonding and reaction [8], and many important catalytic reactions require such sites. Most industrial supported metal catalysts incorporate metal particles much larger than the clusters of interest here; however, some industrial catalysts, including those used for naphtha reforming to convert straight-chain alkanes (e.g., *n*-hexane) into aromatics (e.g., benzene), incorporate clusters of only about ten Pt atoms each, on average [9]. Other industrial supported metal catalysts incorporate even smaller clusters, along with larger particles [10]. Some of the recent motivations for research on supported metal clusters are reports that the catalytic activity of

supported gold clusters is dramatically different from that of bulk gold and is strongly cluster size dependent [11].

This review of the chemistry of supported metal clusters addresses the following topics: (1) synthesis on support surfaces; (2) structural characterization by spectroscopy, microscopy, and other methods; (3) reactivity; and (4) catalysis. The focus is on structurally simple and relatively well characterized samples (although it is emphasized that the standard of structural understanding of surface species is far below than that of molecular species or crystalline structures). The available results demonstrate (1) chemistry of supported organometallic clusters mimicking that of organometallic clusters in solution; (2) insights into the properties of industrial supported metal catalysts (which are highly nonuniform in structure); and (3) fundamental understanding of catalysts at a depth that is unusual for solids.

2
Chemistry of Supported Metal Clusters

2.1
Monometallic Clusters

2.1.1
Synthesis of Metal Carbonyl Clusters and Decarbonylated Clusters

2.1.1.1
Introduction

Metal clusters on supports are typically synthesized from organometallic precursors and often from metal carbonyls, as follows: (1) The precursor metal cluster may be deposited onto a support surface from solution; or (2) a mononuclear metal complex may react with the support to form an adsorbed metal complex that is treated to convert it into an adsorbed metal carbonyl cluster; or (3) a mononuclear metal complex precursor may react with the support in a single reaction to form a metal carbonyl cluster bonded to the support. In a subsequent synthesis step, metal carbonyl clusters on a support may be treated to remove the carbonyl ligands, because these occupy bonding positions that limit the catalytic activity.

These synthesis methods, among others, are reviewed in detail elsewhere [12], and only a brief summary is presented here.

2.1.1.2 Adsorption of Intact Cluster Precursors

Neutral metal carbonyl clusters exemplified by $Ir_4(CO)_{12}$, $Ir_6(CO)_{16}$, and $Rh_6(CO)_{16}$ are adsorbed intact from solution (e.g., *n*-pentane) onto more-or-less neutral supports such as γ-Al_2O_3 or TiO_2. The clusters on these supports can often be extracted intact into solutions such as tetrahydrofuran.

In contrast, when neutral metal carbonyl clusters are adsorbed on basic supports such as MgO or La_2O_3, surface anions typically form (e.g., $[HIr_4(CO)_{11}]^-$ and $[Ir_6(CO)_{15}]^{2-}$ from $Ir_4(CO)_{12}$ and $Ir_6(CO)_{16}$, respectively).

2.1.1.3 Surface-Mediated Synthesis: Efficient Routes to Preparation of Metal Carbonyl Clusters

Supported metal carbonyl clusters are alternatively formed from mononuclear metal complexes by surface-mediated synthesis [5, 13]; examples are $[HIr_4(CO)_{11}]^-$ formed from $Ir(CO)_2(acac)$ on MgO and $Rh_6(CO)_{16}$ formed from $Rh(CO)_2(acac)$ on γ-Al_2O_3 [5, 12, 13]. These syntheses are carried out in the presence of gas-phase CO and in the absence of solvents. Synthesis of metal carbonyl clusters on oxide supports apparently often involves hydroxyl groups or water on the support surface; analogous chemistry occurs in solution [14]. A synthesis from a mononuclear metal complex precursor is usually characterized by a yield less than that attained as a result of simple adsorption of a preformed metal cluster, and consequently the latter precursors are preferred when the goal is a high yield of the cluster on the support; an exception is made when the clusters do not fit into the pores of the support (e.g., a zeolite), and a smaller precursor is needed.

Synthesis of metal carbonyl clusters on oxide surfaces (followed by extraction into a solvent and workup) is occasionally a more convenient and efficient method for preparation of a metal carbonyl cluster than conventional solution chemistry. This synthetic strategy offers the green chemistry advantage of minimizing solvent use, as the reaction often occurs in the absence of solvent.

The field of surface-mediated synthesis of metal carbonyl clusters has developed briskly in recent years [4–6], although many organometallic chemists still seem to be unfamiliar with the methods or consider themselves ill-equipped to carry them out. In a typical synthesis, a metal salt or an organometallic precursor is brought from solution or the gas phase onto a high-area porous metal oxide, and then gas-phase reactants are brought in contact with the sample to cause conversion of the surface species into the desired products. In these syntheses, characteristics such as the acid–base properties of the support influence the chemistry, much as a solvent or coreactant influences the chemistry in a conventional synthesis. An advantage of

this chemistry with gas-phase reactants and those dispersed on solid surfaces is the opportunity for spectroscopic characterization of the products, including intermediates, in the absence of complicating solvent effects.

An early example of surface-mediated synthesis led to the conversion of $Os_3(CO)_{12}$ into $[Os_5C(CO)_{14}]^{2-}$ [13]. Quantitative characterization of the formation of this cluster on MgO by ^{13}C NMR spectroscopy [15] showed that the synthesis gave $[Os_5C(CO)_{14}]^{2-}$ in a yield of about 65%; other products included triosmium and tetraosmium carbonyl clusters. A schematic representation of the surface chemistry is shown in Fig. 1.

Intermediates were also observed in the synthesis of a neutral cluster, $Ir_4(CO)_{12}$, from $Ir(CO)_2(acac)$ in the cages of zeolite NaY; these were characterized by IR and extended X-ray absorption fine structure (EXAFS) spectroscopies, the latter being a technique ideally suited to investigation of small, highly dispersed species present in small amounts in solids. The spectra indicated dimeric intermediates, possibly $Ir_2(CO)_8$ [16], when the reaction was carried out in the near absence of water in the zeolite; in contrast, the reaction in the dehydrated zeolite was faster, and no evidence of intermediates was observed [16].

Major recent developments in efficient surface organometallic synthesis have been reported by the group of Ugo [5], who recognized the value of tuning the basicity of the support surface on which the synthesis takes place. They modified SiO_2 by addition of bases such as Na_2CO_3 and K_2CO_3 and changed the reaction environment, for example, varying the content of CO and water; they used the methods to synthesize $Rh_4(CO)_{12}$, $Rh_6(CO)_{16}$, $[Rh_5(CO)_{15}]^-$, and $[Rh_{12}(CO)_{30}]^{3-}$, for example [5].

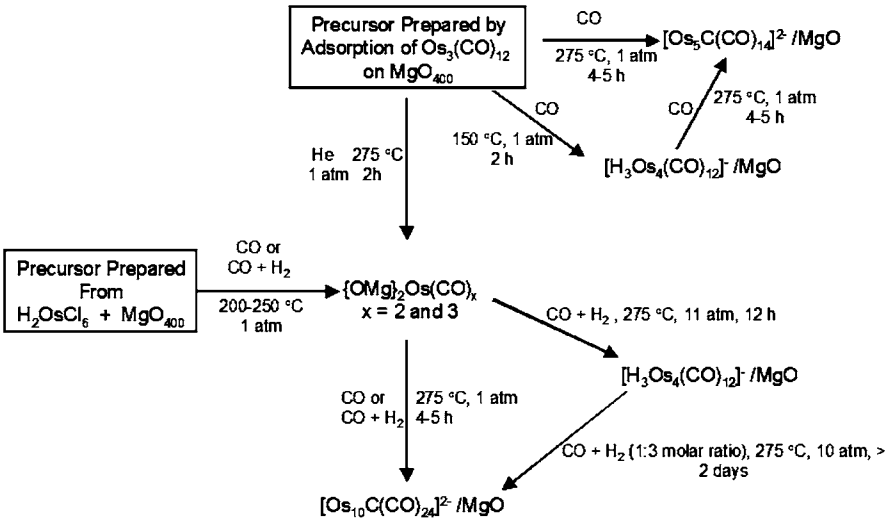

Fig. 1 Surface-mediated synthesis of osmium carbonyl clusters on the surface of MgO

Syntheses in which a reaction of a mononuclear metal complex precursor gives a tethered metal cluster are rare; an early example is the formation of a tetrairidium carbonyl on a phosphine-functionalized polymer [17].

2.1.1.4 Decarbonylation of Supported Metal Carbonyl Clusters

Supported metal carbonyl clusters such as $[Os_5C(CO)_{14}]^{2-}$, $Ir_4(CO)_{12}$, and $Rh_6(CO)_{16}$ are relatively stable and are often used as precursors of other supported metal clusters. Most attempts to investigate the reactivities of supported metal carbonyl clusters have led to the loss of uniformity of the supported species. Treatments intended to remove the CO ligands from supported metal carbonyl clusters typically lead to aggregation to form nonuniform mixtures of clusters and/or fragmentation to form cationic complexes of the metal (support hydroxyl groups may facilitate oxidative fragmentation) [12, 14].

Early interest in forming uniform de-ligated clusters on supports was strong, because these materials were envisaged as a link between molecular metal clusters and the (nonuniform) particles in conventional supported metal catalysts [18]. However, interest in this chemistry declined precipitously as it became evident that most synthetic approaches led to nonuniform samples. Perseverance in the research, however, led to high yields of structurally simple supported clusters such as Ir_4, Ir_6, Rh_6, and Os_5C by mild decarbonylation (in inert gas or in H_2) of supported clusters such as $Ir_4(CO)_{12}$ (or $[HIr_4(CO)_{11}]^-$), $Ir_6(CO)_{16}$ (or $[Ir_6(CO)_{15}]^{2-}$), $Rh_6(CO)_{16}$, or $[Os_5C(CO)_{14}]^{2-}$, respectively [12]. Trial-and-error experimentation determined the conditions of decarbonylations that occur without significant aggregation of the metal, as indicated by EXAFS spectroscopy. Yields of the decarbonylated products have not been determined as quantitatively as one would wish. (Characterization of the decarbonylated samples is presented later.)

Although decarbonylation of supported metal carbonyl clusters sometimes occurs almost without changes in the metal frames, the chemistry is complex and only partially understood. When decarbonylation takes place at elevated temperatures (depending on the support), migration and aggregation of the metal inevitably occur, and these processes are less well understood than the decarbonylation with near retention of the metal frame.

For example, treatment of MgO-supported $[HIr_4(CO)_{11}]^-$ in flowing He at 573 K caused essentially complete removal of the CO ligands, as shown by IR and EXAFS spectra, with the Ir_4 tetrahedra remaining essentially intact, as shown by EXAFS spectra [12]. IR spectra indicated the formation of carbonate and formate on the basic MgO, which evidently was not an inert platform [19]. When the decarbonylation took place in the presence of H_2, the iridium aggregated into larger clusters more readily than when the de-

carbonylation took place in the presence of He. Similar results pertain to the decarbonylation of neutral clusters of Ir and of Rh and to anionic clusters of these metals other than $[HIr_4(CO)_{11}]^-$ [12].

The decarbonylation of oxide-supported metal carbonyls yields gaseous products including not just CO, but also CO_2, H_2, and hydrocarbons [20]. The chemistry evidently involves the support surface and breaking of C – O bonds and has been thought to possibly leave C on the clusters [21]. The chemistry has been compared with that occurring in Fischer–Tropsch catalysis on metal surfaces [20]; support hydroxyl groups are probably involved in the chemistry.

2.1.1.5 Decarbonylation and Recarbonylation of Supported Metal Clusters

When $Ir_4(CO)_{12}$ in the cages of zeolite NaY was decarbonylated by treatment in H_2 at 573 K and treated again in CO, the $Ir_4(CO)_{12}$ clusters were not reformed [22]. In contrast, when the sample containing the decarbonylated $Ir_4(CO)_{12}$ was cooled to liquid nitrogen temperature and treated in CO, IR spectra indicated that the iridium clusters were oxidatively fragmented, giving structures represented as $Ir(CO)_2$ or $Ir(CO)_3$ bonded to the zeolite. When these were treated in CO as the temperature was raised, they reformed $Ir_4(CO)_{12}$ at about 323 K. As the temperature was raised further to about 398 K, the $Ir_4(CO)_{12}$ was converted into $Ir_6(CO)_{16}$. The synthesis chemistry appears to be similar to the solution chemistry of the cluster formation from hydrated $IrCl_3$ in CO under mild conditions (423 K and 1 atm) [23]; this is an example of surface-mediated cluster synthesis that is analogous to the solution synthesis [24]. Knowledge of the solution synthesis chemistry provides a good foundation for prediction of the appropriate surfaces and conditions for surface-mediated synthesis.

2.1.1.6 Structures

There are no known examples of supported clusters dispersed in crystallographically equivalent positions on a crystalline support. Thus, no structures have been determined by X-ray diffraction crystallography, and the best available methods for structure determination are various spectroscopies (with interpretations based on comparisons with spectra of known compounds) and microscopy. The more nearly uniform the clusters and their bonding to a support, the more nearly definitive are the spectroscopic methods; however, the uniformities of these samples are not easy to assess, and the best microscopic methods are limited by the smallness of the clusters and their tendency to be affected by the electron beam in a transmission electron microscope; furthermore, most supported metal clusters are highly reactive and

change upon exposure to air, which almost always precedes examination by transmission electron microscopy (TEM).

A few supported metal clusters have been imaged by TEM, with sharp images having been obtained for clusters on MgO that were inferred to be predominantly $[Os_5C(CO)_{14}]^{2-}$ and Os_5C formed by its decarbonylation [25]. The image in Fig. 2 shows scattering centers with sizes expected for pentaosmium clusters, mixed with some smaller clusters inferred to be intermediates in their synthesis from $Os_3(CO)_{12}$ [15]. The images are consistent with EXAFS spectra indicating that the predominant supported species were $[Os_5C(CO)_{14}]^{2-}$ ions; IR and ^{13}C NMR spectra also support the inference [15].

Good images indicating nearly uniform clusters of other metals are lacking, but evidence from EXAFS spectroscopy, combined with IR spectroscopy and extraction of clusters into solution, has provided a basis for structure determination of a number of small metal carbonyl clusters and clusters formed by their decarbonylation. Compilations of these are reported elsewhere [6, 12, 26].

For example, clusters identified by IR spectra and extraction as $Ir_4(CO)_{12}$ on γ-Al_2O_3 were found by EXAFS spectroscopy to have an Ir–Ir coordination number of nearly 3, consistent with the tetrahedral structure of the metal frame; EXAFS spectroscopy produces the equivalent result for solid $Ir_4(CO)_{12}$ [27]. EXAFS spectroscopy is the most appropriate method for determination of framework structures of supported clusters, but it is limited by the errors to clusters with at most about six metal atoms. Thus, it has been used to determine frameworks that are triangular (EXAFS first-shell metal–metal coordination number of 2), tetrahedral (EXAFS first-shell metal–metal coordination number of 3), and octahedral (EXAFS first-shell metal–metal

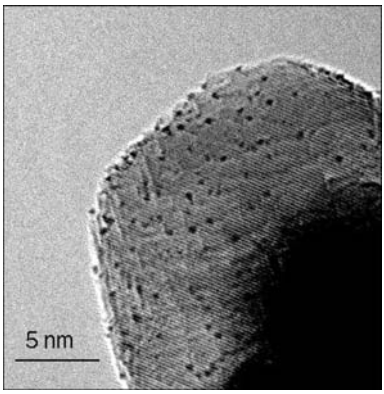

Fig. 2 High-resolution transmission electron micrograph of $[Os_5C(CO)_{14}]^{2-}$ on MgO. This cluster was present with osmium carbonyl clusters with lower nuclearities (containing three and four Os atoms) [25]

coordination number of 4, sometimes bolstered by a second-shell metal–metal coordination number of 1, but unusually good data are required to determine the latter). Because the errors in the EXAFS-determined coordination numbers are relatively large (typically, ± 20%; details are presented elsewhere [26]) and because the clusters do not have unique structures, these framework structures are approximations that would benefit from further scrutiny, for example, by microscopy and theory.

Calculations on the basis of density functional theory have been used to check the structure of Rh_6 clusters supported on zeolite X; the results indicate a slightly twisted prism, nearly matching the octahedron inferred on the basis of the EXAFS data [28, 29]. (These clusters were inferred not to be bare but to have hydride ligands, as described later).

2.1.1.7 Bonding of Clusters to Supports

The interactions between metals and supports in conventional supported metal catalysts have been the focus of extensive research [12, 30]. The subject is complex, and much attention has been focused on so-called strong metal–support interactions, which may involve reactions of the support with the metal particles, for example, leading to the formation of fragments of an oxide (e.g., TiO_2) that creep onto the metal and partially cover it [31]. Such species on a metal may inhibit catalysis by covering sites, but they may also improve catalytic performance, perhaps playing a promoter-like role.

The literature of metal–support interactions includes little about the possible chemical bonding of metal clusters or particles to supports. Supported "molecular" metal clusters with carbonyl ligands removed have afforded opportunities to understand the metal–support interface in some detail, and the results provide insights into the bonding of clusters to supports that appear to be generalizable beyond the small clusters to the larger particles of conventional supported metal catalysts [6].

Structural information about the metal–support interface is provided by EXAFS spectroscopy. The EXAFS data provide average structural information and are most informative when the samples are most nearly uniform.

EXAFS results characterizing metal–oxygen (M– O) contributions in numerous oxide- and zeolite-supported metal clusters (where M is Ru, Rh, Ir, Os, Pt, etc) indicate distances in the range 2.1–2.2 Å [12, 30]. Other metal–oxygen contributions at a distance of typically 2.6 or 2.7 Å (referred to as M– O_l contributions, where l refers to long, in contrast to M– O_s, where s refers to short) are also commonly observed for oxide- and zeolite-supported transition metal clusters [30]. The shorter $M(-O_s)$ distances are bonding distances, essentially matching those in supported metal complexes and those indicated by the crystal structures of molecular metal complexes in which metal ions are bonded to oxygen, exemplified by compounds

that are analogues of supported metal complexes, including, for example, $[Ru(CO)_2(OCOCF_3)(\mu - OSiMe_2CH_2PPh_2)]_2$ and $[Re(CO)_3(\mu_3 - OH)]_4$ [6].

Calculations at the density functional level have been used to represent cluster–support combinations, including representations of the cluster–support interface. The results provide evidence of metal–oxygen bonds, including bond distances and strengths [28, 29, 32]. Results representing Ir_4 in zeolite NaX (chosen as a protypical support because of its crystallinity and relative uniformity), for example, with the clusters assumed to be present at six-rings, as shown in Fig. 3, indicate $Ir - O_s$ distances of about 2.2 Å, in good agreement with the EXAFS values of about 2.1–2.2 Å typical of oxide- and zeolite-supported iridium clusters [32]. Similarly, theoretical results representing Os_5C on MgO (Fig. 4) indicate $Os - O_s$ distances of about 2.1 Å, in good agreement with the EXAFS value of 2.0 Å [15, 33]. (However, the clusters in these samples are inferred not to have been bare—see the next section for elaboration on this point).

The longer metal–oxygen distances of about 2.6 Å observed by EXAFS spectroscopy for these and related supported metal clusters suggest weak interactions between the metal and surface oxygen atoms; these EXAFS contributions are not determined with as much confidence as those characterized by the shorter distances, and the interactions are not well understood.

A result of the calculations at the density functional level is that the shorter metal–oxygen distances are bonding distances indicative of metal cations at the metal–support interface. The bonds are rather strong, in line with theoretical results representing supported mononuclear metal complexes, and they help to explain the stability of extremely small metal clusters on supports. The results confirm the essential agreement between the EXAFS spectra characterizing the shorter metal–oxygen distances in supported mononuclear metal complexes and those in supported metal clusters (even including particles markedly larger than the clusters considered here) [6].

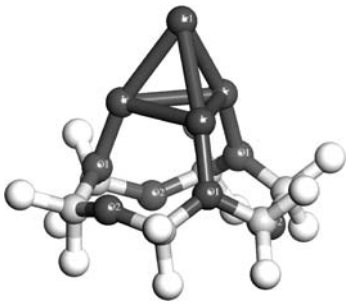

Fig. 3 Ir_4 cluster supported at the six-ring of zeolite NaX as represented by density functional theory; samples were characterized by Extended X-ray absorption fine structure (*EXAFS*) spectroscopy and other techniques [32]

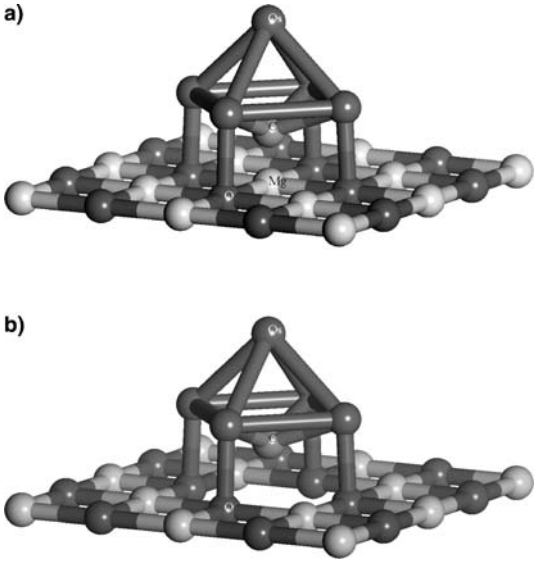

Fig. 4 Osmium clusters supported on MgO(001): **a** $Os_5C/Mg_{13}O_5$ and **b** Os_5C at a surface point V_s defect site [33]; these were represented by density functional theory, and the samples were characterized by EXAFS spectroscopy, transmission electron microscopy, and other techniques [15]

Theoretical results characterizing Rh_6 in zeolite X confirm the inference that the metal atoms in metal clusters and particles at the metal–support interface are positively charged (Fig. 5) [28, 29]. (However, the Rh_6 clusters are inferred not to have been bare—see the next section.) The positive charge of the metal frame is borne almost entirely by the atoms at the metal–support interface; those farther from the interface are essentially uncharged. The theoretical result is consistent with the EXAFS results and bolsters the conclusion that supported metal clusters are bonded to supports by metal–oxygen bonds with distances of about 2.1–2.2 Å [28, 29] (the value calculated for Rh_6 on the zeolite was 2.2 Å). The Mulliken charge of a Rh atom at the metal–support interface in Rh_6 on the zeolite was estimated to be 0.76*e*. This compares with the Mulliken charge of 0.53*e* of the rhodium atom in the mononuclear cationic complex $Rh(CO)_2$ bonded to zeolite USY [28]; the results suggest that the Rh atoms at the interfaces in each sample should be represented formally as Rh(I).

The result indicating that the interface metal atoms in the supported clusters approximated as Rh_6 are charged, whereas those one layer removed from the support surface are not, leads to the question of the charge of the metal atoms in a flat metal raft. The issue has been addressed in experiments with γ-Al_2O_3-supported clusters approximated well as Re_3, which were formed from $H_3Re_3(CO)_{12}$ [34]. The rhenium atoms were inferred on the basis of

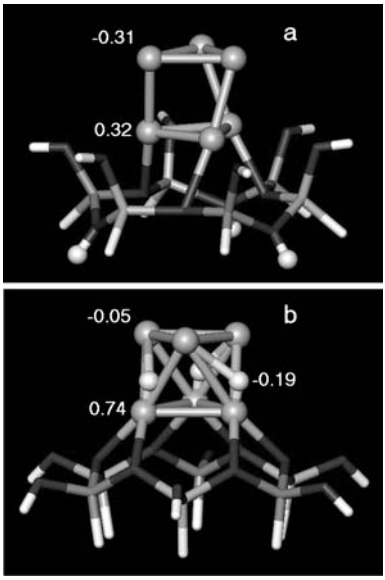

Fig. 5 **a** Model of Rh_6 supported on a zeolite fragment with three bridging hydroxyl groups [28]. **b** Model of Rh_6 with three hydride ligands supported on a zeolite fragment formed by reverse spillover of hydrogen from a zeolite fragment with three hydroxyl groups [28]. Mulliken charges (in units of electronic charge) of the atoms in the supported cluster are shown. This was represented by density functional theory, and the sample was characterized by EXAFS spectroscopy and other techniques

EXAFS data to be present in three-atom rafts bonded to the support; X-ray absorption near-edge and X-ray photoelectron spectra indicated a rhenium oxidation state in the range of roughly +4 to +6. EXAFS indicated a short Re – Re distance (2.67 Å), suggesting a multiple bond. The structure of this sample is only partially understood and is intriguing because it is comparable to structures of numerous compounds with cationic metals and short metal–metal bonds and groups bridging them such as polycarbonate anions [35] (which evidently play a role comparable to that of the oxide support as a ligand).

Calculations at the density functional level were also carried out for Os_5C clusters on MgO (Fig. 4); bonding on the stable square (001) face as well as at defect sites was considered. The results indicate that Os_5C is bonded much more strongly at surface defect sites than at defect-free sites. The bonding energy of Os_5C on the MgO(001) surface at a V_s defect site is 4.84 eV greater than that representing the cluster bonded at a defect-free site on the same MgO surface.

These results seem likely to be general—metal clusters on metal oxides are expected to be present predominantly at defect sites [33].

2.1.1.8 Ligands on Supported Metal Clusters

Metal–metal distances in supported metal clusters (e.g., Ir_4, nearly 2.70 Å) determined by EXAFS spectroscopy essentially match those in coordinatively saturated clusters of the same metal (e.g., $Ir_4(CO)_{12}$). These distances are about 0.2–0.3 Å greater than the metal–metal distances in the free (gas-phase) clusters (e.g., Ir_4, 2.44 Å) [32]. Similar results have been determined for supported Os_5C [33] and Rh_6 [28, 29].

These comparisons prompted the Rösch group [32, 33] to conclude that some ligands remained on the supported clusters after decarbonylation; this conclusion may be quite general—supported metal clusters are highly reactive, and typical oxide and zeolite supports are not unreactive. Thus, a representation of supported clusters such as tetrairidium on γ-Al_2O_3 as Ir_4/γ-Al_2O_3 is a simplification that fails to account for the ligands on the cluster.

The obvious candidate ligands include C (originating from CO ligands of the precursor) and H (originating from OH groups of the support). Vayssilov's [28, 29] calculations for hydride ligands on Rh_6 supported on zeolite X show that they are more strongly bonded than C ligands, and this result suggests that the ligands on the clusters are H and not C; this inference may be rather general for noble metals on supports, but further results are needed to test it. The calculations show that Rh_6 on the six-ring of the zeolite (Fig. 5) with H ligands in bridging positions is markedly stabler (by 370 kJ mol^{-1}) than the bare cluster on the six-ring of the zeolite with hydroxyl groups.

It is evident that the supported clusters have a strong affinity for hydride ligands provided by the support. The process by which the support delivers these ligands is referred to in the catalysis literature as "reverse hydrogen spillover." The opposite process (spillover), well known for supported metals [36], is shown by the theoretical results to be a redox process; in reverse spillover, the support hydroxyl groups oxidize the cluster.

The theoretical and EXAFS results characterizing zeolite-supported Rh_6 raise the question of whether ligand-free clusters (or even ligand-free mononuclear metal complexes) are stable and can even be made on hydroxylated supports [28, 29]. If reverse spillover to make supported metal hydrides is essentially unavoidable, questions are also raised about the interpretation of chemisorption measurements intended to determine the number of bonding sites of (even conventional) supported metal catalysts, which in typical chemisorption experiments need to be cleaned by evacuation to remove adsorbates (ligands). Evacuation can cause removal of H_2, at the expense of support OH groups, but questions remain: are the clusters stable during this process (do they migrate and aggregate, for example), and do their morphologies change?

The commonly investigated ligands on the supported metal clusters mentioned before include CO, hydride, and hydrocarbons. The evidence of hydrides and hydrocarbons is not as strong as one would wish.

^{1}H NMR spectroscopy has been used to detect hydrides on various oxide-supported metals in the presence of H_2 and on La_2O_3-supported Ir_4, in the absence of H_2 [37]. The kinetics of chemisorption of H_2 supports the inference of hydride formation by dissociative adsorption of H_2 [38].

Propylidyne formed from propene on Ir_4 supported on γ-Al_2O_3 was observed by IR and ^{13}C NMR spectroscopies [38]. When ethene or propene was brought in contact with oxide-supported Ir_4 [39, 40], Ir_6 [39, 40], or Rh_6 (A.M. Argo and B.C. Gates BC, unpublished results) in the presence of H_2, hydrocarbon ligands were formed (namely, alkyls and π-bonded alkenes), which have been inferred from IR spectra to be intermediates in hydrogenation to make alkanes, as discussed later. The population of these hydrocarbon ligands on the supported clusters depends sensitively on the conditions, such as reactant partial pressures and temperature.

Much remains to be done to develop the chemistry of organic ligands on supported metal clusters, and substantial progress is to be expected as the samples are well suited to characterization, by IR, NMR, and neutron scattering (F. Li, J. Eckert, and B.C. Gates, unpublished results) spectroscopies, as well as density functional theory.

2.1.2 Bimetallic Clusters

Supported bimetallic catalysts find many industrial applications. Examples include Pt and Rh in automobile exhaust conversion catalysts and Pt and Re (or Pt and Sn or Pt and Ir) in naphtha reforming catalysts.

Synthesis methods such as those described earlier for monometallics have been applied with metal carbonyls incorporating two metals. The resultant supported species may be small supported metal clusters [41, 42], and, as for monometallics, the usual products are supported species that are nonuniform in both composition and structure [42]. There are several examples of well-defined metal carbonyl clusters in this category but hardly any examples of well-defined decarbonylated bimetallics on supports.

Surface-mediated synthesis of bimetallic carbonyl clusters is a rarity; Xu et al. [43] prepared $[PtRh_5(CO)_{15}]^-$ on MgO from Na_2PtCl_6 and $RhCl_3 \cdot xH_2O$ in CO at room temperature; the yield was 84%.

When a supported metal on an oxide is prepared from an adsorbed precursor incorporating a noble metal bonded to an oxophilic metal, the result may be small noble metal clusters, each more-or-less nested in a cluster of atoms of the oxophilic metal, which is cationic and anchored to the support through metal–oxygen bonds [44, 45]. The simplest such structure is modeled on the basis of EXAFS data as Re_4Pt_2, made from $Re_2Pt(CO)_{12}$ (Fig. 6) [45].

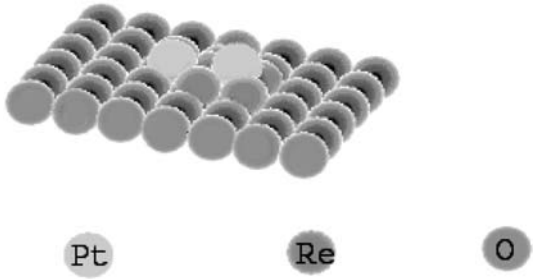

Fig. 6 Simplified model based on EXAFS data of Re_4Pt_2 clusters formed on the surface of γ-Al_2O_3 from $Re_2Pt(CO)_{12}$ [45]

The rhenium interacts strongly with the oxygen atoms of the support and also with platinum; platinum interacts less strongly with the support than rhenium. One is tempted to generalize that when one of the metals in a supported bimetallic cluster is noble and the other oxophilic, the oxophilic metal interacts more strongly with the support than the noble metal; if the bimetallic frame of the precursor is maintained nearly intact, then this metal–support interaction helps keep the noble metal highly dispersed.

Other samples of such "nested" noble metal clusters on oxides have been made from the following precursors: $Pd_2Mo_2(CO)_6(C_5H_5)_2(PPh_3)_2$ [44], $PtMo_2(CO)_6(C_5H_5)_2(PhCN)_2$ [46], $PtW_2(CO)_6(C_5H_5)_2(PhCN)_2$ [47], $Pt_2W_2(CO)_6(C_5H_5)_2(PPh_3)_2$ [48], and $[Ru_{12}C_2Cu_4Cl_2(CO)_{32}][PPN]_2$ [49], among others. Platinum clusters incorporating as few as four atoms each, on average, are indicated by EXAFS data characterizing the Pt – W clusters [48]. The Pt – W samples are quite stable, with the cluster size remaining essentially unchanged after oxidation–reduction cycles at 673 K [47, 48]. The stability is attributed to the nesting by the oxophilic metals and could be a significant advantage in catalytic applications.

When bimetallic clusters incorporating only noble metals are adsorbed on a support and the precursor ligands are removed, the resultant species are usually aggregated and nonuniform. There are only very few examples of supported bimetallics that seem to be even close to uniform. PtRu clusters on γ-Al_2O_3 were prepared by decarbonylation of molecularly adsorbed $Pt_2Ru_4(CO)_{18}$ by treatment in He or H_2 at temperatures in the range 573–673 K [50]. EXAFS data show that the Pt – Ru interactions were largely maintained after decarbonylation, but the Pt – Ru cluster frame was changed. The average Pt – Pt bond distance apparently increased slightly (from 2.66 to 2.69 Å), and the Ru – Ru distance decreased from 2.83 to 2.64 Å. The corresponding Pt – Pt and Ru – Ru coordination numbers were found to be 2.0 and 4.0, respectively, indicating some agglomeration of the metal. The clusters incorporated, on average, fewer than three and six Pt and Ru atoms,

respectively, and appear to be the smallest known supported decarbonylated bimetallic clusters of platinum-group metals.

2.1.3 Reactivity and Catalysis

As site-isolated species, supported metal clusters offer opportunities for investigation of reactivities that are largely absent when clusters are present in solution. In prospect, stable, coordinatively unsaturated clusters can be formed—although it may be difficult to prepare clusters that entirely lack ligands other than the support, because the clusters may react with functional groups on the support to give new ligands, such as hydride, or the clusters might migrate on the support surface to give a mixture of clusters of various sizes (as discussed before).

Propene adsorption on Ir_4/γ-Al_2O_3 at 298 K gave stable cluster-bound μ_3-propylidyne. Propene adsorbed on Ir_4/γ-Al_2O_3 at 138 K reacted at approximately 219 K to form a stable, highly dehydrogenated, cluster-bound species approximated as C_xH_y (possibly C_3H_2 or C_2H) [38]. H_2 reacted with Ir_4/γ-Al_2O_3 at 298 K to form ligands (possibly hydrides) that prevented subsequent reaction of the clusters with propene to form propylidyne. Propylidyne on Ir_4 was stable in He or H_2 as the sample was heated to 523 K, and at this temperature it reacted with oxygen atoms of the support to give CO [38].

Propylidyne on Ir_4 did not undergo isotopic exchange in the presence of D_2 at 298 K [38]. In contrast, propylidyne chemisorbed on extended metal surfaces is hydrogenated in the presence of H_2 (or D_2) and exchanges hydrogen with gaseous D_2 at room temperature; in the absence of H_2, it decomposes thermally to give hydrocarbon fragments at temperatures much less than 523 K. The marked difference in reactivities of propylidyne on metal clusters and propylidyne on extended metal surfaces indicates a requirement of ensembles of more than the three metal surface atoms bonded to propylidyne in the surface reactions [38]. This comparison illustrates the unique reactivity of small site-isolated metal clusters.

Numerous supported metal clusters have been tested as catalysts for alkene hydrogenation, and spectra of the functioning catalysts have been recorded in attempts to identify the catalytically active species and reactive intermediates. EXAFS spectra representing the catalyst/support combinations Ir_4/γ-Al_2O_3, Ir_6/γ-Al_2O_3, and Ir_4/MgO show that the cluster frames were maintained before, during, and after catalysis of propene hydrogenation, provided that the conditions were mild (e.g., room temperature and 1 atm) [39, 40]. When the temperature of catalysis reached about 423 K, the metals aggregated on the support, and the structural simplicity was lost. The data obtained at the lower temperatures are consistent with the identification of the supported clusters themselves as the catalytically active species.

Data such as those of Fig. 7 implicitly show how the rate of catalytic hydrogenation of ethene depends on the intensities of the IR bands characterizing ligands bonded to the clusters; these results suggest that these ligands are reaction intermediates (but they are not sufficient to identify the intermediates with confidence) [39, 40].

Data showing how the catalytic activity for ethene hydrogenation of La_2O_3-supported Rh_6 clusters increased as hydride ligands built up on the clusters are presented in Fig. 8 [37]. These results suggest that hydride ligands are intermediates in the catalytic reaction.

In prospect, structurally well defined supported metal clusters provide the opportunity for resolving support effects from cluster-size effects in catalysis [39, 40]. A family of supported iridium clusters and particles was prepared from $Ir_4(CO)_{12}$ on γ-Al_2O_3 [51]. The smallest clusters were approximately Ir_4, and samples with increasingly larger clusters and particles were prepared by treating Ir_4/γ-Al_2O_3 in H_2 under conditions to cause aggregation and vary the average cluster or particle size. The rate of catalytic hydrogenation of toluene per exposed Ir atom increased by 2 orders of magnitude as the cluster/particle size increased, becoming independent of particle size when the average particle contained about 100 atoms [51]. The data characterizing the larger particles conform to the expected pattern for the "structure-insensitive" hydrogenation reaction, but those for the smaller clusters and particles do not. (A structure-insensitive reaction takes place at approxi-

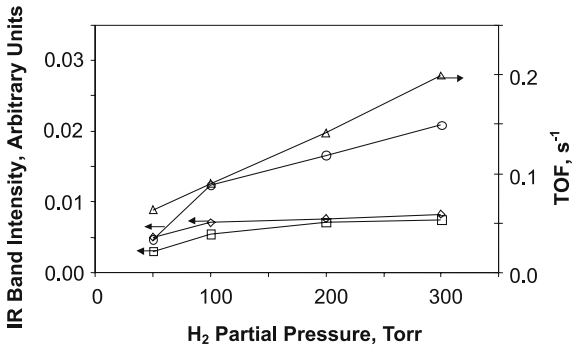

Fig. 7 Dependence of IR band intensities on H_2 partial pressure during ethene hydrogenation catalyzed by Ir_4/γ-Al_2O_3 at 288 K and 760 Torr (40 Torr C_2H_4, 50–300 Torr H_2, and the balance He). The bands at 2990 (*diamonds*) and 2981 cm^{-1} (*squares*) were chosen to represent di-σ-bonded ethene and that at 1635 cm^{-1} (*circles*) to represent water on the γ-Al_2O_3 support. These IR bands were chosen as the best ones to minimize error caused by overlap with other bands. The *triangles* represent the reaction rate expressed as a turnover frequency (*TOF*), the rate of reaction in units of molecules of ethene converted per Ir atom per second. The data indicate a correlation of the band intensities with the TOF, consistent with the suggestion that the ligands represented by the bands are reaction intermediates (but the data are not sufficient to identify the reaction intermediates) [39]

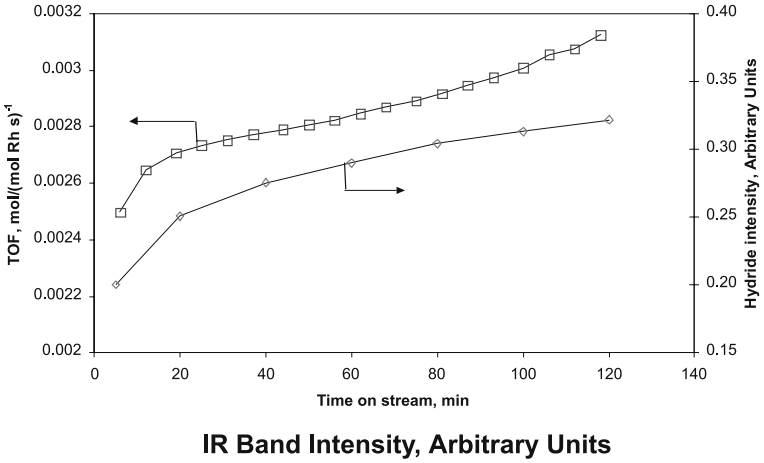

Fig. 8 Dependence of catalytic activity measured by TOF (rate of reaction per Rh atom) (*squares*) and IR intensity of hydride (2020-cm^{-1} mode) (*diamonds*) during the induction period for ethene hydrogenation catalyzed by Rh_6 supported on La_2O_3 at 298 K and atmospheric pressure in a flow reactor (partial pressures in feed: H_2, 348 Torr; C_2H_4, 75 Torr; He, 337 Torr) [37]

mately the same rate per exposed metal atom, independent of the average size of the metal particle in the catalyst or of the metal crystal face that is exposed).

The data show that the supports act as ligands; thus, Ir_4 on MgO was found to be an order of magnitude more active than Ir_4 on γ-Al_2O_3. The data characterize the structures of working catalysts, including the Ir_4 and Ir_6 cluster frames (which remained intact during reaction), the cluster–support interface, and the ligands formed during catalysis. On Ir_4, for example, propene forms both unreactive (inhibitor) ligands (propylidyne) and catalytic intermediates, identified by IR spectroscopy as propyl and π-bonded propene; the support affects which of these hydrocarbon ligands predominate. The reaction intermediates influence the Ir – Ir distance in the clusters and the distance between the Ir atoms and the oxygen atoms of the support that are the longer (nonbonding) distances. Changes in the Ir – Ir and Ir–support oxygen distances were observed when the reactants were brought in contact with the catalyst. The reaction intermediates and the support are mutually interactive ligands [39, 40].

The foregoing results characterizing structurally simple supported metal clusters can be generalized, at least qualitatively, to provide fundamental understanding that pertains to industrial supported metal catalysts, with their larger, nonuniform particles of metal.

The intense recent interest in supported gold catalysts has focused on small, nonuniform clusters (e.g., those supported on TiO_2), which have been

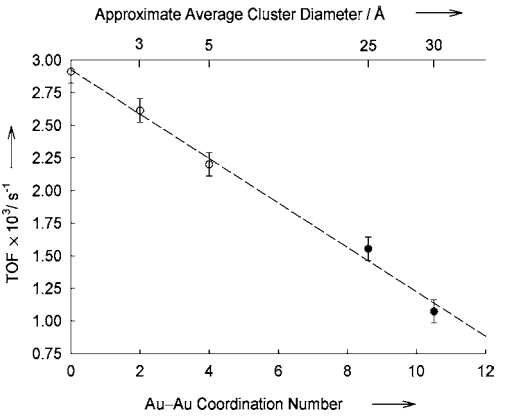

Fig. 9 Dependence of catalytic activity of MgO-supported catalysts containing cationic gold and (except in the most active catalyst) gold clusters for ethene hydrogenation at 760 Torr and 353 K (reactive mixture of He, ethene, and H_2—ethene partial pressure, P_{ethene}, 40 Torr; $P_{hydrogen}$, 160 Torr; the balance He). Note the nonlinearity of the scale at the *top* [53]

inferred to have catalytic activities for CO oxidation that depend strongly on the cluster size [11, 52], some determined by scanning tunneling microscopy [52]. Other data have shown, however, that cationic gold is present in some oxide-supported gold catalysts containing such small clusters, and the activity has been shown to increase with the content of cationic gold [53]. Catalysis of ethene hydrogenation by MgO-supported gold was investigated for a family of catalysts containing (nonuniform) clusters of various average sizes and a catalyst incorporating site-isolated Au(III) complexes, in the absence of clusters (Fig. 9) [54]. The most active catalyst was the one without the clusters, and the activity was attributed to the complexes and not the clusters. This work is a caution about indications of catalysis by supported clusters; more work is needed to resolve the issues of catalysis by supported gold.

Acknowledgements This work was supported by the U.S. Department of Energy, Office of Energy Research, Office of Basic Energy Sciences, contract FG02-04ER15513FG0, and the Petroleum Research Fund, administered by the American Chemical Society.

References

1. Yermakov YI, Kuznetsov BN, Zakharov VA (1981) Studies in surface science and catalysis, vol 8. Elsevier, Amsterdam
2. Ballard DGH (1973) Adv Catal 23:263
3. Basset J-M, Gates BC, Candy J-P, Choplin A, Leconte M, Quignard F, Santini C (eds) (1988) Surface organometallic chemistry: molecular approaches to surface catalysis. NATO ASI series, vol 231. Kluwer, Dordrecht

4. Copéret C, Chabanas M, Saint-Arroman RP, Basset J-M (2003) Angew Chem Int Ed Engl 42:156
5. Cariati E, Roberto D, Ugo R, Lucenti E (2003) Chem Rev 103:3707
6. Guzman J, Gates BC (2003) Dalton Trans 3303
7. Hlatky GG (2000) Chem Rev 100:1347
8. Muetterties EL, Rhodin TN, Band E, Brucker C, Pretzer H (1979) Chem Rev 79:91
9. Jentoft RE, Tsapatsis M, Davis ME, Gates BC (1998) J Catal 179:565
10. Nellest PD, Pennycook SJ (1996) Science 274:413
11. (a) Haruta M (1997) Catal Today 36:153; (b) Haruta M, Daté M (2001) Appl Catal A 222:427
12. Gates BC (1995) Chem Rev 95:511
13. (a) Lamb HH, Krause TR, Gates BC (1986) J Chem Soc Chem Commun 821; (b) Lamb HH, Fung AS, Tooley PA, Puga J, Krause TR, Kelley MJ, Gates BC (1989) J Am Chem Soc 111:8367
14. Lamb HH, Gates BC, Knözinger H (1988) Angew Chem Int Ed Engl 27:1127
15. Bhirud VA, Panjabi G, Salvi SN, Phillips BL, Gates BC (2004) Langmuir 20:6173
16. Li F, Gates BC (2004) J Phys Chem B 108:11259
17. Rafalko JJ, Lieto J, Gates BC, Schrader GL Jr (1978) J Chem Soc Chem Commun 540
18. Basset J-M, Ugo R (1977) Aspects Homog Catal 3:137
19. Alexeev OS, Kim D-W, Gates BC (2000) J Mol Catal A 162:67
20. Smith AK, Theolier A, Basset J-M, Ugo R, Commereuc D, Chauvin Y (1978) J Am Chem Soc 100:2590
21. Alexeev O, Gates BC (1998) J Catal 176:310
22. Beutel T, Kawi S, Purnell SK, Knözinger H, Gates BC (1993) J Phys Chem 97:7284
23. Malatesta L, Caglio G, Angoletta M (1972) Inorg Synth 13:95
24. (a) Smith AK, Hugues F, Theolier A, Basset J-M, Ugo R, Zanderighi GM, Bilhou JL, Bilhou-Bougnol V, Graydon WF (1979) Inorg Chem 18:3104; (b) Basset J-M, Theolier A, Commereuc D, Chauvin Y (1985) J Organomet Chem 279:147
25. Allard LF, Panjabi GA, Salvi SN, Gates BC (2002) Nano Lett 2:381
26. Alexeev O, Gates BC (2000) Top Catal 10:273
27. Maloney SD, Kelley MJ, Koningsberger DC, Gates BC (1991) J Phys Chem 95:9406
28. Vayssilov GN, Gates BC, Rösch N (2003) Angew Chem Int Ed Engl 42:1391
29. Vayssilov GN, Rösch N (2004) J Phys Chem B 108:180
30. Koningsberger DC, Gates BC (1992) Catal Lett 14:271
31. Stevenson S, Dumesic JA, Baker RTK, Ruckenstein E (1987) (eds) Metal-support interactions in catalysis, sintering and redispersion. Van Nostrand Reinhold, New York
32. Ferrari AM, Neyman KM, Mayer M, Staufer M, Gates BC, Rösch N (1999) J Phys Chem B 103:5311
33. Goellner JF, Neyman KM, Mayer M, Nörtemann F, Gates BC, Rösch N (2000) Langmuir 6:2736
34. Fung AS, Tooley PA, Koningsberger DC, Kelley MJ, Gates BC (1991) J Phys Chem 95:225
35. Cotton FA, Lin C, Murillo CA (2001) Acc Chem Res 34:759
36. Conner WC Jr, Falconer JL (1995) Chem Rev 95:759
37. Bhirud VA, Goellner JF, Argo AM, Gates BC (2004) J Phys Chem B 108:9752
38. Argo AM, Goellner JF, Phillips BL, Panjabi GA, Gates BC (2001) J Am Chem Soc 123:2275
39. Argo AM, Odzak JF, Gates BC (2003) J Am Chem Soc 125:7107
40. Argo AM, Odzak JF, Lai FS, Gates BC (2002) Nature 415:623

41. Braunstein P, Rosé J (1999) Braunstein P, Oro LA, Raithby PR (eds) Metal clusters in chemistry. Wiley-VCH, Weinheim, p 616
42. Alexeev O, Gates BC (2003) Ind Eng Chem Res 42:1571
43. Xu Z, Kawi S, Rheingold AL, Gates BC (1994) Inorg Chem 33:4415
44. Kawi S, Alexeev O, Shelef M, Gates BC (1995) J Phys Chem 99:6926
45. Fung AS, Kelley MJ, Koningsberger DC, Gates BC (1997) J Am Chem Soc 119:5877
46. Alexeev O, Kawi S, Shelef M, Gates BC (1996) J Phys Chem 100:253
47. Alexeev O, Shelef M, Gates BC (1996) J Catal 164:1
48. Alexeev O, Graham GW, Shelef M, Gates BC (2000) J Catal 190:157
49. Shephard DS, Maschmeyer T, Sankar G, Thomas JM, Ozkava D, Johnson BFG, Raja R, Oldroyd RD, Bell RG (1998) Chem Eur J 4:1214
50. Alexeev O, Graham GW, Shelef M, Adams RD, Gates BC (2002) J Phys Chem B 106:4697
51. Xiao F-S, Weber WA, Alexeev O, Gates BC (1996) Proc 11th Int Congr Catal 101:1135
52. Valden M, Lai X, Goodman DW (1998) Science 281:1647
53. Guzman J, Gates BC (2004) J Am Chem Soc 126:2672
54. Guzman J, Gates BC (2003) Angew Chem Int Ed Engl 42:690

Top Organomet Chem (2005) 16: 233–259
DOI 10.1007/b138079

Published online: 14 September 2005

Synthesis and Surface Reactivity of Organometallic Nanoparticles

Bruno Chaudret

Laboratoire de Chimie de Coordination du CNRS, 205, route de Narbonne, 31077 Toulouse Cédex 04, France
chaudret@lcc-toulouse.fr

Abstract The use of organometallic precursors allows the synthesis in mild conditions of nanoparticles of uniform small size (1–3 nm) and of a clean surface which can be stabilized by polymers or ligands. These nano-objects display an interesting surface chemistry, comparable to that of molecular species. Synthesis involves classical elementary steps of organometallic chemistry such as substitution and oxidative addition as well as ligand fluxionality. Some catalytic properties of these species have been studied, including a new example of an asymmetric reaction catalyzed by palladium nanoparticles. These objects can, in a second step, grow isotropically into monodisperse systems able to self-assemble anisotropically into nanorods, nanowires or nanocubes according to the system. We report an overview of recent work performed in this field by our research group.

Keywords Organometallic · Nanoparticles · Surface chemistry · Self-organization · Catalysis

1 Introduction

The recent period has evidenced an ever-increasing interest in the chemistry of species of nanometric size [1–14]. Thus, there has been a spectacular development of the use of metal nanoparticles in catalysis for a large variety of reactions, including inter alia hydrogenation, hydrosilylation and carbon–carbon bond formation. A number of groups have contributed to this field and the area has been reviewed comprehensively by Roucoux et al. [10]. In some cases, the reactions have been demonstrated to be enantioselective. This, however, raises in general, and specially for the C – C coupling reactions, the question of the exact nature of the catalyst. In other words: Can a molecular species become colloidal to serve as catalyst in a given reaction, and symmetrically? Can a nanoparticle "dissolve" into a molecular mononuclear complex? These points are generally difficult to address and evidence our lack of knowledge regarding the basic chemistry of metal nanoparticles in solution. Finke has developed the synthesis of noble metal nanoparticles through hydrogenation of olefinic precursors in the presence of polyoxoanionic ligands. He has, in particular, built kinetic models for the growth of rhodium and iridium particles, and addressed specifically the problem of nanoparticle catalysis [11, 12]. Another organometallic approach is that of Günter Schmid who described in the early 1980s the synthesis of a "giant gold cluster": $Au_{55}Cl_6(PPh_3)_{12}$ [13, 14], and has since then pursued the chemistry and physics of such clusters.

The most intensive development of the nanoparticle area concerns the synthesis of metal particles for applications in physics or in micro/nanoelectronics generally. Besides the use of physical techniques such as atom evaporation, synthetic techniques based on salt reduction or compound precipitation (oxides, sulfides, selenides, etc.) have been developed, and associated, in general, to a kinetic control of the reaction using high temperatures, slow addition of reactants, or use of micelles as nanoreactors [15–20]. Organometallic compounds have also previously been used as material precursors in high temperature decomposition processes, for example in chemical vapor deposition [21]. Metal carbonyls have been widely used as precursors of metals either in the gas phase (OMCVD for the deposition of films or nanoparticles) or in solution for the synthesis after thermal treatment [22], UV irradiation or sonolysis [23, 24] of fine powders or metal nanoparticles.

At the end of the 1980s, after having developed very mild conditions for the synthesis of unstable dihydrogen complexes [25], we reasoned that a similar procedure could allow control of the growth of very large organometallic

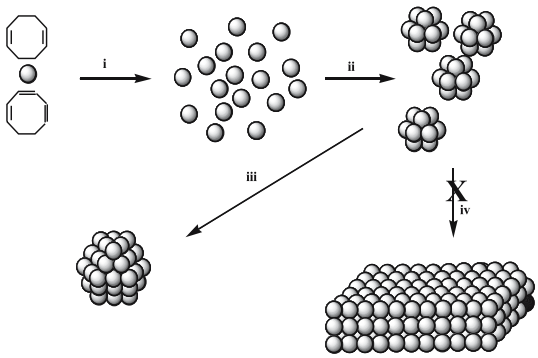

Scheme 1 Illustration of the general synthetic method followed in our group for the synthesis of metal nanoparticles: *i* decomposition of the precursor, nucleation; *ii* first growth process; *iii* ripening or coalescence leading to size and shape controlled objects through addition of stabilizers which prevent the full precipitation of the metal (*iv*)

clusters or very small nanoparticles. The advantage of organometallic chemistry lies in the precise control of the reaction conditions and therefore of the surface of the particles, namely absence of oxidation, number and nature of surface species (ligands), etc. Other advantages could be the control of the surface reactivity and stepwise growth of the clusters. Furthermore, we thought that the particles could be characterized both by techniques usual in the field of nanomaterials (TEM, HRTEM, SEM, XRD, WAXS, XPS) and by techniques derived from molecular chemistry (spectroscopies: IR, UV, NMR in solution and in the solid state; magnetic measurements) (Scheme 1). The ideal precursor is an organometallic complex containing ligands, preferentially olefinic or polyolefinic, able either to be hydrogenated to give a bare metal atom, which would condense in the reaction medium or to be substituted by CO to give an unstable intermediate. The second approach, using CO, had a few precedents [26–28] at the time we started this research whereas the first approach, using a hydrogenation reaction, had none.

These points will be developed in the following section.

2
Organometallic Synthesis of Metal Nanoparticles

The synthesis procedure consists in removing the ligands from an organometallic complex in the mildest possible conditions and with the minimum of potentially pollutant reactants. The ideal case is the reaction of an olefinic precursor with dihydrogen, which leads to the production of an alkane unable in these conditions to produce strong bonds with the growing metal surface [29]. Precursors of this type are for example $Ni(C_8H_{12})_2$ [30] and

$Ru(C_8H_{10})(C_8H_{12})$ [31]. Both complexes decompose satisfactorily under dihydrogen in mild conditions. Complexes accommodating allylic groups may also decompose easily, for example $Co(C_8H_{13})(C_8H_{12})$ [32] or $Rh(C_3H_5)_3$. Other types of complexes may however be used when such olefinic precursors are not available. For example, $M(dba)_2$ (dba = dibenzylidene acetone; M = Pd; Pt) [26–28, 33, 34] is a good precursor for the preparation of nanoparticles of Pd or Pt after treatment with dihydrogen. Mixed complexes such as $Rh(acac)(C_8H_{12})$ [35] (acac = $(CH_3CO)_2CH$) or $CpCu^tBuNC$ (Cp = C_5H_5) [36] also decompose in mild conditions but release potential ligands of the particle namely dba, isonitrile, acacH, or the corresponding diol after hydrogenation (which may or may not perturb the surface). Recently we found that bis(trimethylsilyl)amide complexes of first row transition metals ($M[N(SiMe_3)_2]$; M = Mn, Fe, Co) [37] were excellent precursors when reduced olefinic complexes were not available. The hydrogenation of the precursor produces the corresponding amine, which we have shown to interact weakly with the particle surface and not to modify the physical properties of the particles.

Another approach can be the displacement of the surface ligands by a reactive gas such as CO, leading to unstable intermediates that will eventually condense into particles. This procedure can be applied to $M(dba)_2$ (dba = dibenzylidene acetone; M = Pd; Pt) [26–28, 33, 34]. In this case, however, CO remains at the surface of the growing clusters and may modify their chemistry. The reaction conditions (temperature, gas pressure, concentration of precursors and stabilizers) have a strong influence on the nature of the particles formed, primarily on their size.

Using a polymer that serves only as a sterical stabilizer for the growing particles, we synthesized a number of nanoparticles of various types of (Fe, Co, Ni, Ru, Rh, Pd, Pt, Cu, Ag, Au, In) [29]. Typically olefinic precursors ($Ru(\eta^4 - C_8H_{12})(\eta^6 - C_8H_{10})$, $Co(\eta^3 - C_8H_{13})(\eta^4 - C_8H_{12})$, $Pt(dba)_2$, etc.) are hydrogenated which leads to nanoparticles of 1–3 nm mean size according to the reaction conditions. At these small sizes, the particles are generally facetted nanocrystals which adopt the structure of the bulk element (Ru: hcp [38]; Ni, Pd, Pt: fcc [33, 34]). For first row transition metals, whether prepared from an olefinic or an amide precursor, we observed that the smallest particles display an unusual polytetrahedral structure [39, 40]. For example, Co nanoparticles of mean size 1.6 or 2.0 nm and prepared by hydrogenation of $Co(\eta^3 - C_8H_{13})(\eta^4 - C_8H_{12})$ display this structure whereas larger particles of 4.5 nm mean size display the hcp structure of bulk cobalt. Another anomaly is the case of indium which displays a melting point of 156.6 °C in the bulk but the nanoparticles of which display a "pseudo-liquid" structure at room temperature [41].

Bimetallic nanoparticles may also be prepared in one step using this procedure and a mixture of the precursors in solution (Pd – Cu, Ru – Pt, Co – Ru, Co – Rh, Co – Pt, Ni – Fe) [29]. The particles may form an alloy at all com-

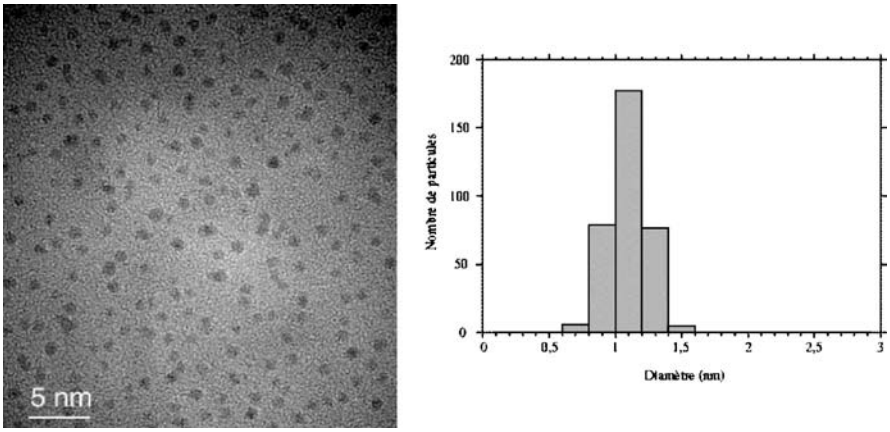

Fig. 1 TEM micrograph and size distribution of Ru_3Pt nanoparticles embedded in PVP (mean diameter ca. 1.2 mm)

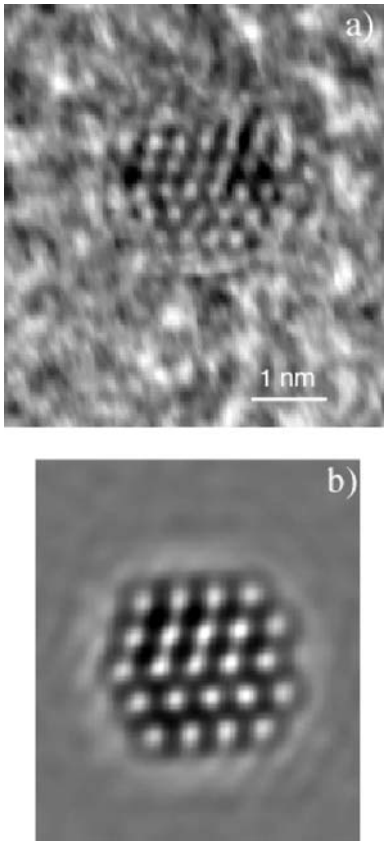

Fig. 2 HREM micrograph of a Ru_3Pt nanoparticle in PVP showing the twinning (**a**) and image simulation (**b**)

positions when the elements display the same bulk structure (Pd – Cu) [42]. In this case, a solid solution is obtained for which we have demonstrated the dynamics of the first layers. Structural changes as a function of particle composition [43] and segregated structures [44, 45] may also be observed. The most spectacular case is that of the Ru – Pt particles [43]. A dissolution of ruthenium into the platinum lattice is observed up to the critical composition $Pt - Ru_3$, which indeed corresponds to the limit of solubility of ruthenium into the platinum lattice in the bulk (Fig. 1, Fig. 2). Before this composition, the particles are fcc and at higher Ru content they become hcp. At the critical composition, the particles are strictly monodisperse, very small, and display a twinning plane in the equatorial plane of the particle corresponding to a hcp default stack in an fcc particle.

2.1 Surface Characterization

Before studying the reactivity of the nanoparticles, it is necessary to evaluate whether the synthetic method employed would lead to particles of "clean" unoxidized surface, able to react with incoming molecules. For this purpose we used, besides physical techniques (which are sometimes difficult to handle due to the high oxidability of particles prepared in this way), molecular methods, namely IR and NMR spectroscopy, as well as magnetic measurements which can give a precise description of the surface properties of the particles.

2.1.1 Infrared Spectroscopy

In order to test the clean, unoxidized nature of the nanoparticle surfaces, we first used CO as a probe molecule to evaluate the electron density at the surface. It was demonstrated that the CO stretching frequency values measured by IR spectroscopy in solution were in good agreement with the values measured on aggregates in ultrahigh vacuum. The presence of some surface oxidation leads to an important shift of this value towards high frequencies. In palladium nanoparticles, a correlation has been established between the ratio of linear to bridge CO groups and the size of the particles [46]. Furthermore, upon monitoring the addition of thiols to Pt nanoparticles covered with CO, it was possible to observe the displacement of some surface CO ligands and, for the remaining ligands, the shift to low frequency of the CO stretch resulting from the electronic enrichment of the particle.

For bimetallic Pd – Cu particles, the coordination of CO to surface Cu and Pd sites has been directly observed together with a surface reconstruction at room temperature [42]. Thus, under vacuum, there is an enrichment of the bimetallic particle surface in Cu. Upon addition of CO, the IR spectrum dis-

plays bands attributed to CO on Cu. However, the particles slowly evolve at room temperature and the IR spectrum shows after several hours a typical spectrum for CO on Pd, hence evidencing the enrichment in Pd of the particles surface. After placing the particles in vacuo overnight and again adding CO, a typical spectrum for CO on Cu was again visible showing the reversibility of this surface reconstruction.

These simple experiments demonstrate the clean, unoxidized character of the nanoparticles together with their surface dynamic at room temperature.

2.1.2 NMR Spectroscopy

This technique is the most widely used and the most useful for the characterization of molecular species in solution. Nowadays, it is also one of the most powerful techniques for solids characterizations. Solid state NMR techniques have been used for the characterization of platinum particles and CO coordination to palladium. Bradley extended it to solution ^{13}C NMR studies on nanoparticles covered with ^{13}C-enriched carbon monoxide [47]. In the case of ruthenium (a metal giving rise to a very small Knight shift) and for very small particles, the presence of terminal and bridging CO could be ascertained [47]. In the case of platinum and palladium colloids, indirect evidence for CO coordination was obtained by spin saturation transfer experiments [47].

The NMR of ligand-protected nanoparticles is little developed; however, several recent studies demonstrate that it is possible to observe long chain ligands bound to metal particles by ^{1}H and ^{13}C NMR spectroscopy [31, 48–52]. In this case, the nuclei close to the metal surface are not visible primarily because of the slow tumbling of the metal particle in solution. Although limited, this technique can give very useful information on the dynamics of the surface ligands. We thus found that thiolate ligands linked to platinum nanoparticles would not undergo any exchange process with free thiols. This demonstrates that the thiolate ligands are firmly linked to platinum and contrasts with the observations carried out on amines coordinated to ruthenium, palladium, and platinum nanoparticles. Thus, we observed in ^{13}C NMR spectroscopy a single peak for the different carbons of the ligand molecule. However, the linewidth of the signal was dependent upon the nature of the carbon. The three carbons (α, β, γ) next to the amino group, the ones likely to be coordinated to the metal, were not visible until a significant amount of extra ligand was added to the NMR tube and appeared broadened, whereas the methyl group at the other extremity of the alkyl chain of the ligand did not show any significant broadening. Another interesting observation is that in the case of ruthenium, these three peaks appeared at the chemical shift of the free ligand whereas in the case of platinum, an important shift, specially of the β carbon was detected. This most probably results from the absence of

Knight shift in the case of ruthenium and the presence of an important one in platinum (Fig. 3, Fig. 4).

These experiments allowed observation of ligand exchange at the surface of the particle and therefore allow introduction of some rationale in the chemistry of these species. However, it would be much more important to be able to directly follow the fate of the active surface species (hydrides, alkyl groups, olefins, carbenes, etc.) as is commonly performed in molecular chemistry. The first and the most important surface ligand is no doubt the hydride, which is an intermediate in many catalytic reactions. We therefore concentrated on the identification of this species on ruthenium nanoparticles (which do not display any Knight shift) by solution NMR, gas phase NMR, magic angle spinning (MAS) solid state NMR and static solid state NMR at variable temperature [53]. Dissolution in THF of ruthenium particles prepared by hydrogenation of Ru(COD)(COT) in the presence of hexadecylamine (HDA) leads to dihydrogen evolution in solution. Attempts at observing the desorption of H_2 in vacuo and upon heating from a solid sample of the colloid were unsuccessful, but addition of D_2 led to the immediate formation of HD, hence revealing the presence of chemically linked hydrogen species (hydrides). After exposing the particles to D_2, a solid state ^{2}D NMR experiment was carried

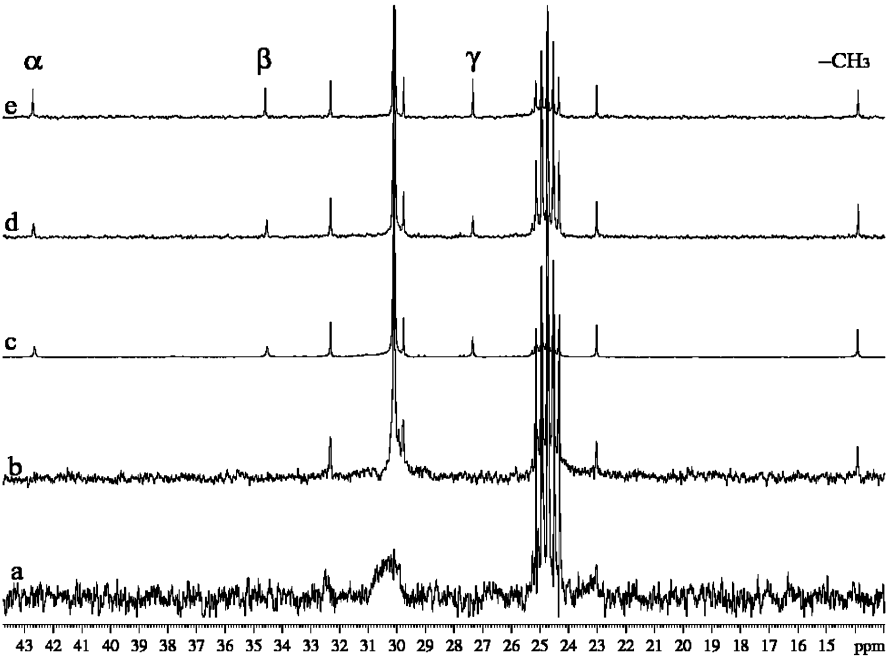

Fig. 3 ^{13}C NMR spectra (d^8-THF, 101 MHz) of$C_{16}H_{33}NH_2$ stabilized ruthenium colloid (**a**), $C_{16}H_{33}NH_2$ stabilized ruthenium colloid + excess $C_{16}H_{33}NH_2$ (**b**), (**c**), (**d**), $C_{16}H_{33}NH_2$ (**e**)

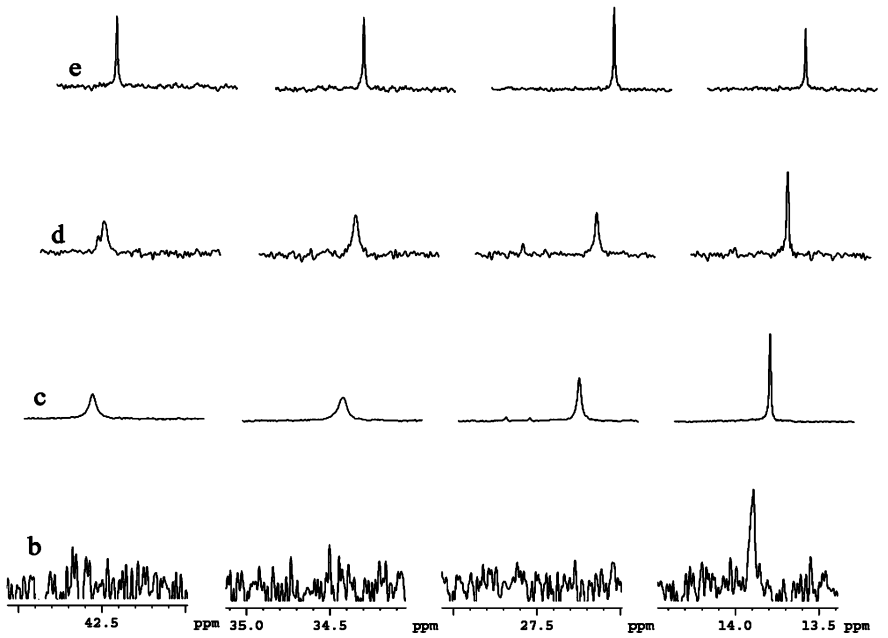

Fig. 4 Enlargement of Figs. 3b,c,d,e for comparison of linewidths

out at various rotation rates. In this way it was possible to detect directly the surface deuterides and, moreover, to demonstrate that these surface species display a high mobility, intermediate between that of deuterons linked to a ligand like HDA and that of gas phase D_2. These results are in agreement with theoretical calculations predicting a high mobility for hydrides linked to a ruthenium surface. It was additionally possible to characterize the deuteration of the alkyl chain of HDA resulting from H/D exchange at the surface of the particle [53].

All these experiments show that the use of various NMR techniques can indeed contribute to the precise characterization of "organometallic nanoparticles".

2.1.3 Magnetic Measurements

For iron, cobalt, nickel, and their alloys, the most sensitive technique for characterizing the particle surface is the measurement of magnetic properties. Thus, we synthesized cobalt nanoparticles of 1.6 nm (ca. 150 atoms), 2 nm (ca. 300 atoms) and 4 nm (a few thousand atoms) mean size. The structure of the particles is hcp in the latter case and polytetrahedral in the first two cases. The 4 nm particles display a saturation magnetization equal to that of bulk

cobalt (1.72 μ_B) whereas the smaller particles do not saturate at 30 T. Furthermore, they display a saturation magnetization higher than the bulk (2.1 and 1.9 μ_B/cobalt atom at 30 T for particles of 1.6 and 2.0 nm, respectively) [54]. These results are very similar to those found by Billas et al. on time-of-flight clusters in ultrahigh vacuum [55]. This suggests a direct correspondence between the physical properties of gas phase aggregates and those of prepared in solution using the organometallic approach. In a similar way, bimetallic Co – Ru, Co – Rh [44, 45] and Co – Pt [56] nanoparticles of low size dispersity and defined compositions have been synthesized. These species, and specially the Co – Rh particles, also display a very important excess of magnetization compared to bulk values, which is attributed in the Co – Rh case to the strong polarization of Rh in the vicinity of Co [44, 45].

These experiments have recently been extended to the case of iron. The synthesis of small Fe particles has long been difficult due to the lack of suitable precursor. However, using the complex $Fe[N(SiMe_3)_2]_2$ as precursor, we have obtained nanoparticles of low size dispersity and displaying a magnetization 5 T higher than in bulk iron and comparable to that of gas phase aggregates [57].

In order to validate the results obtained on our particles, we reacted them with various ligands and/or contaminants and measured their magnetic properties again. It was found that surface oxidation or coordination of π-accepting ligands such as CO lead to a strong decrease of the particle magnetization. In contrast, purely σ-donating ligands do not affect the magnetism of the particles [58].

3
Surface Organometallic Chemistry on Nanoparticles

An organometallic complex consists of a central metal atom and a number of ligands, which can be schematically classified into three groups:

1. Ancillary ligands, the role of which is to stabilize complexes or nanoparticles and liberate a vacant coordination site when necessary
2. Active ligands, which may take an important role in the reactivity of the complexes/nanoparticles (e.g., hydrides, alkyl groups, carbenes, etc.)
3. Directing ligands, which will orientate the reactivity of the complexes/particles (for example asymmetric ligands such as DIOP or BINAP)

Such ligands may also coordinate to the surface of nanoparticles and strongly influence their chemistry, it is therefore important to gain information on their presence and mode of bonding.

3.1
Active Ligands

The most important ligand in organometallic chemistry, as far as catalytic reactivity is concerned, is the hydride. Since our synthesis method involves the decomposition of an organometallic precursor and the growth of particles under a dihydrogen pressure, we have attempted to characterize the presence of surface hydrides by a variety of NMR methods. Thus, as described in the preceding chapter, we used solution NMR, gas phase NMR, magic angle spinning (MAS) solid state NMR and static solid state NMR at variable temperatures [53]. We found that surface hydrides are indeed present on the ruthenium surface, as deduced from solution and gas phase studies. These species can then be observed directly by solid state NMR and display a very high mobility, in agreement with recent theoretical calculations. Furthermore, we could show that these surface hydrides display a high reactivity. Thus when HDA-coordinated Ru nanoparticles were reacted in solution at room temperature with 1 bar D_2, we evidenced a rapid H/D scrambling all over the alkyl chain of the amine. If the reaction is carried out on a solid sample of the colloid, only the "mobile" carbons of the chain are deuterated. This demonstrates the high reactivity of these surface hydride for a complex reaction implying both C – H (C – D) and H – H (D – D) activation.

3.2
Ancillary Ligands

The syntheses described in the preceding section can be performed using as stabilizers the classical ligands of organometallic chemistry (e.g., amines, thiols ,or phosphines) instead of polymers. The amount of ligand added allows control of the particle growth and therefore the size.

3.2.1
Alcohols

Using weak stabilizers such as alcohols during the decomposition of $Ru(C_8H_{10})(C_8H_{12})$ by H_2 leads to a colloidal solution stable for long periods of time (over 1 year) when kept under argon. Exposure to air or addition of pentane under argon leads to precipitation of the particles. In the latter case, the isolated particles burn in air, hence demonstrating the reactivity of their surface, whereas in the former case the particles are stable because of the formation of a passivation layer of RuO_2 [59, 60]. The particles prepared in neat methanol are very large, polycrystalline (ca. 76 nm) (Fig. 5), mesoporous and display a relatively large specific area ($> 40\ m^2g^{-1}$). In THF/methanol mixtures, the size of the polycrystalline particles remains of the same order of magnitude as those in neat methanol up to a THF content of 25 vol % after

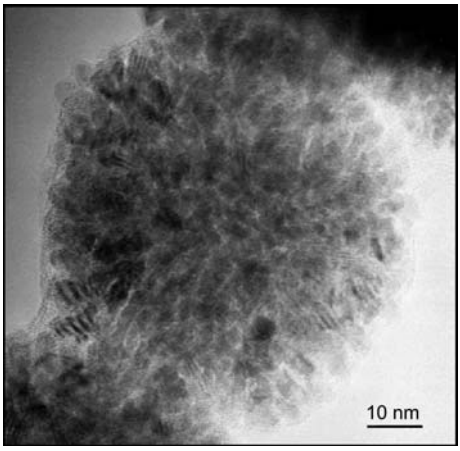

Fig. 5 HREM micrograph of ruthenium sponge-like particles obtained in pure methanol

which the size decreases linearly with the THF content: for a THF content in the solution of 50 vol %, the size of the particles is 47 nm, for 90 vol % 20 nm, and for 97.5 vol %, ca. 3–6 nm. A similar trend, namely size decrease, is observed upon changing MeOH for higher alcohols. The size of the particles is ca. 5 nm when the reaction is carried out in ^{i}PrOH and ca. 2.5 nm in pentanol. Finally, it was found that for reactions carried out in MeOH/THF mixtures, addition of cyclooctane leads to an increase in the size of the particles.

These surprising results were attributed to the segregation of cyclooctane resulting from hydrogenation of the ruthenium precursor and the rest of the solvent. In this respect, the larger droplets would be formed in the most polar solvent systems and hence the most segregated medium. This is in excellent agreement with the sizes of the particles measured in neat alcohols. The most lipophillic one (pentanol) gives rise to the smallest particles [59, 60].

In the MeOH/THF mixtures, the change in polarity of the medium resulting from the composition changes may account for the apparent correlation observed between the size of the particles and the MeOH content. The mesoporous, polycrystalline nature of the large particles suggests that, during the growth process, nanocrystallites synthesized at the early stage of the reaction may be connected by ruthenium atoms or particles resulting from the decomposition of the remaining starting material [59, 60].

When the reaction is carried out in heptanol [61], the particles are monodisperse in size (3 nm), well dispersed in the solvent, and adopt the hcp structure of bulk ruthenium. They can be isolated and re-dissolved in various solvents, including d^8-THF for NMR analysis. In this case, it is clear that coordinated heptanol is present at the surface of the particles and acts as a weakly coordinating ligand. In this case, the presence of surface hydrides was demonstrated by NMR techniques.

3.2.2 Amines

Amines are weak ligands, which may easily be displaced from the nanoparticles surface and allow the further growth of nanoparticles through coalescence. This is revealed, as described in the preceding section, by solution ^{13}C NMR studies which evidence a fast exchange at the NMR time scale between free and coordinated amines [31]. This study carried out on ruthenium [31], palladium [62], and platinum [63] shows in each case that the fluxionality of the ligand is associated with a coalescence of the particles into nanorods/nanowires of monodisperse diameter and polydisperse length (Fig. 6, Fig. 7). This surprising result is attributed to the templating effect on the growth of the nanoparticles of the long chain amine ligands (HDA for example) which may organize inside the solution. Increasing the amine concentration leads to a modification of the shape of the particles characterized,

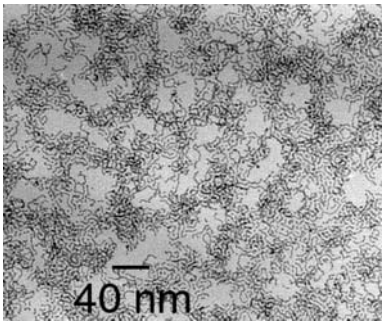

Fig. 6 TEM micrograph of hexadecylamine stabilized platinum nanoparticles showing the formation of nanowires

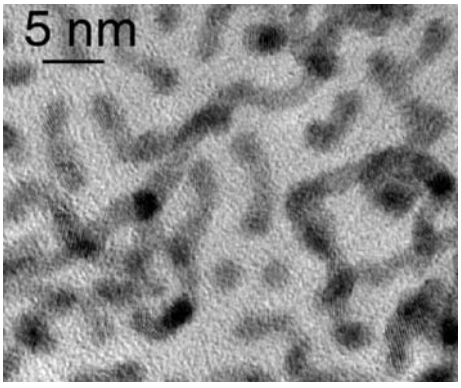

Fig. 7 HREM micrographs of hexadecylamine stabilized platinum nanoparticles showing the formation of nanowires

according to the different systems, by a decrease of the aspect ratio of the particles. They become more isotropic and, in the case of palladium for example, spherical. In contrast, the use of amines as reaction medium leads to very long nanowires, and the same fluxional behavior has been observed. Amines are therefore very useful ligands when attempting to grow nanoparticles of anisotropic shape.

3.2.3 Thiols

Thiols are known to be excellent ligands for the stabilization of gold and platinum nanoparticles. In this respect, we did not observe any fluxional behavior [31, 52] in solution NMR experiments for thiols coordinated to the surface of noble metal particles (Fig. 8). However, in the case of ruthenium, we found the slow catalytic formation of alkyl disulfides [31]. After exclud-

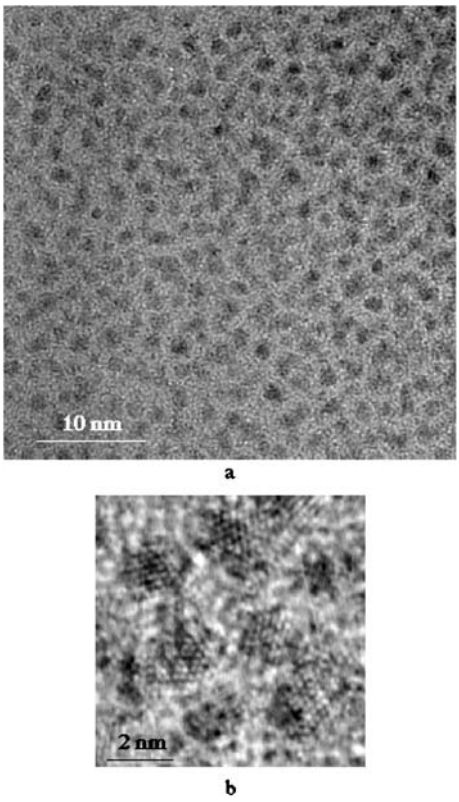

Fig. 8 TEM (**a**) and HREM (**b**) micrographs of octanethiol stabilized platinum colloid showing nearby particles with no coalescence

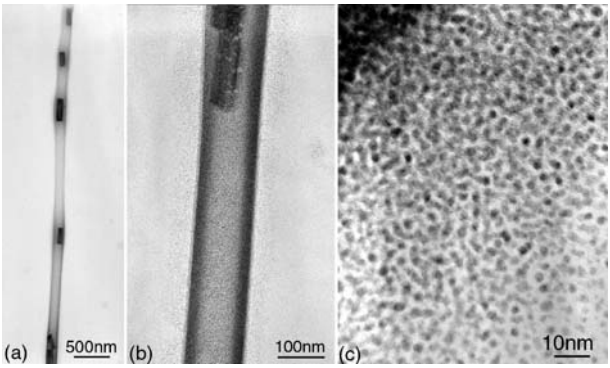

Fig. 9 Transmission Electron Micrographs od sauper-structures resulting from the self-assembly of 1.6 mm Pt particles stabilizes half by $4-HO-C_6H_4-SH$ and half by $4-NH-2-C_6H_4-SH$: **a** $\times 15\,000$; **b** $\times 100\,000$; **c** $\times 600\,000$

ing the presence of an oxidation reaction, we can propose an initial surface reaction between the thiols and the surface of the particle leading to thiolate ligands followed by coupling of thiolato ligands at the surface of ruthenium, finally producing alkyl disulfides.

It is possible to take advantage of the strong coordination of sulfur to platinum to build "supramolecular" networks incorporating the metal particles. Thus platinum particles of 1.6 nm mean size can be prepared using as protecting ligands thiophenols substituted in the 4 position by an hydroxo, carboxylate or amino group [64]. Self-assembly of the nanoparticles is observed for the colloids stabilized by 4-HO-C_6H_4-SH or 4-HOOC-C_6H_4-SH. If a mixture containing a 1 : 1 mixture of the 4-HO-C_6H_4-SH and 4-H_2N-C_6H_4-SH is used, the particles self-organize into very long nanotubes, the walls of which are constituted of a monolayer of platinum nanoparticles (Fig. 9).

3.2.4 Phosphines

PPh_3 is probably the most common ligand of organometallic chemistry. It has been used successfully by G. Schmid in gold nanoclusters [1–9, 13, 14] and can also be used for stabilizing Pt nanoparticles of very small size (1.2 nm) [34]. These particles adopt an icosahedral structure and under CO give rise to an interesting equilibrium. Thus, they are prepared through addition of PPh_3 to fcc particles resulting from the addition of CO (1 atm) to $Pt(dba)_2$ in THF. Interconversion between the two colloids and therefore the two structures is possible by addition of CO on one side or of PPh_3 on the other [34].

Chelating di- or more generally, polyphosphines may also be used as stabilizers of nanoparticles. Reactions with ruthenium and palladium show that

the use of phosphines such as $Ph_2P(CH_2)_{10}PPh_2$, $[Ph_2P(CH_2)_2](PPh)$ and $[Ph_2P(CH_2)_2](NC_3H_7)$ lead in each case to very stable particles of ca. 2 nm mean size. No coalescence, or changes in size or shape were observed with these particles, hence confirming the stabilizing effect of the ligands.

3.3 Directing Ligands

The coordination of ligands at the surface of metal nanoparticles has to influence the reactivity of these particles. However, only a few examples of asymmetric heterogeneous catalysis have been reported, the most popular ones using a platinum cinchonidine system [65, 66]. In order to demonstrate the directing effect of asymmetric ligands, we have studied their coordination on ruthenium, palladium, and platinum nanoparticles and the influence of their presence on selected catalytic transformations.

Nanoparticles of both ruthenium and platinum can be prepared using asymmetric oxazolines or amino alcohols as ligands [67]. In both cases, the ligands provide an excellent stabilization of the particles, which can be handled like molecular species. The platinum particles give rise to self-organized super-structures adopting shapes of wires or of pseudo-crystals. The ruthenium particles are very small (1–2 nm according to the ligand) and can be used in catalytic reactions such as asymmetric hydrogenation or asymmetric hydrogen transfer. In this case a distinct reactivity has been found using an asymmetric oxazoline between molecular species and nanoparticles. The nanoparticles are more active but much less selective than the corresponding molecular complexes. Addition of excess ligands slows the catalytic reaction but leads to a modest but real increase in the enantiomeric excess. This therefore suggests that asymmetric catalysis can indeed take place in solution on such large chemical species [68].

Another well-established reaction in homogeneous catalysis, namely palladium-catalyzed allylic alkylation, was chosen for comparing the reactivity of molecular complexes and nanoparticles. If the molecular system was very active, a very unusual and unanticipated result was obtained: a very large kinetic preference for one of the enantiomer in the colloidal system [69]. A number of control experiments, including recycling and poisoning experiments with Hg and CS_2, were carried out in order to distinguish between the molecular and the colloidal system and, more precisely, to determine whether the catalytic activity of the colloid arises from very small amounts of palladium going from the colloidal to the molecular state. The most determining experiments were carried out upon adjusting the kinetics of the molecular and the colloidal system. Since a possible explanation for the observed reactivity could be the dissolution of the colloid into a small amount of molecular complexes, we diluted the molecular system until reaching the same initial rate for the colloidal and the molecular systems. However, we found that this

procedure led to an observed kinetic preference k_R/k_S of ca. two in the molecular system and of ca. 15 in the colloidal one. This strongly suggests the existence of two distinct catalytic systems, one of which is due to a preference for surface coordination of one of the substrate enantiomers [69].

In summary, we found that ligands indeed coordinate at the surface of nanoparticles and that they can be firmly or loosely attached to this surface according to their chemical nature. Furthermore, the ligands influence the reactivity of the metal nanoparticles. This is important in catalysis but, as we will see later in this paper, is also important for the control of the growth of metal nanoparticles of defined size and shape.

4
Organization of Nanoparticles

In order to make practical use of the physical properties of nanoparticles, whether individual or collective, one has to find a way to address them. If we leave out the near field techniques, this in turn requires that the particles be monodisperse and organized in two or three dimensions. It is therefore necessary to imagine techniques allowing the self-organization and even, ideally, the crystallization of nanoparticles into super-lattices.

4.1
Hydrogen Bond Network

The first idea is to use techniques that have common molecular chemistry, namely create hydrogen bond networks. This requires that the nanoparticles be stabilized with polyfunctional ligands containing a function strongly bound to the nanoparticle surface (thiol, phosphine) and a function able to participate to hydrogen bonds (amine, alcohol, acid). For example, we prepared independently 1.6 nm platinum nanoparticles stabilized by *para*-hydroxythiophenol or by *para*-aminothiophenol. Upon reacting an equimolar mixture of both, extended super-structures were produced as monolayers, nanotubes or 3D super-lattices [64]. The walls of the nanotubes consist of one monolayer of self-assembled nanoparticles and reach millimeter lengths. In none of these super-structures have the particles changed size or shape. Other types of organic ligands can lead to interesting monodimensional superstructures [67].

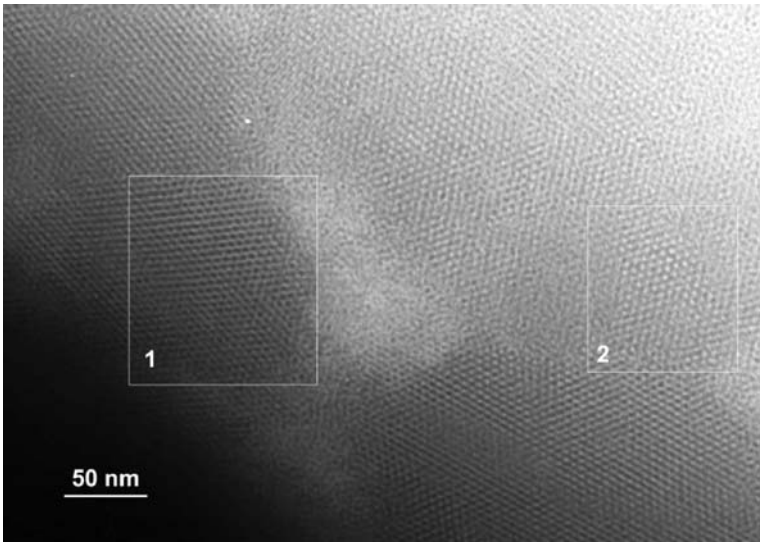

Fig. 10 Self-organisation of Ni-Fe nanoparticles on a carbon substrate: (1) multi-layers; (2) mono-layer.

4.2 Self-organization

The most common method for preparing nanoparticle super-lattices is to use monodisperse nanoparticles either resulting from a controlled synthesis or from size selection after synthesis and to let them self-assemble onto various substrates (microscopy carbon grid, silicon wafer, glass, etc.). We have employed this technique with indium nanoparticles obtained by UV irradiation of organic solutions of InCp in the presence of HDA [41]. Extended 2D organizations were observed on the microscopy grids upon deposition of a drop of the reaction solution. Using concentrate solutions, it was possible to obtain multilayers displaying a 3D fcc organization. Similarly, Ni – Fe nanoparticles were prepared by thermal decomposition of a mixture of precursors ($Fe(CO)_5$ and $Ni(COD)_2$) in the presence of HDA. They give rise to extended 2D and 3D organizations when deposited on a microscopy grid (Fig. 10) [70].

4.3 Crystallization

One of the main challenges in the field is the controlled crystallization of the nanoparticles into 3D super-lattices, similar to artificial opals but including much smaller individual particles. For this we have used electrically charged stabilizers (ligands and surfactants). For example, the photochemical decomposition of the precursor $[Sn(NMe_2)_2]_2$ in the presence of HDA

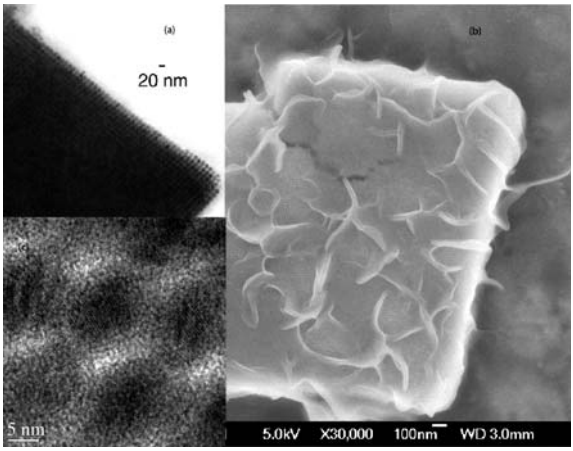

Fig. 11 Formation of crystalline 3D super-lattices of tin nanoparticles: **a** TEM view of a facetted super-crystal; **b** SEM image showing particles included into a super-crystal as well as the organic surrounding; **c** High resolution micrograph showing the alignment of the tin atomic planes inside the super-structure

leads to large cubic particles (ca. 100 nm). However, when introducing 10% of the hydrochloride of HDA (HDAHCl) large super-crystals fall out of the solution. The super-crystals are shown to contain monodisperse, slightly ovoid nanoparticles displaying aligned crystalline axes. The space group of the super-lattice is not compact (monoclinic), which is in agreement with a real crystallization of both the particles and their ligand shell (Fig. 11) [71].

This process of crystallization using charges was extended to other systems using as an alternative mixtures of amines and long chain carboxylic acids. In this way, super-lattices of nanorods of cobalt and of nanocubes of iron were prepared (vide infra).

In summary, super-lattices may be obtained using the established techniques of self-organization but also a technique derived from molecular chemistry, the creation of hydrogen bond networks. In addition, the crystallization of nanoparticles inside 3D super-crystals may be achieved using ionic stabilizers.

5
Shape Control of Nanoparticles

The physical properties of metal nanoparticles are very size-dependent. This is clear for their magnetic properties, for which the shape anisotropy term is very important. This is also true for the optical properties of nanoparticles displaying plasmon bands in the visible range (Cu, Ag, Au) and for III-V

or II-VI semi-conductors. This is less clear for the chemical properties of nanoparticles although studies carried out on monocrystals demonstrate the difference in catalytic activity of different surfaces of the same element. In order to achieve this control it is possible to grow the particles inside confined "host" structures (mesoporous silica, micelles) or to favor a privileged axis of growth through preferred coordination of ligands on selected crystalline faces. It is also possible to use ligand mixtures that may act both as growth inhibitors of selected faces and as surfactants to host the growing particles. These ligands mixtures typically contain an amine and a carboxylic acid or an amine an ammonium salt. The ligands are able to react on one another to give rise to catanionic systems. The bonus of the use of such systems is therefore the presence of charges which may favor the formation of super-lattices.

5.1
Confinement in a Mesoporous Silica

The synthesis of nanoparticles can be carried out using a mesoporous silica as templating agent. However, even in this case, the functionalization of the pores with organic derivatives is necessary to obtain a good dispersion of the nanoparticles within the silica matrix [72]. Thus, decomposition of Ru(COD)(COT) by dihydrogen may occur inside or outside the pores of a mesoporous silica. However, if the pores are functionalized with phosphonate groups, which may act as weak ligands for ruthenium, the growth of ruthenium occurs selectively within the pores. Furthermore, at a high metal concentration, the growing particles are mobile within the pores and may coalesce to yield encapsulated ruthenium nanorods. In a similar way, indium, gold or platinum nanoparticles may be included in the pores of mesoporous silica [73].

5.2
Use of Long Chain Organic Ligands

There is presently only a little information on the organization of long chain alkyl molecules such as amines and carboxylic acids in organic solutions. Therefore, it is necessary to gain knowledge about this organization, the technique of choice being small angle neutron scattering. Meanwhile, we directly explored the influence of these ligands on the growth of metal nanoparticles in solution.

Thus, the decomposition of $Ni(COD)_2$ by dihydrogen in the presence of HDA yields nanoparticles, the aspect ratio of which depends upon the ligand concentration. Thus for one or less equivalent HDA, the reaction produces isotropic Ni particles whereas using ten equivalent HDA, nanorods, monodisperse in diameter, are obtained [74]. The formation of nanowires can also be promoted by a rapid decomposition process. This is illustrated by the decom-

position of InCp in the presence of UV irradiation and HDA which leads to very long In bct nanowires [75]. In the case of cobalt, using a mixture of long chain amine and oleic acid, 4 nm isotropic nanoparticles are initially obtained. These particles coalesce at 150 °C under H_2 to give nanorods, the aspect ratio of which only depends upon the chain length of the amine ligand (Fig. 12) [76]. When using stearic acid instead of oleic acid and HDA, all the nanorods formed in the solution self-organize into an unprecedented 2D hexagonal network (Fig. 13) [78]. Whereas the nanoparticles are superpara-

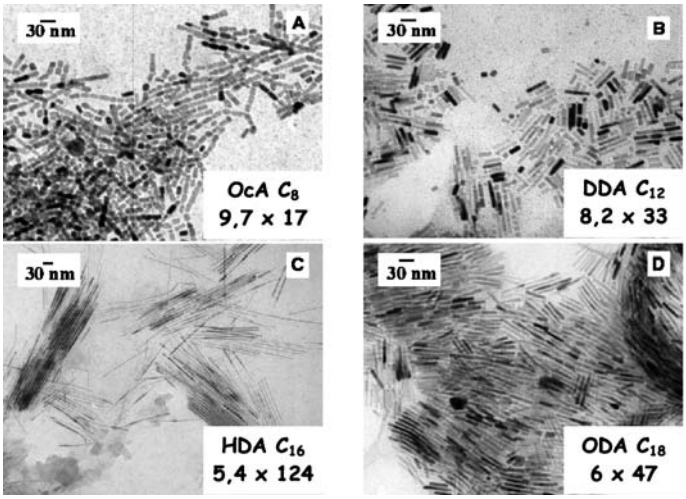

Fig. 12 Cobalt nanorods synthesized in the presence of a mixture of oleic acid and: **a** octylamine; **b** dedecylamine; **c** hexadecylamine; **d** octadecylamine

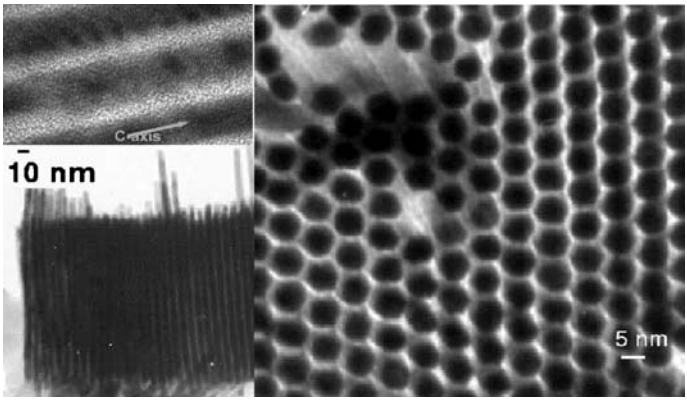

Fig. 13 Super-lattice of cobalt nanorods: **a** Top view hexagonal; **b** vue de côté; **c** image à haute résolution

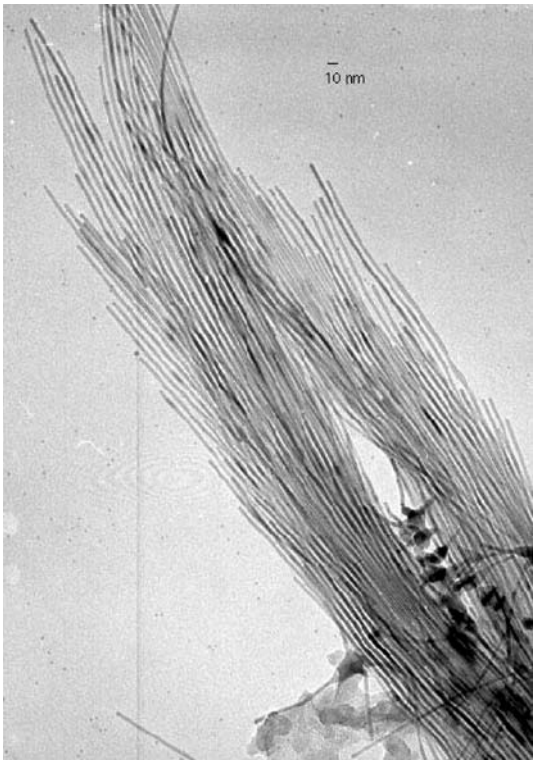

Fig. 14 Transmission electron micrograph of Cobalt Nanowires

magnetic, the nanorods are ferromagnetic at room temperature and could in principle be used for magnetic information storage [76, 77].

Interestingly, a careful study of the particles obtained at the early stage of the reaction by ultramicrotomy shows that most of them are included into 3D crystalline super-lattices. A high resolution micrograph evidences the coalescence of selected particles inside this super-lattice. It is puzzling that the same ligand systems (long chain amine + carboxylic acids) are used for building nanoparticles super-lattices and for controlling the shape of nano-objects. It is therefore possible that the two facts are related and that the anisotropic shape of the particles is due to their growth within the super-lattice created by the self-organization of the particles in a way similar to that observed in mesoporous silica. It is also noteworthy that dihydrogen is necessary for the transformation of the initially formed isotropic nanoparticles into nanorods. This emphasizes the role of surface organometallic chemistry for the growth of nanomaterials. The presence of dihydrogen should allow, through a metathesis reaction, removal of the initially firmly coordinated caboxylate ligands. This would leave surface hydrides, which could favor the particle coalescence, like in the case of ruthenium.

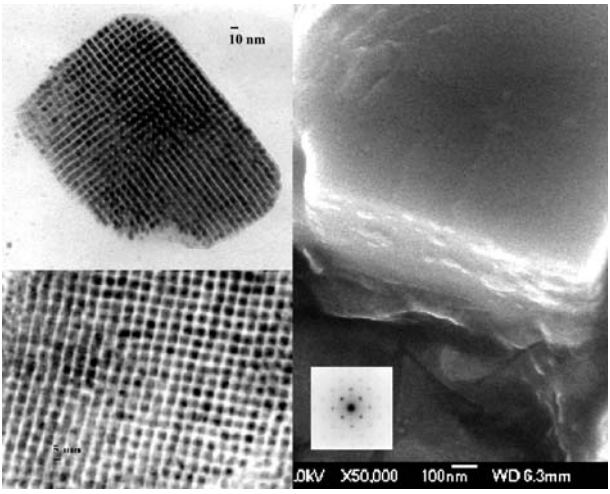

Fig. 15 Super-lattices of iron nanocubes: **a** SEM micrograph of a "super-cube"; **b** TEM micrograph of a super lattice; **c** TEM micrograph after ultramicrotomy

The ligand mixture can control not only the aspect ratio of nanorods but also the length of nano-objects. Thus changing the relative ligand ratio from 1 : 1 in the preceding case to 2 oleic acid : 1 HDA leads to the formation of very long cobalt nanowires, monodisperse in diameter (4 nm) and displaying a length of several hundred microns (Fig. 14) [78]. These nanowires are monocrystalline and monodomain are revealed by magnetic holography studies.

This study could be extended to the synthesis of iron nanoparticles. Using $Fe[N(SiMe_3)_2]_2$ as precursor and a mixture of HDA and oleic acid, spherical nanoparticles are initially formed as in the case of cobalt. However, a thermal treatment at 150 °C in the presence of H_2 leads to coalescence of the particles into cubic particles of 7 nm side length. Furthermore, these particles self-organize into cubic super-structures (cubes of cubes; Fig. **??**) [79]. The nanoparticles are very air-sensitive but consist of zerovalent iron as evidenced by Mössbauer spectroscopy. The fact that the spherical particles present at the early stage of the reaction coalesce into rods in the case of cobalt and cubes in the case of iron is attributed to the crystal structure of the metal particles: hcp for cobalt, bcc for iron.

In summary, control of the surface chemistry and the presence of clean surfaces allow the coalescence of initially isotropic nanoparticles into regular, often monodisperse, nano-objects of anisotropic shape (cubes, rods, wires). It is possible that the inclusion of the initially present nanoparticles into superlattices play an important role in these coalescence processes.

6 Conclusion

In summary, we have described our approach towards the synthesis of novel nano-objects consisting of a metal core and a surface that may be functionalized by addition of organic ligands. TEM pictures of the metal core of these nanoparticles appear similar to those of particles commonly used in heterogeneous catalysis or to colloids prepared by well-known reduction methods. However, the organometallic approach displays several specificities which can be summarized as follows:

1. The organometallic approach is a low temperature approach, which means that in general synthesis of the particles, and therefore many characteristics of the nano-objects, can be controlled:
   - Size and size dispersity of the particles
   - Structure of the particles, which may be different from that thermodynamically stable in the reaction conditions, e.g., the polytetrahedral structure found for cobalt nanoparticles
   - Composition in case of bimetallic species
2. The organometallic approach allows control of the surface. It is therefore possible to prepare species displaying a clean surface able to adsorb small molecules (CO, H_2) or large ligands (phosphines, amines, thiols, polydentate ligands, etc.).
3. The surface properties of these nano-objects match those of metal nanocrystals prepared in ultrahigh vacuum, for example the C – O stretch of adsorbed carbon monoxide or the magnetic properties of cobalt particles embedded in PVP. This demonstrates the "clean" character of the surface of these particles and its availability for reactivity studies.
4. These nano-objects display an organometallic surface chemistry comparable to usual organometallic moieties and which can be studied by classical spectroscopic methods: substitution reactions leading to structural changes in the particles, the fluxional or non-fluxional behavior of surface ligands, the formation and observation of surface hydride species, the monitoring of catalytic reactions etc.
5. These species display a very rich potential of reactivity, which may concern fields as diverse as dihydrogen formation and storage or asymmetric catalysis.
6. Finally, the shape and self-assembly of these particles can also be controlled which gives rise to novel nanomaterials displaying interesting physical properties in the fields of semi-conductors, magnetism, or optics.

All these elements suggest that there is a strong potential for organometallic chemists to enter this research area concerning the synthesis and properties of metal nanoparticles. This should lead to impressive developments in the field of surface organometallic chemistry in the future.

Acknowledgements The authors thank the students and colleagues that have participated in the work over the years. In addition, we gratefully acknowledge CNRS, MENRT, EC:TMR network CLUPOS for support.

References

1. Schmid G (ed)(2004) Nanoparticles, from theory to applications. VCH, Weinheim
2. de Jongh LG (1994) Physics and chemistry of metal cluster compounds. Kluwer, Dordrecht
3. Klabunde KJ, Cardenas-Trivino G (1996) In: Fürstner A (ed) Active metals: preparation, characterization, applications. VCH, Weinheim pp. 237–277
4. Toshima N, Yonezawa T (1998) New J Chem, p 1179
5. Lewis LN (1993) Chem Rev 93:2693
6. Lewis LN (1998) In: Adams RD, Cotton FA (eds) Catalysis by di- and polynuclear metal cluster complexes. Wiley-VCH, Weinheim p 373
7. El-Sayed MA (2001) Acc Chem Res 34:257
8. Bönnemann H, Richards RM (2001) Eur J Inorg Chem 2455
9. Feldheim DL, Foss CA Jr (eds) (2002) Metal nanoparticles. Marcel Dekker, New York
10. Roucoux A, Schulz J, Patin H (2002) Chem Rev 102:3757
11. Weddle KS, Aiken III JD, Finke RG (1998) J Am Chem Soc 120:5653
12. Widegren JA, Finke RG (2003) J Mol Catal A 191:187
13. Schmid G (1992) Chem Rev 92:1709
14. Schmid G, Bäumle M, Geerkens M, Heim I, Osemann C, Sawitowski T (1999) Chem Soc Rev 28:179
15. Sun S, Murray CB, Weller D, Folks L, Moser A (1989) Science 2000:287
16. Puntes VF, Krishnan KM, Alivisatos AP (2001) Science 291:2115
17. Puntes VF, Zanchet D, Erdonmez CK, Alivisatos AP (2002) J Am Chem Soc 124:12874
18. Park SJ, Seungsoo K, Lee S, Khim ZG, Char K, Hyeon T (2000) J Am Chem Soc 122:8581
19. Peng ZA, Peng X (2001) J Am Chem Soc 123:1389
20. Pileni P (2002) In: Feldheim DL, Foss CA Jr (eds) Metal nanoparticles. Marcel Dekker, New York p 207
21. Hierso JC, Satto C, Feurer R, Kalck P (1996) Chem Mater 8:390
22. Phillips J, Clausen B, Dumesic JA (1980) J Phys Chem 84:1814
23. Suslick KS, Hyeon T, Fang M (1996) Chem Mater 8:2172
24. de Caro D, Ould Ely T, Mari A, Chaudret B, Snoeck E, Respaud M, Broto J-M, Fert A (1996) Chem Mater 8:1987
25. Sabo-Etienne S, Chaudret B (1998) Coord Chem Rev 178–180, 381
26. Bradley JS, Millar J, Hill EW, Melchior M (1990) J Chem Soc Chem Commun 705
27. Bradley JS, Millar J, Hill EW (1991) J Am Chem Soc 113:4016
28. Bradley JS, Hill EW, Klein C, Chaudret B, Duteil A (1993) Chem Mater 5:254
29. Philippot K, Chaudret B (2003) In: Astruc D (ed) Dendrimères et nanosciences. Compte-Rendus Acad Sciences 6:1019
30. Ould Ely T, Amiens C, Chaudret B, Snoeck E, Verelst M, Respaud M, Broto J-M (1999) Chem Mater 11:526
31. Pan C, Pelzer K, Philippot K, Chaudret B, Dassenoy F, Lecante P, Casanove M-J (2001) J Am Chem Soc 123:7584
32. Osuna J, de Caro D, Amiens C, Chaudret B, Snoeck E, Respaud M, Broto J-M, Fert A (1996) J Phys Chem 100:14 571

33. Duteil A, Quéau R, Chaudret B, Mazel R, Roucau C, Bradley JS (1993) Chem Mat 5:341
34. Rodriguez A, Amiens C, Chaudret B, Casanove M-J, Lecante P, Bradley JS (1996) Chem Mat 8:1978
35. Zitoun D, Respaud M, Fromen MC, Casanove MJ, Lecante P, Amiens C, Chaudret B (2002) Phys Rev Lett 89:37 203
36. de Caro D, Wally H, Amiens C, Chaudret B (1994) J Chem Soc Chem Comm 1891
37. Andersen RA, Faegri KJ, Green JC, Haaland A, Lappert MF, Leung WP, Rypdal K (1988) Inorg Chem 27:1782
38. Pan C, Dassenoy F, Casanove MJ, Philippot K, Amiens C, Lecante P, Mosset A, Chaudret B (1999) J Phys Chem B 103:10 098
39. Osuna J, de Caro D, Amiens C, Chaudret B, Snoeck E, Respaud M, Broto J-M, Fert A (1996) J Phys Chem 100:14 571
40. Dassenoy F, Casanove M-J, Lecante P, Verelst M, Snoeck E, Mosset A, Ould Ely T, Amiens C, Chaudret B (2000) J Chem Phys 112:8137
41. Soulantica K, Maisonnat A, Chaudret B, Fromen M-C, Casanove M-J, Lecante P (2001) Angew Chem (Int Ed) 40:448
42. Bradley JS, Hill EW, Chaudret B, Duteil A (1995) Langmuir 11:693
43. Dassenoy F, Casanove M-J, Lecante P, Pan C, Philippot K, Chaudret B (2001) Phys Rev B B63:235 407
44. Zitoun D, Respaud M, Fromen M-C, Casanove M-J, Lecante P, Amiens C, Chaudret B (2002) Phys Rev Lett 89:37 203
45. Zitoun D, Amiens C, Chaudret B, Fromen M-C, Lecante P, Casanove M-J, Respaud M (2003) J Phys Chem B 107:6997
46. Bradley JS, Hill EW, Behal S, Klein C, Chaudret B, Duteil A (1992) Chem Mat 4:1234
47. Bradley JS, Millar J, Hill EW, Behal S, Chaudret B, Duteil A (1991) Faraday Discuss Chem Soc 92:255
48. Terrill RH, Postlethwaite TA, Chen C-H, Poon C-D, Terzis A, Chen A, Hutchison JE, Clark MR, Wignall G, Londono JD, Superfine R, Falvo M, Johnson CS Jr, Samulski ET, Murray RW (1995) J Am Chem Soc 11:7–12 537
49. Badia A, Gao W, Singh S, Demers L, Cuccia L, Reven L (1996) Langmuir 12:1262
50. Badia A, Cuccia L, Demers L, Morin F, Lennox RB (1997) J Am Chem Soc 119:2682
51. Hostetler MJ, Wingate JE, Zhong C-J, Harris JE, Vachet RW, Clark MR, Londono JD, Green SJ, Stokes JJ, Wignall GD, Glish GL, Porter MD, Evans ND, Murray RW (1998) Langmuir 14:17
52. Dassenoy F, Philippot K, Ould Ely T, Amiens C, Lecante P, Snoeck E, Mosset A, Casanove M-J, Chaudret B (1998) New J Chem 22:703
53. Pery T, Pelzer K, Matthes J, Buntkowsky G, Philippot K, Limbach H-H, Chaudret B, Submitted
54. Respaud M, Broto J-M, Rakoto H, Fert AR, Thomas L, Barbara B, Verelst M, Snoeck E, Lecante P, Mosset A, Osuna J, Ould Ely T, Amiens C, Chaudret B (1998) Phys Rev B 57:2925
55. Billas IML, Châtelain A, de Heer WA (1994) Science 265:1682
56. Ould Ely T, Pan C, Amiens C, Chaudret B, Dassenoy F, Lecante P, Casanove M-J, Mosset A, Respaud M, Broto J-M (2000) J Phys Chem B 104:695
57. Margeat O, Amiens C, Chaudret B, Respaud M, Lecante P (unpublished results)
58. Cordente N, Amiens C, Chaudret B, Respaud M, Senocq F, Casanove M-J (2003) J Appl Phys 94:6358
59. Vidoni O, Philippot K, Amiens C, Chaudret B, Balmes O, Malm J-O, Bovin J-O, Senocq F, Casanove M-J (1999) Angew Chem 38:3736

60. Pelzer K, Vidoni O, Philippot K, Chaudret B, Collière V (2003) Adv Funct Materials 13:118
61. Pelzer K, Philippot K, Chaudret B (2003) Zeitschrift Phys Chem 217:1539
62. Ramirez E, Jansat S, Philippot K, Lecante P, Gomez M, Masdeu-Bultó AM, Chaudret B (2004) J Organomet Chem 689:4601
63. Ramirez E, Eradès L, Philippot K, Chaudret B (unpublished results)
64. Gomez S, Erades L, Philippot K, Chaudret B, Collière V, Balmes O, Bovin J-O (2001) Chem Commun 1474
65. Bönnemann H, Braun GA (1997) Chem Eur J 3:1200
66. Köhler JU, Bradley JS (1998) Langmuir 14:2730
67. Gomez M, Philippot K, Collière V, Lecante P, Muller G, Chaudret B (2003) New J Chem 27:114
68. Gomez M, Philippot K, Chaudret B (unpublished results)
69. Jansat S, Gómez M, Philippot K, Muller G, Guiu E, Claver C, Castillón S, Chaudret B (2004) J Am Chem Soc 126:1592
70. Dumestre F, Martinez S, Zitoun D, Fromen M-C, Casanove M-J, Lecante P, Respaud M, Serres A, Benfield RE, Amiens C, Chaudret B (2004) Faraday Discuss Chem Soc 125:265
71. Soulantica K, Maisonnat A, Fromen M-C, Casanove M-J, Chaudret B (2003) Angew Chem (Int Ed) 42:1945
72. Guari Y, Thieuleux C, Mehdi A, Reyé C, Corriu RJP, Gomez-Gallardo S, Philippot K, Chaudret B (2003) Chem Mat 15:2017
73. Guari Y, Soulantica K, Philippot K, Thieuleux C, Mehdi A, Reyé C, Chaudret B, Corriu RJP (2003) New J Chem 27:1029
74. Cordente N, Amiens C, Respaud M, Senocq F, Chaudret B (2001) Nano Letters 1:565
75. Soulantica K, Maisonnat A, Senocq F, Fromen M-C, Casanove M-J, Chaudret B (2001) Angew Chem (Int Ed) 40:2983
76. Dumestre F, Chaudret B, Amiens C, Fromen M-C, Casanove M-J, Renaud P, Zurcher P (2002) Angew Chem (Int Ed) 41:4286
77. Dumestre F, Chaudret B, Amiens C, Respaud M, Fejes P, Renaud P, Zurcher P (2003) Angew Chem (Int Ed) 42:5213
78. Snoeck E, Dunin-Borkowski RE, Dumestre F, Renaud P, Amiens C, Chaudret B, Zurcher P (2003) App Phys Lett 82:88
79. Dumestre F, Chaudret B, Amiens C, Renaud P, Fejes P (2004) Science 303:821

Top Organomet Chem (2005) 16: 261–279
DOI 10.1007/b138080

Published online: 10 September 2005

Stabilized Noble Metal Nanoparticles: An Unavoidable Family of Catalysts for Arene Derivative Hydrogenation

Alain Roucoux

UMR CNRS 6052 "Synthèses et Activations de Biomolécules",
Ecole Nationale Supérieure de Chimie de Rennes – Institut de Chimie de Rennes,
Avenue du Général Leclerc, 35700 Rennes, France
Alain.Roucoux@ensc-rennes.fr

Abstract Transition-metal nanoparticle science is a strategic research area in material development due to their particular physical and chemical properties. Today, catalysis is the usual application of metal nanoparticles synthesized by a variety of methods. This chapter reviews the recent progress in the hydrogenation of monocyclic aromatic compounds by noble metal nanoparticles in various liquid media. The review begins with an introduction to nanoparticle science and to our main interest of arene derivative hydrogenation. Then, Sect. 2 describes several efficient stabilized catalytic systems in total hydrogenation of classical benzene derivatives under mild conditions. Some examples of significant results obtained in partial hydrogenation of benzene or anisole by soluble nanocatalysts are also presented in Sect. 3.

Keywords Arenes · Catalysis · Hydrogenation · Nanoparticles

Abbreviations
TOF turnover frequency

TTO total turnover
PVP polyvinylpyrrolidone
S/C substrate/catalyst
Conv. conversion rate
TEM transmission electron microscopy
XRD X-ray diffraction
XPS X-ray photoelectron spectroscopy
COD cyclooctan-1,5 diene
COT cyclooctan-1,3,5 triene
iPr isopropyl
tBu tertiobutyl

1 General Aspects

1.1 Arene Hydrogenation

The total hydrogenation of benzene derivatives represents an important industrial catalytic transformation, in particular with the conversion of benzene into cyclohexane, a key intermediate in adipic acid synthesis, which is used in the production of Nylon-6,6 (Scheme 1). This reaction is still the most important industrial hydrogenation reaction of monocyclic arenes [1].

Moreover, the increasing industrial demand for low-aromatic diesel fuels [2] stimulated by the discovery that diesel exhaust particles generate various respiratory allergies, contributes to developing this area of research area [3–5].

The partial arene derivative hydrogenation into cyclohexene or cyclohexadiene as intermediates is also investigated. The process developed by Asahi Chemical Industry in Japan is an example of the selective formation of cyclohexene [6]. In the future, this reaction could be an active area of research due to the potential of the intermediate in organic synthesis.

Finally, hydrogenation of aromatic rings in synthetic or natural polymers such as polystyrene or lignin, respectively, is also investigated for various applications. The polystyrene hydrogenation process developed by Dow Plastics for media applications is an interesting example [7, 8].

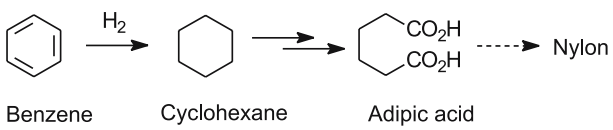

Scheme 1 Synthetic route to adipic acid

Traditionally, monocyclic arene hydrogenation is carried out in drastic conditions with heterogeneous catalysts [9–18] such as Rh/Al_2O_3 and Raney Nickel or metal sulfides. Nevertheless, some pure homogeneous systems have been reported [19–23].

In the past five years, the use of nanoparticles in this active research area has received increased attention since some homogeneous catalysts have been shown to be "nanoheterogeneous" [24–26]. Today, soluble noble metal nanoparticles are considered as reference in monocyclic arene catalytic hydrogenation under mild conditions and several stabilized systems have been reported [27, 28].

1.2 Nanoparticle Concepts

Catalysis is the essential application of metal nanoparticles but, due to their particular physical and chemical properties, they also find application in such diverse fields as photochemistry, electronics, optics or magnetism [29–37]. Zero-valent nanocatalysts can be obtained from two strategic approaches according to the nature of the precursor namely (i) well-known transition metal salts reduction [27]; (ii) organometallic compounds able to decompose in nanomaterials [38]. Today, the key goal is the development of reproducible nanoparticle (or modern nanoclusters) syntheses in opposition to larger particles and bulk material [30]. Consequently, nanoclusters should be or have at least (i) a specific size (1–10 nm); (ii) a well-defined surface composition; (iii) reproducible syntheses and properties; and (iv) isolable and redissolvable. Several synthetic methods are mainly described: (i) chemical reduction; (ii) thermal, photochemical or sonochemical decomposition; (iii) metal vapor synthesis; and (iv) electrochemical reduction [27, 30]. Nevertheless, whatever the method used a protective agent is generally necessary to prevent the aggregation of the colloids formed into bulk material. This aggregation leads to the loss of the properties associated to the colloidal state of these particles. The stabilization of metallic colloids and thus the means to preserve their finely dispersed state is a crucial aspect to consider during their synthesis. Several general discussions on the stability of colloids and nanoclusters have already been reported [29, 30].

At short interparticle distances, the van der Walls forces show that two metallic particles will be mutually attracted. In the absence of repulsive forces opposed to the van der Walls forces the colloidal metal particles will aggregate. Consequently, the use of a protective agent able to induce a repulsive force opposed to the van der Walls forces is necessary to provide stable nanoparticles in solution. The general stabilization mechanisms of colloidal materials have been described in Derjaguin–Landau–Verway–Overbeck (DLVO) theory. [40, 41] Stabilization of colloids is usually discussed

in terms of two general categories: (i) charge stabilization and (ii) steric stabilization.

1.2.1 Electrostatic Stabilization

Ionic compounds such as halides, carboxylates or polyoxoanions, dissolved in (generally aqueous) solution can generate electrostatic stabilization. The adsorption of these compounds and their related counter ions on the metallic surface will generate an electrical double-layer around the particles (Fig. 1). The result is a coulombic repulsion between the particles. If the electric potential associated with the double layer is high enough, then the electrostatic repulsion will prevent particle aggregation [27, 30].

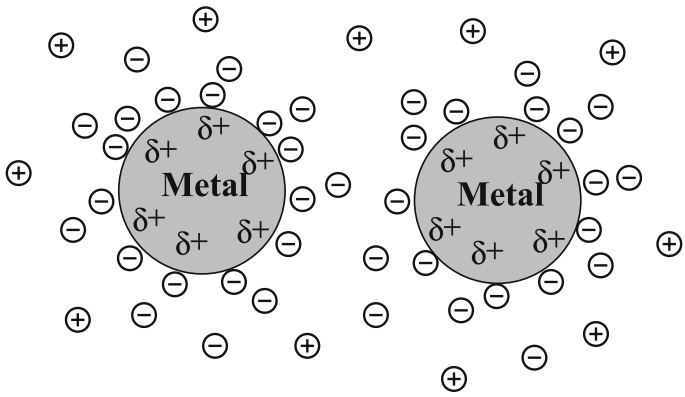

Fig. 1 Schematic representation of electrostatic stabilization

Colloidal suspensions stabilized by electrostatic repulsion are very sensitive to any phenomenon able to disrupt the double layer like ionic strength or thermal motion.

1.2.2 Steric Stabilization

Transition metal colloids can also be prevented from agglomeration by polymers or oligomers [27, 30, 42, 43]. The adsorption of these molecules at the surface of the particles provides a protective layer. In the interparticle space, the mobility of adsorbed molecules should be reduced decreasing the entropy and thus increasing the free energy (Fig. 2).

A second effect is due to the local growth of adsorbed macromolecules as soon as the two protective layers begin to interpenetrate. This results in an osmotic repulsion to restore the equilibrium by diluting the macromolecules

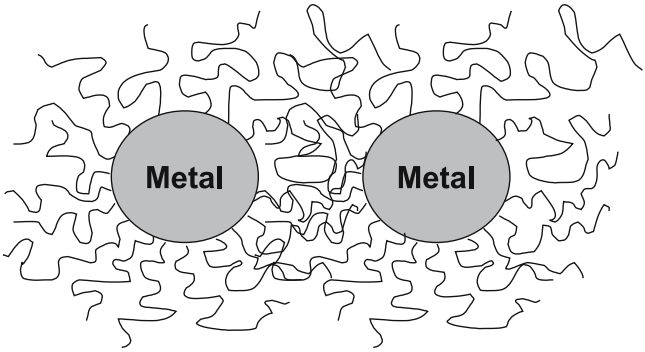

Fig. 2 Schematic representation of steric stabilization

and thus separating the particles. By contrast with the electrostatic stabilization which is mainly used in aqueous media, the steric stabilization can be used in the organic or in the aqueous phase. Nevertheless the length and/or the nature of the macromolecules adsorbed influence the thickness of the protective layer and can thus modify the stability of the colloidal metal particles.

The electrostatic and steric effects can be combined to stabilize nanoparticles in solution. This kind of stabilization is generally provided by means of ionic surfactants [44–47]. These compounds bear a polar head group able to generate an electric double layer and a lypophilic side chain able to provide steric repulsion. The electrosteric stabilization can be also obtained from polyoxoanions such as the couple ammonium (Bu_4N^+)/polyoxoanion ($P_2W_{15}Nb_3O_{62}{}^{9-}$). The significant steric repulsion of the bulky Bu_4N^+ countercations associated with the highly charged polyoxoanion (Coulombic repulsion) provide an efficient electrosterical stability towards agglomeration in solution of the resultant nanocatalysts [28, 30].

Finally, the term steric stabilization could be used to describe protective transition-metal colloids with traditional ligands or solvents [38]. This stabilization occurs by (i) the strong coordination of various metal nanoparticles with ligands such as phosphines [48–51], thiols [52–55], amines [54, 56–58], oxazolines [59] or carbon monoxide [51]; (ii) weak interactions with solvents such as tetrahydrofuran or various alcohols. Several examples are known with Ru, Pt and Rh nanoparticles [51, 60–63]. In a few cases, it has been established that a coordinated solvent such as heptanol is present at the surface and acts as a weakly coordinating ligand [61].

Finally, the development of modified nanoparticles with a better lifetime and activities for various applications in catalysis remains an important challenge. Several recent investigations have made possible interesting results in various research areas around soluble nanoparticles: synthesis, characterizations and their applications. In this context, total, partial or selective arene hydrogenations have received considerable attention and could still be

a promising application for future studies. This second section describes significant results obtained in various media by several catalytic systems. Four approaches seem to be highly efficient according to (i) the protective agent: PVP, Polyoxoanion, surfactant and ionic liquids; and (ii) the nature of the precursor: metal salts or organometallic compounds.

2
Total Hydrogenation by Protected Nanocatalysts

2.1
PVP Stabilization

The immobilization of metal nanoparticles in a water soluble polymer material such as polyvinylpyrrolidone (PVP) has been largely described. The groups of Choukroun and Chaudret reported the preparation and characterization of rhodium nanoparticles embedded in PVP [64]. Rhodium (0) colloids are prepared starting from the organometallic $[RhCl(C_2H_4)_2]_2$ complex with two equivalents of Cp_2V as the reducing agent in the presence of PVP. A black solid is separated from the THF solution showing from 5 to 10 wt % of rhodium in the polymer (Fig. 3).

The solid is used as a heterogeneous catalyst or as a water-soluble system in biphasic conditions in the hydrogenation of benzene and phenylacetylene [65]. The heterogeneous system Rh-PVP is investigated in the solid/liquid catalytic hydrogenation of benzene with a ratio of 1/34 000 at 80 °C and 20 bar H_2. The conversion into cyclohexane is about 60% after 200 h of reaction time. In a water/benzene biphasic condition at 30 °C and under 7 bar H_2, complete hydrogenation (Scheme 2) for a molar ratio of 2000 is observed after 8 h giving a TOF = 675 h^{-1} (related to H_2 consumed), never-

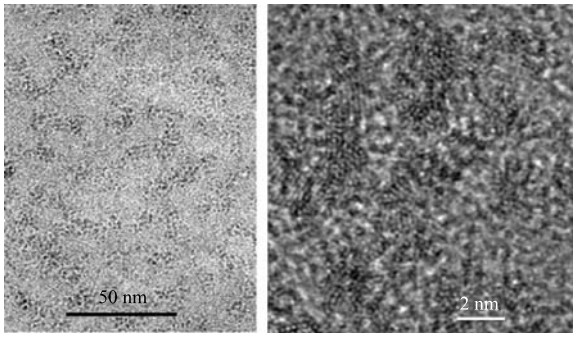

Fig. 3 PVP-protected rhodium nanoparticles **a** TEM micrograph **b** HREM micrograph

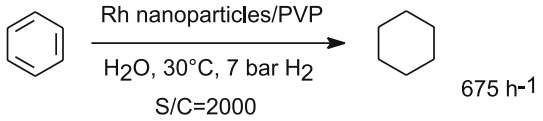

Scheme 2 Benzene hydrogenation by Rh/PVP system

theless, in methanol solution, no reaction is observed with soluble nanoparticles.

The presence of soluble Rh nanoparticles after catalysis is demonstrated by TEM. The kinetic of the catalytic reaction was found to be zero-order in respect to the substrate and first order with respect to hydrogen and catalyst. Curiously, under the same conditions (60 °C, 7 bar H_2), ethylcyclohexane is not detected at the end of phenylacetylene hydrogenation and the formation of methylcyclohexane from toluene was only obtained under drastic conditions 40 bar H_2 and 80 °C.

Finally, the groups of Chaudret and Choukroun have demonstrated that PVP-protected native Rh nanoparticles synthesized by an organometallic approach are active in the hydrogenation of benzene in a biphasic mixture.

A similar polymer-stabilized colloidal system is described by James and coworkers [66]. Rhodium colloids are obtained by reducing $RhCl_3$, $3H_20$ with ethanol in the presence of PVP. The monophasic hydrogenation of various substrates such as benzyl acetone and 4-propylphenol and benzene derivatives was performed under mild conditions (25 °C and 1 bar H_2). The nanoparticles are poorly characterized and benzyl acetone is reduced with 50 TTO in 43 h.

2.2 Stabilization in Ionic Liquids

In 2003, Dupont and coworkers have described the use of room-temperature imidazolium ionic liquids for the formation and stabilization of transition-metal nanoparticles. Rhodium(0) and iridium(0) nanoparticles are prepared from $RhCl_3$, $3H_2O$, and $[Ir(COD)Cl]_2$, respectively, in dry 1-butyl-3-methylimidazolium hexafluorophosphate (BMI PF6) ionic liquid under hydrogen pressure (4 bar) and 75 °C. Anhydrous conditions are necessary to avoid the partial decomposition of the ionic liquid into phosphates. The nanoparticles are isolated by centrifugation or used for hydrogenation reactions. TEM and XRD analysis show the formation of zero-valent metal nanoparticles around 2.0–2.5 nm in diameter. The isolated colloids can be used as solids (heterogeneous catalyst), in acetone (homogeneous catalyst) or re-dispersed in BMI PF6 (biphasic system) for benzene hydrogenation studies [67]. Lower reaction times for total hydrogenation are observed when the reaction is performed under homogeneous or heterogeneous conditions. Nevertheless, the interest in the use of ionic liquid is to promote a biphasic

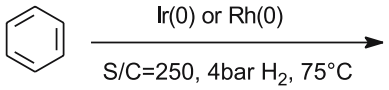

	TOF (h^{-1})		
	BMI PF_6	no solvent	acetone
Ir	50	125	200
Rh	11	21	16

Scheme 3 Hydrogenation of benzene by nanoparticles in various media

catalytic system for the recycling of these ionic liquid-stabilized nanoparticles. The mixture forms a two-phase system constituted by the lower phase containing the catalyst in the ionic liquid and the upper phase containing the organic products. In this condition, the performances were limited and no recycling studies were performed. A comparison of the nature of the metal shows that iridium(0) nanoparticles are much more active for the benzene hydrogenation than their rhodium(0) analogues (Scheme 3).

Iridium and rhodium nanoparticles have also been studied in the hydrogenation of various aromatic compounds. In all cases, total conversions were not observed in BMI PF6. TOFs based on mol of cyclohexane formed were 44 h^{-1} for toluene hydrogenation with Ir (0) and 24 h^{-1} and 5 h^{-1} for *p*-xylene reduction with Ir(0) or Rh(0) nanoparticles, respectively. The *cis*-1,4-dimethylcyclohexane is the major product and the *cis*/*trans* ratio depends on the nature of the metal: 5 : 1 for Ir(0) and 2 : 1 for Rh(0). TEM experiments show a mean diameter of 2.3 nm and 2.1 nm for rhodium and iridium particles, respectively. The same nanoparticle size distribution is observed after catalysis (Fig. 4).

Similarly to Iridium and rhodium nanoparticle studies, Dupont describes benzene hydrogenation in various media by platinum(0) nanoparticles prepared by simple decomposition of $Pt_2(dba)_3$ in BMI PF_6 at 75 °C and under 4 bar H_2 [68]. The Pt nanoparticles were isolated by centrifugation and char-

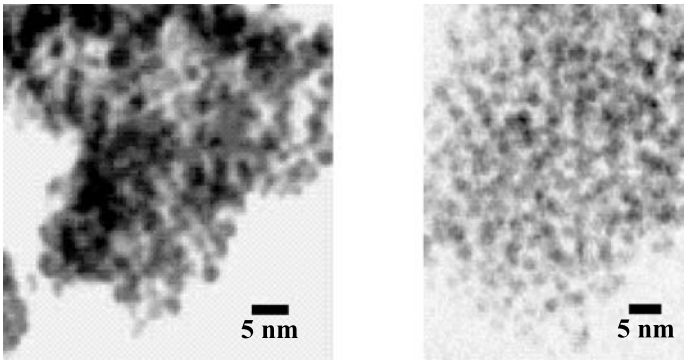

Fig. 4 TEM observation of nanoparticles after catalysis. Rh (*left*) and Ir (*right*)

acterized by TEM observations showing the formation of Pt(0) particles of 2–2.5 nm in diameter. The isolated material was used for benzene hydrogenation after re-dispersion in the ionic liquid or used as a heterogeneous catalyst. Best results were obtained in heterogeneous (solventless) conditions TOF = 28 h^{-1} for 100% of conversion but the TOF dramatically decreased in biphasic liquid-liquid conditions (BMI PF_6) up to 11 h^{-1} at 46% of conversion justifying the absence of recycling studies with this substrate. Recently, Dupont and coworkers have reported the preparation of Ru(0) nanoparticles made of reducing organometallic compound Ru(COD)(COT) in 1-*n*-butyl-3-methylimidazolium hexafluorophosphate room temperature ionic liquid (BMI PF_6) with hydrogen pressure [69]. TEM experiments show Ru(0) nanoparticles with an average diameter of 2.6 ± 0.4 nm inside spherical superstructures of 57 ± 8 nm (Fig. 5). XRD and XPS analysis indicated that the solid is made of particles consisting of hexagonal closed-packed ruthenium and the presence of a passivated surface layer due to an external surface ruthenium atom oxidation.

The isolated Ru(0) nanoparticles were used as solids (heterogeneous catalyst) or re-dispersed in BMI PF6 (biphasic liquid-liquid system) for benzene hydrogenation studies at 75 °C and under 4 bar H_2. As previously described for rhodium or iridium nanoparticles, these nanoparticles (heterogeneous catalysts) are efficient for the complete hydrogenation of benzene (TOF = 125 h^{-1}) under solventless conditions. Moreover, steric substituent effects of the arene influenced the reaction time and the decrease in the catalytic TOF: 45, 39 and 18 h^{-1} for the toluene, iPr-benzene, tBu-benzene hydrogenation, respectively. Finally, The hydrogenation was not total in BMI PF_6, a poor TOF of 20 h^{-1} at 73% of conversion is obtained in the benzene hydrogenation.

In summary, Dupont and coworkers have developed an organometallic approach for the stabilization of various zero-valent nanoparticles in the ionic liquid BMI PF_6. Transition metal nanoparticles of 2.0–3.0 were obtained with

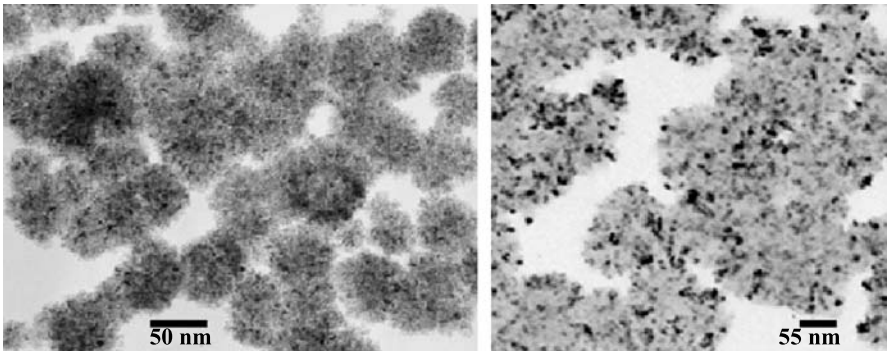

Fig. 5 TEM observation of Ru(0) nanoparticle superstructures (*left*) and inside the superstructures (*right*)

a narrow size distribution. Characterization studies have shown the interaction of the ionic liquid with the particle surface. These nanoparticles are efficient catalysts for the hydrogenation of benzene and classical derivatives (Ir > Ru > Rh ≈ Pt) nevertheless; best performances are obtained in heterogeneous or homogeneous conditions. In biphasic liquid-liquid conditions, the main goal in terms of product separation and catalyst recycling, the results show lower efficiency and nanoparticles stabilized in ionic liquid should be optimized in the future.

2.3 Stabilization by Polyoxoanion

Finke and coworkers have developed an efficient soluble nanocluster arene hydrogenation catalyst in terms of catalytic lifetime. This research group describes the use of polyoxoanion- and ammonium-stabilized rhodium zero-valent nanoclusters which combine electrostatic stabilization (high polyoxoanion charge $P_2W_{15}Nb_3O_{62}^{9-}$) and associated tetrabutylammonium and polyoxoanion steric stabilization components $[(Bu_4N^+)_9 \cdot (P_2W_{15}Nb_3O_{62}^{9-})]$ [30]. The nanocluster catalyst is formed in situ by reducing organometallic precursor $[Bu_4N]_5Na_3[(COD)Rh \cdot P_2W_{15}Nb_3O_{62}]$ with H_2 in a monophasic propylene carbonate solution. This organometallic approach allows reproducible preparation of stabilized nanoparticles starting from a well-defined complex in terms of composition and structure. TEM analyses after ether precipitation show the formation of zero-valent nanoparticles with an average diameter of 5.3 nm containing around 5700 Rh atoms (Fig. 6) [26]. The authors have shown the influence of the nanocluster formation conditions on the average diameter.

The polyoxoanion-stabilized Rh(0) nanoclusters were investigated in anisole hydrogenation [26]. The catalytic reaction experiments were performed in a single phase using a propylene carbonate solution under mild conditions: 22 °C, 3.7 bar of H_2. In these standard conditions, anisole hydrogenation with a ratio S/Rh = 2600 was performed in 120 h giving a TTO of 1500 ± 100. The effects on catalytic performance of added proton donors such as $HBF_4 \cdot Et_2O$ or H_2O which increase the catalytic activity were investigated. With 10 equivalent of $HBF_4 \cdot Et_2O$ added versus Rh, Finke reports

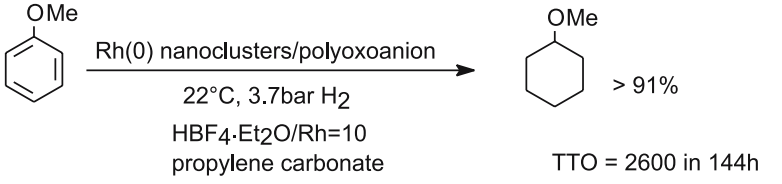

Scheme 4 Hydrogenation of anisole by polyoxoanion-stabilized Rh(0) nanocluster catalyst

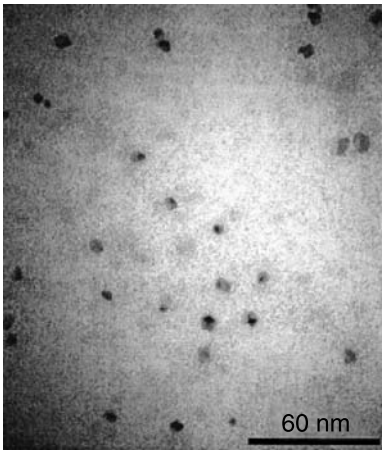

Fig. 6 TEM observation of Rh(0) nanoclusters prepared under H_2 in propylene carbonate

2600 TTO for complete anisole hydrogenation in 144 h at 22 °C and 3.7 bar of H_2 (Scheme 4).

A similar result is obtained with 30 equivalents of H_2O added but a long reaction time is required namely 215 h. Nevertheless, in all cases a black precipitate of bulk Rh(0) is visible at the end of the reaction justifying the destabilization of nanoclusters due to the interaction of H^+ or H_2O with the basic $P_2W_{15}Nb_3O_{62}^{9-}$ polyoxoanion. Finally, the partial hydrogenation of anisole to yield 1-methoxycyclohexane (up to 8%) with a soluble nanocluster catalyst has been reported by Finke and coworkers (see Sect. 3).

2.4 Stabilization by Surfactant

A typical approach to stabilize colloids in the aqueous phase and to prevent their aggregation is the use of tetraalkylammonium salts. The first colloidal catalytic system was observed in 1983–1984 by Januszkiewicz and Alper [70, 71] which used an organometallic approach for the hydrogenation of several benzene derivatives in biphasic conditions using [RhCl(1,5-hexadiene)]$_2$ and the tetraalkylammonium bromide as the protective agent. Under atmospheric hydrogen pressure and room temperature, up to 100 TTO are observed. A similar system is described by Lemaire and coworkers for hydrogenation of dibenzo-18-crown-6-ether ($DB_{18}C_6$, 20 mol) into the major product syn,anti-dicyclohexano-18-crown-6-ether in 1 h starting with $RhCl_3$, $3H_2O$ as the metal salt precursor and methyltrioctylammonium chloride [72, 73]. TEM experiments show the presence of nanoparticles in the 2–3 nm size range. In 1997–1998, James and coworkers described rhodium and ruthenium colloidal preparation stabilized by tetrabutylammonium

salts for the hydrogenation of lignin model compounds containing the 4-propylphenol fragment under a biphasic medium and various conditions (20–100 °C, 1–50 bar H_2) [74–76]. Organometallic and metal salt approaches were investigated with various precursors such as $[RhCl(1,5\text{-hexadiene})]_2$, $[RhCl(COD)]_2$,$[Rh(OC_6H_5)(COD)]_2$, $RhCl_3$, $3H_2O$ and $RuCl_3$, $3H_2O$. The best result is obtained for the hydrogenation of 2-methoxy-4-propylphenol by ruthenium nanoparticles with 300 TTO in 24 h.

Recently, progress has been made based on the use of surfactants as protective agents. In 1999, our group prepared an aqueous suspension of rhodium(0) colloids by reducing $RhCl_3$, $3H_2O$ with $NaBH_4$ in the presence of highly water soluble *N*,*N*-dimethyl-*N*-cetyl-*N*-(2-hydroxyethyl)ammonium salts (counter anion: Br, Cl, I, CH_3SO_3, BF_4) which provide an electrosterical stabilization. Nanoparticles catalyze the hydrogenation of various mono-, di-substituted and/or functionalized arene derivatives in pure biphasic liquid-liquid (water/substrate) media at room temperature and under atmospheric hydrogen pressure [44–46]. Significant results have been obtained for the hydrogenation of anisole with 2000 TTO in 37 h (Scheme 5). The nanoparticle catalyst can be separated by simple decantation or the product extracted with an appropriate solvent.

The durability of the catalytic system was investigated by employing it in five successive hydrogenations. Similar TOFs were observed due to the water solubility of the protective agent which retains nanoparticles in aqueous phase. The comparative TEM studies show that (i) the average particle size was 2.2 ± 0.2 nm; (ii) the counter anion of the surfactant does not allow a major influence on the size; and (iii) nanoparticle suspensions have a similar size distribution after catalysis.

The efficient hydrogenation of various benzene compounds in biphasic systems has also been described by similar surfactant-protected iridium(0) nanoparticles [47]. The solubility of the nanoparticles was assured by 10 equivalents of water-soluble *N*,*N*-dimethyl-*N*-cetyl-*N*-(2-hydroxyethyl)-ammonium chloride salt. TEM observations show that the particles are monodispersed in size with an average diameter of 1.9 ± 0.7 nm (Fig. 7).

The hydrogenation of arenes is performed at room temperature and under 40 bar of H_2. In all cases, the conversion is complete after a few hours. 3000 TTO are demonstrated for anisole hydrogenation in 45 h (Scheme 5).

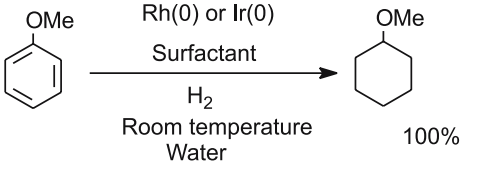

	Rh (1bar H_2)	Ir (40bar H_2)
TOF(h^{-1})	188	200
TTO	2000	3000

Scheme 5 Hydrogenation of anisole by surfactant-stabilized Rh(0) and Ir(0) catalysts

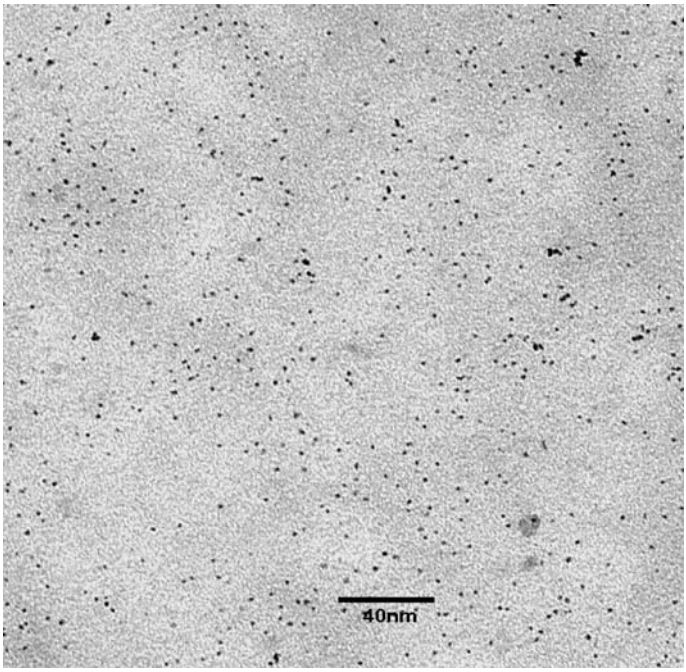

Fig. 7 TEM micrograph of Ir(0) nanoparticles

The catalytic lifetime was studied by reusing the aqueous phase for three successive hydrogenation runs of toluene, anisole and cresol. Similar turnover activities were observed during the successive runs. These results show the good stability of the catalytically active iridium suspension as previously described with rhodium nanoparticles.

The selectivity in the hydrogenation of di-substituted benzenes such as xylene, methylanisole, cresol was also reported. In all cases, the *cis*-compound is largely the major compound > 80%. The ratio *cis*/*trans* decreases with the position of the substituents $o > m > p$ but the identity of the metal does not seem important with this surfactant-stabilized system [45, 47].

Finally, these aqueous suspensions of rhodium(0) and iridium(0) are the most efficient systems for the hydrogenation of a large variety of mono-, di-substituted and/or functionalized arene derivatives. Moreover, in our approach, the reaction mixture forms a typical two-phase system with an aqueous phase containing the nanoparticle catalyst able to be easily reused in a recycling process.

In 1999, Albach and Jautelat described in a patent the use of a sulfobetaine as the surfactant to stabilize Ru, Rh, Pd, Ni nanoparticles and bimetallic mixtures [77]. Benzene, cumene and isopropylbenzene are reduced in biphasic media under various conditions 100–150 °C and 60 bar of H_2. 250 TTO are

demonstrated but no recycling process of the aqueous suspensions of colloids stabilized by the dodecyldimethylammonium propanesulfonate is reported.

Finally, Jessop and coworkers describe an organometallic approach to prepare in situ rhodium nanoparticles [78]. The stabilizing agent is the surfactant tetrabutylammonium hydrogen sulfate. The hydrogenation of anisole, phenol, *p*-xylene and ethylbenzoate is performed under biphasic aqueous/supercritical ethane medium at 36 °C and 10 bar H_2. The catalytic system is poorly characterized. The authors report the influence of the solubility of the substrates on the catalytic activity. *p*-xylene was selectively converted to *cis*-1,4-dimethylcyclohexane (53% versus 26% *trans*) and 100 TTO are obtained in 62 h for the complete hydrogenation of phenol, which is very soluble in water.

To conclude, we have described four significant catalytic systems based on the use of various protective agents: PVP, polyoxoanion, surfactants and ionic liquids. These studies have essentially shown two approaches to preparing nanocatalysts according to the nature of the precursor: metal salts or organometallic compounds. The choice depends on the medium of the reaction: organic, aqueous, mono- or biphasic and so the protective agent employed but also in order to obtain a better control of the size and clean surfaces. Nevertheless, in all cases, "near" monodispersed colloidal suspensions are obtained and provide efficient activity and catalytic lifetime for the hydrogenation of monocyclic arene derivatives. A comparison of stabilized catalytic systems for the hydrogenation of benzene and anisole has been previously reported by our group and shows very competitive nanoparticle systems in this research area [47].

3
Partial Hydrogenation by Nanocatalysts

For some years, the total hydrogenation of monocyclic arene compounds has been largely studied and results are now very efficient. In the future, the partial arene derivative hydrogenation into cyclohexene or cyclohexadiene should be highlighted as key intermediates in organic synthesis. The hydrogenation to corresponding cycloalkenes is usually carried out with a heterogeneous catalyst in particular ruthenium catalysts [79]. The process developed by Asahi Chemical Industry in Japan is a significant example of the selective formation of cyclohexene [6]. The reaction is performed in a tetraphasic system: gas, oil, water and solid. The "bulk" catalyst containing ruthenium particles is prepared by reducing a ruthenium compound in the presence of zinc as a co-catalyst. The heterogeneous catalyst consists of particles with an average crystalline particle diameter of 20 nm. Dispersing agents such as various metal oxides, hydroxides, or hydrates have been used

to limit agglomeration and to extend the life of the catalyst, nevertheless the true nature of the catalyst (ruthenium and zinc oxidation states) has not been established. The selectivity for cyclohexene is very high and a yield of 60% for cyclohexene is obtained at 150 °C and under 50.4 bar of H_2.

In fact, partial hydrogenations are rarely described with soluble nanoparticle catalysts. Two examples are explained in the literature, one reported by Finke and coworkers in the hydrogenation of anisole with polyoxoanion-stabilized Rh(0) nanoclusters [26] and one reported by Dupont and coworkers in the hydrogenation of benzene with nanoscale ruthenium catalysts in room temperature imidazolium ionic liquids [69]. In these two cases, the yields are very modest.

3.1 Polyoxoanion-Stabilized Rh(0) Nanoclusters

The hydrogenation of anisole with polyoxoanion-stabilized Rh(0) nanoclusters yields 91% of methoxycyclohexane (Sect. 2.3), nevertheless the authors also observed the partial hydrogenation product (up to 8%) and the hydrogenolysis product in trace amounts (cyclohexane and methanol < 1%) [26]. The catalytic hydrogenation to 1-methoxycyclohexene was investigated under various conditions such as higher temperature and added solvents or equivalent of protective agent. Under standard conditions (22 °C, 40 psig H_2, S/Rh = 2600), the partial hydrogenation product was obtained with an initial selectivity of 30% and the maximum yield was 2.1%. At 78 °C, 1-methoxycyclohexene is obtained with a yield of 8% corresponding to an unprecedented selectivity for a partial hydrogenation of an aryl ether with a soluble nanocatalyst system (Scheme 6). Nevertheless, complete deactivation occurred within about 1 h (conv. 41%) showing the limit of this catalytic system. The authors mentioned no effects on catalytic performances of added $P_2W_{15}Nb_3O_{62}^{9-}$ polyoxoanion or solvents (H_2O, acetone).

TEM experiments show nanoparticles with an average diameter of 5.7 nm similar to the initial diameter consequently, Finke and coworkers concluded that deactivation at 41% of conversion was due to a surface deactivation of their nanocatalyst.

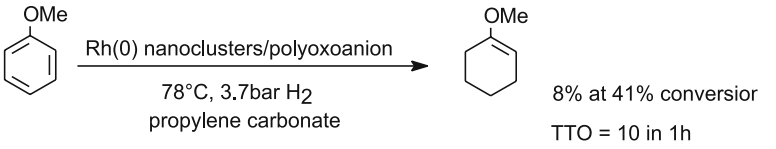

Scheme 6 Partial hydrogenation of anisole by polyoxoanion-stabilized Rh(0) nanocluster catalyst

In summary, partial hydrogenation of anisole to 1-methylcyclohexene by polyoxoanion-stabilized Rh(0) nanoclusters is very modest but could in the future be an interesting additive study in the monocyclic arene hydrogenation research area.

3.2
Ionic Liquids-Protected Ru(0) Nanoparticles

Recently, Dupont has used the recommended Chaudret's method (organometallic approach, [60, 62]) to generate well-defined Ru(0) nanoparticles [69]. The controlled decomposition of a Ru(COD)(COT) dispersed in 1-butyl-3-methylimidazolium hexafluorophosphate room temperature ionic liquid (BMI PF_6) with hydrogen produces Ru(0) nanoparticles with an average particle size of 2.6 ± 0.4 nm. These nanoparticles (heterogeneous catalysts) are efficient for the hydrogenation of benzene and its derivatives under solventless conditions at 75 °C and under 4 bar of H_2 (see Sect. 2.2). The authors describe the partial hydrogenation of benzene to cyclohexene with a process based on the different benzene/cyclohexene solubility in BMI PF_6 with a Ru(0) nanoparticles containing phase. Dupont and coworkers demonstrate selectivities up to 39% in cyclohexene at very low benzene conversion (< 1%) and a maximum yield of 2% is obtained (Scheme 7).

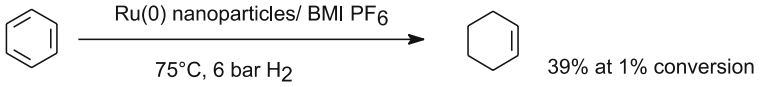

Scheme 7 Partial hydrogenation of benzene by Ru(0) nanocatalysts in room temperature imidazolium ionic liquid

As judiciously reported by the authors, the yields are too low for technical applications but this reaction represents the second example of partial hydrogenation of monocyclic arene by soluble transition metal nanoparticles.

4
Conclusion

We have described four significant catalytic systems consisting of stabilized metal nanoparticles in the hydrogenation of monocyclic aromatic compounds. Four noble metals are efficient in this reaction: Rh, Ru, Ir, and Pt. Several stabilization methods have been described which represent typical nanoparticle stabilizers: polymers, surfactants, polyoxoanions and ionic liquids. Two approaches are developed for the preparation of nanocatalysts which provide interesting results in catalytic applications: the reduction starting with an organometallic precursor or a metal salt. The organometallic

approach is more interesting to control the clean surface but requires the synthesis of the appropriate precursor. Whatever approach is used, the soluble nanoparticle catalysts are efficient for arene hydrogenation under mild conditions in which very high activity and lifetime are achieved. Two catalytic systems can directly be used in biphasic liquid-liquid media for a potential recycling process without a re-dispersion step, one developed by J. Dupont in ionic liquids and one based on an aqueous suspension developed by our team. Undoubtedly, the system consisting of surfactant-stabilized Rh(0) nanoparticles is the best in terms of recycling. In many cases, TEM studies of nanoparticles show an average particle size of 2–3 nm. Moreover, a variety of additional techniques derived from the solid state are commonly used to achieve precise composition (EDX), crystal structure (HREM, XRD), and a fine distribution of metal-metal bonds (WAXS) of nanoparticle aggregates.

Two soluble nanocatalysts have been investigated in partial hydrogenation. The results obtained by Finke or Dupont's catalysts are unsatisfactory but prove that nanoparticles are a potential catalyst for this reaction. In summary, partial hydrogenation of benzene and its derivatives is still a challenge but will be the focus of future research.

Finally, a second area of research for nanoparticles is their immobilization on various supports. The deposition of well-defined nanoparticles on a support by different methods should advantageously replace traditional heterogeneous catalysts in terms of activity and selectivity.

References

1. Weissermel K, Arpe HJ (1993) Industrial Organic Chemistry. VCH, New York, 2nd ed., 343
2. Stanislaus A, Cooper BH (1994) Catal Rev 36:75
3. Casillas AM, Hiura T, Li N, Nel AE (1999) Ann. Allergy Asthma Immunol 83:624
4. Nel AE, Diaz-Sanchez D, Ng D, Hiura T, Saxon A (1998) J Allergy Clin Immunol 102:539
5. Enya T, Suzuki H, Watanabe T, Hirayama T, Hisamatsu Y (1997) Environ Sci Technol 31:2772
6. Nagahara H, Ono M, Konishi M, Fukuoka (1997) Appl Surf Sc 121/122:448
7. Hucul DA, Hahn SF (2000) Adv Mater 12:1855
8. Tullo A (1999) New DVDs provide opportunities for polymers. Chemical and Engineering News 77:14
9. Augustine RL (1996) In: Heterogeneous Catalysis for the Synthetic Chemistry, Chap. 17. Marcel Dekker, New York
10. Siegel S (1991) In: Trost BM, Fleming I (eds) Comprehensive Organic Synthesis Vol 5. Pergamon Press, New York
11. Eisen MS, Marks TJ (1992) J Am Chem Soc 114:10358
12. Keane MA (1997) J Catal 166:347
13. Gates BC (1992) Catalytic Chemistry, Chap 6. Wiley, New York
14. Gao H, Angelici RJ (1997) J Am Chem Soc 119:6937

15. Startsev AN, Rodin VN, Aleshina GI, Aksenov DG (1998) Kinet Catal 39:221
16. Startsev AN, Zakharov II, Rodin VN, Aleshina GI, Aksenov DG (1998) Kinet Catal 39:507
17. Yang H, Marks TJ (1998) J Am Chem Soc 120:13533
18. Yang H, Gao H, Angelici RJ (2000) Organometallics 19:622
19. Collman JP, Hegedus LS, Norton JR, Finke RG (1987) In: Principles and Applications of Organotransition Metal Chemistry, Chap. 10. University Science Books, Mill Valley
20. Plasseraud L, Süss-Fink G (1997) J Organomet Chem 539:163
21. Garcia Fidalgo E, Plasseraud L, Süss-Fink G (1998) J Mol Catal A Chem 132:5
22. Dyson PJ, Ellis DJ, Parker DG, Welton T (1999) Chem Commun 25
23. Süss-Fink G, Faure M, Ward TR (2002) Angew Chem Int Ed 41:99
24. Dyson PJ (2003) Dalton Trans 2964
25. Widegren JA, Finke RG (2003) J Mol Catal A Chem 198:317
26. Widegren JA, Finke RG (2002) Inorg Chem 41:1558 and 41:1625
27. Roucoux A, Schulz J, Patin H (2002) Chem Rev 102:3757
28. Aiken III JD, Finke RG (2003) J Mol Catal A Chem 191:187
29. Bradley JS (1994) In: Schmid G (ed) Clusters and Colloids: From Theory to Application. VCH, New York, pp 459–536
30. Finke RG (2002) In: Feldheim DL, Foss CA, Foss CA Jr (eds) Metal Nanoparticles: Synthesis, Characterization and Applications, Chap. 2. Marcel Dekker, New York, pp 17–54
31. Rao CNR, Kulkarni GU, Thomas PJ, Edwards PP (2000) Chem Soc Rev 29:27
32. Maier SA, Brongersma ML, Kik PG, Meltzer S, Requicha AG, Atwater HA (2001) Adv Mater 13:1501
33. Kamat PV (2002) J Phys Chem B 106:7729
34. Murray CB, Sun S, Doyle H, Betley T (2001) Mater Res Soc Bull 26:985
35. Pileni MP (2001) Adv Funct Mater 11:323
36. Goia DV, Matijevic E (1998) New J Chem 22:1203
37. Henglein A (1989) Chem Rev 89:1861
38. Philippot K, Chaudret B (2003) C R Chimie 6:1019
39. Henglein A (1985) In: Bicke HF (ed) Modern Trends of Colloid Science in Chemistry and Biology. Birkhauser, Basel, p 126
40. Overbeek JTG (1981) In: Goodwin JW (ed) Colloidal Dispersions. Royal Society of Chemistry, London, pp 1–23
41. Evans DF, Wennerström H (1999) In: The Colloidal Domain, second Edition. Wiley-VCH, New York
42. Hunter RJ (1987) In: Foundations of Colloid Science. Oxford University Press, New York, Vol. 1, 316
43. Napper DH (1983) In: Polymeric Stabilization of Colloidal Dispersions. Academic Press, London
44. Schulz J, Roucoux A, Patin H (1999) Chem Commun 535
45. Schulz J, Roucoux A, Patin H (2000) Chem Eur J 6:618
46. Roucoux A, Schulz J, Patin H (2002) Adv Synth & Catal 345:222
47. Mévellec V, Roucoux A, Ramirez E, Philipot K, Chaudret B (2004) Adv Synth & Catal 346:72
48. Schmid G, Pfeil R, Boese R, Bandermann F, Meyers S, Calis GHM, Van Der Velden JWA (1981) Chem Ber 114:3634
49. Amiens C, De Caro D, Chaudret B, Bradley JS, Mazel R, Roucau C (1993) J Am Chem Soc 115:11638

50. Duteil A, Schmid G, Meyer-Zaika W (1995) J Chem Soc Chem Commun 31
51. Rodriguez A, Amiens C, Chaudret B, Casanove MJ, Lecante P, Bradley JS (1996) Chem Mater 8:1978
52. Dassenoy F, Philippot K, Ould Ely T, Amiens C, Lecante P, Snoeck E, Mosset A, Casanove MJ, Chaudret B (1998) New J Chem 22:703
53. Chen S, Kimura K (2001) J Phys Chem B 105:5397
54. Pan C, Pelzer K, Philippot K, Chaudret B, Dassenoy F, Lecante P, Casanove MJ (2001) J Am Chem Soc 123:7584
55. Gomez S, Erades L, Philippot K, Chaudret B, Collière V, Balmes O, Bovin JO (2001) Chem Commu 1474
56. Schmid G, Morun B, Malm JO (1989) Angew Chem Int Ed Engl 28:778
57. Schmid G, Maihack V, Lantermann F, Peschel S (1996) J Chem Soc Dalton Trans 589
58. Schmid G, Emde S, Maihack V, Meyer-Zaika W, Peschel S (1996) J Mol Catal A Chem 107:95
59. Gomez M, Philippot K, Collière V, Lecante P, Muller G, Chaudret B (2003) New J Chem 27:114
60. Vidoni O, Philippot K, Amiens C, Chaudret B, Balmes O, Malm JO, Bovin JO, Senocq F, Casanove MJ (1999) Angew Chem Int Ed 38:3736
61. Pelzer K, Philippot K, Chaudret B (2003) Z Phys Chem 217:1539
62. Pelzer K, Vidoni O, Philippot K, Chaudret B, Colliere V (2003) Adv Funct Mater 13:118
63. Wang Y, Ren J, Deng K, Gui L, Tang Y (2000) Chem Mater 12:1622
64. Choukroun R, De Caro D, Chaudret B, Lecante P, Snoeck E (2001) New J Chem 25:525
65. Pellagatta JL, Blandy C, Collière V, Choukroun R, Chaudret B, Cheng P, Philippot K (2002) J Mol Catal A Chem 178:55
66. Hu TQ, James BR, Lee CL (1997) J Pulp Pap Sci 23:200
67. Fonseca GS, Umpierre AP, Fichtner PFP, Teixeira SR, Dupont J (2003) Chem Eur J 9:3263
68. Scheeren CW, Machado G, Dupont J, Fichtner PFP, Teixeira SR (2003) Inorg Chem 42:4738
69. Silveira ET, Umpierre AP, Rossi LM, Machado G, Morais J, Soares GV, Baumvol IJR, Teixeira SR, Fichtner PFP, Dupont J (2004) Chem Eur J 10:3734
70. Januszkiewicz KR, Alper H (1983) Organometallics 2:1055
71. Januszkiewicz KR, Alper H (1984) Can J Chem 62:1031
72. Drognat-Landré P, Lemaire M, Richard D, Gallezot P (1993) J Mol Catal 78:257
73. Drognat-Landré P, Richard D, Draye M, Gallezot P, Lemaire M (1994) J Catal 147:214
74. Hu TQ, James BR, Rettig SJ, Lee CL (1997) Can J Chem 75:1234
75. Hu TQ, James BR, Lee CL (1997) J Pulp Pap Sci 23:153
76. James BR, Wang Y, Alexander CS, Hu TQ (1998) Chem Ind 75:233
77. Albach RW, Jautelat M (1999) Bayer AG, German Patent DE 19807995
78. Bonilla RJ, Jessop PG, James BR (2000) Chem Commun 941
79. Kluson P, Cerveny L (1995) Appl Catal 128:13

Author Index Volumes 1–16

The volume numbers are printed in italics

Subject Index